Historical sea-level changes in Australia: Testing the Arctic ice melt hypothesis

Sophie Lauren Williams

Doctor of Philosophy

University of York
Environment and Geography
December 2021

Abstract

Rates of regional and global sea-level rise during the 20th century were faster than in any century over the last 3000 years. Sea-level rise accelerated between ~1850 and ~1950, before greenhouse gases became the dominant forcing agent, which suggests, in part, a natural origin. The acceleration appears to have been more rapid in the Southern Hemisphere, which, according to geophysical theory, could point at a contribution from Northern Hemisphere land-based ice melt. More high-resolution relative sea level (RSL) reconstructions from the Southern Hemisphere are needed to test this hypothesis, and to complement a limited dataset of proxy and tide-gauge records. This study establishes three new RSL records for southeastern Australia (covering ~1830 – 2018) from analyses of salt-marsh sediments. New training sets of contemporary salt-marsh foraminifera were used for transfer-function analyses to derive palaeo sea-level estimates. High-resolution chronologies were established via Accelerator Mass Spectrometry radiocarbon, radiogenic lead, stable lead isotope ratios and pollen analyses. The new records demonstrate that, when corrected for glacio-isostatic adjustment, sea level has risen by ~0.2 – 0.3 m since ~1830 in southeastern Australia. Rates of sea-level rise were especially high over the first half of the 20th century, with maximum average rates of 4.0 (-0.4 – 7.1 95 % confidence range) mm yr^{-1}, but there is regional variability between sites. A modelled sea-level budget indicates that the acceleration was initially driven by the barystatic component (including gravity, rotation and deformation), but subsequently amplified and driven by sterodynamic sea-level change. An analysis of the sea-level fingerprints of the barystatic component to 20th century global sea-level rise points at a significant input from the Greenland (17 %) and Antarctic Ice Sheets (11 %) as well as glaciers in Alaska (14 %), the Russian Arctic (10 %), western Canada and the US (9 %), south Asia and southern Andes (8 % each).

"Do not think for one minute that because you are who you are, you cannot be who you imagine yourself to be."

Dr Jedidah Isler

Contents

List of Tables

List of Figures

Acknowledgements

First and foremost I would like to thank my primary supervisors **Professor Roland Gehrels** and **Dr Ed Garrett** for supporting me over the last four years. Roland taught me the ropes and introduced me to the wonderful world of foraminifera and salt marshes. My favourite PhD times were spent during those sunny evenings in Australia drinking Fat Bastard wine and going on splendid walks. Ed joined a few years into my project and my meetings with him were one of the highlights of my week. He did a wonderful job of guiding me through the ups and downs of the PhD journey and I feel extremely fortunate to have him join my team - my thesis would not be what it is without him.

Secondly, I would like to thank my co-supervisors, **Dr Patrick Moss**, **Dr Soenke Dangendorf** and **Dr Andrew Sole** for their advice and support over the years. A special thanks goes to Patrick for hosting me in Brisbane for several months over the course of the PhD. Meeting and staying with his wonderful family was a highlight of the field campaign.

I would not have considered doing a PhD if it wasn't for the guidance and encouragement from some excellent lecturers during my undergraduate and master's degrees. A special thanks goes to **Dr Karen Bacon**, **Dr Graeme Swindles** and **Dr David Naafs** encouraging me to turn my passion and curiosity for palaeoenvironmental science into a doctorate. During my PhD I also had support from some fantastic female role models: **Dr Fiona Hibbert**, **Dr Niamh Cahill** and **Dr Maria Gehrels**, thank you all for your knowledge, advice and help over the years.

I have heard many people say that a PhD can be a lonely experience, but I was extremely fortunate to have been surrounded by a wonderful cohort of students. I found a lifelong friend in **Luke Andrews**. I have lost count of how many hours, days, weeks, months we spent in the Richard Payne Laboratory looking down microscopes and listening to a random podcast or our favourite soundtracks. I have never laughed so much as during my time spent with him, and I feel so fortunate that we undertook this journey together (even if I did think I was going to meet my untimely end in Cary Numan several times). I was also very fortunate to do my PhD only a year behind **Graham Rush**. From that first croggy I knew we were destined to be good friends, although, I almost fell out with him when he made me do my first ever coring in Aberdeen in December… not really a gentle introduction to our research!

A special thanks also goes to: **Lucy McMahon**, **Lauren Rawlins**, **Tom Sinclair**, **Dave Shaw**, **Katarina Jerbic, Katey Valentine**, **Alex Burkitt**, **Ruochan Ma**, **George Day**, **Abbie Mycroft** and **Nat Anderson.** I have never met a bunch of more supportive and kind individuals and I feel so grateful that I had them to lean on. Thanks also to the ladies of ENV 218 - **Laura Chapman**, **Zakiya Al-Alfifi**, **Talia Contreras**, **Dayang Siti Maryam Binti Mohd Hanan**, **Polly Burns**, **Karla Beltran** and **Sarah Spooner.** They saw me laugh at my desk, they saw me cry at my desk and they brought me into their group with open arms. They continued to give me words of encouragement years after they had all finished and I will never forget their thoughtfulness and friendship. All in all, I could not have asked for a better group of postgraduates to do this wild journey alongside.

The sea-level discussion group: **Graham Rush**, **Geoff Richards**, **Dayang Siti Maryam Binti Mohd Hanan**, **Lucy Wheeler**, **Lucy McMahon**, **Martina Conti**, **Ed Garrett**, **Fiona Hibbert** and

Tabitha Kabora must be credited for keeping me (mostly) sane! Thank you for those much needed coffee breaks and for providing wonderful academic and emotional support during my time at York.

The laboratory and fieldwork behind this PhD was supported by many colleagues. **Patrick Moss**, **Dr Matt-Meredith Williams** (and family), **Rebecca Bartlett**, **Nick Bowden**, **Phillip Stewart**, **Katarina Jerbic**, and **Claire Ellison** aided my field campaigns. I was (and still am) astounded by the generosity of the palaeo community to help fellow scientists - it was an immense pleasure working with you all. Thanks also to **Dr Ian Miller**, **Dr Nicola Atkinson**, **Vanessa Pashley**, **Dr Mark Garnett**, **Dr Josanne Newton, Atun Zawadzki, Sabika Maizma,** and **Dr Suzanne Maclachlan** and the team at BOSCORF who all contributed to laboratory work associated with this project. **Claire Ellison**, **Rebecca Bartlett**, **Kallen Marecic** and **Jody Daniels** all completed fantastic dissertations which have been extremely valuable to this study. **Maria Gehrels** and **Mike Beckwith** provided outstanding technical support throughout the entire PhD and I cannot thank them enough for their time and patience as I got to grips with everything in those early years.

This PhD would not have been possible without financial support from my funding body – **The Natural Environment Research Council** (**Adapting to the Challenges of a Changing Environment** – ACCE DTP; NE/ L002450/1), as well as the **Menzies Centre for Australian Studies** and the **Quaternary Research Association** who funded, in part, the field campaigns. Thank you also to **PALSEA** for funding several conference trips which were invaluable for my personal growth in the early years of my PhD. **Dr Robin Edwards** (**Trinity College Dublin**) and **Dr David Rippin** (**University of York**) examined this thesis and conducted my

viva and I would like to thank them both for taking the time out to read my work and for an enjoyable and thought-provoking discussion.

I would also like to take this moment to acknowledge the **First Australians** and pay my respects to the elders, past, present and future. I am so glad to see the importance of Indigenous expertise increasingly recognised in our field.

Finally, and most importantly, I want to express my gratitude to my friends and family for their unwavering support over the last four years. This journey has been incredible, but difficult at times and their confidence in me never faltered. Thank you to **Julien** for believing in me since day one - my days were made far easier knowing he was there at the end of it all and, above all, thank you to my **mum**. It is hard to find the words to express how unbelievably grateful I am to her for everything. She taught me my work ethic, she encouraged my passions and she told me "you got this" countless times. I will never really know the sacrifices she made to get me here, but I think her hard work has paid off. Mum, I owe **you** all of this.

Author's Declaration

I declare that this thesis is a presentation of original work and that I am the sole author, except where due acknowledgement is given (see statement of contributions). **Chapter 5** has been published and parts of **Chapter 6** and **Chapter 7** have been compiled in a manuscript and submitted for publication. All co-authors have contributed to the work associated with these chapters. A statement of contributions page has been added to this thesis to credit their contributions.

This work has not previously been presented for an award at this, or any other, University. All sources are acknowledged as references.

The following publications have arisen from this work:

Williams, S., Garrett, E., Moss, P., Bartlett, R. and Gehrels, W., 2021. Development of a Regional Training Set of Contemporary Salt-Marsh Foraminifera for Late Holocene Sea-Level Reconstructions in southeastern Australia. *Open Quaternary*, *7*(1). doi:10.5334/oq.93

Williams, S.L., Garrett, E., Moss, P.T., Dangendorf, S., Hibbert, F.D., Atkinson, N.R., Pashley, V., Millar, I.L., Garnett, M.H., Zawadzki, A., Gehrels, W.R. Relative sea-level changes in southeastern Australia during the 19th and 20th centuries. (*In review*).

The results of this work have been presented at the following conferences and events:

Williams, S.L., Garrett, E., Moss, P.T., Dangendorf, S., and Gehrels, W.R. 2021. "Historical sea-level changes in Australia". *Australian Quaternary Association Biennial Conference (AQUA),* (Online). 8 – 9 July.

Williams, S.L., Garrett, E., Moss, P.T., Bartlett, R.E., Gehrels, W.R. 2020. "Development of a training set for high-resolution sea-level reconstruction in southeastern Australia using salt-marsh foraminifera". *Australian Quaternary Association (AQUA) Pop Up e-Conference,* (Online). 1 – 2 July.

Williams, S.L. "Searching for fingerprints of Arctic ice melt in southeastern Australia". 2019. *SERCE GIA workshop*, Canadian Museum of Nature, Ottawa, Canada. 24-26 September.

Williams, S.L. "Reconstructing sea level in southeastern Australia: The case of our rising sea". 2019. *Quaternary Research Association (QRA) Postgraduate Symposium*, University of York, York. 28 – 30 August.

Williams, S.L, Gehrels, W.R., Moss, P.T, Dangendorf, S., Sole, A., 2019. "Searching for fingerprints of early 20th century ice melt in Australian salt marshes". *20th Congress of the International Union for Quaternary Research (INQUA),* Dublin, Ireland. 24 – 31 July.

Williams, S.L, Gehrels, W.R., Moss, P.T, Dangendorf, S., Sole, A., 2019. "Searching for fingerprints of early 20th century ice melt in Australian salt marshes". *PALSEA Dublin,* Dublin, Ireland 21 – 22 July.

Williams, S.L. "Historical sea-level changes in Australia: Testing the Arctic ice melt hypothesis". 2019. *Invited speaker*, University of Queensland, Queensland, Australia.

Williams, S.L. "Historical sea-level changes in Australia: Testing the Arctic ice melt hypothesis". 2018. *Yorkshire Palaeo Group Autumn Meeting*, Sheffield Hallam, Sheffield. 28 November.

Williams, S.L. "Historical sea-level changes in Australia: Testing the Arctic ice melt hypothesis". 2018. *Physical and Environmental Geography research group talk*, University of York, York.

Williams, S.L. "Digging in mud: How Australian salt marshes can resolve the mysteries of a faraway melting Ice Sheet". 2018. *Quaternary Research Association (QRA) Postgraduate Symposium*, University of Glasgow, Glasgow. 22 – 24 August.

Williams, S.L. "Historical sea-level changes in Australia: Testing the Arctic ice melt hypothesis". 2018. *Environment and Geography Department Postgraduate Conference*, University of York, York. 22 – 23 March.

Signed:

Date: 27/4/2022

Statement of contributions

Contributions to field work

Roland Gehrels, Patrick Moss, Katarina Jerbic, Phillip Stewart, Claire Ellison and Rebecca Bartlett: aided with data acquisition in the field

Contributions to laboratory work

Maria Gehrels: stained foraminifera

Mike Beckwith: post-processed dGPS data

Kallen Marceic, Atun Zawadzki and Sabika Maizma: prepared and analysed ^{210}Pb samples

Kallen Marceic, Claire Ellison, Jody Daniels and Patrick Moss: prepared and analysed pollen and charcoal samples

Nicola Atkinson, Ian Millar and Vanessa Pashley (British Geological Survey): prepared and analysed stable lead isotope samples (I attended training)

Colleagues at SUERC, ANSTO and UCI: analysed ^{14}C samples (I attended training)

Colleagues at BOSCORF: ran cores through μXRF-ITRAX (I attended training)

Contributions to statistical analyses

Ed Garrett: ran TPXO8-Atlas global tidal modelling

Soenke Dangendorf: ran Gaussian process regressions on the relative-sea level reconstructions, ran GIA models, generated sea-level budget estimations and fingerprint estimations

Fiona Hibbert: generated code and ran the optimisation model for fingerprinting analyses, generated code to remove sterodynamics from sea-level index points

Niamh Cahill: generated code for error-in-variables analyses and change-point analyses

Contributions to reviewing and editing

All original material was written by myself. Sections intended for publication within **Chapters 3**, **4**, **5** and **6** and **7** have been reviewed and edited by co-authors:

Roland Gehrels, Ed Garrett, Patrick Moss, Soenke Dangendorf, Fiona Hibbert, Nicola Atkinson, Ian Millar, Mark Garnett, Vanessa Pashley and Atun Zawadzki.

Journal reviewers provided comments on Williams et al. (2021), which were incorporated into **Chapter 5**.

Abbreviations

AIS Antarctic Ice Sheet
AHD Australian height datum
AMO Atlantic Multidecadal Oscillation
Boot Bootstrapped/ bootstrapping
cal. yr BP Calibrated year before present (present = 1950 AD)
CI Confidence interval
CRS Constant rate of supply
DCA Detrended correspondence analysis
DCCA Detrended canonical correspondence analysis
DIC Deviance information criterion
EAIS East Antarctic Ice Sheet
EIV Error-in-variables
ENSO El Niño Southern Oscillation
ETCW Early twentieth century warming
GCSL Glacio-isostatic adjustment corrected sea level
GIA Glacio-isostatic adjustment
GMSL Global mean sea level
GRD Gravity, rotation and deformation
GrIS Greenland Ice Sheet
HAT Highest astronomical tide
HOF Highest occurrence of foraminifera
IBE Inverse barometer effect
IOD Indian Ocean Dipole
IPO Interdecadal Pacific Oscillation
LAT Lowest astronomical tide
LG Lutregala
LGM Last Glacial Maximum
LIA Little Ice Age
LOI Loss on ignition
LSP Little Swanport
MinDC Minimum dissimilarity
MAT Modern analogue technique
MCMC Markov Chain Monte Carlo
MHW Mean high water
MSL Mean sea level
MTL Mean tide level
MTR Mean tidal range
NAO North Atlantic Oscillation
PAM Partitioning around medoids
PDF Probability distribution function
PDO Pacific Decadal Oscillation
PLS Partial least squared
pMC Percentage modern carbon
PMSE Palaeomarsh surface elevation
PSA Particle size analysis/analyses
RCM Regional climate model
RGI Randolph Glacier Inventory
RSL Relative sea level
RMSEP Root mean squared error of prediction
SAM Southern Annular Mode
SLE Sea-level equivalent
SLIP Sea-level index point
SMB Surface mass balance
SWLI Standardised water-level index
TAR Tarra
VLM Vertical land motion
VA Visual assessment
WAIS West Antarctic Ice Sheet
WAP Wapengo
WAPLS Weighted averaging partial least squares
^{14}C Radiocarbon
^{210}Pb Radiogenic lead
$^{206}Pb/^{207}Pb$ Stable lead isotope

For mum – *This thesis is as much your accomplishment as it is mine. Thank you.*

Chapter 1 of 8

Introduction

1.0 Background

Sea-level rise is one of the major consequences of climate change affecting millions of people worldwide (*e.g.* Dangendorf et al. 2019; Fox-Kemper et al. 2021; Kopp et al. 2014). Understanding the mechanisms and drivers behind sea-level change is therefore vitally important. By placing near-term changes into a long-term perspective, we can establish whether current trends are comparable to or exceed past trends (Clark et al. 2016). Quantifying any long-term deviations from the background rate is crucial for informing current and future mitigation and adaptation strategies. However, investigating long-term changes in sea level is difficult because there are few tide-gauge records that extend beyond ~150 years (Hogarth, 2014b).

Proxy-based sea-level records can supplement instrumental data and can extend sea-level records through the Common Era and further back in time (*e.g.* Gehrels et al. 2020; Kemp et al. 2015, 2017a, 2018; Kopp et al. 2016). High-resolution proxy records of sea-level change can be derived from salt marshes, as they accrete in fine layers in response to sea-level rise. These records often have decadal to centennial resolution and high vertical precision (*e.g.* Gehrels et al. 2008; 2012; 2020; Kemp et al. 2011; 2015; 2017a; Long et al. 2014; Saher et al. 2015). In order to generate the palaeo sea-level estimates, we establish sea-level index points (SLIPs) using salt-marsh sediments and the microfossils preserved within them (*e.g.* foraminifera, diatoms, pollen and testate amoebae). SLIPs have a known age (which we can establish from radiometric and relative dating techniques) and elevation (microfossil assemblages occupy distinct vertical niches within the tidal frame – known as their indicative range; **Figure 1**). The indicative ranges of microfossils can be quantified using

statistical techniques called transfer functions (Sachs, Webb and Clark, 1977) which allow robust assessments of vertical uncertainties in the resulting reconstructions (*e.g.* Callard et al. 2011; Rush et al. 2021; Williams et al. 2021). In (sub)tropical regions like Northern Australia, proxy sea-level records have also been established from mangrove sediment (*e.g.* Woodroffe et al. 2015), but these reconstructions can be affected by age reversals resulting from bioturbation and sediment dynamics (Punwong, Marchant and Selby, 2013; Sefton, Woodroffe and Ascough, 2021).

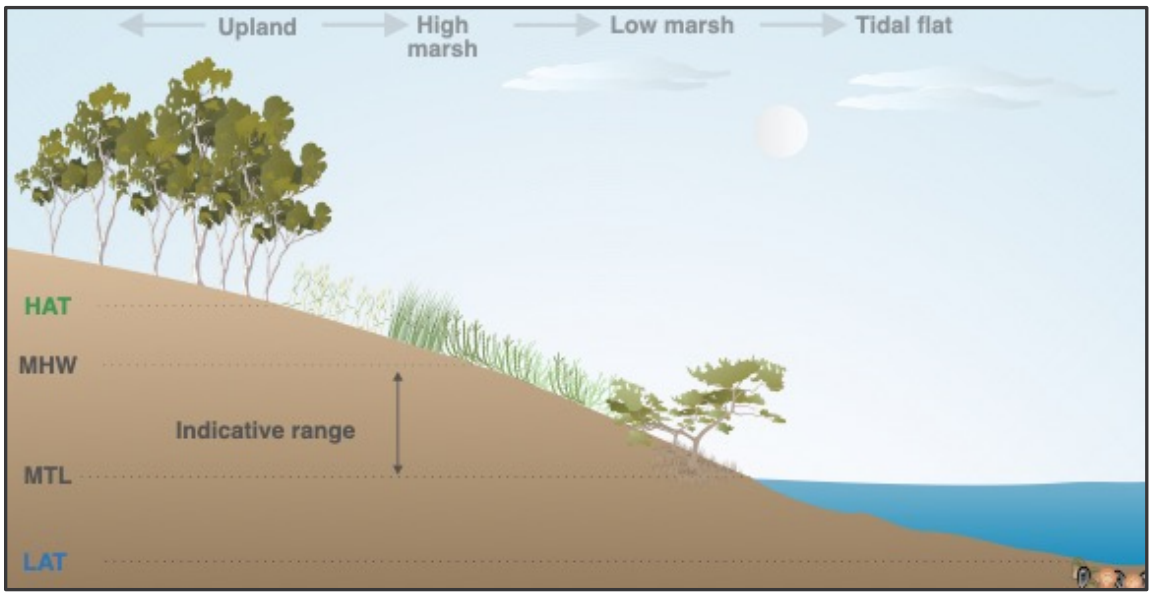

Figure 1. Schematic of a salt-marsh environment showing marsh vegetation zones and water reference levels – HAT = Highest Astronomical Tide, MHW= Mean High Water, MTL= Mean tide level, LAT= Lowest Astronomical Tide. The indicative range of a proxy tells us where in the tidal frame it occurs. (Figure uses and adapts icons from the Integration and Application Network - ian.umces.edu/media-library).

Global mean sea-level rise is defined as the increase in the volume of the ocean divided by the ocean surface area (Gregory et al. 2019). Ocean volume is driven by changes in both the mass (the barystatic component, *i.e.* sea-level rise resulting from the addition of ocean water

mass which previously resided within the land as land water storage or land ice), and density (the steric component, *i.e.* sea-level change as a result of both thermosteric sea-level rise which is due to the change in in-situ temperature, and halosteric sea-level rise which is due to the change in salinity; Gregory et al. 2019). Global mean sea-level rise, therefore, is the sum of the thermosteric and barystatic components (Gregory et al. 2019). Locally and regionally, sea level can also be affected by sterodynamic changes (*i.e.* relative sea-level change due to changes in ocean density and circulation). Relative sea-level (RSL) rise is the change in sea level with respect to the land (Church et al. 2013; Gregory et al. 2019). Changes in RSL can be attributed to all of the above processes, but also changes in the land height (*i.e.* vertical land motion; VLM), which must be accounted for in the records. A dominant effect on RSL records today is the ongoing process of glacio-isostatic adjustment (GIA) *i.e.* deformation of the solid Earth as a result of past changes in land ice since the last glacial period (*e.g.* Gregory et al. 2019; Khan et al. 2015; Stuhne and Peltier, 2015). The effect of GIA is greater on relative sea-level records in the near-field (*i.e.* sites in close spatial proximity to past and present centres of grounded ice) than those in the far-field (Clark, Farrell and Peltier, 1978). RSL records are also affected by gravity, rotation and deformation (GRD) which results from the contemporary surface-mass redistribution of ocean water due to changes in ice mass and terrestrial water storage (Frederikse et al. 2020).

Many of these RSL records have now clearly demonstrated that from at least the start of the 20th century onwards, sea level has substantially deviated from the late Holocene background rate. The rates of the 20th century sea-level rise were faster than those during any of the preceding 3000 years (Kopp et al. 2016). Over the first half of the 20th century, global sea level was primarily driven by the barystatic component, which was responsible

for ~80 % of global mean sea-level rise (Frederikse et al. 2020; **Figure 2**). Thermosteric sea-level rise then increased over the latter half of the century and into the 21st century (Frederikse et al. 2020; **Figure 2**).

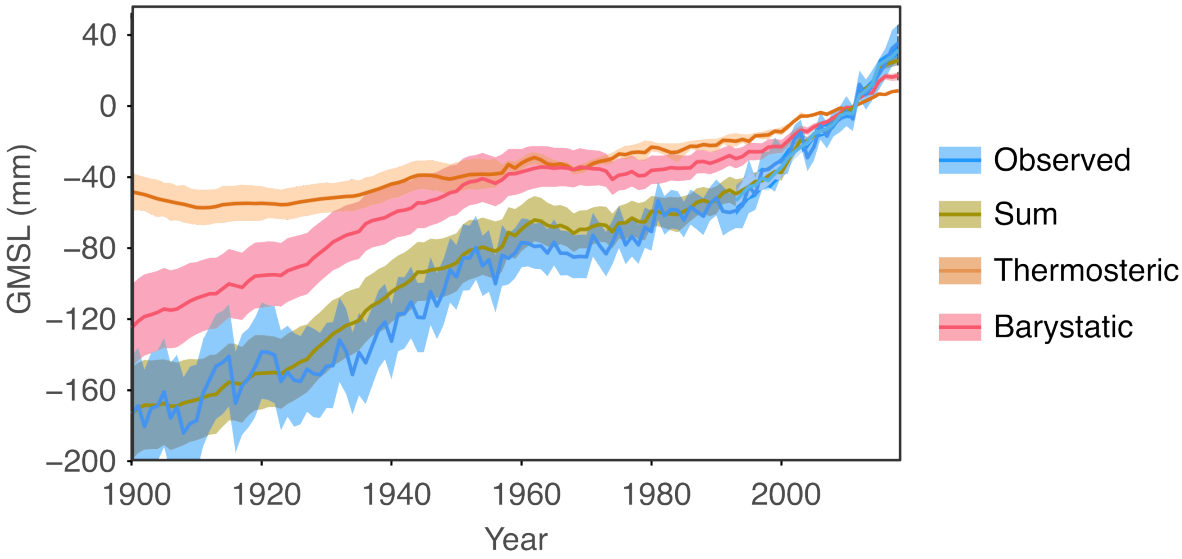

Figure 2. Temporal variations in the barystatic and thermosteric components, showing their sum and the observed global mean sea level (GMSL) since 1900. Figure adapted from Frederikse et al. (2020).

Whilst there are numerous Common Era relative sea-level records from salt marshes in the Northern Hemisphere, and especially around the North Atlantic (*e.g.* Barnett et al. 2019; Gehrels et al. 2005; 2006, 2020; Kemp et al. 2011, 2017a, 2017b, 2018; Long et al. 2014; Saher et al. 2015), records from tectonically stable regions of the Southern Hemisphere are rare, with only a few high-resolution proxy records from this region (Frederikse et al. 2021; Gehrels et al. 2008; 2012; Grenfell et al. 2012; Strachan et al. 2014). None of these salt-marsh records extend beyond ~1000 years (although some coral microatoll records from the south-central Pacific Ocean do (*e.g.* Goodwin and Harvey, 2008; Hallmann et al. 2018; Woodroffe et al. 2012). Furthermore, not only is there a lack of proxy-based records, but also a paucity

of instrumental data, as most long-term tide gauge records are located in the Northern Hemisphere (and especially in Europe and North America; Hogarth, 2014b; **Figure 3**). Therefore, the development and expansion of proxy-based records from the Southern Hemisphere is crucial for supplementing sparse tide-gauge data. Assessing the reliability of these proxy-based reconstructions is achieved by comparing periods in time where instrumental and proxy records overlap. Whilst some records agree well (*e.g.* Gehrels et al. 2005; Long et al. 2014), some do not (*e.g.* Engelhart et al. 2009; Gehrels et al. 2012; Grenfell et al. 2012), and this necessitates more investigations into the discrepancy between proxy and instrumental data.

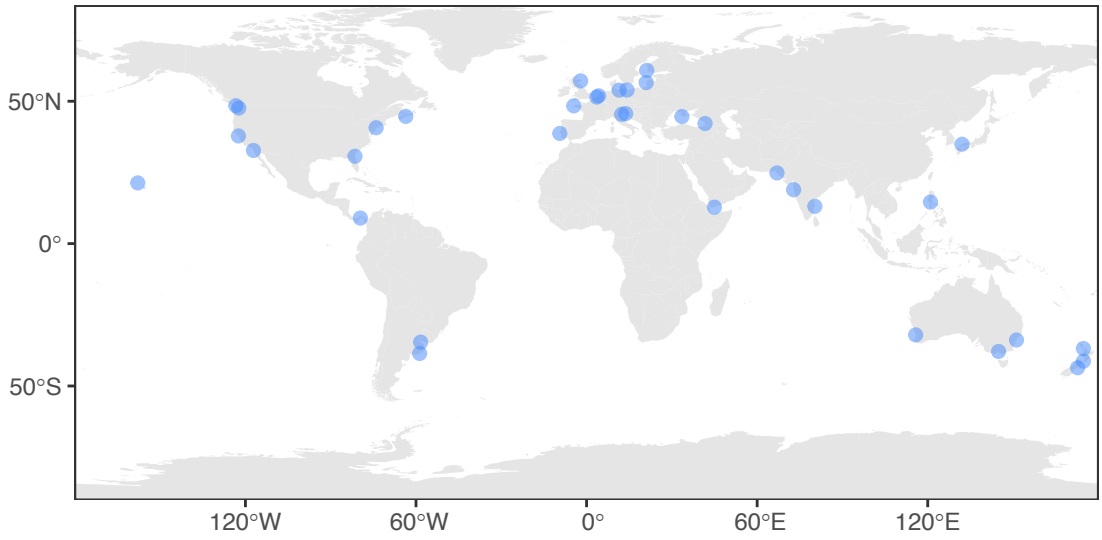

Figure 3. Locations of long-term tide-gauge records from various coastal regions. Long tide-gauge records are biased towards the Northern Hemisphere. Figure adapted from Hogarth (2014b).

Many of the proxy-based records suggest a sea-level acceleration between ~1850 and ~1950 (*e.g.* Engelhart et al. 2009; Gehrels et al. 2008; 2012; Kemp et al. 2011; 2017b; 2018; Long et al. 2014). Whether these inflexions represent one or multiple accelerations is uncertain, as

records indicate different timings in the sea-level acceleration, with estimates between ~1800 to ~1900 at their oldest and ~1950 to ~1965 at their youngest (**Figure 4**).

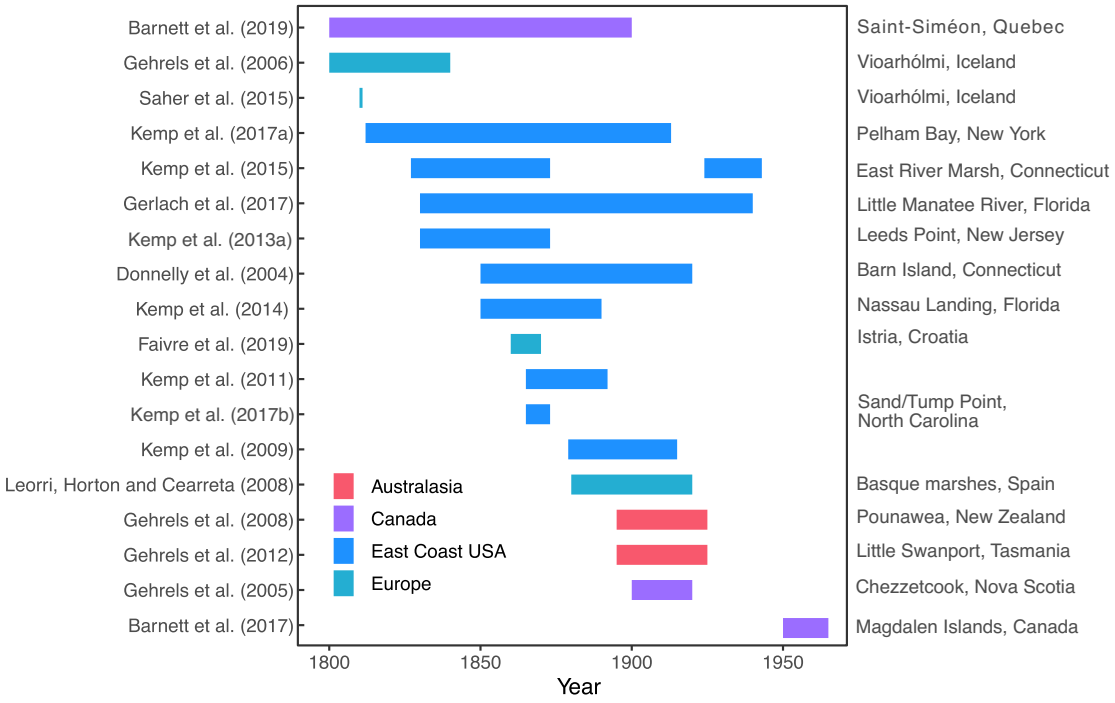

Figure 4. Timings of the modern sea-level acceleration recorded in proxy-based sea-level records from around the world.

The ~1850 to ~1950 sea-level acceleration occurred before anthropogenic forcing became dominant (Slangen et al. 2016), and so must, in part, have a natural origin. As barystatic sea-level rise was dominant over this period, a possible explanation may be melting of land-based ice (Frederikse et al. 2020; Malles and Marzeion, 2021; Parkes and Marzeion, 2018). Estimates suggest that Northern Hemisphere land-based ice (*i.e.* the Greenland Ice Sheet and Arctic glaciers) has contributed significantly more to GMSL than Southern Hemisphere land-based ice over the 20th century (Adhikari et al. 2018; Frederikse et al. 2020; Malles and Marzeion, 2021). Meltwater from the Greenland Ice Sheet (GrIS) and Arctic glaciers results in higher magnitude rises in the mid latitudes of the Southern Hemisphere and lower magnitude rises around the ice mass (Bamber and Riva, 2010; **Figure 5**). This is because an

ice mass has a gravitational pull on the surrounding ocean and, therefore, the water is held up in retention to the ice sheet. However, once the ice body loses mass as it melts during an interglacial period for example, the gravitational pull weakens, the land rebounds, and sea-level falls in the near-field and rises in the far-field (**Figure 5**). The effect of this is termed GRD (Gregory et al. 2019). These fingerprint models can be used to assess the contribution (in sea-level equivalent) from ice-mass change of different ice sources to sites around the world (*e.g.* Dangendorf et al. 2017). When the barystatic component is isolated in RSL records, fingerprinting can provide a useful tool to estimate the role of different ice bodies in driving sea-level rise.

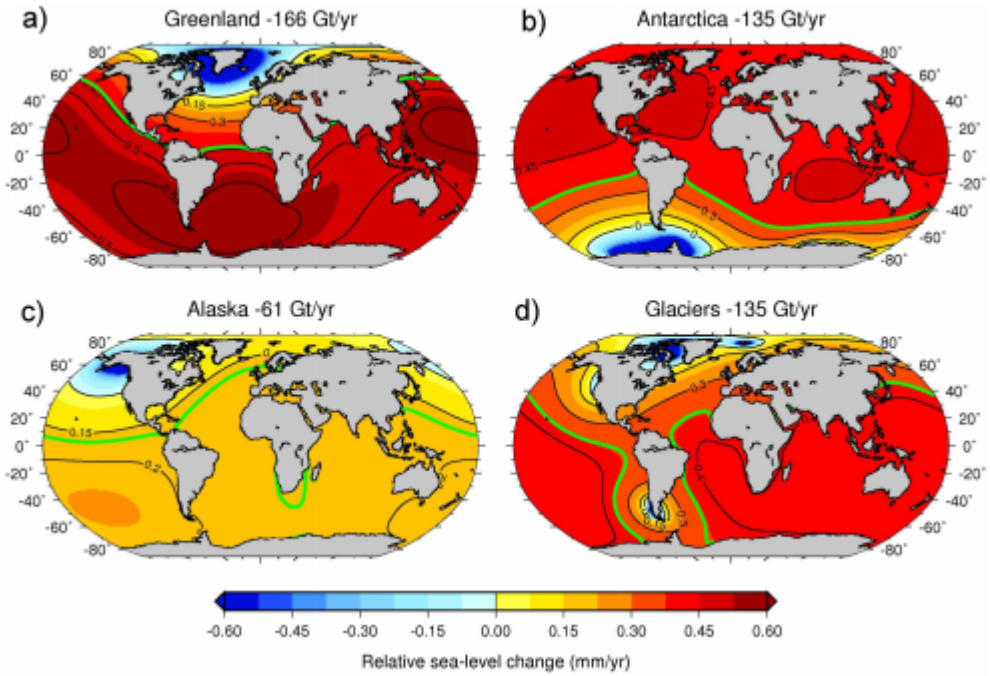

Figure 5. Sea-level change due to ice-mass loss in **A.** Greenland, **B.** Antarctica, **C.** Alaska **D.** Glaciers for the period 2000 – 2008. Green line indicates global average eustatic relative sea level. Figure from Bamber and Riva (2010).

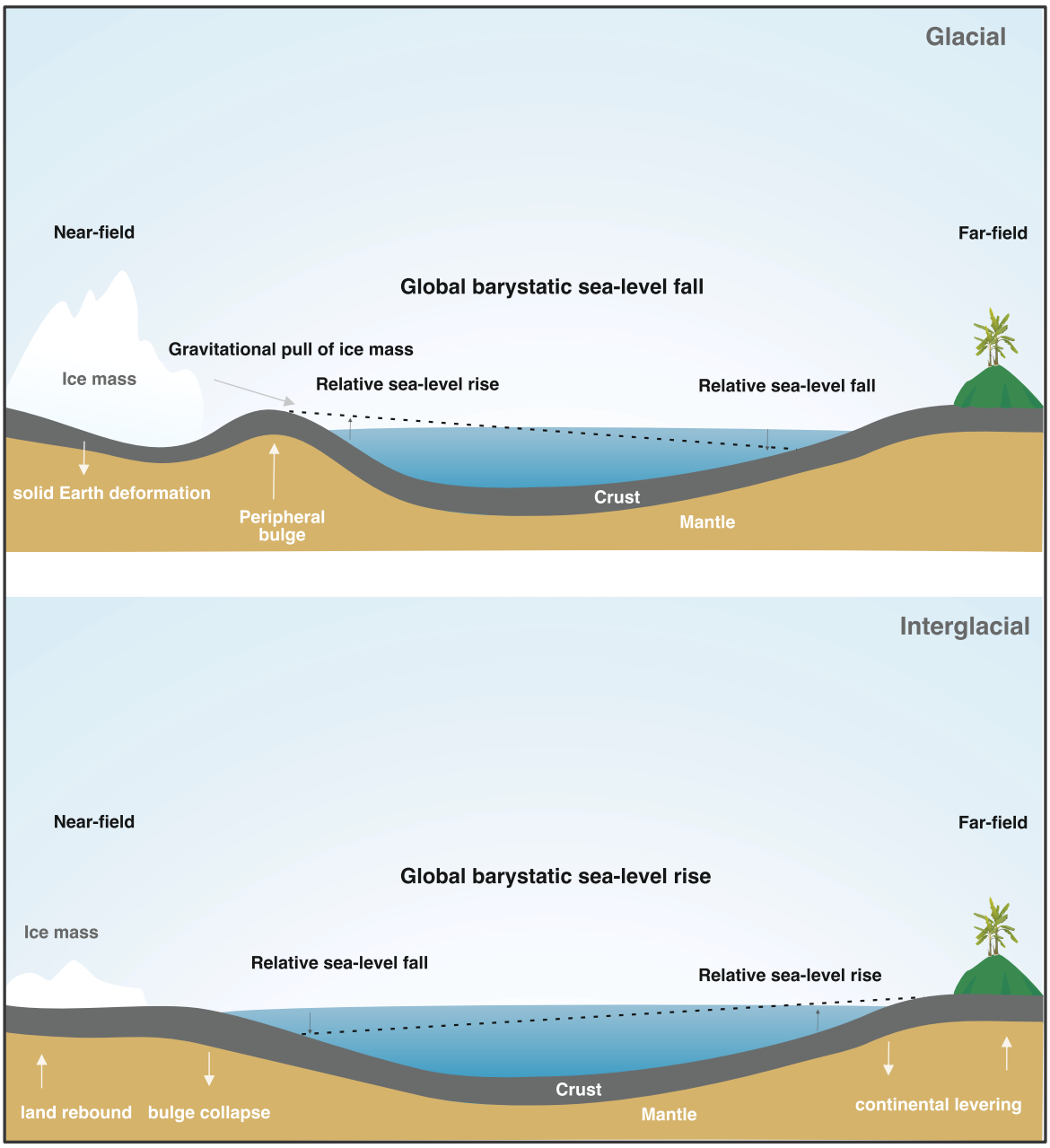

Figure 6. Schematic of relative sea-level change in the near and far field during a glacial and interglacial period following ice mass gain (glacial) or loss (interglacial) and the redistribution of water masses (*i.e.* the 'fingerprint'). Figure adapted from Rovere, Stocchi and Vacchi (2016). Figure uses and adapts icons from the Integration and Application Network – (ian.umces.edu/media-library).

Proxy records from Australia and New Zealand suggest more rapid rates of sea-level rise compared to those from the Northern Hemisphere (*e.g.* Gehrels et al. 2006, 2008; 2012;

Grenfell et al. 2012; Kemp et al. 2011), with inflexion rates up to 3.2 mm yr^{-1} larger in the Southern Hemisphere compared to the Northern (Gehrels et al. 2012), which could point to a Northern Hemisphere source for the sea-level acceleration (Gehrels and Woodworth, 2013). However, currently, proxy data from Australia and New Zealand suggest faster rates of sea-level rise than the instrumental data from the same region (Gehrels et al. 2008; 2012; Grenfell et al. 2012). Therefore, there is a possible discrepancy between the records that warrants further investigation. The long-term tide gauges from Australia themselves are problematic, often with poor temporal and spatial resolution until around the mid 20th century (Hogarth 2014a; 2014b; White et al. 2014). A more detailed exploration of this phenomenon is given in **Chapter 2**.

1.1 Thesis hypothesis, aims and objectives

This thesis sets out to test the hypotheses that:

(i) Sea-level rise between ~1850 and ~1950 was faster in southeastern Australia than in the North Atlantic region.

If confirmed, geophysical theory predicts that far-field (*i.e.* Northern Hemisphere) ice melt may explain the difference. Therefore, a second hypothesis to be tested in this study is that:

(ii) Arctic land-based ice melt was responsible for the global sea-level acceleration(s) between ~1850 and ~ 1950.

Three new palaeo sea-level records from southeastern Australia were established in this study to test hypothesis i. Modelling and sea-level fingerprinting were used to test hypothesis ii.

The following objectives are identified:

1. **Record and analyse the distribution of modern foraminiferal assemblages from salt marshes in southeastern Australia to create new sea-level transfer function models for the region.**

   Currently, only one local transfer function is available for southeastern Australia from Little Swanport, Tasmania (Gehrels et al. 2012). This study will create three new training sets of modern foraminifera from southeastern Australia and investigate how the new and existing training sets can be combined into sub-regional and regional training sets, analysing their predictive performance. It will also compare the distribution of modern foraminifera at the new sites to those elsewhere in Australia and New Zealand.

2. **Document the stratigraphy of the sites and undertake foraminiferal analyses on representative salt-marsh cores.**

   Site stratigraphy will be logged in order to document coastal change at the sites and to locate the area of the marsh where the deepest peat is, as this is likely to yield the longest record of sea-level change. To obtain palaeo sea-level estimates from the salt-marsh records, detailed analyses of the fossil foraminifera will be undertaken. Fossil foraminifera will be calibrated using transfer functions to obtain palaeomarsh surface elevation estimates for each sample downcore. The reliability of the palaeomarsh surface elevation estimates will be assessed using a statistical approach.

3. **Establish a chronology for each core using a multiple dating approach.**

   To gain a high-resolution chronology, previous studies looking at historical sea-level changes (*e.g.* Gehrels et al. 2008; 2012; Kemp et al. 2011) have undertaken a multiple dating approach using radiocarbon dating – (Accelerator Mass Spectrometry ^{14}C bomb-spike, high precision *i.e.* multiple target (Marshall et al. 2007) and routine), radionuclide analyses (^{137}Cs, ^{210}Pb) and relative dating (stable lead isotope ratios, pollen, charcoal, base metals). This thesis will also use the same techniques to establish chronologies for each site. The European settlement history of each site will be investigated in order to establish dates for potential chronohorizons in the core. Previously, ^{210}Pb dates have been analysed in traditional models such as the constant rate of supply model which uses the decay equation of ^{210}Pb to convert data into to calendar dates (Appleby and Oldfield, 1978). A new age-depth program has recently been developed called *rplum* (Blaauw, 2021) which negates the need to model "modelled data" and has been shown to produce more accurate age estimations than the traditional models (Aquino-López et al. 2020). Therefore, this study will create age-depth models using the chronological data and compare ^{210}Pb age estimates from the traditional and *rplum* models.

4. **Reconstruct the timing and magnitude of sea-level rise across southeastern Australia at three sites.**

   In order to reconstruct the timing and magnitude of sea-level rise in southeastern Australia, SLIPs for each core will be generated by combining the palaeo sea-level estimates with the chronology estimates. From this, Gaussian

process regressions will be performed on the data to obtain rates of sea-level rise. The trends between the sites will be compared in order to determine the timing and magnitude of sea-level rise in the region.

5. **Compare the novel sea-level records to sea-level fingerprint models, ocean dynamic models and historical records of ice melt.**

   The difference in the rates of 19th and 20th century (*i.e.* pre and post acceleration) sea-level rise will be compared in the new proxy records as well as other global records to determine the magnitude of the acceleration in both hemispheres. The sterodynamic component will be accounted for using an ocean reanalysis model. These corrected rates will be compared to sea-level fingerprint models and historical records of ice melt to determine whether Arctic ice melt could have been responsible for the sea-level acceleration between ~1850 – 1950.

1.2 Thesis structure

This thesis is comprised of traditional chapters as well as a published research paper. **Chapter 2** is a literature review which summarises the different estimates of global mean sea-level rise since 1900. The chapter then explores the contribution of land-based ice (both glacier and ice sheet) to sea-level rise over the 19th and 20th century, as well as documenting historical periods of accelerated ice loss and the potential causes. It then discusses sea-level fingerprinting and the use of it in sea-level studies. Finally, the chapter gives an expanded discussion on the discrepancy between proxy and instrumental data in Australia. **Chapter 3** gives a regional overview of the climate, geology and late Holocene palaeoenvironmental and sea-level history of southeastern Australia, as well as a description of the study sites.

The chapter then documents the European settlement and pollution history of the region in order to establish dates for chronohorizons which may be apparent in the sediment cores. **Chapter 4** documents the methods used to achieve the thesis objectives including field methods, foraminiferal, sedimentological and chronological laboratory analyses, as well as statistical and modelling analyses. **Chapters 5** and **6** present the main results of the thesis. **Chapter 5** is based on a paper that has been published in the journal Open Quaternary (Williams et al. 2021) and presents the modern foraminifera data and transfer functions. To avoid repetition, the study sites and methods in this paper have been removed as they are presented in Chapters **3** and **4**. As this is a collaborative paper between several co-authors, the author contributions have been outlined at the start of the chapter. **Chapter 6** presents the litho- and biostratigraphies of the study sites, the palaeomarsh surface elevation estimates, the age-depth models and the relative sea-level reconstructions. **Chapter 7** discusses the key findings of **Chapter 6** and uses sea-level fingerprinting to test the Arctic ice melt hypothesis. This is achieved using either error-in-variables regression (proxy data) or least squared regression analyses (tide-gauge records) to ascertain the magnitude in the change of the rate of sea-level rise between the 19th and 20th century at sites from around the world, and an optimisation model to find the combination of fingerprints that most closely match the observations. **Chapter 8** summarises the key finding of the study and gives recommendations for future work.

Chapter 2 of 8

Literature review

2.0 Introduction

As **Chapter 1** demonstrated, many relative sea-level records suggest recent high rates of sea-level rise from ~1850 – 1950 that substantially deviate from the late Holocene background rate. A recent paper by Frederikse et al. (2020) showed that the barystatic contribution (from both glaciers and ice sheets) to global mean sea-level was especially high over the first half of the 20th century, and currently, proxy records from around the world suggest that the spatial pattern of this acceleration may point to a Northern Hemisphere source, *i.e.* the Greenland Ice Sheet and Arctic glaciers. The aim of this literature review, therefore, is to assess the contribution of land-based ice (glaciers and ice sheets) to sea level from ~1850 – 1950, as well as to ascertain the timings of accelerated ice mass loss over this period and potential causes.

In order to achieve these aims, the review first compares modelled instrumental global mean sea level (GMSL) records since ~1900 to discern the rate of sea-level rise over this period. Second, it collates the timings of rate changes in sea level from ~1800 – 1965 from proxy-based relative sea-level reconstructions to determine whether the onset of modern sea-level rise was synchronous around the world. Third, the literature review summarises the contributions of glaciers and the GrIS to GMSL, as well as expanding on why the contribution from Southern Hemisphere land-based ice (*i.e.* Southern Hemisphere glaciers and the Antarctic Ice Sheet) is less certain. Fourth, it summarises developments in the field of sea-level fingerprinting since its inception two decades ago. Finally, the review expands the discussion on the discrepancy between instrumental and proxy sea-level data in historical records from Australia and New Zealand that was introduced in **Chapter 1** to explain the difficulties of comparing proxy and instrumental data in Australasia.

2.1 Historical reconstructions of sea-level rise

2.1.1 Global mean sea-level rise

Instrumental records of GMSL are largely constructed from compilations of tide-gauge data (satellite altimetry data have only been available since ~the early 1990s). Reconstructions of historical GMSL therefore differ between models based upon their methodological approaches in their reconstructions. Church and White (2011) and Ray and Douglas (2011) combined static spatial patterns constrained from satellite altimetry observations with temporal data from tide gauges, whereas Jevrejeva et al. (2014) averaged regional sea-level curves by stacking rates of individual tide-gauge data into a global reconstruction. Similar approaches to Jevrejeva et al. (2014) were also taken by Calafat, Chambers and Tsimplis (2014) and Wenzel and Schröter (2010). The Jevrejeva et al. (2014) model extended back the furthest, estimating GMSL from the early 19th century onwards. However, prior to 1850, the record is based only upon data from three Northern Hemisphere tide-gauge records and carries large vertical uncertainties. All these studies estimated ~1.6 – 1.9 mm yr^{-1} GMSL rise since 1900 (**Figure 7**; **Table 1**).

Hay et al. (2015) developed an approach where tide-gauge data were used alongside ensembles of model estimates of the spatial fingerprints of ocean dynamics, GIA and ice melt (both ice sheets and glaciers) and other contributions from VLM. This new way of modelling resulted in a lower rate of 20th century GMSL rise than previous estimates (1.2 ± 0.2 mm yr^{-1}) and Hay et al. (2015) suggested that the previous models had overestimated GMSL rise. Subsequent reconstructions by Dangendorf et al. (2017; 2019) and Frederikse et al. (2020) follow more closely the methods of Hay et al. (2015) than of the

earlier estimates. Dangendorf et al. (2017; 2019) and Frederikse et al. (2020) stated that the earlier models were too linear and had estimates larger than the sum of the individual contributors. The Frederikse et al. (2020) model revised estimates of these contributing processes (*i.e.* glaciers and ice sheets, thermal expansion and terrestrial water storage) suggesting a trend of 1.6 ± 0.3 mm yr^{-1} for the period of 1900 – 2018.

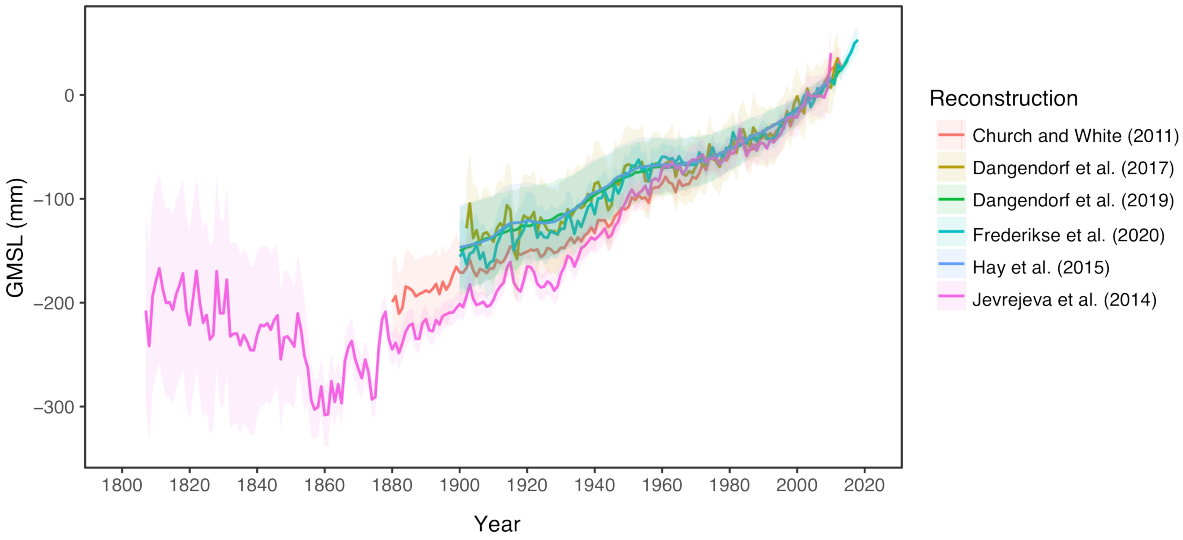

Figure 7. Global mean sea-level rise estimates since ~1800.

Table 1. Global mean sea-level rise estimates since 1900.

Reconstruction	Time period of reconstruction	Global mean sea-level rise (mm yr^{-1})
Calafat, Chambers and Tsimplis (2014)	1900 – 2002	1.9 ± 0.2
Church and White (2011)	1900 – 2009	1.7 ± 0.2
Dangendorf et al. (2017)	1902 – 1990	1.1 ± 0.3
Dangendorf et al. (2019)	1900 – 2015	1.6 ± 0.4
Frederikse et al. (2020)	1900 – 2018	1.6 ± 0.3
Hay et al. (2015)	1901 – 1990	1.2 ± 0.2
Hay et al. (2017)	1901 – 1990	1.1 ± 0.3 (Kalman smoother) 1.3 ± 0.2 (Kalman filter)
Jevrejeva et al. (2014)	1900 – 1999	1.9 ± 0.3
Ray and Douglas (2011)	1900 – 2007	1.7 ± 0.3
Wenzel and Schröter (2010)	1900 – 2006	1.6 ± 0.3

Kemp et al. (2015) undertook change-point analysis of the Jevrejeva et al. (2014) reconstruction and identified two intervals where the rate of sea-level rise increased. These were 1827 – 1860 and 1924 – 1943. Church and White (2011) found that an acceleration in the rate of global sea-level rise occurred in the 19th century from ~1880, with a secondary rise ~1930. In the shorter reconstructions, Dangendorf et al. (2017; 2019), Frederikse et al. (2020) and Hay et al. (2015) demonstrated continuous rise throughout the 20th century.

2.1.2 Local and regional sea-level rise

As highlighted in **Chapter 1**, proxy-based sea-level reconstructions from salt-marsh deposits extend back in time beyond the tide gauge and satellite records (*e.g.* Kopp et al. 2016). Regional records show different patterns in sea-level rise since the pre-industrial era, as well as different timings in the onset of modern sea-level rise, with some showing increases in sea level from the 18th century (*e.g.* Faivre et al. 2019; Gehrels et al. 2020; Kemp et al. 2017c; Long et al. 2014; Saher et al. 2015; Shaw et al. 2018), whereas others show little variability until a positive inflexion in either the late 19th century or early 20th century (*e.g.* Donnelly et al. 2004; Engelhart et al. 2009; Gehrels et al. 2004; 2005a; Kemp et al. 2011; 2013b; Leorri, Horton and Cearreta, 2008; **Figure 4**).

It appears that the 1850 – 1950 acceleration is muted in some parts of Europe or is recorded later than in records from the western North Atlantic and Australasia. For example, Barlow et al. (2014) found in their records from Scotland that, whilst the biostratigraphy suggests a mid-20th century change in sea level, the change in the rate of relative sea level was either not large enough in magnitude, or was too short-lived to be recognisable in their sea-level reconstruction. This was also noted by Long et al. (2014) where change-point analysis did not detect any significant changes in the rate of sea-level rise over the period. This is found not only in the proxy records, but also in European tide-gauge records which suggest a more gradual long-term acceleration from 1850 – 1950 compared to others from around the world (*e.g.* Gehrels and Woodworth, 2013). However, recent instrumental data from Hogarth et al. (2021) does find a late 19th century acceleration in national records from the UK (~1888), and this acceleration has also been identified in proxy records from France

(Rossi et al. 2011) and Spain (Leorri, Horton and Cearreta, 2008). However, these records have been criticised for a lack in precision of both vertical and chronological data and Long et al. (2014) stated that more data are needed to be confident in the reconstructions, especially given the large uncertainties.

These relative sea-level records show considerable regional variability, with the North American proxy records generally suggesting an earlier onset of sea-level rise compared to the Australasian records, but also a slower rate (*e.g.* Kemp et al. 2011; 2017a; 2017b). The differences in the timing of the acceleration between the records may either be a result of dating uncertainties or could reflect real non-synchroneity between the records. Similarly to the global signal, it remains uncertain whether the relative records document one sea-level rise since the start of the 19th century or whether this is two separate rises with a first acceleration in the mid 19th century ~1850 and a second acceleration ~1920. The next section of this literature review considers both the Northern and Southern Hemisphere contribution of land-based ice (both glaciers and ice sheets) to sea-level rise over this same period.

2.2 The contribution of land-based ice to sea level over the 19th and 20th century

N.B. This section will refer to mass loss from glaciers and ice sheets in both gigatons (Gt) and in sea-level equivalent (SLE). To calculate SLE from ice mass the following equation is applied:

SLE (mm) = mass of ice (Gt) × (1/361.8)

For more detailed information on the conversion of Gt to SLE please refer to Davies (2021) and references therein.

Mass changes of glaciers and ice sheets occur due to both changes in the surface mass balance (SMB), as well as ice discharge (*i.e.* dynamic ice loss) at the grounding line. Both are dependent on oceanic and atmospheric conditions (*e.g.* van den Broeke et al. 2009). SMB is the difference between accumulation (from solid precipitation *i.e.* snow) and ablation (ice melt and sublimation), whereas dynamic ice loss at the grounding line is related to accelerated flow at marine-terminating outlets as a result of oceanic and or atmospheric warming. This causes decreased buttressing which leads to extensive upglacier ice thinning which drives further loss (*e.g.* King et al. 2020).

2.2.1 Glaciers

Estimates of glacier contribution to GMSL have been made by analysing glacier length change over time alongside *in situ* mass balance measurements and modelling (*e.g.* Marzeion et al. 2017). Several studies (*e.g.* Leclercq, Oerlemans and Cogley, 2011; Malles and Marzeion, 2021; Marzeion, Jarosch and Gregory, 2014; Zemp et al. 2019) have attempted to quantify the contribution of global glaciers to GMSL over varying time periods, with the oldest dating to back to ~1800 (**Figure 8**). Estimates largely vary due to the number of glaciers included within the dataset (both length records and geodetic and glaciological mass balance observations). Data from Leclercq et al. (2014) suggested that most glaciers did not begin to rapidly retreat until after ~1800, with periods of advance and retreat since ~1760 (Csatho et al. 2008; Lea et al. 2014; Leclercq, Oerlemans and Cogley, 2011; Leclercq et

al. 2014). The end of the Little Ice Age (LIA) ~1850 likely triggered the onset of the melting of some glaciers (Csatho et al. 2008; Lea et al. 2014). The most recent estimates suggest that from 1901 – 2018, glaciers (excluding the Antarctic periphery) have contributed 69.2 ± 24.3 mm sea-level equivalent (or 0.59 ± 0.21 mm yr^{-1}; Malles and Marzeion, 2021). This represents a significant proportion (~33 %) of the observed sea-level rise over the 20th century (Frederikse et al. 2020). Glaciers in the Arctic have contributed the most to GMSL, with glaciers in the Southern Hemisphere, Europe and Middle East contributing far less. For example, from 1901 – 1990, globally, glaciers contributed 0.56 ± 0.27 mm yr^{-1} to GMSL. Out of that, Arctic glaciers were responsible for 0.34 ± 0.62 mm yr^{-1} which equates to ~62 % (Malles and Marzeion, 2021).

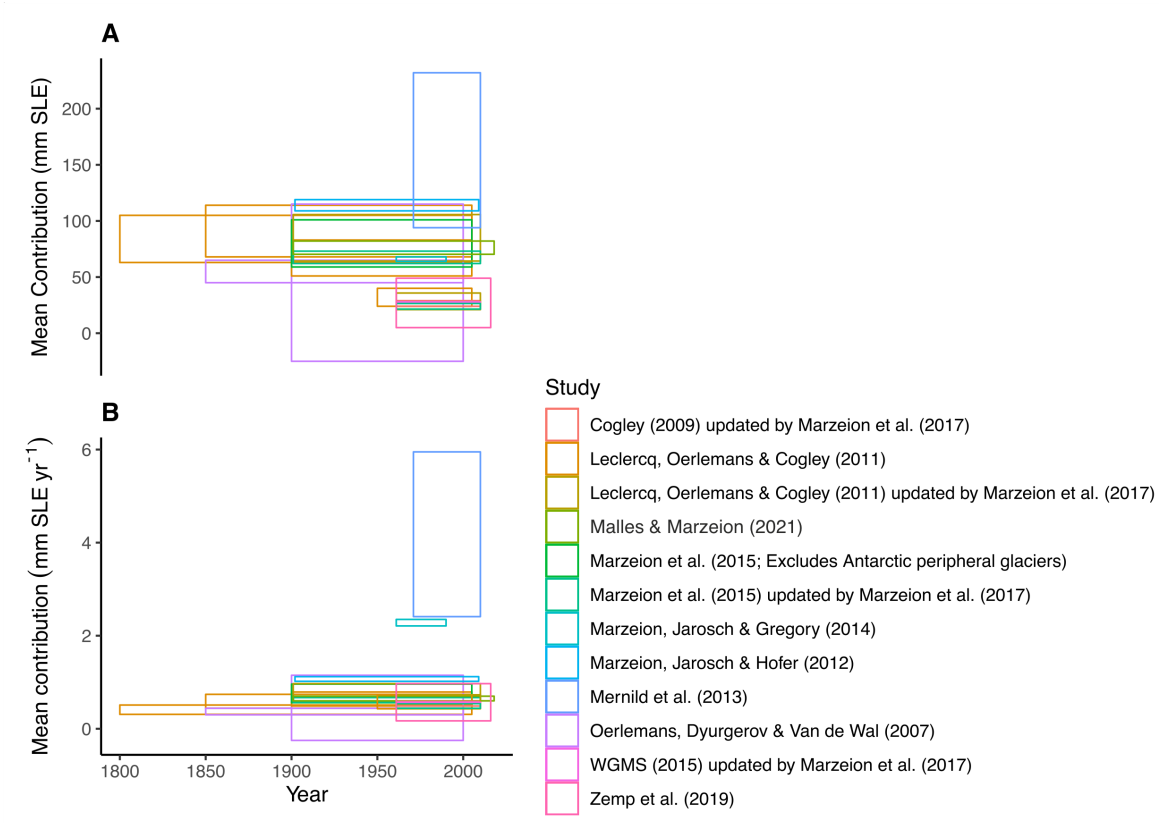

Figure 8. A. Estimations of global glacier contribution to global mean sea level (GMSL) over the 19th and 20th century. **B**. Rate of glacier contribution to GMSL. Contribution errors are represented by the vertical lines and the time period of the study is represented by the horizontal lines.

2.2.2 The Greenland Ice Sheet

Observational evidence has shown that there was considerable mass loss of the GrIS during the 20th century (Kjeldsen et al. 2015; **Figure 9**; **Figure 10**). Between 1980 – 2012, the average SMB was 361 ± 40 Gt yr^{-1} with a negative trend over time (mainly due to increased runoff (Shepherd et al. 2020)). In the first half of the 20th century, the greatest negative mass-balance rates occurred during the 1920s and early 1930s, which also correlates with extensive glacier retreat in southeastern Greenland (Bjørk et al. 2012; Briner et al. 2020). Since 1972, the largest contributions to global sea-level rise have come from northwest (4.4 ± 0.2 mm), southeast (3.0 ± 0.3 mm), and central west (2.0 ± 0.2 mm) Greenland, with a total 13.7 ± 1.1 mm for the Ice Sheet (Mouginot et al. 2019).

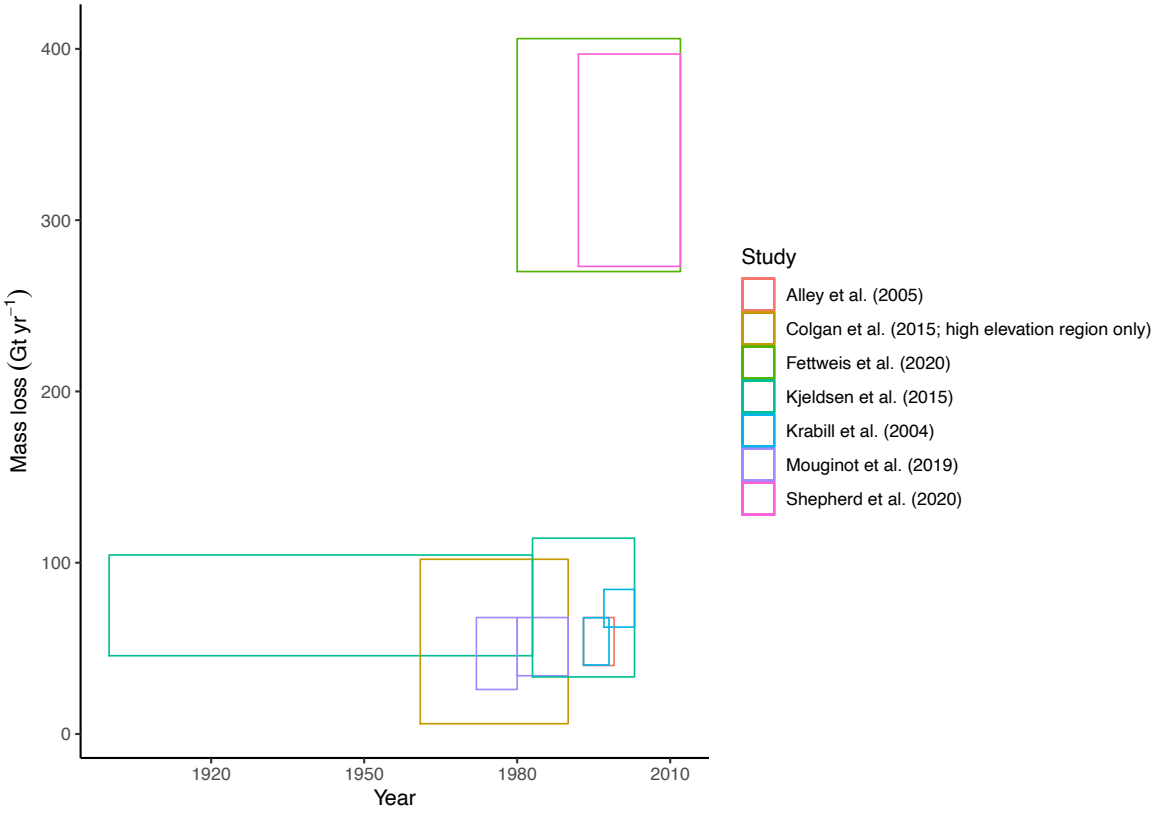

Figure 9. Mass loss estimates of the Greenland Ice Sheet from 1800 – 2016. Mass loss errors (1 σ) are represented by the vertical lines and the time period of the study is represented by the horizontal lines.

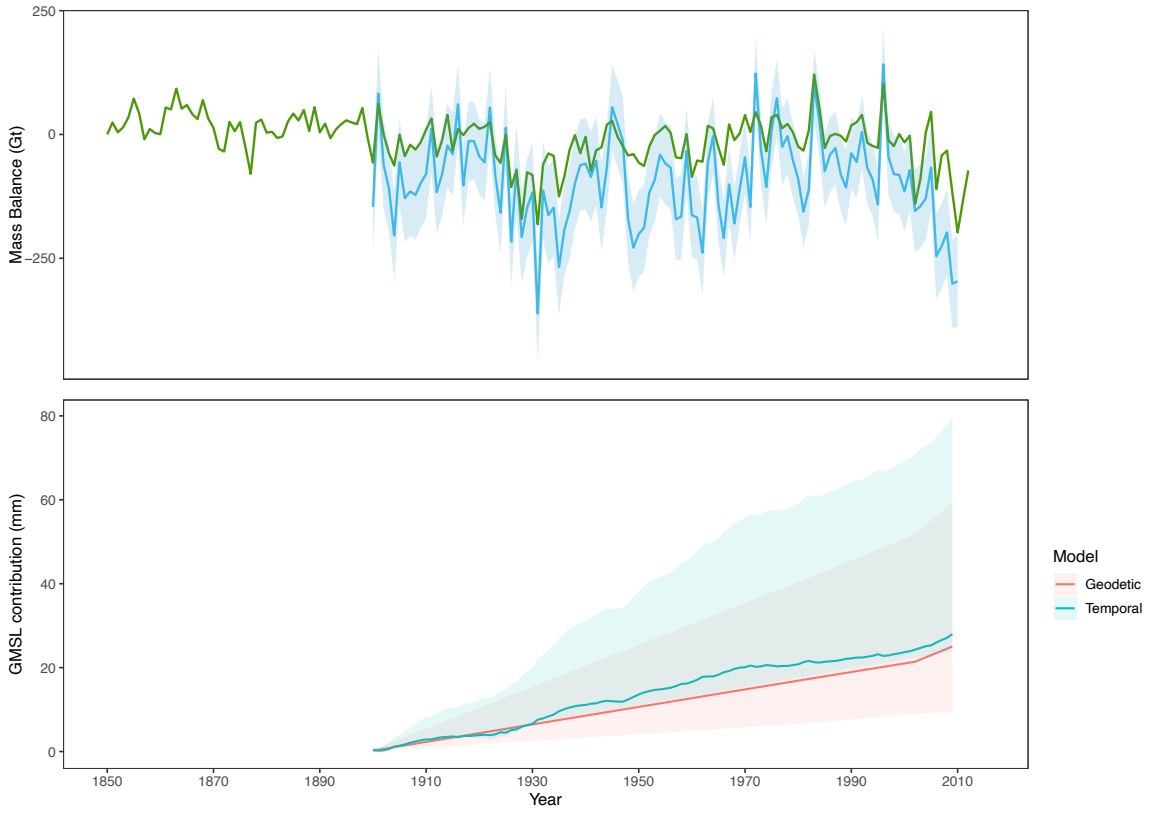

Figure 10. Top panel. Annual observed mass balance of the Greenland Ice Sheet from 1850 – 2012 with 1 σ errors (where available) from Kjeldsen et al. (2015; blue) and Briner et al. (2020; green). **Bottom panel.** Contribution from the Greenland Ice Sheet to global mean sea level from the geodetic and temporal mass balance reconstruction approaches with 1 σ errors from Kjeldsen et al. (2015). The geodetic approach uses airborne and satellite altimetry combined with a digital elevation model to estimate mass balance. The temporal approach uses *in situ* determination of accumulation and ablation for the mass balance year.

Modelling of GrIS SMB has shown the regime in the 1920s was comparable to that during the 2000s, where the Ice Sheet experienced high melt and low precipitation (*e.g.* Box, 2013; Fettweis et al. 2017; Wilton et al. 2017). There are quite large differences in estimates of surface mass loss over the 19th and 20th century (*e.g.* Fettweis et al. 2017; Kjeldsen et al. 2015; Wilton et al. 2017; **Figure 11**; **Figure 12**), which largely seem driven by which record of mean annual precipitation is chosen for the time series, or by which model is chosen *e.g.*

positive degree day, energy balance model, general circulation model or regional climate model (RCM). Overall, polar RCMs perform the best compared to observations, in particular for simulating precipitation patterns, but are more computationally expensive than other models (Fettweis et al. 2020). SMB model outputs show that the Ice Sheet SMB was generally higher in the second half of the 20th century compared to the earlier half, indicating ice sheet growth (at least until the final decade; **Figure 12**).

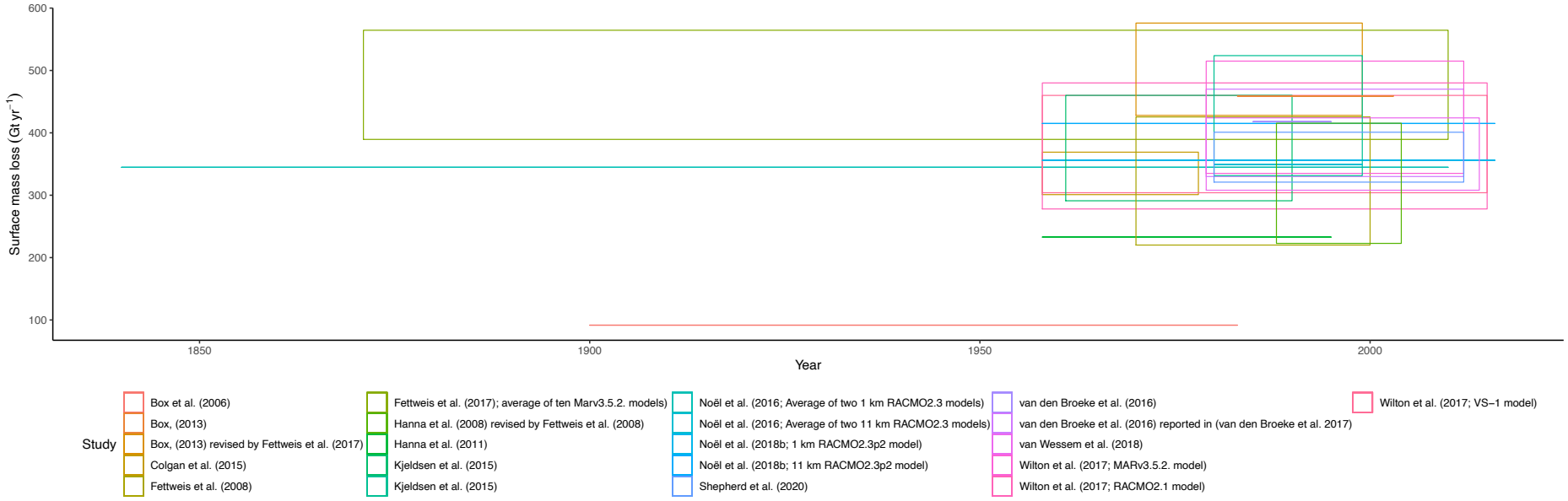

Figure 11. Surface mass loss of the Greenland Ice Sheet from 1840 – 2004. Horizontal lines denote time period of study and vertical lines denote mass loss uncertainty (where applicable - 1 σ vertical lines).

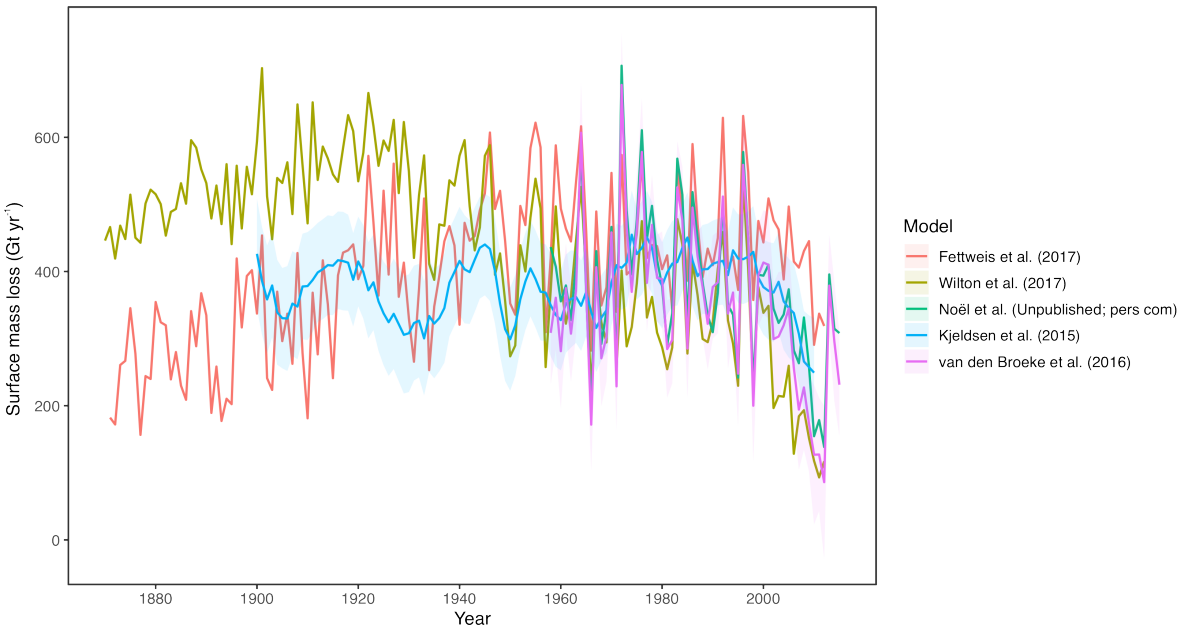

Figure 12. Estimates of historical Greenland surface mass loss from recent studies. Shaded areas show 1 σ errors (where given).

Few studies have looked at dynamic ice loss beyond the mid-late 20th century due to the limited observations prior to the satellite era. From those that extend back to ~1960, data show in nearly all regions of the GrIS, ice discharge has increased from the mid 20th century to present (Mouginot et al. 2019; Rignot et al. 2008; **Figure 13**). Over the past four decades, on average, dynamic ice loss has contributed 66 ± 8 % of the mass loss versus 34 ± 8 % for SMB (Mouginot et al. 2019). Recent data show between 1985 – 1990 the average dynamic ice loss was 17 ± 6 Gt yr^{-1}, and ice thickness has decreased from the 1980s until present (King et al. 2020).

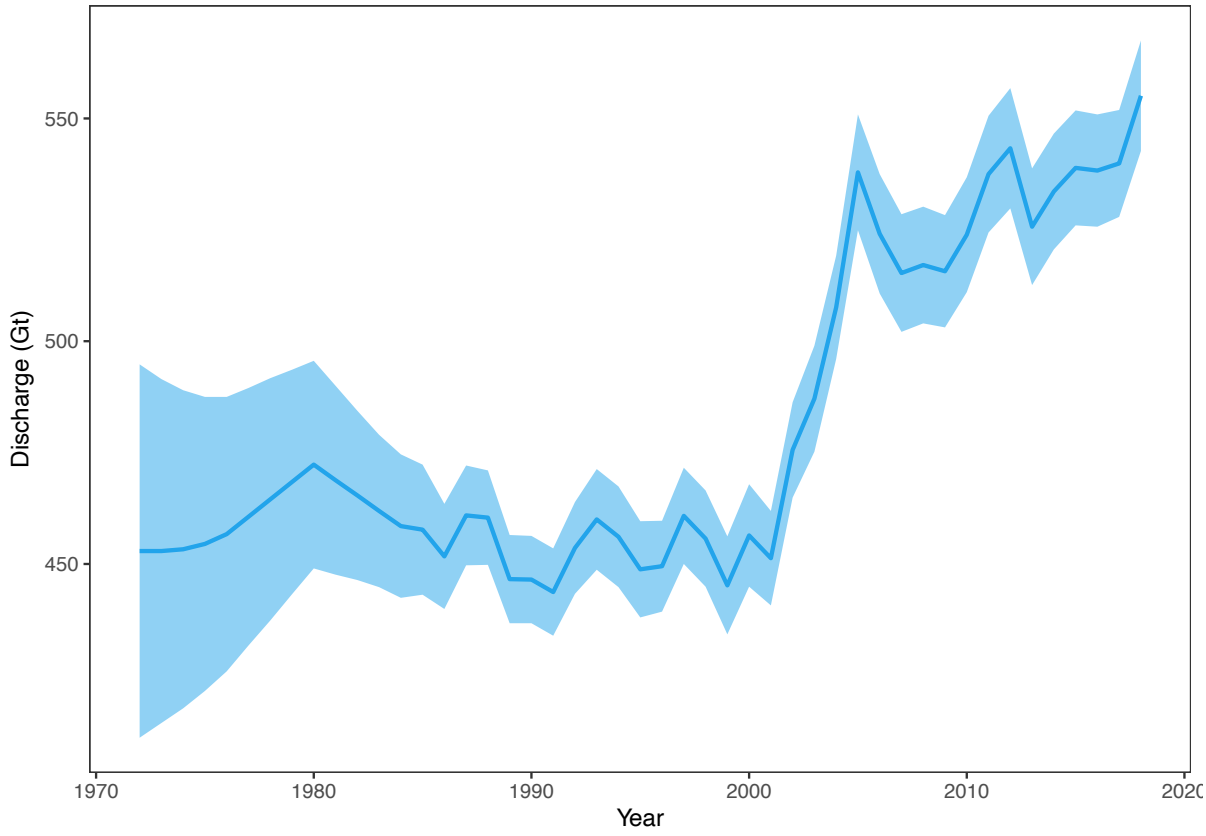

Figure 13. Mean yearly flux in discharge for the Greenland Ice Sheet from 1972 – 2017 (blue line) with 1 σ error showing increasing discharge over time with an acceleration from ~2000. Data from Mouginot et al. (2019).

2.2.3 Southern Hemisphere land-based glaciers

As mentioned in **Chapter 1**, the contribution from Southern Hemisphere glaciers such as those located in New Zealand, the low latitudes and the southern Andes has been assumed to have been a lot lower over the 19th and 20th century compared to their Northern Hemisphere counterparts. From 1901 – 1990, there has been a maximum estimated contribution of ~0.1 mm yr^{-1} from glaciers in the lower latitudes, southern Andes and New Zealand, compared to ~0.6 mm yr^{-1} from Arctic glaciers (excluding Greenland peripheral glaciers; Malles and Marzeion, 2021). However, mass loss of glaciers from many of these

regions is poorly constrained in comparison to Northern Hemisphere regions due to both limited field exploration, as well as complications with modelling mass loss due to the high number of marine-terminating glaciers in areas like the southern Andes (Malles and Marzeion, 2021).

2.2.4 The Antarctic Ice Sheet

In comparison to Greenland, the contribution of the Antarctic Ice Sheet (and its peripheral glaciers) is not well established (Frederikse et al. 2020). Current evidence suggests that only towards the end of the 20th century did the Antarctic Ice Sheet begin to make substantial contributions to GMSL (~0.05 mm yr^{-1} SLE; Adhikari et al. 2018; Frederikse et al. 2020), although, mass balance observations only extend back until around the mid-20th century (Rignot et al. 2019). Contributions over the latter decades of the 20th century are mostly assumed to have come from the West Antarctic Ice Sheet, whilst the East Antarctic Ice Sheet is largely assumed to have remained in balance (Shepherd et al. 2018).

2.2.5. Historical periods of accelerated glacier mass loss

As highlighted in section 2.2.1, globally, some glaciers began losing mass from as early as ~1800, with a pronounced trend in the Arctic (Leclercq et al. 2014; Marzeion et al. 2015). Evidence from ice-rafted debris around Greenland suggests periods of high iceberg rafting from 1796 until the 1830s with a major peak around 1829 and from 1880 – 1940 (Wangner et al. 2018, 2020). Malles and Marzeion (2021) modelled mass change rate of glaciers in Randolph glacier inventory regions and showed that in many cases, mass loss rates were higher in the period 1901 – 1940 than the middle of the 20th century (*i.e.* 1941 – 1980 and

1901 – 1990; **Table 2**). In most regions, glacier mass loss rates increased until ~1930 after which the mass loss rate decelerated until ~1980 when accelerations began again (Malles and Marzeion, 2021).

Table 2. Ensemble mean regional mass change rate estimates in mm SLE yr^{-1} for different time periods over the 20th century. Table adapted from Malles and Marzeion (2021). The greatest mass change rates for each region has been highlighted in bold.

Region	1901 – 1940	1941 – 1980	1901 – 1990	1971 – 2018	Total mass change
Alaska	0.08±0.17	0.05±0.03	0.06±0.07	**0.09±0.03**	0.28±0.3
Arctic Canada (North)	**0.10±0.10**	0.06±0.04	0.08±0.05	0.09±0.02	0.33±0.21
Arctic Canada (South)	**0.08±0.10**	0.03+0.03	0.06±0.04	0.04±0.00	0.21±0.17
Greenland periphery	**0.17±0.13**	0.05±0.06	0.10±0.08	0.07±0.04	0.39±0.31
Iceland	0.01±0.01	0.01±0.00	0.01±0.00	0.01±0.00	0.04±0.00
Svalbard	0.05±0.02	0.03±0.01	0.04±0.01	**0.06±0.01**	0.18±0.05
Scandinavia	0.00±0.00	0.00±0.00	0.00±0.00	0.00±0.00	0.00±0.00
Russian Arctic	**0.06±0.10**	0.05±0.01	0.05±0.05	**0.06±0.01**	0.22±0.17

Observational evidence from Greenland largely agrees with model outputs. Bjørk et al. (2012) analysed frontal behaviour of 132 glaciers along the Greenland coastline and

identified two periods of significant recessional retreat: 1933 – 1943 and 2000 – 2010. It has been shown that peripheral glaciers and ice caps retreated faster between 1910 – 1932 than 2000 – 2013 (22.1 ± 6.4 m yr^{-1} and 12.2 ± 1.8 m yr^{-1}) (Bjørk et al. 2018). New evidence has shown that there was a major ice tongue collapse of the Kangerlussuaq Glacier (one of Greenland's largest outlet glaciers) between 1932 – 1933 which resulted in a 9 km retreat (Vermassen et al. 2020). This retreat exceeds any of the glacier's recent retreat events (Vermassen et al. 2020). Similar results regarding the timing of the retreat in the early 20th showing that past retreat rates from 1880 – 1930 were larger than present-day (Khan et al. 2014; 2020).

Many other glaciers around Greenland have also shown similar patterns of extensive loss in the early 20th century especially from ~1920 – 1930 (*e.g.* Andresen et al. 2012, 2017; Howat and Eddy, 2011; Johansson et al. 2020; Khan et al. 2020; Vermassen et al. 2019). The Jakobshavn Isbræ has one the most complete and longest records which shows that the glacier retreated steadily from the 1850s until the 1950s at an average rate of ~300 m yr^{-1} (Csatho et al. 2008). Two rapid periods of thinning of this glacier have been identified in the early 20th century including 1902 – 1913 and 1930 – 1959 (Csatho et al. 2008; Khan et al. 2020); however the fastest observed retreat occurred between 1929 – 1942 and averaged 500 m yr^{-1} (Howat and Eddy, 2011). The front then remained almost unchanged until the end of the century (Howat and Eddy, 2011; Lloyd et al. 2011). Mass loss of the Jakobshavn Isbræ in the early 1900s was comparable to present-day rates (Khan et al. 2020). Similar patterns in the timing of glacier retreat have also been reported elsewhere outside of Greenland, with many studies also reporting retreating glaciers in other Arctic regions during the late 19th century or early 20th century (*e.g* Björnsson et al. 2013; Błaszczyk, Jania

and Kolondra, 2013; Hannesdóttir et al. 2015; Kavan, 2020; Pálsson et al. 2012; Sigurðjsson, Jónsson and Jóhannesson, 2007).

2.2.6. Historical periods of accelerated ice sheet mass loss

Several studies (Briner et al. 2020; Fettweis et al. 2017; Kjeldsen et al. 2015; Wilton et al. 2017) have shown that the GrIS was subject to mass loss in the first half of the 20th century, although timings differ. The modelled SMB from Wilton et al. (2017) suggests a major decline between the mid-1920s and early 1960s; however results from Wake et al. (2009) only note this decline in the 1920s. Significant declines in sea ice surrounding Greenland are observed from ~1910 – 1960 (Brennan, Hakim and Blanchard-Wrigglesworth, 2020; Trusel et al. 2018) with increases ~1960 (Trusel et al. 2018). More recent developments using the previously mentioned RCMs specifically designed for polar regions have suggested that the Ice Sheet lost mass ~1930 (Fettweis et al. 2017).

It is difficult to ascertain the runoff history of the GrIS prior to 1930 as many of the models predict different scenarios. Some models suggest continuous runoff increase from 1900 – 1930 (Fettweis et al. 2017), whereas others suggest a runoff decrease from 1900 – 1920 followed by a melt increase, reaching a maximum at the beginning of the 1930s (Box, 2013; Fettweis et al. 2017). There is also significant variability in instrumental and observational data. Precipitation conditions and trends in meteorological data from both ice cores and weather stations since 1890 vary, with some suggesting increased snowfall 1910 – 1940 and some suggesting reduced snowfall (Mernild et al. 2015). These differences seem regionally dependent. Some observationally constrained models have even suggested initiation of

GrIS melt following the onset of industrial-era warming in the mid-1800s (Trusel et al. 2018). Noël et al. (2018) state that coarser-resolution SMB models (such as the 11 km RACMO2.3p2 models) insufficiently model GrIS SMB and that future efforts should be concentrated on high-resolution models *i.e.* 1 km to gain realistic measurements of GrIS SMB.

However, as demonstrated, the GrIS mass balance did not become significantly negative until the 20th century (Kjeldsen et al. 2015). This could suggest two accelerations in sea level: the acceleration witnessed ~1850 may have been caused by the onset of melting glaciers and the ~1920 – 1940 acceleration may have been caused by negative mass balance of the GrIS and other Arctic land-based glaciers during the early twentieth century warming (ETCW).

2.3 Causes of the warming

Both global atmospheric and ocean temperatures have been shown to rise significantly during the ETCW (Friedman et al. 2020; Hegerl et al. 2018). The signal was especially strong in Arctic instrumental and proxy records (Abram et al. 2016; Andresen et al. 2012; 2017; Wangner et al. 2020; **Figure 14**). The warming has been linked to both internal climate variability (*e.g.* Chylek et al. 2016; Svendsen et al. 2018*)* and changes in external radiative forcing (Haustein et al. 2019). The degree to which either, or both, contributed to the ETCW is still debated (*e.g.* Bokuchava and Semenov, 2020; Haustein et al. 2019). The contribution of each will be considered here.

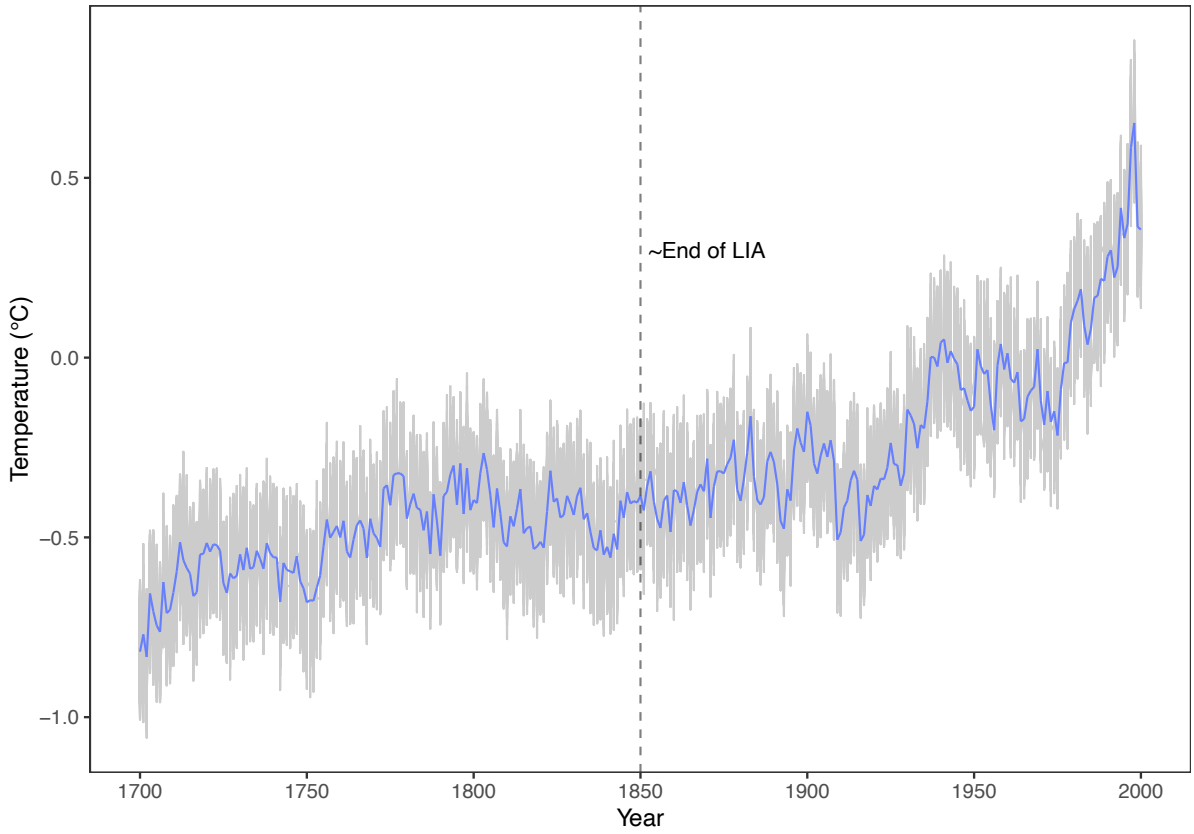

Figure 14. Time series of Arctic temperature changes from 1700 – 2000 from a Bayesian hierarchical model (PAGES2K ensemble) showing ensemble mean (purple) and ensemble members (grey). Data from Neukom et al. (2019). LIA= Little Ice Age.

2.3.1. External forcings

Some studies (*e.g.* Haustein et al. 2019; Hegerl et al. 2018; 2019) suggest strong external forcing in the early 20th century. Haustein et al. (2019) suggested that 98 % of 20th century warming can be explained by external forcing. Greenhouse gas emissions since the industrial revolution have caused a detectable warming from 1900 (*e.g.* Abram et al. 2016; Hegerl et al. 2019; Schurer et al. 2013) and simulations suggested they could have caused up to half of global warming between 1910 – 1940 (Egorova et al. 2018). Increasingly, studies are now suggesting that anthropogenic influences dominated the ETCW (*e.g.* Friedman et al. 2020; Fyfe et al. 2013; Najafi, Zwiers and Gillett, 2015). It is now generally agreed within

the literature that greenhouse gases largely drove the warming (Hegerl et al. 2018; 2019), however, the degree to which the other external forcings contributed to the ETCW is still debated (Hegerl et al. 2018). Tropospheric aerosols and internal climate variability have also played a role in cooling from the end of the ETCW until ~1970 (Hegerl et al. 2018).

Increases in insolation are observed over the 20th century (Hegerl et al. 2018; 2019) and Suo et al. (2013) proposed that much of the warming in the Arctic can be explained by intensified solar radiation and a decline in volcanic activity between 1920 and 1950. Some subsequent studies (Egorova et al. 2018; Perner et al. 2019) have agreed and state that the effect of insolation was enhanced due to the decline in tropospheric aerosols over the 20th century, but also suggest that anthropogenic drivers played a role. Results from other studies however (Fyfe et al. 2013; Rohde et al. 2013) suggest that changes in insolation have not contributed to recent warming and that the observed warming can be explained by volcanism and anthropogenic effects. Volcanic eruptions were quite frequent throughout the 19th century; there was 29 major (*i.e.* Volcanic Explosivity Index >4) eruptions between 1800 – 1900 (Newhall and Self, 1982). However, these became less frequent after the eruption of Santa Maria (1902) and Katmai (1912; Hegerl et al. 2018) and could have led to the positive forcing (Hegerl et al. 2019; **Figure 15)**.

There may be a discrepancy between studies that argue insolation was an important driver and those that suggest it was not, because estimates of insolation over the ETCW are extremely variable and therefore affect model outputs depending on which values are used (Hegerl et al. 2018; Przybylak et al. 2020). Finally, anthropogenic aerosols have also been argued as a key driver of the ETCW, with Carslaw et al. (2013) suggesting that these early

emissions may have caused substantial impacts in a less polluted atmosphere, but uncertainties associated with this are large (Hegerl et al. 2019). Currently, better estimates of the external forcings are needed for a clearer understanding of the effect of each on the ETCW.

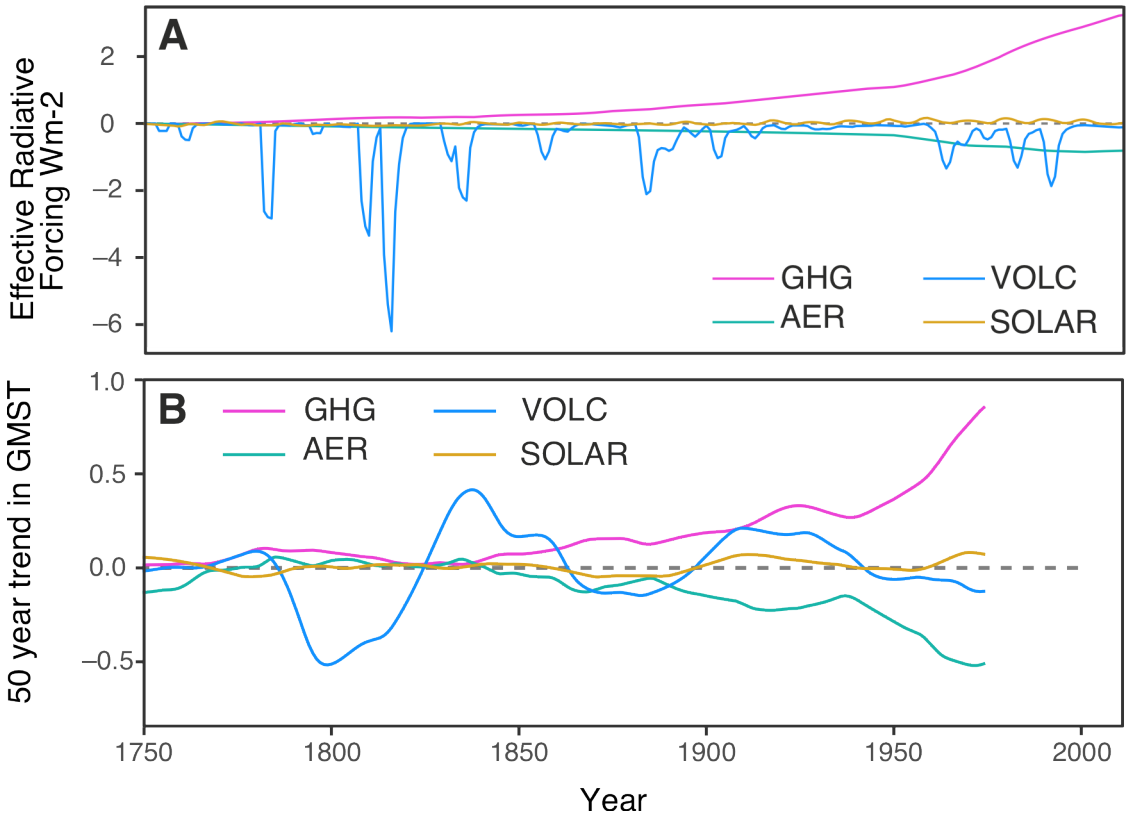

Figure 15. A. 3-year running mean of individual radiative forcings from the industrial era – present from IPCC AR5. **B.** Running 50 year trends in individual external forcings. GHG = Greenhouse gases, AER = Aerosols, VOLC= volcanism, SOLAR = solar insolation, GMST = Global mean surface temperature. Figure adapted from Hegerl et al. (2019).

2.3.2. Decadal climate variability

Other studies (*e.g.* Bokuchava and Semenov, 2020; Polyakov et al. 2010; Svendsen et al. 2018; Xiao et al. 2020) argued that external forcing alone is not enough to explain the observed warming in the Arctic over the ETCW and suggest that internal climate variability must have also played a role. After a long time of no real pronounced trend over the second half

of the 19th century, a marked-long term decrease in the North Atlantic Oscillation (NAO) occurred between the early 20th century and the 1970s (Hegerl et al. 2019). Decreases in the NAO can lead to warm temperatures over parts of Greenland, as well as the North Atlantic (Hegerl et al. 2019; Wegmann et al. 2020) and this has been suggested as a primary cause of the ETCW (*e.g.* Polyakov et al. 2010). Arctic warming leading to enhanced ice loss has been found to correlate with negative phases of the NAO (Andresen et al. 2012; Trusel et al. 2018; Wegmann et al. 2020) and ocean models have shown that atmospheric circulation such as that caused by the NAO can induce anomalously high northern heat transport in the North Atlantic, which drives Arctic warming with a lag time of around a decade (Müller et al. 2015). Beitsch, Jungclaus and Zanchettin, (2014) proposed that internal variability of the Northern Hemisphere climate alone is sufficient to reproduce warm events similar to those of the ETCW in the Arctic region and no external forcing is needed.

Other modes of natural climate variability such as the Atlantic Multidecadal Oscillation and the Pacific Decadal Oscillation (AMO and PDO respectively) have also been discussed as potential contributors to the ETCW (*e.g.* Hegerl et al. 2018; Johannessen et al. 2016; Tung and Zhou, 2013; Zhou and Tung, 2013), as both peak during the ETCW (**Figure 16**). The AMO has been shown in some studies to have potentially contributed up to 16 % of the observed warming (Fyfe et al. 2013), and significant correlations have been found between the AMO and declining Arctic sea ice during the ETCW (Bokuchava and Semenov, 2020). The PDO may act synchronously with the AMO, and Johannessen et al. (2016); Tokinaga, Xie and Mukougawa, (2017); Wegmann, Brönnimann and Compo, (2017) and Xiao et al. (2020) have suggested that the a combination of the two contributed to the ETCW However, some evidence has implied that the AMO does contribute but the PDO does not (Chylek et

al. 2016), and other evidence has suggested that the PDO has contributed but the AMO has not (Svendsen et al. 2018). Svendsen et al. (2018) argued that previous studies did not isolate the PDO and it in itself can explain the majority of observed warming. Therefore, it is still unclear and further work is needed to ascertain the potential contribution of each forcing.

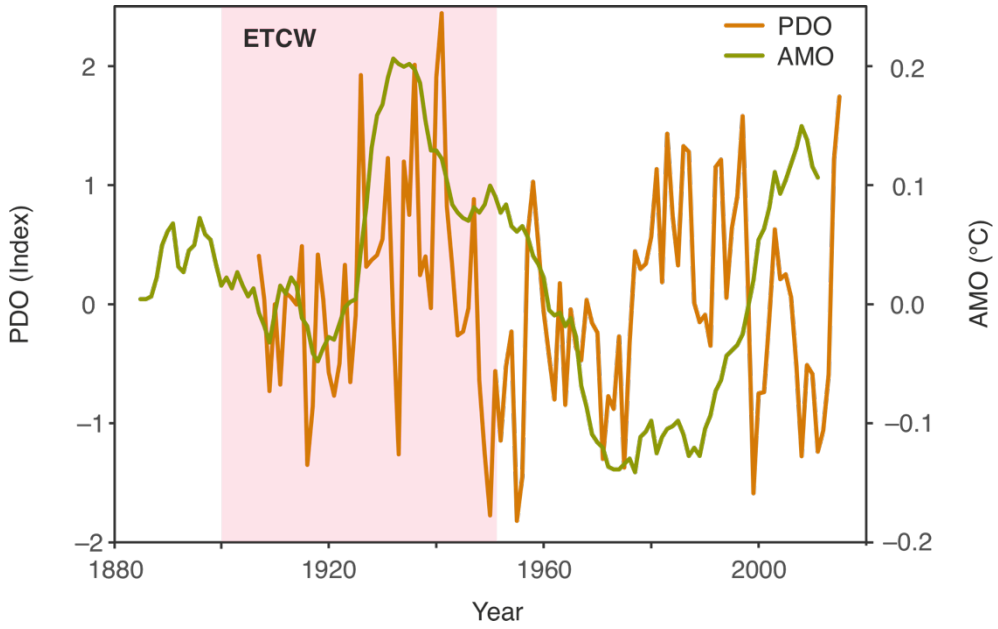

Figure 16. Fluctuations in the Atlantic Multidecadal Oscillation (AMO) and the Pacific Decadal Oscillation (PDO). Red box indicates the Early Twentieth Century Warm Period. Figure adapted from Hegerl et al. (2018).

It is probable that the ETCW in the Arctic was driven by a combination of the two (Chylek et al. 2016; Fyfe et al. 2013; Hegerl et al. 2018, 2019; Xiao et al. 2020). A large proportion of the warming can be explained by external large-scale climate forcing and a smaller proportion by internal climate variability (Fyfe et al. 2013). A complex combination of external forcings, amplified by positive Arctic feedbacks from internal modes and anthropogenic factors are likely are responsible for the warming (*e.g.* Bokuchava and Semenov, 2020). The relative contribution of each external forcing and or internal mode

seems to currently depend on model parameters and it still remains unclear which is the most likely driver of the warming after greenhouse gas emissions.

2.4 Sea-level fingerprinting

As demonstrated in **Chapter 1**, melting of an ice sheet or glacier leads to a non-uniform distribution of meltwater and subsequent spatial variability in sea-level change (*e.g.* Khan et al. 2015; Mitrovica et al. 2011). In far-field regions, sea level can reach a value ~30 % higher than the globally averaged rise (Tamisiea and Mitrovica, 2011). The signature or "fingerprint" of this ice melt can therefore be traced spatially. Sea-level fingerprinting attempts to map and estimate the contribution of ice loss to GSML and is calculated using an equation which takes into account the effect of GRD (*e.g.* Riva et al. 2017). The first attempt to amalgamate sea-level fingerprinting into estimates of GMSL change was done by Mitrovica et al. (2001). One of the ice masses they studied was the GrIS and they used sea-level fingerprinting to estimate the contribution of the Ice Sheet to GMSL. Several other studies have since attempted this, with varying results (**Table 3**).

Table 3. Estimated contributions from the Greenland Ice Sheet to global mean sea level over the 20th century using sea-level fingerprinting.

Study	Estimated contribution (mm yr^{-1})
Mitrovica et al. (2001)	~0.6
Nakada and Inoue (2005)	~1.0
Plag (2006)	~0.1
Hay et al. (2013)	~0.3
Hay et al. (2017)	~0.1

The early estimates of Mitrovica et al. (2001) and Nakada and Inoue (2005) tended to be higher than those calculated from observed rates of GrIS mass loss. If we take the most up to date estimates of GrIS contribution to GMSL from Kjeldsen et al. (2015), they suggests a contribution of 0.3 ± 0.1 mm yr^{-1} over 1900 – 1983. This means that these early sea-level fingerprint models suggested ~0.3 – 0.7 mm more rise per year than observations. This may be because the sea-level fingerprint models assumed constant rates of GrIS mass loss over the 20th century, which, as previous sections of this review highlight, is inaccurate. Newer attempts used a Bayesian methodology (Hay et al. 2013, 2015). These models used Kalman smoother and Gaussian process regression to estimate the processes responsible for the spatial variation in sea level. Hay et al. (2015) used these techniques to obtain the GMSL rates of 1.2 ± 0.2 mm yr^{-1} (Kalman smoother) or 1.1 ± 0.4 mm yr^{-1} (Gaussian process regression) shown in section 2.1.1. Hay et al. (2017) developed further on the 2015 study and estimated a GrIS melt rate of 0.14 ± 0.02 mm yr^{-1}.

Sea-level fingerprinting has since been successfully used in sea-level studies to assess and potentially explain the recent temporal and spatial trends in sea-level change (*e.g.* Gehrels et al. 2020). Estimates of GrIS mass loss support the hypothesis that the GrIS may have been in part responsible for the rapid rise in sea level observed in Australian and New Zealand historical records from ~1850 – 1950 (Gehrels et al. 2012; Gehrels and Woodworth, 2013). Possible evidence of this phenomenon has not only been observed in Australasia, but America too (*e.g.* Engelhart et al. 2009; Kemp et al. 2018; Kopp et al. 2014, 2015), with increasing rates of sea level observed latitudinally north – south, postulated to be the result of GrIS melt. Sea-level fingerprinting cannot determine which specific ice body melt has come from *i.e.* it cannot determine which specific Arctic ice cap melt has come from, as there is correlation between the estimates of the individual sources (Hay et al. 2017); however, the total sum of ice melt contribution can be determined as shown in this section, and so fingerprinting remains a useful tool for sea-level scientists.

2.5 The discrepancy between proxy and instrumental relative sea-level records from Australia

Whilst Australia is a region which would experience higher magnitude rates of sea-level rise owing to Northern Hemisphere ice melt (both GrIS and Arctic glaciers), and proxy records from the region suggest this (Gehrels et al. 2008; 2012; Grenfell et al. 2012), tide-gauge records suggest much slower rates of sea-level rise. For example, the New Zealand average rate (1891 – 2013) calculated from tide gauges at Auckland, Wellington, Lyttelton, New Plymouth and Dunedin was 1.5 ± 0.2 mm yr^{-1} (Denys et al. 2020) which is ~1 mm yr^{-1} less than the proxy record suggests. This discrepancy also occurs in the Tasmanian record (**Figure 17**). Whilst the proxy-based records suggest highest rates occurred in the first half

of the 20th century, especially ~1910, long tide-gauge records from Fort Denison, Sydney do not suggest a sea-level acceleration until ~1940 – 1960 (**Figure 17**; PSMSL, 2021). At Fremantle, between 1915 – 1960, instrumental data suggest sea level rose at an average of 2.2 ± 0.5 mm yr^{-1}. This is ~2 mm a year less than the proxy data record and at Hobart, the average rate is 1.5 ± 0.7 mm yr^{-1} from 1889 – 1972 (Hunter, 2007).

The earliest known direct measurements of sea level in Australia came from Port Arthur, Tasmania (1841 – 1842; White et al. 2014), but in southeastern Australia generally, long-term tide-gauge data are quite spatially sparse and temporally patchy in nature. There are also only a few records that extend back to the 19th century, with numbers only increasing ~1960. Some tide gauges such as Hobart, Fort Denison, Sydney and Newcastle are also problematic because they have datum shifts and or have been subject to land subsidence (Hunter, 2007; Watson, 2011; White et al. 2014). White et al. (2014) suggest that Australian individual tide-gauge records are too short and contain too much variability for detection of statistically significant accelerations in sea-level rise in Australia. Furthermore, due to the large distance between tide-gauge records and the proxy sites in Australia and New Zealand, comparisons between the two are difficult. Grenfell et al. (2012) suggested that compression in salt-marsh cores may be a reason for the discrepancy; however compression experiments from Brain et al. (2012) have shown that these salt marshes are not susceptible to compression, therefore the reason(s) for this discrepancy is still unknown. Burgette et al. (2013) advocate for combining instrumental records in order to obtain more accurate estimates of relative sea-level change.

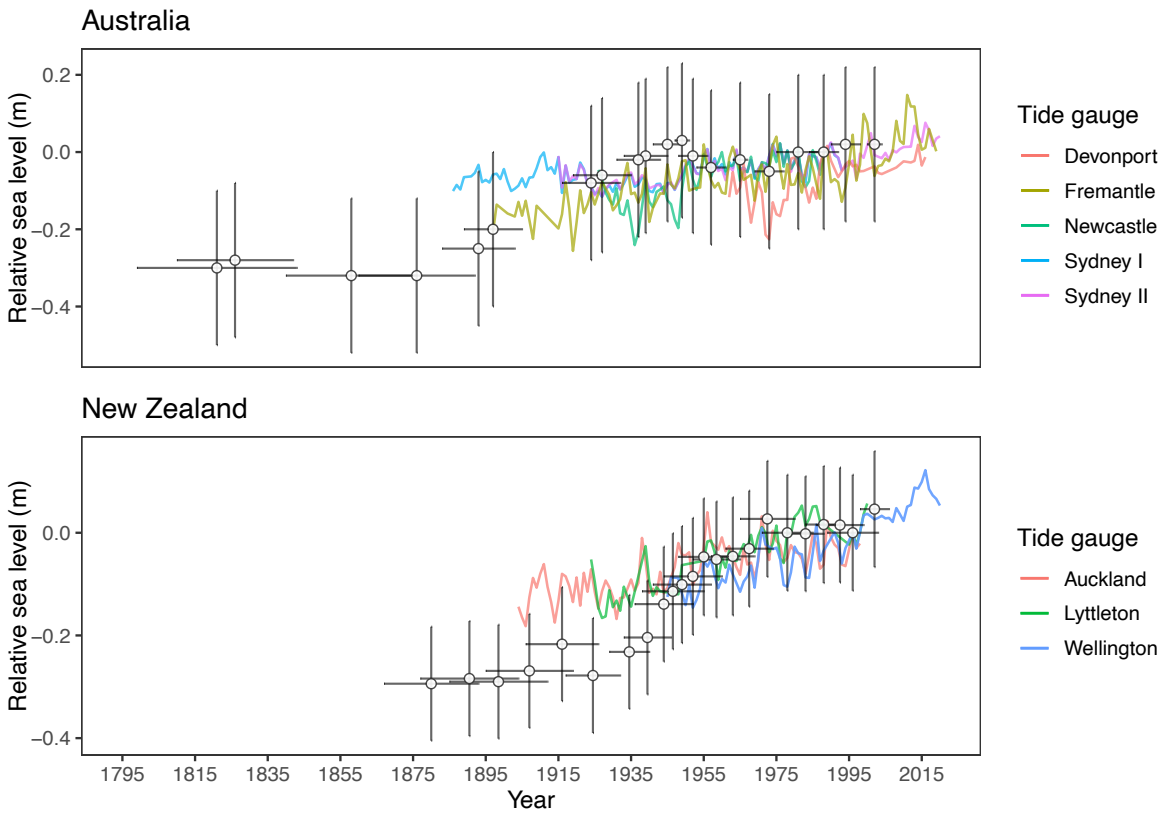

Figure 17. Comparison of long term tide-gauge records from southeastern Australia and New Zealand with existing proxy data (Gehrels et al. 2008; 2012). Data are uncorrected for vertical land motion. Also shown is the Fremantle (Western Australia) record as it is one of the few long-term tide-gauge records from the region. Data are available from PSMSL (2021).

2.6 Synthesis

This review has summarised the potential contribution of land-based ice (including glaciers and the ice sheets) to sea level since ~1850 to assess its likelihood as a driver of the sea-level acceleration ~1850 – 1950. Due to a lack of long-term tide-gauge records, most global reconstructions do not extend beyond ~1900 and, as such, prior to this period uncertainties are large. Estimates of GMSL since 1900 range from ~1.2 mm yr^{-1} to ~1.9 mm yr^{-1} as a result of differing reconstruction methodologies. The most current estimate suggests a global trend of ~1.6 mm yr^{-1} since 1900. All records show continuous rise over this period.

The barystatic component dominated sea-level rise over the early half of the 20th century, with the largest contribution coming from glaciers followed by the GrIS (Frederikse et al. 2020). Currently, (limited) evidence suggests that Southern Hemisphere land-based ice has not contributed significantly to 20th century sea-level rise, though further work is needed in the area to ascertain the contribution over the recent past and Common Era. Contributions from the steric component were low over the early 20th century, but increased over the century (Frederikse et al. 2020).

As mentioned in **Chapter 1**, there are now numerous proxy-based relative sea-level records that can extend these GMSL predictions back into the 18th century and beyond. Most of these records come from the North Atlantic where a sea-level acceleration is witnessed primarily ~1850 – 1860, although some records show a rise as early as 1812 (*e.*g. Kemp et al. 2017a). Records from Australia and New Zealand identify a slightly later sea-level acceleration ~1895 – 1920 (Gehrels et al. 2008; Gehrels et al. 2012) and some records from America and Canada have also identified an acceleration after 1920 (Barnett et al. 2017; Gehrels et al. 2005). This could mean that the earlier acceleration is possibly associated with the melting of glaciers worldwide (~1850) following the end of the LIA (*e.g.* Lea et al. 2014), and the second may be associated with melting of the GrIS during the ETCW in the Arctic (from ~1920). This non-synchroneity however could also be a result of age errors.

Both empirical and modelling studies have shown that both glaciers and the GrIS have lost mass from the 19th century to present (*e.g.* Malles and Marzeion et al. 2021; Kjeldsen et al. 2015; Wilton et al. 2017; Zemp et al. 2019). Rapid ice loss has occurred primarily after 1920 which correlates with a period of anomalously warm temperatures in the Arctic at the start

of the 20th century (Kjeldsen et al. 2015). Causes of the ETCW are still debated within the literature (*e.g.* Bokuchava and Semenov, 2020; Haustein et al. 2019; Svendsen et al. 2018; Xiao et al. 2020), but the two main hypothesises suggest increased external forcings over this time period, primarily from greenhouse gas emissions (*e.g.* Haustein et al. 2019), as well as changes in internal climate variability likely related to the NAO, AMO or PDO (*e.g.* Johannessen et al. 2016; Tokinaga, Xie and Mukougawa, 2017; Svendsen et al. 2018; Wegmann, Brönnimann and Compo, 2017). Future work in this area will help to resolve the cause of this temperature anomaly.

Sea-level fingerprinting demonstrates that meltwater from the Northern Hemisphere results in relative sea-level rise in the mid latitudes of the Southern Hemisphere (*e.g.* Bamber and Riva, 2010) and may explain why relative sea-level reconstructions from Australia and New Zealand suggest faster rates of sea-level rise during the earlier half of the 20th century compared to North American and European records. However, there is a discrepancy between proxy records and instrumental data in sea-level records from Australia and New Zealand, with long-term tide gauge records suggesting slower rates of sea-level rise over the 20th century than the proxy records (Gehrels et al. 2008; 2012). It is difficult to compare instrumental and proxy records in this region, because the tide gauges are generally too short to capture the acceleration, and a dense network of tide gauges are only available from ~1960 onwards (White et al. 2014). In the early records, there are problems associated with datum shifts, subsidence and the digitisation of the records which also make them unreliable. More proxy-based records are needed from the region to investigate the ~1850 – 1950 sea-level acceleration and to elucidate whether Northern Hemisphere ice was responsible for the rise.

Chapter 3 of 8

Study sites

3.0 Introduction

This chapter introduces the physical setting of the three salt-marsh sites in southeastern Australia which are used to test the hypothesis, aims and objectives outlined in **Chapter 1**. Section 3.1. provides a broad regional overview of the physical geography and climate of southeastern Australia. Section 3.2 summarises the late Quaternary palaeoenvironmental history and section 3.3 presents the mid – late Holocene sea-level change in the region. Section 3.4 presents the field sites, and finally section 3.5 and 3.6 summarise the European settlement and pollution history of the sites which are important for providing chronostratigraphic horizons that are key to the chronologies that underpin the sea-level reconstructions.

3.1 Regional overview

3.1.1 Climate

The Australian continent spans 30° of latitude from the tropics in the north, to the mid-latitudes in the south, and as a consequence the continent experiences significant regional climate variability. In the north, tropical systems dominate and there are two main seasons. Moving southwards, the influence of the tropical systems decrease, and extra-tropical weather systems dominate. The rainfall cycle becomes weaker and the temperature contrast increases, resulting in four distinct seasons. This study is focussed on sites in southeastern Australia in the sub-tropics. The region has been termed the "Southern Slopes" by the Commonwealth Scientific and Industrial Research Organisation (CSIRO) (Grose et al. 2015) and extends from Wollongong in the North (34.4 °S) to the Islands off the south-east Cape

in Tasmania (43.8 °S) (**Figure 18**). The Southern Slopes can be further sub-divided into Western Victoria, Eastern Victoria, southeastern New South Wales, Western Tasmania and Eastern Tasmania. This region of Australia has many of the coolest, high-altitude areas in Australia but also has extensive lowland coastal regions. The Southern Slopes largely have a temperate, maritime climate with an annual mean temperature of ~8° C in the elevated regions of Tasmania and Victoria, to ~14° C in the lowlands, although temperatures can reach over 24° C in January and down to 0° C in July (Grose et al. 2015).

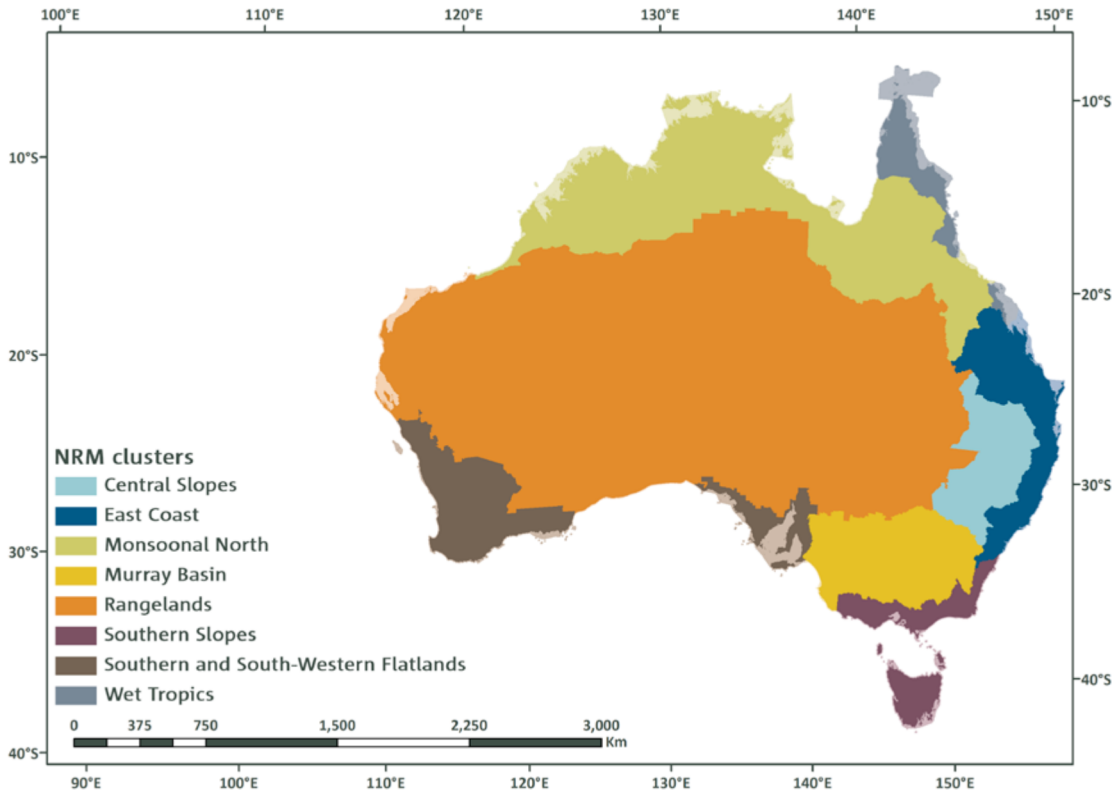

Figure 18. Regions of Australia split into national resource management clusters (NRMs) which can be used to split the physiographic characteristics of different regions of Australia (Figure from Grose et al. 2015).

The amount of rainfall the region receives is variable, but it is generally higher in the cooler months (**Figure 19**). In Tasmania, rainfall is largely driven by the Southern Annular Mode

(SAM) and in Victoria and south-east New South Wales by low pressure systems (Grose et al. 2015). In the winter and spring, rainfall is also influenced by the El Niño Southern Oscillation (ENSO) and the Indian Ocean Dipole (IOD). When La Niña combines with a negative IOD phase, rainfall is largely higher than average, and when an El Niño combines with a positive IOD phase, rainfall is largely lower than average (Risbey et al. 2009). Furthermore, the SAM also influences rainfall, leading to a complex interplay between the modes (Hendon, Lim and Nguyen, 2014). As well as the tropical and extra-tropical modes, the Southern Slopes are situated within the falling arm of the Hadley Cell and the northern edge of the 'Roaring Forties' westerlies and so the region often receives regular cold fronts.

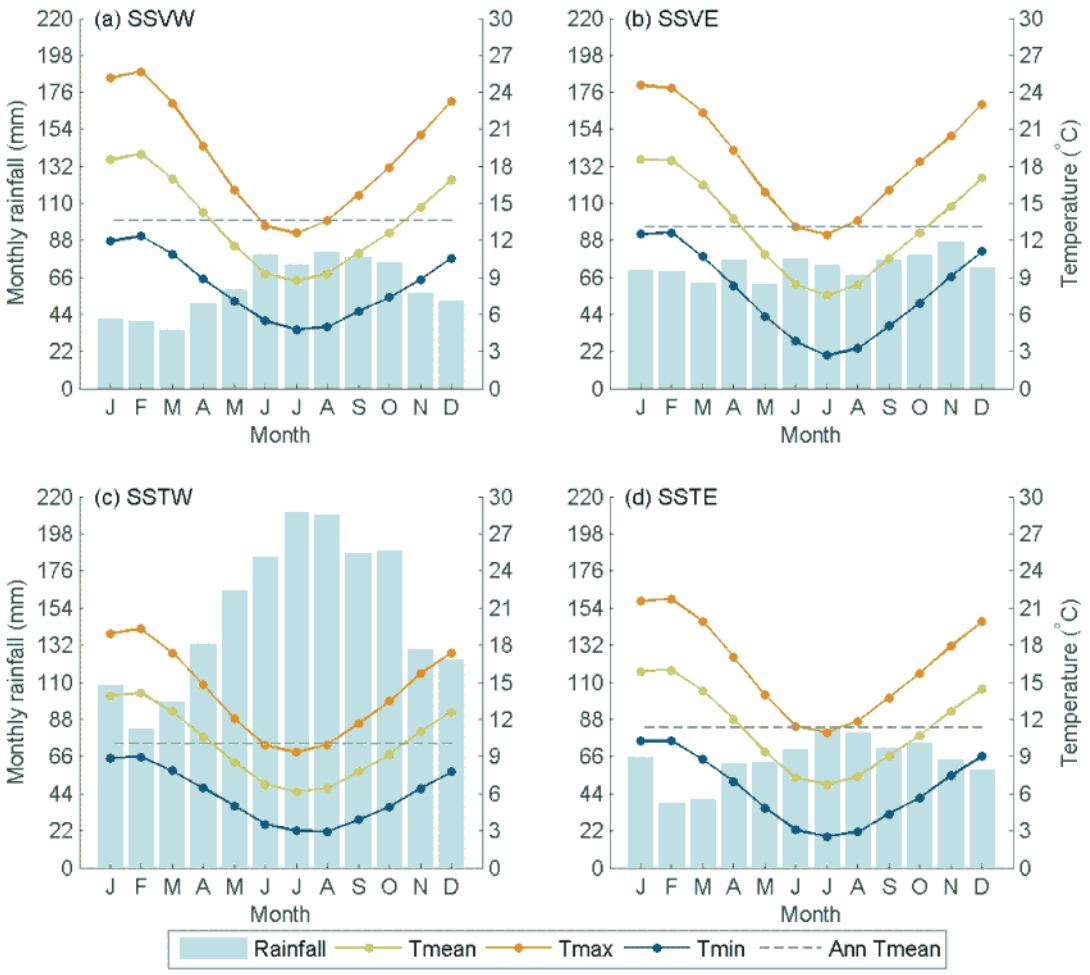

Figure 19. Monthly rainfall (blue bars) and temperature for the southern slopes cluster **A.** Victoria West, **B.** Victoria East and south-east New South Wales, **C.** Tasmania West, and **D.** Tasmania East (1986 – 2005). Tmean is monthly mean temperature (green line), Tmax is monthly mean daily maximum temperature (orange line), Tmin is monthly mean daily minimum temperature (blue line) and Ann Tmean is the annual average of mean temperature (grey line). Figure from Grose et al. (2015).

3.1.2 Geology

The geology of southeastern Australia is complex and is better detailed in the local site descriptions (see section 3.4); however, generally, much of western Victoria is covered in extensive basalt plains (Grose et al. 2015; Pilia et al. 2015) and Silurian/Devonian sedimentary rocks. Towards the east and over into southern New Southern Wales, the geology is dominated by Triassic-Jurassic and Late Devonian sedimentary rocks and Ordovician sedimentary rocks with Devonian and Ordovician granites (*e.g.* Pilia et al. 2015; **Figure 20**). The geology of western Tasmania is comprised of many different Palaeozoic sequences ranging from Meso-Neoproterozoic to Cretaceous in age. In the north-east of Tasmania, the geology is mainly comprised of Devonian-Carboniferous granites and marine quartz turbidites. Southeastern Tasmania is largely comprised of Carboniferous-Jurassic sedimentary rocks with some Devonian-Carboniferous granites (*e.g.* Hong et al. 2019; **Figure 20**).

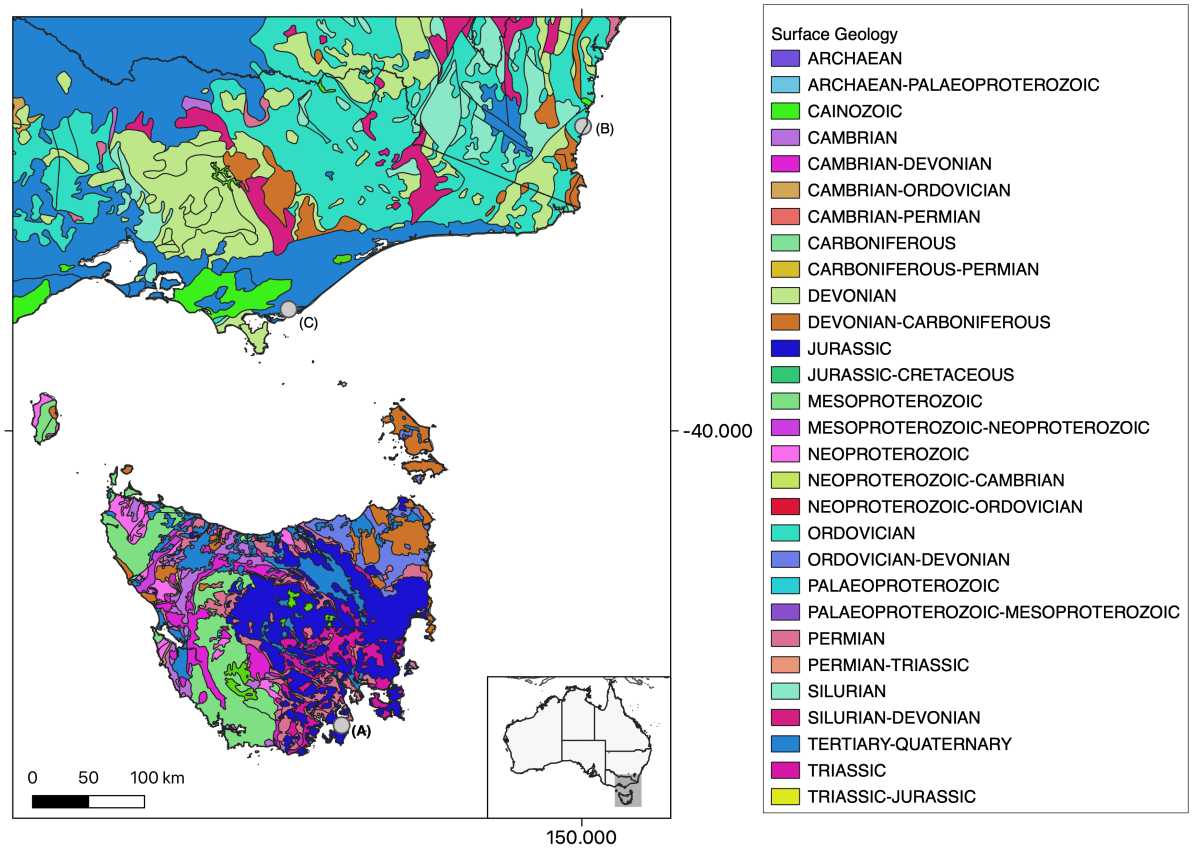

Figure 20. Surface geology of southeastern Australia (Eastern Victoria and south-east New South Wales as well as Northern Tasmania) showing site locations of **A.** Lutregala, **B.** Wapengo and **C.** Tarra. Data from Shaw et al. (2000).

3.2 Late Quaternary history and vertical land motion

Evidence of the Late Pleistocene glaciation has been found in Australia, with a period of significant cooling and increased aridity starting ~30 ka and peaking ~23 and 18 ka (Williams et al. 2013). Annual temperatures decreased by as much as 10° C compared to present day (Miller et al. 1997); However the glaciation was relatively small and restricted to southern Australia, only extending as far north as southern New South Wales (Barrows et al. 2001). It occurred on mountains generally higher than 1000 m above sea level (Colhoun

and Barrows, 2011). The glaciation was most extensive in western Tasmania, with two ice caps forming on the central Plateau and West Coast Ranges, and valley and cirque glaciers forming on surrounding mountains (Barrows et al. 2002; Colhoun and Barrows, 2011). Ice cover only occurred during the Last Glacial Maximum (LGM) and for a brief time following the LGM. There is no evidence for a readvance during the Younger Dryas or the Antarctic Cold Reversal (Barrows et al. 2002). As glaciation of the region was limited, no effect from regional GIA is expected at the study sites.

Continental levering as a result of meltwater loading (*i.e.* hydro-isostasy) produced VLM of the Australian continent during the Holocene (Lambeck and Nakada, 1990). Because of the irregular shape of the Australian coastline and shallow continental shelf (especially on the East Coast; *e.g.* Brooke et al. 2017), there is a non-uniform pattern of VLM across the continent (Fleming et al. 2012; Lewis et al. 2013), with subsidence in offshore locations and upward tilting of locations further inland away from the shelf margins (Lambek and Nakada, 1990). In southeastern Australia, the width of the continental shelf (*i.e.* the Gippsland and Eastern Tasmanian shelf) is narrow, and coastal sites are sufficiently close to the shelf margin to be tilted downwards, resulting in subsidence (**Figure 21**). Australia is largely considered tectonically stable (*e.g.* Lewis et al. 2013; Nakada and Lambeck, 1989), but does experience occasional earthquake activity (*e.g.* Leonard, 2008).

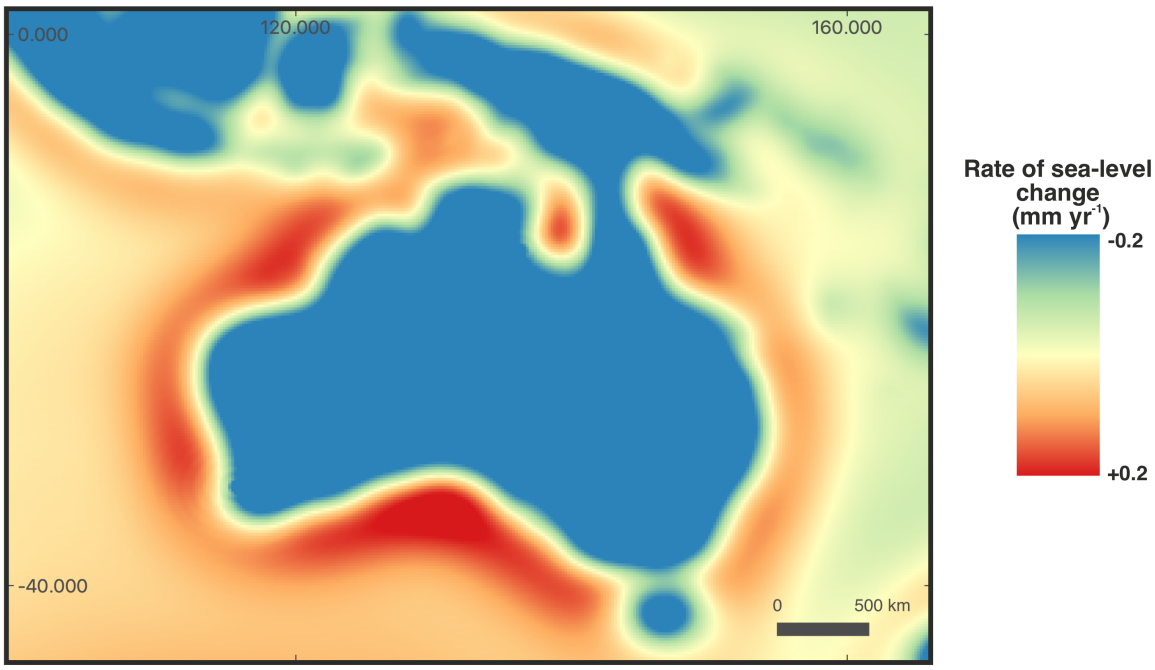

Figure 21. Rate of sea-level change across Australia due to vertical land motion – data from the ICE-6G_C model (Peltier, Argus and Drummond, 2015).

3.3 Sea level from the Last Glacial Maximum to present

Following the Last Glacial Maximum, in southeastern Australia, sea level rose until it reached a highstand in the mid Holocene (*e.g.* Khan et al. 2015; Lewis et al. 2013; Sloss et al. 2018; Williams et al. 2018; **Figure 22**). Estimates from north Australia suggest that the highstand reached 2.8 ± 0.4 m above present at 5 ka (Woodroffe, 2009), whereas estimates from southeastern Australia suggest a highstand of 1.4 ± 0.1 m at 5.5 ka (Sloss, Murray-Wallace and Jones, 2007). The timing and the magnitude of the highstand in Australia depends on GIA, and so is variable around the continent as well as on and offshore (Nakada and Lambeck, 1989). Initially, studies found evidence that dated the highstand around

Australia to between ~6000 – 5500 cal. yr BP (Gill, Lang and Boyd, 1982; Nakada and Lambeck, 1989). Since then, evidence has showed the highstand varied systematically around the continental margin, occurring earlier on the East Coast and later on the West Coast (Nakada and Lambeck, 1989). Originally, there was no evidence for a highstand in Tasmania, however, Fletcher and Thomas (2010) analysed both benthic marine diatom and wetland vegetation records in western Tasmania, and found evidence of a highstand ~6300 – 5800 cal. yr BP. Other studies have since found earlier evidence of the highstand commencing to 8000 – 7000 years ago (Lewis et al. 2013; Sloss, Murray-Wallace and Jones, 2007). A more recent study suggested a synchronised highstand down the East Coast from Northern Queensland to Southern Tasmania at 6880 ± 50 cal. yr BP (Dougherty et al. 2019). The refined age appears to be concurrent with major ice loss from both Ice Sheets (*e.g.* Jones et al. 2015), and the authors state that these may have played in role in driving the highstand. Currently, the best evidence for the highstand is largely found in Northern Queensland near the Great Barrier Reef, as well as along the New South Wales Coast (Dougherty et al. 2019; Nakada and Lambeck, 1989).

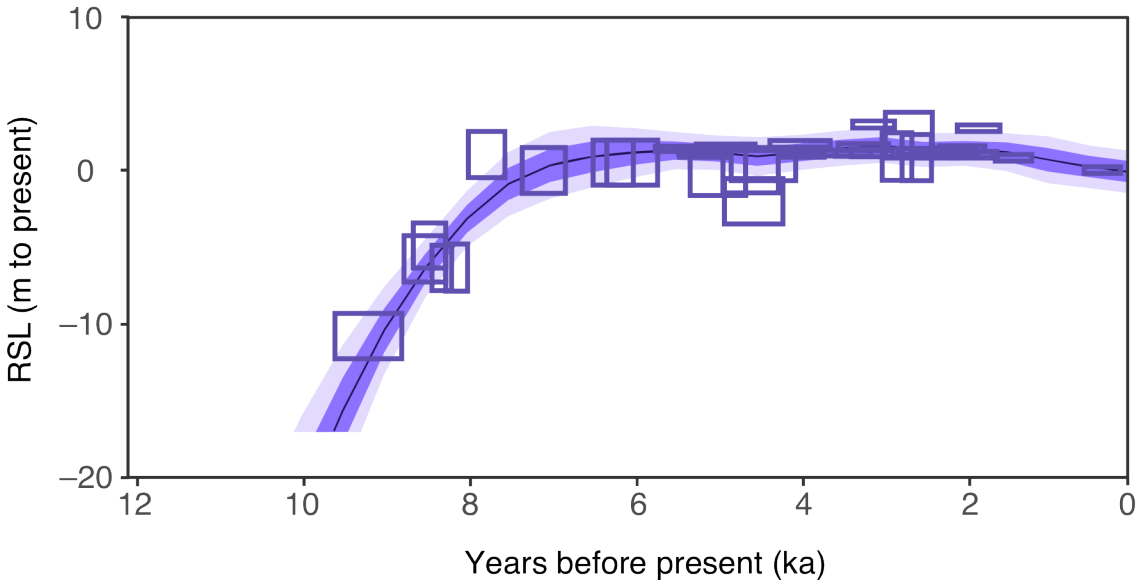

Figure 22. Relative sea-level reconstruction from New South Wales, Australia from the Holocene to present. Gaussian process regression model ran by Khan et al. (2015) showing mean and 1 σ (dark purple) and 2 σ errors (light purple). Sea-level index points shown by the rectangles. Original data from Sloss, Murray-Wallace and Jones (2007). Figure adapted from Khan et al. (2015).

Following the highstand, sea level fell gradually to its present level (Gehrels et al. 2008; Lewis et al. 2013; Woodroffe, 2009). Sea level then began to diverge from the Holocene background rate ~1500 (Gehrels et al. 2008; Masselink and Gehrels, 2015). The rate of 20th century sea-level rise was 1.5 ± 0.4 mm yr^{-1}. Gehrels et al. (2012) note that the greatest rises occurred between 1900 – 1950 (4.2 ± 0.1 mm yr^{-1} compared with 0.7 ± 0.6 mm yr^{-1} between 1950 – 2000). Spatially, the nearest proxy record to Tasmania comes from New Zealand (Gehrels et al. 2008). In southern New Zealand, sea level began rising slowly at 0.3 ± 0.3 mm year^{-1} from 1500 to 1900 until the rapid rise ~1900, where during the 20th century, the rate increased to 2.8 ± 0.5 mm yr^{-1}.

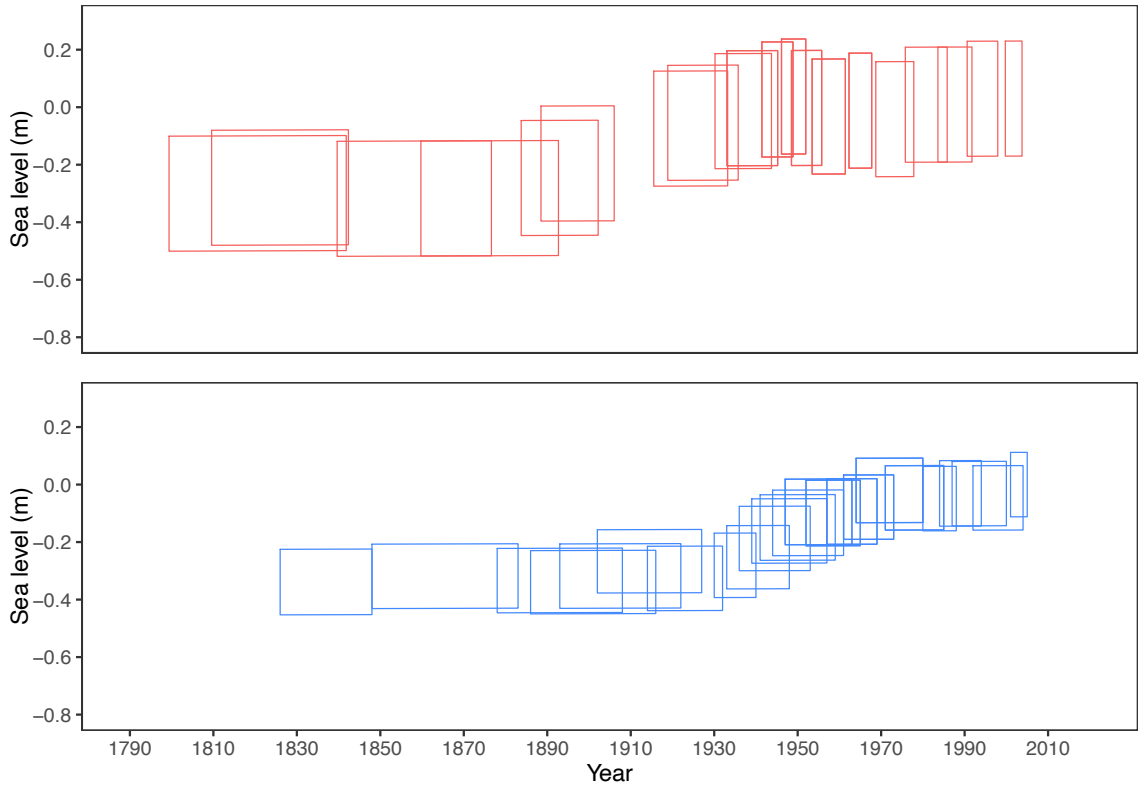

Figure 23. Upper panel. Relative sea-level reconstructions from Tasmania (Gehrels et al. 2012) and **Lower panel.** New Zealand (Gehrels et al. 2008; Garrett et al. 2022). Sea-level reconstructions have been updated to SHCal20. Boxes show 2 σ vertical and horizontal errors. Data are corrected for GIA using estimates from Caron et al. (2018).

From the 1960s, trends in relative sea-level rise from Australian tide-gauge records show an average rate of 1.4 ± 0.2 mm yr^{-1}; this ranged from 0.9 mm yr^{-1} at Fort Denison to 2.6 mm yr^{-1} at Darwin (White et al. 2014). When the Southern Oscillation Index signal is removed, the average trend is 1.6 ± 0.2 mm yr^{-1} over the period. From the 1990s, the corresponding average Australian trend in relative mean sea-level change was 4.5 ± 1.3 mm yr^{-1}, however this was 2.7 mm yr^{-1} after the signal correlated with the Southern Oscillation Index was removed, and 3.1 mm yr^{-1} after allowance for GIA and atmospheric pressure changes (White et al. 2014). Therefore, a complex interplay between past sea-level

change and the ongoing GIA response, climate modes and atmospheric pressure changes drive sea-level variability in southeastern Australia.

3.4 Study sites

3.4.1 Introduction

Salt marshes that are connected to the open ocean are regularly inundated by the tide and therefore have the potential to provide records of past sea-level change. In order to achieve the aims set out in **Chapter 1**, three new salt-marsh sites were selected in southeastern Australia - one each in Victoria, New South Wales and Tasmania (**Figure 24**). The new sites have minimal evidence of anthropogenic disturbance, are located in bedrock-framed inlets, and have small tidal ranges (≤1.25 m). These factors are important to maximise the likelihood that tidal ranges have not changed significantly over time, as this could have affected the vertical foraminiferal zonation.

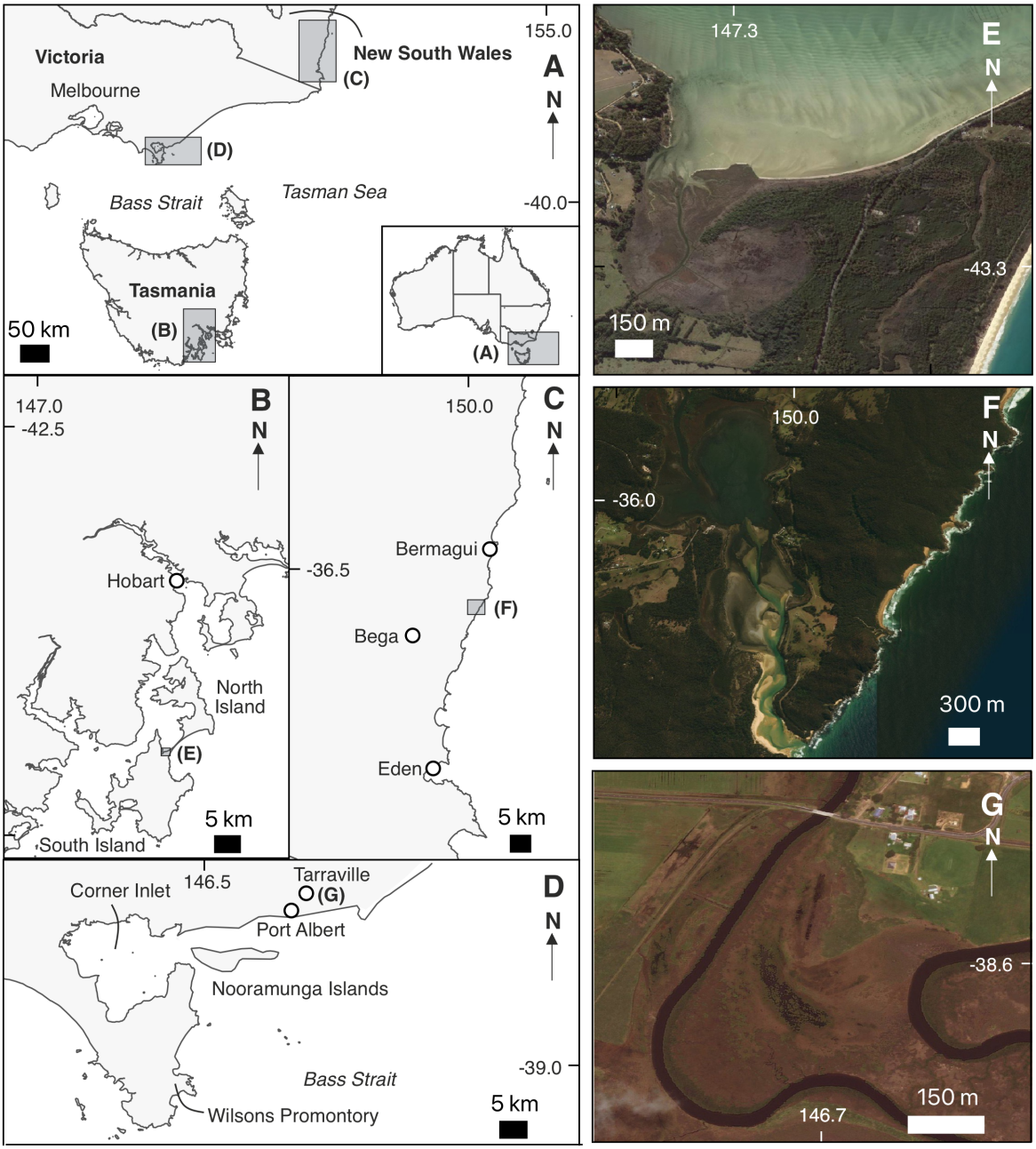

Figure 24. A. Regional map showing broad overview of study areas in the grey bounding boxes as well as states and state boundaries, major cities and seas. **B.** Study region on Tasmania showing the location of Lutregala salt marsh in the grey bounding box on South Bruny Island. **C.** Study region in Victoria showing the location of Tarra salt marsh by the white marker. **D.** Study region in New South Wales showing the Wapengo salt marsh in the grey bounding box. **E.** Lutregala salt marsh. **F.** Wapengo salt marsh. **G.** Tarra salt marsh.

3.4.2 Lutregala

Lutregala salt marsh is located on Bruny Island (Indigenous name is lunawanna-allonah) which lies off the coast of Tasmania (lutruwita), around 70 km south-west of Hobart (nipaluna; **Figure 24b**). An isthmus called 'The Neck' joins North and South Bruny Island, with Lutregala, ~ 0.4 km^2 in area, fronting onto Simpsons Bay on South Bruny Island (Prahalad and Jones, 2013). Due to its sheltered and shallow nature, Simpsons Bay includes several wetland areas (Clark, Cochran and Mazengarb, 2011). The bay is joined to the D'Entrecasteaux Channel, which is located between Bruny Island and mainland Tasmania. The average salinity in Simpsons Bay changes very little annually, with a mean salinity of 32.8 ppt in the bay (Crawford and Mitchell, 1999) and 31.5 – 34.7 ppt in the surrounding D'Entrecasteaux Channel (Parsons, 2012). The mean nearshore water temperature is 13.88° C (Crawford and Mitchell, 1999) and tidal modelling suggests that the tidal range is microtidal (0.47 m; Williams et al. 2021). At the northern extent of Lutregala, tidal channels and creeks are prevalent. The largest creek, Simpsons Creek, runs through the length of the salt marsh and is part of a larger low-lying saline marsh system supplied by freshwater originating in the South Bruny Range (Bryant, 2018). The site and immediate surroundings are underlain by sub and supra-littoral Quaternary deposits, as well as Quaternary alluvium, aeolian dunes, and sheet sand deposits, as well as surrounded by Triassic sandstone and Jurassic Dolerite to the northwest and Permian mudstone formations to the southeast (Farmer and Forsyth 1993; **Figure 20**).

At Lutregala, the upland is characterised by regenerating grazing land and sclerophyll forest, consisting primarily of *Eucalyptus ovata* (black gum) dry forest with a grassy

understorey (vegetation zone 1; Z1) (**Figure 25**). There is a patch of *Eucalyptus amygdalina* (coastal black peppermint) forest and *E. ovata* dry forest located on a dune system at the Simpson Bay beach side of the salt marsh (northeast area). Whilst all flora is found throughout the salt marsh, the dominance of the plants varies. The marsh is characterised by salt-loving plants. Higher elevations are largely characterised by *Juncus krausii* (salt-marsh rush) and *Gahnia filum* (chaffy saw sedge). Towards the mid – low elevations, *Sarcocornia quinqueflora* (beaded glasswort) dominates. There is also a low abundance of *Tecticornia arbuscula*, (shrubby glasswort), *Samolus repens* (sea primrose) and *Suaeda australis* (seablite) in the salt marsh (vegetation zone 2; Z2).

Figure 25. Vegetation zonation at Lutregala marsh showing upland Sclerophyll woodland, the main marsh flora and the unvegetated mudflat.

3.4.3 Wapengo

Wapengo salt marsh is located around 30 km south of Bermagui in southern New South Wales (**Figure 24c**). The salt marsh, which is around 0.51 km^2 in extent (Creese et al. 2009), is located at the northern end of the Wapengo Lake estuary. Towards the southern end, the estuary has a narrow bedrock-framed mouth (Bithry Inlet). The bottom of the channel is 1.2 m below mean high tide (Roper et al. 2011) and is not fast flowing (Scammell, Batley and Brockbank, 1991). Whilst some sites along this coastline are occasionally cut off from the open ocean, the entrance to Wapengo is permanently open (Scanes et al. 2007), and so Wapengo continuously maintains a connection to the ocean. Due to the proximity to the Bithry Inlet, the site has a high salinity, with multiple recordings from 2010 – 2012 showing salinity in the range of ~34 – 37 ppt (Garside et al. 2014). The average temperature in the estuary is ~16° C (Garside et al. 2014) and the modelled mean tidal range is 0.95 m (Williams et al. 2021). The underlying geology of Wapengo is a formation known as the Adaminaby Group, which comprises Late Ordovician turbidities of metagreywacke and phyllite (Rickard and Love, 2000; **Figure 20**).

At Wapengo there is a *Eucalyptus sieberi* (stringybark) dry forest with a shrub understorey, which transitions into a narrow fringe of coastal *Melaleuca* (tea tree) forest just above the salt marsh (vegetation zone 1; Z1). *Sarcocornia quinqueflora* is most dominant at higher marsh elevations and declines in dominance at elevation declines. *Juncus kraussii* is dominant at both high and low elevations with a decline at mid elevations. *Gahnia filum* is present sporadically at high elevations but increases in abundance as elevation declines and is dominant towards the lower end of the salt marsh. *Tecticornia arbuscula* and

Distichlis distichophylla (Australian salt grass) also increase in abundance as elevation declines. In the salt marsh there is also a low presence of *S. australis* and *Disphyma crassifolium* (rounded-leaved pigface) (these zones are defined at vegetation zone 2; Z2). Towards the seaward end, a transitional zone sees the appearance of *Avicennia marina* (grey mangrove) interspersed with *T. arbuscula* and *D. distichophylla* (vegetation zone 3; Z3), this develops into a dense mangrove forest at the lower elevations (vegetation zone 4; Z4) (**Figure 26**).

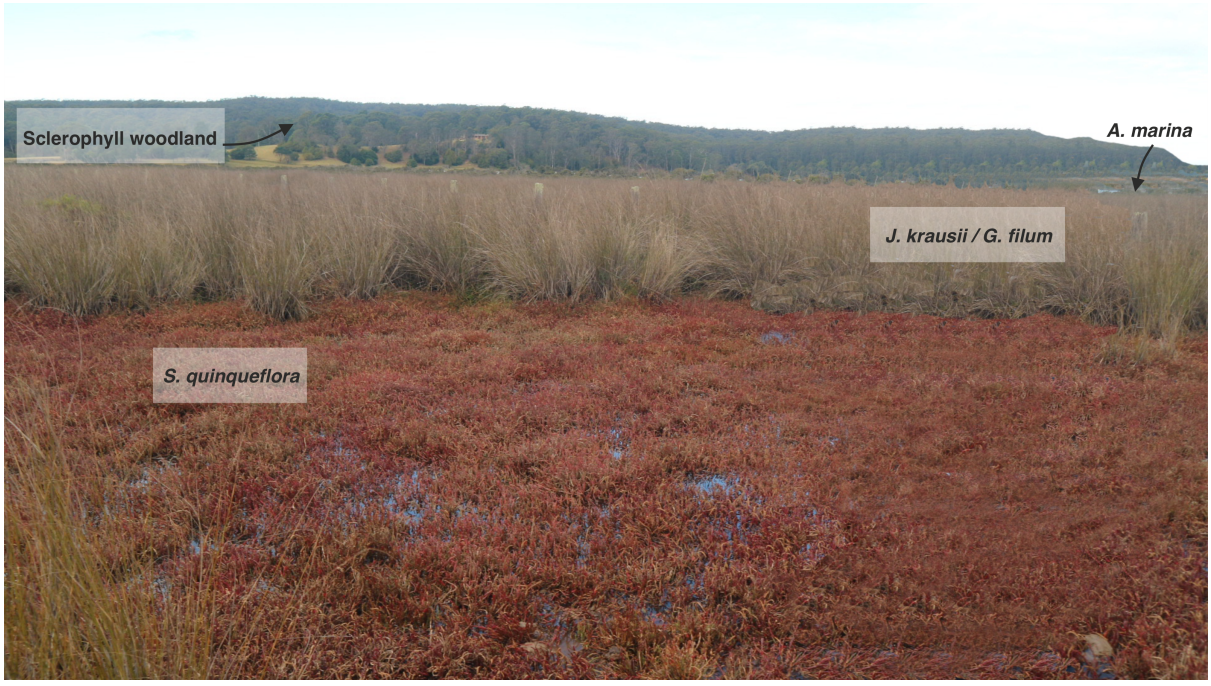

Figure 26. Vegetation zonation at Wapengo marsh showing upland Sclerophyll woodland, the main marsh flora and mangrove forest at the southern entrance of the marsh.

3.4.4 Tarra

Tarra salt marsh is located along the Nooramunga coast in the Nooramunga national park in East Gippsland ~4 km from Port Albert. The coast on which the salt marsh has formed is sheltered and is characterised by extensive sand and mud flats, tidal channels and sandy

barrier islands known as the Nooramunga islands (Australian Government, Department of Sustainability, Environment, Water, Population and Communities, 2011; Bird, 2010; Sinclair and Boon, 2012). Tidal modelling estimates a tidal range of 1.25 m (Egbert and Erofeeva, 2010) and the salt marsh is sheltered from strong wave action by the Nooramunga islands. The underlying geology of the Nooramunga park is comprised of Quaternary alluvium and colluvium, and Quaternary dune deposits with Neogene and Palaeogene deposits to the north and north east and the Cretaceous Strzelecki Group to the north west (Australian Government Bioregional Assessments, 2015; **Figure 20**). The Nooramunga coast itself is Pleistocene in age (Bird, 2010). Historical aerial imagery and maps from the Nooramunga coast show that there have been no significant changes in the positions of barrier islands and inlets over the last half century (Rosengren, 1989; Vic Basemap Services, State Government of Victoria, 2021), and it is expected that the Tarra marsh/river has maintained a constant open connection to the ocean.

A narrow fringe of *Melaleuca* is present around the marsh (defined as vegetation zone 1; Z1) which transitions into a marsh dominated by *S. repens, S. quinqueflora, J. krausii, D. distichophylla* and *T. arbuscula* (vegetation zone 2; Z2). All vegetation is present throughout the marsh, but the dominance varies. *D. distichophylla* and *S. quinqueflora* are most dominant at higher elevations and decline at lower elevations and *J. krausii, S. australias* and *T. arbuscula* are sparse at higher elevations and increase at lower elevations. The marsh is fronted by *Avicennia marina* (vegetation zone 3; Z3). Unlike Wapengo, there is no transitional zone between the marsh vegetation and the mangrove.

Figure 27. Vegetation zonation at Tarra marsh showing upland Sclerophyll woodland, the main marsh flora and mangrove forest that fronts the marsh.

3.5 European settlement and pollution history

3.5.1 Introduction

An investigation into a site's land-use history can aid with identifying chronohorizons in salt-marsh records which can be used when establishing a chronology (*e.g.* Kemp et al. 2012b). This last section of the chapter investigates the European settlement and pollution history of the sites which has yielded useful markers in previous work in the region (Gehrels et al. 2008; 2012).

3.5.2 Lutregala

There is evidence from midden deposits of Aboriginal occupation of Bruny Island extending back 6000 years, although there has been little archaeological research on the island. The island was visited by the French Bruni D'Entrecasteaux Expedition in the late 18th century, which noted that the island was occupied by the Nuenone people (Johnson and McFarlane, 2015). Permanent European settlement of North Bruny commenced in ~1818 (Nethery, 2012) and from the 1830s onwards, the North Island was predominantly used for timber, fruit growing, fishing, and sheep and cattle grazing (Jackson, 2006). However, official settlement of South Bruny Island was not recognised until the 1850s – 1870s when the dominance of the coal mining and timber industry grew in importance.

Following European settlement in Tasmania, several studies have found an increase in the abundance of woody and herbaceous species, as well as an introduction of exotic pasture species (Kershaw, Bulman and Busby, 1994; Romanin et al. 2016). Between 1930 – 1940 pine plantations were introduced at Cloudy Bay and Ventenat Point (Davis, 1990) on the South Island. The fire history from sites located on Tasmania shows an increase in charcoal abundance immediately succeeding European settlement, with an increase between 1850 – 1980 (Romanin et al. 2016). This indicates that burning post-settlement was occurring on much more frequent timescales than it was under Aboriginal management. After 1989, there are a declining number of fire records (Marsden-Smedley, 1998; Mooney et al. 2011; Romanin et al. 2016), suggesting a decrease in burning as a method of land clearance.

Despite these modifications to the landscape, population on the island remained low throughout the 19th and 20th century with ~311 residents across the North and South island in the 1970s (Jackson, 2006). After this, population grew quite rapidly, especially during the 1990s, and had doubled by 2001 to 600 (Jackson, 2006). By 2011, there were 534 living on the South Island alone (Australian Bureau of Statistics, 2021). Therefore, much of the European impact on the island has been relatively recent. In terms of mining history, there was a coal mine on the South Island which operated from 1879 – 1890 (Bacon, 1986). The coal seams were thin and small and so the mine was deemed of little economic importance and has not been mined since. The closest large refinery to South Bruny is the Risdon refinery (**Figure 28**). It was built adjacent to the Derwent River near Hobart and commenced operations in 1917. In 1924, the first Tasmanian ore from Rosebery, New South Wales was processed. Production at the mine has continued to the present day, with several major ores mined over that period of time including the Broken Hill lead-zinc-silver ore between 1930 – 1936 (Townsend and Seen, 2012). Major concerns about the dumping of mine waste into the Derwent were raised in the early to mid 1970s and pollution highs are recorded in the river around this time (Townsend and Seen, 2012).

Perhaps of greater significance to the wider Tasmanian settlement history is the Mt Lyell copper-silver-gold mining field on Tasmania which has been in operation for over 100 years (Augustinus et al. 2010; Bell and McCarthy, 2011; Corbett, 2001; Raymond, 1996; **Figure 28**). Excavation initially commenced in 1893 resulting in in two successful mines, two smelters, two towns and two ports (Weston, 2010; 2018). The company saw a highly successful decade in copper mining from ~1930. Production of copper rose gradually until 1933 and

peaked in 1935 (Weston, 2010). Copper production still remains high at the mine, with over 22,000 tonnes mined in 2012 (MDO, 2019).

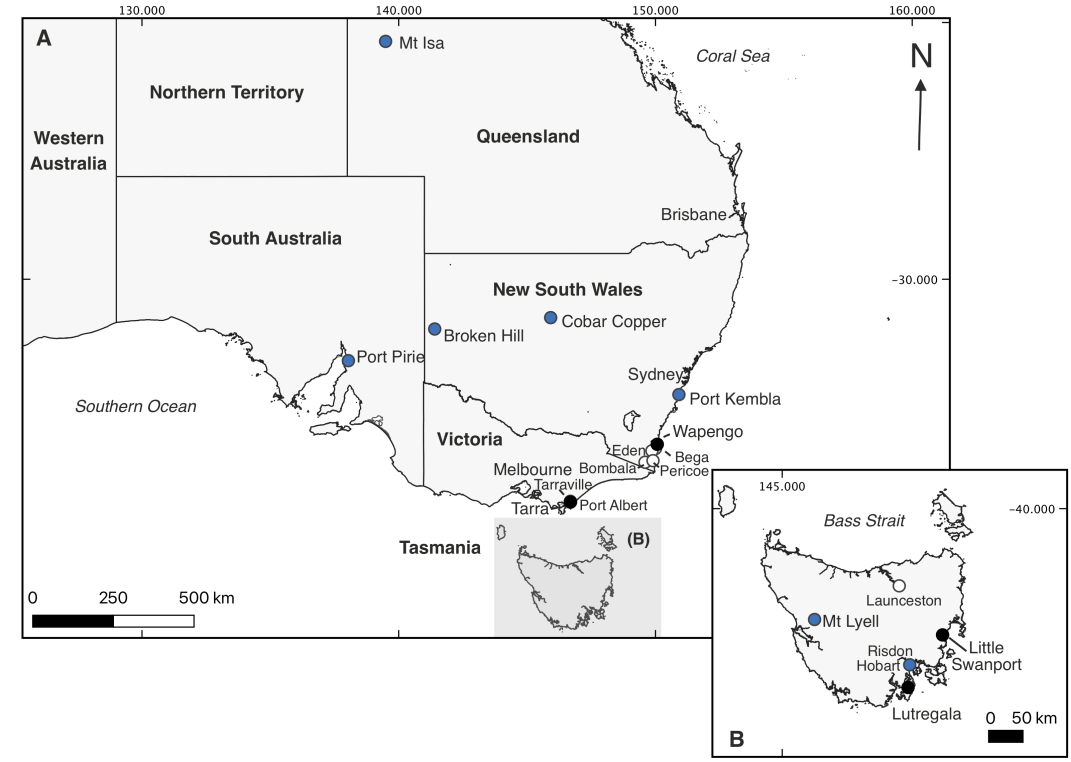

Figure 28. Locations of the mines in southeastern Australia that became the major emitters of pollution during the 19th and 20th century (blue icons), towns and cities (white) and study sites (black).

3.5.3 Wapengo

The oldest archaeological site in the vicinity of Wapengo Marsh is at Burrill Lake (around 150 km away; and has been dated to 21,000 years ago (Lampert, 1971). The site was occupied by the Yuin people at the time of European settlement and there is evidence that they had been in the area for at least 6,000 years (Byrne, 1983; DECCW, 2011). The area was settled in 1830 and was further expanded in 1835 (Bayley, 1942; Bazley, 2015; Lunney and Leary, 1988). The main land uses were both grazing of cattle and sheep, and wool and meat

production. Ecosystems in the Bega district were severely altered within months of settlement by grazing and the introduction of invasive and non-native plant and tree species (Lunney and Leary, 1988). The Robertson Land Act was passed in 1861 which allowed for the intensification of activity in the area (Griffiths, 2002; Keith and Bedward, 1999). This encouraged a wave of migration (Spooner, 2005), and by 1861, the population of Bega stood at 625. In Eden, (one of the biggest towns in the area) this had grown to around 4000 by 1878 (Lunney and Leary, 1988).

The timber industry exploited the forests in the Bega valley and the surrounding hills and the whole region had virtually been cleared by 1910. After the 1920s, the clearance rate dropped, and very little amounts of new land were cleared. Pine plantations were established over marginal grazing lands and native forest at Bombala and Pericoe during the 1970s and 1980s (Keith and Bedward, 1999). More broadly, across southern NSW, pine plantations were established over the late 1960s and early 1970s, with a peak in 1985. This was then reduced between 1990 – 1994 (Australian Bureau of Agricultural and Resource Economics, 2000).

From European settlement until 1988, 14 major fires were recorded in the Bega region (Lunney and Leary, 1988). Two of the largest and most destructive fires documented in the region occurred in 1884 and 1952 (Scott, 1999; Whittaker et al. 2020). A fire in 1980, originating in Mumbulla (~8 km from Wapengo) reached Wapengo and has been documented in the fire history of the site (Lunney, Cullis and Eby, 1987) and another wildfire is recorded as occurring in the Mumbulla precinct in 1968.

Near the study site is the Dargues gold mine and the Woodlawn Project which mines zinc and copper (NSW mining, 2020). However, mining appears minimal in the area, and a study looking at heavy metal concentration in the catchment (including in the Wapengo Lake estuary) only found evidence of very low levels of pollution (Mackay et al. 1975). Further north, two major mines are the Port Kembla and Cobar Copper mines. At Port Kembla, a copper refinery and smelter was set up in the area in 1908 and a related manufacturing company arrived in 1916 (Eklund, 2002; Weston, 2018). Copper smelting continued in the region until around the late 1990s (Weston, 2018) and finally halted in 2003 (He and Morrison, 2001; Huo, Crisp and Cohen, 1999; Martley, Gulson and Pfeifer, 2004). The Cobar copper fields were discovered in 1870 (Mudd, 2009). In 1917 the mine launched a smelter capable of smelting up to 100 – 150 tonnes per day. Until 1953 (the opening of Mt Isa), it was one of the biggest producers of copper in NSW (Mudd, 2009).

3.5.4 Tarra

There is evidence for Aboriginal occupation in the Gippsland region through the discovery of Aboriginal lithics (Brooks, Lawrence and Lennon, 2011). Archaeology suggests human occupation for at least 5 ka (McNiven, 2000). Port Albert (Aboriginal name Tarra Warackel) as well as the Albert and Tarra rivers were settled by Europeans ~1830 (South Gippsland Pioneers' Society, 1920). Victorian settlement may have been as early as 1835; however, documented settlement of the Tarraville and Port Albert area is from 1841 onwards (Caldow, 2003). By the end of 1843, a number of buildings had been constructed in the town and the population stood at 56 (Caldow, 2003). Ten years later, this figure had raised to 270 and by 1857, 339 people were recorded as living in Tarraville (Caldow, 2003).

The early days of Gippsland land use were primarily focussed on pastoralism. The dairy industry began in the region as soon after settlement. Towards the end of the 1860s, the land around South Gippsland was nominated for selection under the Lands Act 1869. This act encouraged an intensification of land-use change in the area (South Gippsland Pioneers' Society, 1920) and thus activity in the region increased. By the 1870s, felling began on a larger scale. Similarly to Bega, the majority of the scrub in the region had been cleared by the end of the 18th century and early 19th century (1890 – 1910) (Frost, 1997; Lindenmayer, 2007; South Gippsland Pioneers' Society, 1920). Pine plantations were established in the nearby Strzelecki Ranges during the 1940s (Mainville, 2007).

There are numerous gold mines in Gippsland, and indeed, these mines were a primary reason for the population boom in the Victorian state in the 1850s (Mudd, 2007). Other mines within the region include the black coal deposits of the Strzelecki Group. Most of the coal in the South Gippsland area was mined in the late 19th century to mid 20th century (Australian Government Bioregional Assessments, 2018). There is little evidence however for mining activity within the immediate vicinity of the Tarra site. However, both Tarra and Wapengo are located southeast of the Broken Hill mine and may have been exposed to pollutants from the prevailing westerlies (Marx et al. 2010).

3.5.5 Lead pollution

Broken Hill is arguably one of the single-most important mines in the history of European settlement, as it completely revolutionised metal mining not only in Australia, but worldwide. Lead mining in particular reached new levels of operation and production after

the discovery of the Broken Hill lead-silver-zinc ore body in 1883 (Boreland and Lyle, 2009; Lyle et al. 2006; Mudd, 2009; Solomon, 1988). The first ore from Broken Hill was smelted at Spotswood, Victoria. However, business grew so quickly that later on in 1885, smelting began on-site. From 1885 – 1897, both open-cut mining and smelting of the ore body was conducted on site, with up to 28 smelters in operation (Woodward, 1965). Figures have estimated lead smelting emissions at Broken Hill to total 46,400 tonnes between 1886 – 1897 and 167,000 tonnes at Port Pirie between 1889 – 1982, with the majority of the emissions being created within the first few decades until ~1920 (Van Alphen, 1991).

Broken Hill thus became one of the first significant contributors to anthropogenic lead emissions in the Australian environment. Exportation of lead continued at exceptionally large rates and was the primary mined metal at Broken Hill. However, around 1897 zinc was also mined (McQueen, 2015). The zinc furnaces ran from 1902 – 1921 (Woodward, 1965). Between 1946 – 1950, Broken Hill produced 10.7 % of the world's lead (Solomon, 1988). The Broken Hill lead ore comprises its own distinct isotopic signature ($^{206}Pb/^{207}Pb$ 1.04; $^{206}Pb/^{204}Pb$ ~16.00; $^{208}Pb/^{207}Pb$ 2.33; Kristensen and Taylor, 2016; Chiaradia et al. 1997) and Mt Isa also has a similarly low isotopic signature ($^{206}Pb/^{207}Pb$ 1.04; $^{206}Pb/^{204}Pb$ ~16.12; $^{208}Pb/^{207}Pb$ 2.31; Chiaradia et al. 1997).

An increase in lead concentration is seen in many environmental archives shortly after European settlement (from ~1890 onwards; Marx et al. 2010; McConnell et al. 2015; Serrano et al. 2016; Van de Velde et al. 2005; Wu et al. 2016), as well as a corresponding change in the isotopic composition of the lead (*e.g.* Kristensen, Taylor and Flegal, 2017; **Figure 29**). This is attributed to mining at Broken Hill and subsequent smelting at Broken Hill and Port

Pirie (Vallelonga et al. 2002). Marx et al. (2010), whose record derives from a peat bog in southern New South Wales, also find a period of initial mining activity dating to 1850 before the more marked decrease in 1890 (**Figure 29**). In Antarctica, Vallelonga et al. (2002) identify two other distinct periods of lead pollution in their Law Dome record, one between 1919 – 1948 where $^{206}Pb/^{207}Pb$ ratios increase to values ~1.17 – 1.18 and then another between 1956 – 1989 where values decrease again.

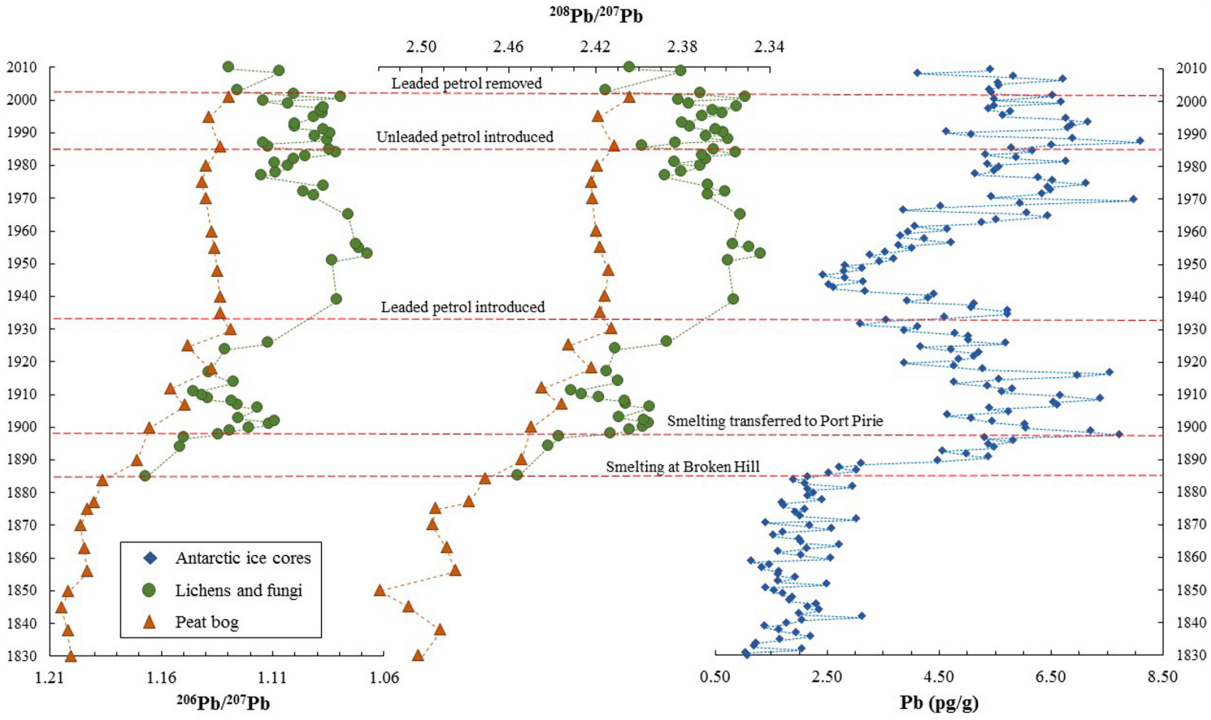

Figure 29. Changes in the composition of stable lead isotope $^{206}Pb/^{207}Pb$ from 1830 – 2010 from various environmental archives. Variations in isotopic composition can be seen when smelting at Broken Hill mine began in 1884 from more radiogenic values of $^{206}Pb/^{207}Pb$ ~1.17 to less radiogenic values of $^{206}Pb/^{207}Pb$ ~ 1.12 (seen in peat bog and lichen records). Figure from Kristensen, Taylor and Flegal (2017). Dates on figure: Smelting at Broken Hill ~1885, smelting transferred to Port Pirie ~1889, leaded petrol introduced 1932, unleaded petrol introduced 1985 and leaded petrol removed 2002. This study aims to identify the Broken Hill event and Pb pollution maximum ~1960 – 1980 prior to the isotopic decline following the introduction of unleaded petrol and removal of leaded petrol towards the end of the 20th century and start of the 21st century.

The introduction of leaded petrol (1932) and unleaded petrol (1985) as well as the removal of leaded petrol in Australia in 2002 may also provide chronostratigraphic markers in the records (Kristensen, Taylor and Flegal, 2017). A Southern Hemisphere pollution maximum was reached between 1960 – 1980 in the 20th century (Kristensen, 2015; Vallelonga et al. 2002), and a peak in Australian petrol lead emissions is recorded in the early 1970s (**Figure 30**). Lead pollution can be seen in the lichen and fungi records from Sydney where significant declines in the $^{206}Pb/^{207}Pb$ isotopic compositions are observed from the end of the 19th century to the 1970s. The following decades are then characterised by lower lead levels as a result of the introduction of unleaded petrol and the ban of leaded petrol. As a response to these regulatory changes, $^{206}Pb/^{207}Pb$ isotopic compositions increase, especially from 1995 onwards (Wu et al. 2016).

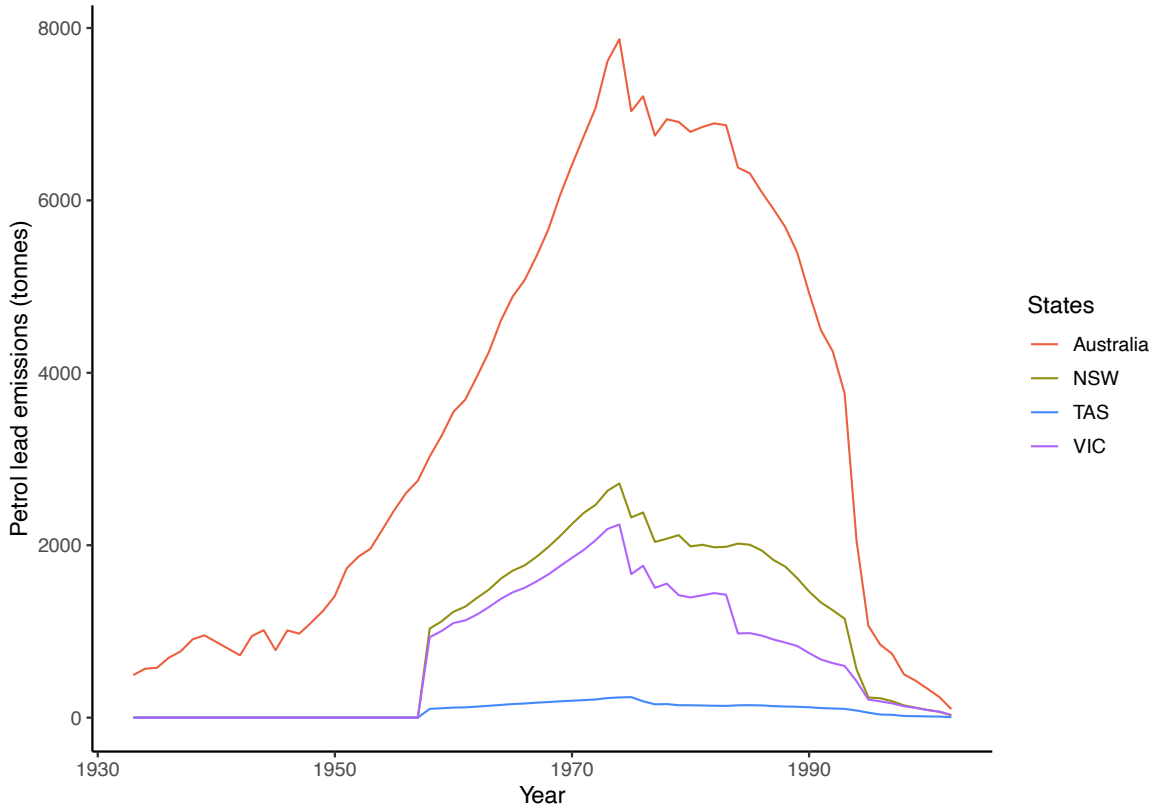

Figure 30. Calculated lead emissions from leaded petrol in Australia and within New South Wales, Victoria and Tasmania individually. The lead maximum is reached between 1960 – 1980 with a peak in the early 1970s. NSW= New South Wales, TAS= Tasmania, VIC= Victoria. Figure adapted from Kristensen (2015).

At Little Swanport (Gehrels et al. 2012), several isotopic markers are apparent in the lead profile of the core, including the Southern Hemisphere increase in atmospheric lead pollution in the 1890s, the late 1940s minimum (Wolff and Suttie, 1994), the leaded petrol signal and the widespread smelting of zinc since the 1930s (which required coal burning and consequently causes a lower $^{206}Pb/^{207}Pb$ ratio (Mudd, 2009).

The onset of Southern Hemisphere pollution can be found as far as Antarctica (McConnell et al. 2015; Planchon et al. 2003), with ice cores showing increases in lead towards the end of the 19th century. The cores show a decrease in lead concentration from ~1910 until the

rise of leaded petrol (McConnell et al. 2015), which either suggests a decrease in the ores smelted at Broken Hill and Port Pirie, or could reflect the modernisation of the smelters. Furthermore, not only do the cores show increases in lead concentration, the isotopic composition of the lead also changes to the characteristic structure of the Broken Hill ore. The low isotopic ratios observed in the cores suggest that Broken Hill was the source for rapidly increasing lead fluxes and emissions after 1891 (Vallelonga et al. 2002).

3.6 The potential use of chronostratigraphic markers in this study

An investigation of historical records and documentation surrounding both land-use change and mining history in southeastern Australia has shown that evidence of European settlement should be visible within the palaeoenvironmental records at the sites. Dates from historical documentation have been collated from this section and are used in **Chapter 6** to constrain the resulting chronologies. Using evidence from archival information and historical documentation, the following potential chronohorizons are established (**Table 4**).

Table 4. Summary table of chronostratigraphic markers and their representative year as detailed in historical records.

Site	Marker	Cause	Year	Reference
Lutregala	Pollen	Initial deforestation and introduction of exotic taxa	~1850 – 1870	Personal communication with Bruny Island Historical Society (2021)
Lutregala	Pollen - *Pinus*	Pine plantations established	1930 – 1940	Davis (1990)
Wapengo	Pollen	Initial settlement – Deforestation and introduction of exotic taxa	1830 – 1840	Lunney and Leary (1988)

Wapengo	Pollen - *Pinus*	Pine plantations established	~1965 – 1989	Australian Bureau of Agricultural and Resource Economics (2000); Keith and Bedward (1999); Scott (1999)
Wapengo	Charcoal	Fire	1884 1952 1968 1980	Lunney, Cullis and Eby (1987); Lunney and Leary (1988)
Tarra	Pollen	Initial settlement and introduction of exotic taxa	1841	Caldow (2003)
Tarra	Pollen	Introduction of pine in Victoria	~1850	Mooney and Dodson (2001)
Tarra	Pollen - *Pinus*	Pine plantation established in ranges near Tarra	1940 – 1950	Mainville (2007)
All sites	Charcoal	Change in fire regime following European settlement	Settlement date for each site	–
All sites	$^{206}Pb/^{207}Pb$	Sustained increase in Broken Hill pollution	1890 – 1900	Van de Velde et al. (2005); Gehrels et al. (2012)
All sites	$^{206}Pb/^{207}Pb$	Start of post WW2 decline	1946 – 1950	Vallelonga et al. (2002); Gehrels et al. (2012)
All sites	$^{206}Pb/^{207}Pb$	Leaded petrol introduction	1932	Kristensen,Taylor and Flegal (2017)
All sites	$^{206}Pb/^{207}Pb$	Pb maximum	~1974	Kristensen (2015)
All sites	$^{206}Pb/^{207}Pb$	Unleaded petrol introduced	1985	Kristensen,Taylor and Flegal (2017)
All sites	$^{206}Pb/^{207}Pb$	Leaded petrol removed	2002	Kristensen,Taylor and Flegal (2017)

3.7 Summary

The study area for this thesis is southeastern Australia, in particular three sites located in southern New South Wales, eastern Victoria and southern Tasmania as this area is suitable to test the hypothesis outlined in **Chapter 1**. All sites are located along a microtidal coast with bedrock framed inlets. Attempts have been made to choose sites with little evidence of human disturbance with the aim of sampling sites that have not changed vastly over time. Sites are largely tectonically stable, although there is ongoing VLM as a result of continental levering. Following the LGM, sea level in Australia rose until reaching a mid-Holocene highstand ~6000 cal. yr BP, this was temporally variable around the continent. Sea level then gradually fell until ~500 years ago when it began to rise as it departed from the Holocene background rate. Proxy records from Australia and New Zealand show a period of rapid rise between ~1850 – 1950, although the number of proxy records are limited. Sea level in Australia is affected by ongoing VLM as well as the Southern Oscillation Index and changes in atmospheric pressure. European settlement of the sites occurred in the 19th century and several markers as a result of both the introduction of exotic flora, change in fire use, mining history and lead pollution may be apparent in the salt-marsh records from the sites. Identifying these in the records will aid chronology establishment.

Chapter 4 of 8

Methods

4.0 Introduction

This chapter outlines the methodologies used to address the research questions summarised in **Chapter 1.** First, it describes field methods used to collect surface and core samples at the study sites in southeastern Australia (Lutregala, Wapengo and Tarra), and details how elevation and tidal data were obtained for said samples. Second, the chapter describes laboratory methods that were used to prepare and analyse microfossil and sediment samples. Third, the chapter outlines the statistical analyses undertaken to generate transfer functions for palaeomarsh surface elevation estimations and documents how RSL was calculated. Fourth, the chapter describes the methods used to obtain a chronology for each core. Finally, the chapter details modelling used for RSL reconstruction, assessment of the rates and magnitudes of RSL changes and sea-level fingerprinting.

4.1 Fields methods

4.1.1 Modern foraminifera sampling

Two transects at each site from upland to tidal flat were established in order to obtain samples from all of the ecological zones observed in each salt marsh. At the sampling locations, samples ~1 cm in thickness and 12.5 cm^3 in volume were collected (**Figure 31**). Marsh flora was also noted along each surface transect concurrently to sampling.

4.1.2 Core sampling

An initial inspection along coring transects was done at each site with a hand-held gauge corer (0.5 m × 3 cm) to ascertain the area of the marsh with the thickest salt-marsh peat that

might provide the longest sea-level record (**Figure 31**). Master cores were taken from each site using either a wide-diameter gouge (0.5 m × 6 cm) or Russian peat sampler (0.5 m × 6 cm). For Lutregala and Tarra, additional replicate cores were also collected in April 2019.

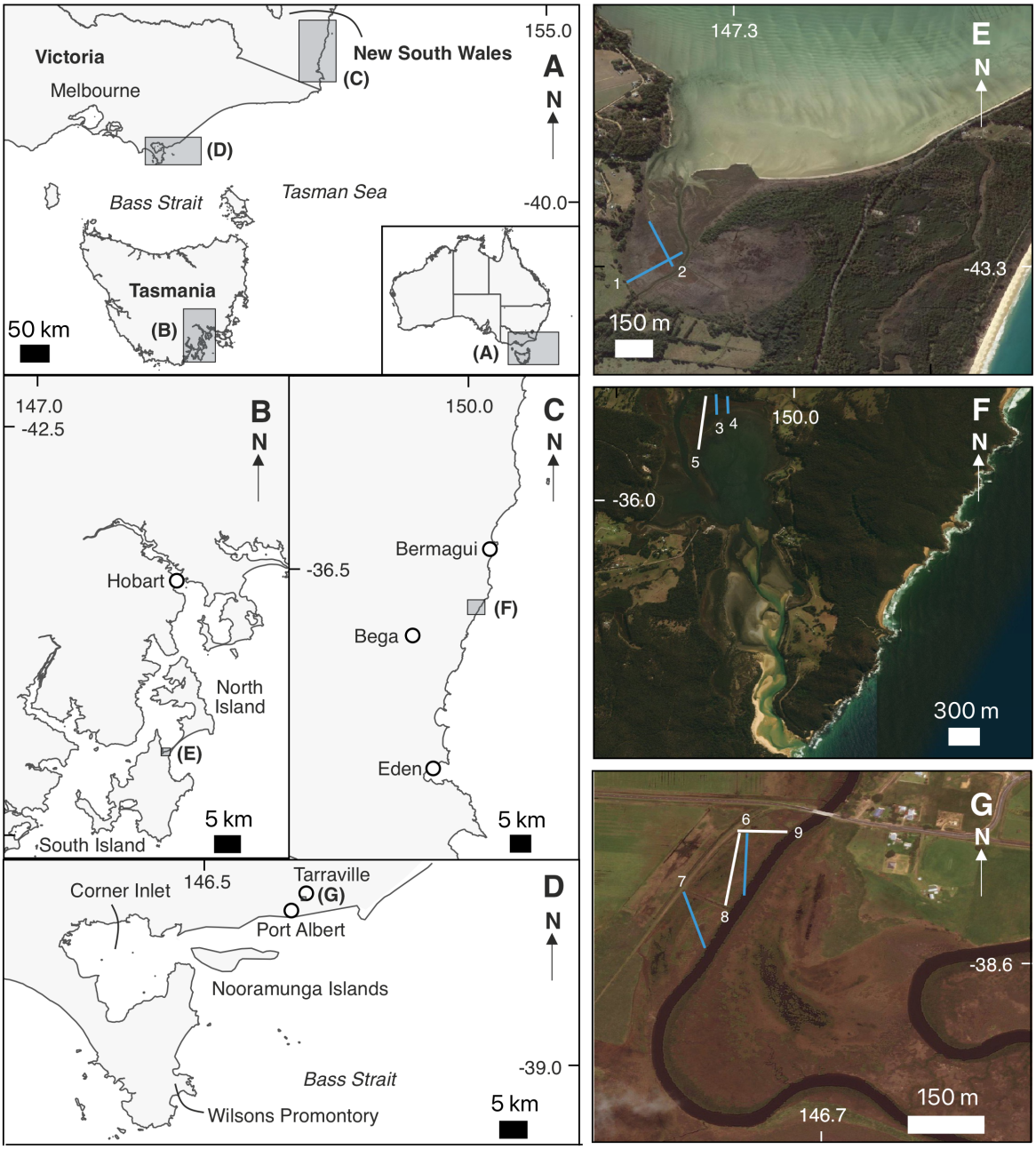

Figure 31. Surface and coring transects and master core locations at **E.** Lutregala, **F.** Wapengo and **G.** Tarra. Corresponding transects (Lutregala - Transects 1 and 2; Wapengo – Transects 3, 4 and 5 and Tarra – Transects 6, 7, 8 and 9). *N.B.* Blue transects = transects used for both coring and surface samples, white transects = transects used only for coring.

4.2 Elevation and tidal data

To enable inter-site comparison, the height of all samples (modern and core) were related to the Australian Height Datum – Geocentric Datum 2020 (AHD). Sample elevations were established using both a Trimble M1 (DR2") total station and a Trimble R4 real-time kinematic GPS relative to a temporary benchmark. To survey sample heights into the geodetic datum, a 'rapid static' method was employed between the temporary benchmark and a local geodetic benchmark. Mean sea level (MSL) and highest astronomical tide (HAT) were obtained from the Australian National Tide Tables (AHP11; Australian Government, Department of Defence, 2020) using data from the nearest local tide station to each site (**Table 5**).

As the tide gauges are located 20 – 50 km from the salt marshes, spatial differences in tidal range were checked using the TPXO8-Atlas global tidal model (Egbert and Erofeeva, 2010). The tidal range at the Hobart tide gauge is 0.81 m (Australian Government, Department of Defence, 2020) and the TPXO8-Atlas global tidal model indicated a minor difference in tides (0.02 m difference in MSL – HAT range) between the tide gauge and Lutregala (Egbert and Erofeeva, 2010). The tidal range at the Bermagui tide gauge is 1.01 m (Australian Government, Department of Defence, 2020) and the TPXO8-Atlas global tidal model indicated no difference in tidal range between the tide gauge and the entrance to Wapengo Lake estuary (Egbert and Erofeeva, 2010). Finally, the tidal modelling predicts a tidal range of 1.25 m at Tarra and a 0.2 m difference between the MSL – HAT range between the site and the tide gauge. Tidal range between sites was normalised using a Standardised Water-Level Index (SWLI; Zong and Horton, 1999). Wright, Edwards and van de Plassche

(2011) suggest using the highest occurrence of foraminifera (HOF) as the upper datum, as non-linearity between elevation and tidal inundation is most pronounced in the high marsh. Therefore, the following equation was applied:

$$SWLI_n = \frac{100(h_n - h_{MSL})}{h_{HOF} - h_{MSL}} + 100$$

Where $SWLI_n$ is the Standardised Water-Level Index for sample n, h_n is the sample elevation, h_{MSL} is the elevation of mean sea level (MSL), and h_{HOF} is the elevation of the HOF. A SWLI of 100 is MSL and the HOF is 200.

Table 5. Tidal data used to calculate Standardised Water-Level Index (SWLI) values.

Site	Local tide station	Mean sea level (m AHD)	Highest occurrence of foraminifera (HOF) (m AHD)
Lutregala	Hobart	0.05	0.96
Wapengo	Bermagui	-0.03	1.07
Little Swanport (previously published data from Callard et al. (2011)	Spring Bay	0.04	0.76
Tarra	Port Welshpool	-0.02	1.62

4.3 Laboratory methods

4.3.1 Foraminifera samples

Prior to analysis, surface samples and cores were kept refrigerated below 4° C (Edwards and Wright, 2015). A volume of 5 cm^3 of each surface sample was subsampled using a scalpel to remove sediment from the surface sample and a graduated cylinder to measure volume. Samples were shipped to the University of York and stained immediately upon arrival using a buffered solution of rose Bengal and ethanol for 24 hours to distinguish between live and dead specimens (Walton, 1952). Most studies typically stain within 24 hours of collection (*e.g.* Shaw et al. 2016); however, experiments have shown that even after death, foraminiferal protoplasm can stain over a month after collection (Murray and Bowser, 2000). Subsequently, samples were sieved through 500 μm and 63 μm sieves, and the residue from the 63 μm sieve was collected for foraminiferal analyses. Samples were preserved in a solution of deionised water and 30 % ethanol until analysis. Core samples were taken at 1 cm continuous intervals and were prepared in the same manner as surface samples. Samples from top 10 cm of each core were stained with rose Bengal as the majority of infaunal live foraminifera live in the top 10 cm of the sediment (*c.f.* Hayward et al. 2014 and references therein).

As sample counts of ~50 – 200 are sufficient for low diversity assemblages typical of salt-marsh environments (Edwards and Wright, 2015; Fatela and Taborda, 2002; Grenfell et al. 2012; Kemp, Wright and Cahill, 2020), samples were split into eight equal aliquots using a wet splitter (Scott and Hermelin 1993). Samples were counted wet via light microscopy using a Zeiss Stemi DV4 microscope at 80× – 320× magnification and identified with

reference to Hayward, Le Coze and Gross (2019). Taxonomic consistency was retained between this study and the Callard et al. (2011) study, identifying *Trochamminita* as two distinct species: *Trochamminita salsa* and *Trochamminita irregularis*. The dead assemblage was enumerated, as dead foraminifera have been shown to be a better analogue for fossil assemblages compared to living. This is due to the fact that dead assemblages are independent of factors such as seasonality, minimise temporal variability in modern distributions and are less likely to result in taphonomic bias arising from the dissolution of certain, usually calcareous, species (*e.g.* Grenfell et al. 2012; Horton and Edwards, 2006; Horton and Murray, 2006; Wright, Edwards and van de Plassche, 2011; Walker et al. 2020). Where possible, a count of at least 200 individuals per sample was taken (*e.g.* Chen et al. 2020; Figueira and Hayward, 2014); however, where counts were less than 200, the entire sample was counted.

4.3.2 Pollen and macrocharcoal analyses

Pollen and microcharcoal analyses were conducted at the University of Queensland to provide additional chronohorizons by Dr Patrick Moss. Pollen preparation methods followed those outlined in Moss et al. (2013) and macrocharcoal preparation followed guidelines in Stevenson and Haberle (2005). Pollen and charcoal were subsampled at 1 or 2 cm intervals.

4.3.3 Loss on ignition

Samples (2 cm^3 in volume) were taken at 1 cm intervals downcore for loss on ignition (LOI). Crucibles were weighed empty and subsequently the wet weight of the combined sample

and crucible were noted. Samples were dried overnight (~18 hours) at 105 °C to remove moisture. Following that, samples were subject to a 550 °C burn and a 950 °C burn with a burn time of four and two hours respectively, following guidelines in Heiri, Lotter and Lemcke (2001). Between the burns, the 550 °C ignition weight of the samples was noted in order to obtain the organic carbon percentage, and following the 950 °C burn, the crucible was weighed again in order to obtain the inorganic carbon percentage.

4.3.4 Particle size analyses

Samples were taken at 1 cm intervals downcore for particle size analysis (PSA). Samples weighed at least 1 g, however, weight varied by organic content and for samples with higher percentages of organic carbon (calculated from LOI analyses), ~2 – 4 g of sediment was taken, so that sufficient minerogenic particles were present for accurate analysis. Samples were digested in 10 ml 30 % hydrogen peroxide (H_2O_2) overnight and heated on a hotplate at 50 °C. Another 10 ml H_2O_2 added the following day to remove any residual organic material. H_2O_2 was continually added until reactions stopped, and all organic material had been digested. Samples were then heated at 70 °C to reduce down, and 2 ml of 10 % HCL was added to samples to remove any organics. Samples were then centrifuged three times at 3500 rpm for 8 minutes, decanting excess water each time. 2 ml sodium hexmetaphosphate $(NaPO_3)^6$ were added to all samples. After vortexing to ensure an even distribution of all grain sizes, all samples were analysed using a Malvern Mastersizer Hydro 2000 laser granulometer, following the standard operating procedures of the equipment. A test sand with a known uniform grain size was used to calibrate the machine at the start of each day.

4.4 Statistical analyses

4.4.1 Training set screening

Transfer function models using only agglutinated foraminifera were employed following Edwards and Horton (2000). Local training sets from Lutregala and Wapengo were combined with a previously published training set from Little Swanport (Callard et al. 2011). Prior to statistical analyses, calcareous species were removed from the training sets (*Quinqueloculia* sp., *Haynesina germanica*, and *Elphidium* sp.) as these species are susceptible to dissolution and are rarely preserved within the fossil salt-marsh sediments (*e.g.* Milker et al. 2015b). Calcareous species totalled 159 out of 27,390 individuals (~0.6% of the combined training set), 157 of which came from Little Swanport (Callard et al. 2011). Samples with total count sizes less than 50 were also removed as they are deemed statistically unreliable (Kemp, Wright and Cahill, 2020).

4.4.2 Clustering and ordination

Partitioning around medoids (PAM) clustering and silhouette analysis (Rousseeuw, 1987; Kaufman and Rousseeuw, 1990) were employed to determine biozones present within the training sets using the *'cluster'* (Maechler et al. 2013) and *'Factoextra'* (Kassambara and Mundt, 2017) packages in statistical software R (R Core Team, 2020). Only species distributions against elevation was analysed, as this is largely considered to be the environmental variable most responsible for influencing species distributions (*e.g.* Horton et al. 2003; Horton and Murray, 2007; Shaw et al. 2016). PAM was favoured over alternative hierarchical clustering methods, such as k-means, as it is considered more statistically robust (Kemp et al. 2012a). The PAM method minimizes a sum of dissimilarities which

means there is no requirement for clusters to have a certain size and structure (Chen et al. 2020; Kaufman and Rousseeuw, 1990; Kemp et al. 2012a). The optimal number of clusters was determined using the average silhouette method, where a silhouette width (Si) of 1 indicates a sample to be perfectly assigned to the cluster, while -1 indicates incorrect assignment (Kaufman and Rousseeuw, 1990).

Detrended correspondence analysis (DCA; Hill and Gauch, 1980) was also performed on the training sets using R packages '*vegan*' (Oksanen et al. 2007) and *cluster*. Ordination plots provide further information on groupings within a training set and have typically been used to show difference and similarity amongst samples. The plots indicate which samples contain higher or lower abundances of certain species based on their distribution around the species' centroid (ter Braak and Verdonschot, 1995). Samples with similar composition are located close together in ordination space, whereas those with dissimilar compositions will plot further away from each other on the ordination plot (Kemp, Horton and Culver, 2009).

4.4.3 Transfer function development

In previous sea-level reconstruction studies, transfer functions have typically been applied using training sets of data local (*i.e*. within a few kilometres) to the fossil record. However, many studies have advocated for combining training sets from a broad region (*i.e.* from hundreds of kilometres; *e.g.* Barlow et al. 2013; Gehrels, Roe and Charman, 2001; Hocking, Garrett and Cisternas, 2017; Watcham, Shennan and Barlow, 2013; Wilson and Lamb, 2012) to generate regional training sets. Some studies have also sub-divided regional training sets

into sub-regional training sets by grouping training sets from sites located in fairly close spatial proximity (*e.g.* Hocking, Garrett and Cisternas, 2017). These studies highlight that whilst the precision of the resulting models often decreases, accuracy increases by providing more modern analogues for the fossil assemblages in cores. In this study, training sets were created at varying spatial scales from local up to regional in order to assess how both accuracy and precision alter with increased spatial extent.

To investigate whether the relationship between foraminiferal assemblage and elevation is unimodal or linear, a detrended canonical correspondence analysis (DCCA) was performed in CANOCO version 4.5 (ter Braak and Smilauer, 2002). Following Birks (1995), it was assumed that axis one gradients greater than two standard deviations indicate that species respond unimodally to elevation. Based on the DCCA result, either Partial Least Squares (PLS) or Weighted Averaging Partial Least Squares (WAPLS; ter Braak and Juggins, 1993; ter Braak et al. 1993) regression models were employed in R package '*Rioja*' (Juggins, 2020).

Following guidelines from Barlow et al. (2013) and Kemp and Telford (2015) a 'minimum adequate model' approach was employed where no more than three components were used to avoid over-fitting data, and the 5 % improvement in root-mean-squared-error-of-predictions (RMSEP) rule was used as guidelines for the use of additional components. Transfer function performance was assessed via cross-validated model statistics. Bootstrapping was chosen as the cross-validation method because it provides sample-specific errors (ter Braak and Juggins, 1993). In line with the recommendations of Kemp and Telford (2015), outlier removal was limited to a single pass to leave as much natural variability in the models as possible. Only samples with cross-validated residuals

exceeding two standard deviations from the mean were considered for removal from the training set (Juggins and Birks, 2012). Species optima and tolerances were calculated using the R package '*palaeoSig'* (Telford, 2011).

4.4.4 Generating palaeomarsh surface elevation estimates

Palaeomarsh surface elevation (PMSE) estimates were calculated in '*Rioja*' using the chosen sea-level transfer functions (**Chapter 5**) to generate estimates for fossil samples in the master cores. PMSE estimates were only quantified for samples counts >50 individuals as below this, counts were deemed too low and unreliable to calculate an indicative meaning (see Kemp, Wright and Cahill, 2020).

4.4.5 Assessing reconstructive performance

In order to assess the reliability of the PMSE estimates, the fossil assemblages were compared with modern ones by employing the modern analogue (MAT) technique in *'Rioja'*. Whilst numerous dissimilarity methods (*i.e.* chi squared, euclidean, bray) can be utilised, the squared chord distance dissimilarity method was used in this study as it performs well with percentage counts rather than raw counts, and it down-weights rare species (*i.e.* noise) to highlight the principal patterns in the assemblage data (*i.e.* signal). The threshold between good, fair (also known as close), and poor modern analogues was using the dissimilarity between the samples in the modern training set. In line with recommendations from Kemp and Telford (2015), the 20th percentile was chosen as the threshold for analogy as the diversity of the modern training sets is low. Following

Watcham, Shennan and Barlow, (2013), "good" and "fair/close" analogues were defined as the 5th and 20th percentiles respectively. While Watcham, Shennan and Barlow (2013) use the term "close" rather than "fair", this study uses the term "fair" as it is more consistent with the terms "good" and "poor".

4.4.6 Calculating relative sea level

In order to calculate relative sea level, the following equation was used:

$$S = H - I$$

Where S is sea level, H is the sample height (in AHD) and I is the indicative meaning (*i.e.* PMSE estimate). Cores were considered compaction free due to the minimal compaction observed in the thin salt-marsh sediments from the region (Brain et al. 2012; Gehrels et al. 2012).

4.5 Chronological analyses

4.5.1. ^{210}Pb

Preparation and analyses of the ^{210}Pb samples were undertaken at ANSTO by alpha particle spectrometry, with 35 samples analysed in total across the three cores. Samples were processed for the determination of total ^{210}Pb, measured indirectly from its progeny polonium-210 (^{210}Po) and supported ^{210}Pb, measured from its grandparent radioisotope radium-226 (^{226}Ra). Unsupported ^{210}Pb activity was estimated by subtracting supported

^{210}Pb from the total ^{210}Pb activity.

4.5.2. Stable lead isotope (^{206}Pb/^{207}Pb, ^{208}Pb/^{207}Pb, ^{206}Pb/^{204}Pb and ^{208}Pb/^{206}Pb)

Stable Pb isotope analyses were undertaken at the Geochronology and Tracers Facility at the British Geological Survey, using a Nu Instruments, Nu Plasma HR, MC-ICP-MS (multi-collector-inductively coupled plasma-mass spectrometer). Sediment sample were taken at 1 cm contiguous intervals and prepared for isotope analysis. 500 mg of sediment were taken from each sample and the wet weight was noted. Samples were digested in 2 ml 16 M HNO_3 and heated overnight at 105 °C. For the extraction, samples were dissolved in an acid solution comprised of 2 ml 16 M HNO_3, 2 ml $HClO_4$ and 1 ml 29 M HF and heated overnight in an Evapoclean ® at 120 °C, subsequently being heated at 150 °C until all solution had evaporated. Following extraction, 2 ml 9 M HBr acid was added to the samples. Samples were left to dissolve on a hot plate heated to 105 °C overnight.

Samples were centrifuged for 5 minutes at 3500 rpm prior to loading on the columns (5 ml). For the columns, AG1X8 resin was firstly added, followed by a full column of MilliQ water and 6 M HCl × 3. Next, half a column of MilliQ water was added, followed by half a column of 0.5 M HBr, and the samples were added to the columns. Following this, 1 ml 0.5 M HBr was added, then 2 ml of 0.5 M HBr. Subsequently, the sample was collected in 3 ml of 6 M HCl. A few drops of 8 M HNO_3 were added and samples were dried down on a hot plate at 105 °C.

Prior to analysis, each sample was spiked with a thallium (Tl) solution, which is added to allow for the correction of instrument induced mass bias. Samples were then introduced

into the instrument via an ESI 50µl/min PFA micro-concentric nebuliser attached to a de-solvating unit, (Nu Instruments DSN 100). Faraday collectors were configured to allow for the detection of ^{204}Pb, ^{206}Pb, ^{207}Pb, ^{208}Pb and, additionally: ^{203}Tl and ^{205}Tl (for the aforementioned mass bias correction), and ^{202}Hg to allow correction of the ^{204}Hg interference on ^{204}Pb. Each individual acquisition consisted of 75 ratios, collected at 5-second integrations, following a 60 second de-focused baseline. The precision and accuracy of each method was assessed through repeat analysis of NBS 981 Pb reference solution (also spiked with Tl). The average values obtained for each of the mass bias corrected NBS 981 ratios were compared to the known values for this reference, (taken from Thirlwall (2002), Pb double spike: $^{206}Pb/^{204}P$ = 16.9417, $^{207}Pb/^{204}Pb$ = 15.4996, $^{208}Pb/^{204}Pb$ = 36.724, $^{207}Pb/^{206}Pb$ = 0.91488, $^{208}Pb/^{206}Pb$ = 2.1677). All sample data were subsequently normalised, according to the relative deviation of the measured reference values from the true value. Internal uncertainties (the reproducibility of the measured ratio) were propagated relative to the external uncertainty (*i.e.* the excess variance associated with the reproducibility of the NBS 981 reference material analysed during the session).

4.5.3 ^{14}C

Samples for ^{14}C were analysed at the Scottish Universities Environmental Research Centre (SUERC), the University of California, Irvine (UCI) or the Australian Nuclear Science and Technology Organisation (ANSTO). Samples were subsampled at continuous 0.5 cm intervals at the University of York to find dateable material for radiocarbon analyses. Any dateable organic material greater than 1 mg that was lying horizontally (assumed to be deposited on the top of the marsh) and away from the edges of the core (to avoid contamination of modern material) was taken for radiocarbon analyses. Where plant

macrofossils were absent, bulk sediment samples were used, however this was avoided unless necessary. All samples were dried at 40 °C overnight in sterilised aluminium foil boats and their dry weight noted. Samples were then stored in glass vials until analysis. All samples were treated using the standard procedures described in Gehrels et al. (2012).

Bomb-spike AMS ^{14}C was employed for sediments younger than ~60 years old and high-precision (multiple target) AMS ^{14}C (Marshall et al. 2007) or routine bulk was used for sediments for sediments older than ~60 years old. Five routine precision samples were ran on the accelerator mass spectrometer (AMS) at the Scottish Universities Environment Research Centre (SUERC), 15 "small samples" were measured at the University of California, Irvine (UCI). A further 5 bulk sediment samples were ran at the Australian Nuclear Science and Technology Organisation (ANSTO) in Australia. Preparation of additional standards was required to match the sample carbon weights and data were corrected for modern carbon contamination using the data from process background and the standards.

4.5.4 μXRF-ITRAX

μXRF-ITRAX analyses were undertaken at the NERC facility BOSCORF, Southampton, UK. A core from each site was scanned with a Molybdenum X-ray tube with a step size of 1000 microns at 45 kV and 40 mA and an exposure time of 0 ms. Before scanning, cores were subject to decontamination by removing the very surface layers of the core and were subsequently covered with an ultra-thin conductive plastic film.

Raw data were cleaned by removing any samples with a validity of 0 and by removing the data at the bottom of the cores which were deemed to be an artefact of the scanner and not representative of the real data. Elemental data were normalised and expressed as count rates of detected florescence data per unit time ($kcps^{-1}$). The sum of the Mo incoherent (Inc) and Mo coherent (Coh) scattering was used, as it accounts for density and moisture content (Burn and Palmer, 2014; Kylander et al. 2011; Mackenzie et al. 2017). Base metals interrogated for chronostratigraphic markers included Zn, Cu and Pb.

4.6 Age-depth modelling

Bayesian age-depth modelling of dates (^{14}C, ^{210}Pb and calendar) was undertaken in the R package (R Core Team, 2020) '*rplum*' (Blaauw, 2021). For post-bomb ^{14}C dates, the SH Zone 1 – 2 calibration curve was employed (Hua et al. 2013), for pre-bomb ^{14}C dates the SHCal 2020 curve was employed (Hogg et al. 2020). ^{210}Pb ages were calculated in *rplum* using their depth in the core (cm), density (g/cm^3), total ^{210}Pb (Bq/kg), sample thickness (cm) and supported ^{210}Pb(Bq/kg) values. Bulk density was calculated at ANSTO using their standard operating procedure. Like traditional constant rate of supply models (*e.g.* Appleby and Oldfield, 1978), *rplum* assumes a constant rate of supply of ^{210}Pb; however, it separates the age-depth modelling process from the ^{210}Pb decay equation by using a self-adjusting Markov Chain Monte Carlo (MCMC) algorithm (Sim et al. 2021). Calendar dates were identified from chronostratigraphic markers in the stable lead isotope, pollen and charcoal data and assigned a normal distribution, with a mean and uncertainty based upon dates in the literature. Details on the individual priors used in each age-depth model are given in **Chapter 6**.

4.7 Reconstructing sea level

A Gaussian process regression, accounting for both temporal and vertical uncertainties was used to model sea level at Lutregala, Wapengo, and Tarra. These were ran by Soenke Dangendorf. Covariance was represented by a Matérn function, and all parameters were estimated using an automatic hyperparameter optimisation algorithm which was implemented in MATLAB's '*fitrgp*' function. Both chronological and vertical uncertainties were assumed to be normally distributed, whereby temporal correlations were considered for vertical uncertainties. A Monte Carlo approach using 5000 iterations was used to estimate sea-level change at each site over time. Reconstructions were GIA-corrected using estimates from the Caron et al. (2018) model. This model considers uncertainties by varying the rheology and ice history in each realisation. A representative set of 5000 GIA model iterations were used to obtain RSL estimates at each site. From the ensemble, median values and 95 % confidence limits (2.5 and 97.5th percentiles) were extracted.

The selection of tide-gauge stations to compare to the proxy records was based both on the geographical distance to the proxy sites and the temporal availability (only stations with more than 20 years of data were used). Stations in close proximity to the marshes are limited to the last ~30 years, but long-term tide gauge stations are located 100s of kilometres from the sites (**Figure 32**).

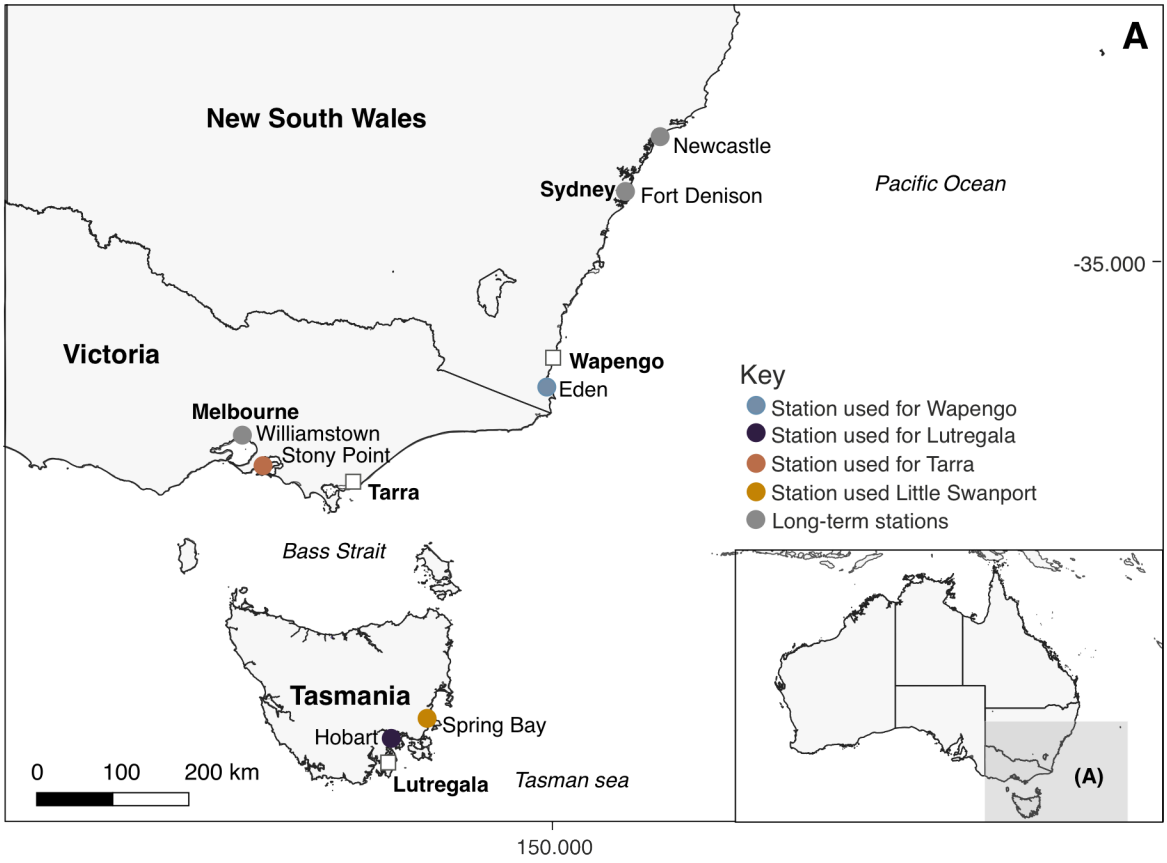

Figure 32. Locations of the tide gauges closest to each site (coloured dots) and locations of long-term tide gauges (grey dots).

As there are no long-term tide gauges in the close vicinity of the marshes, additional data in the form of sea-level budgets (*i.e.* modelled estimates of the contributing components to sea-level rise) for each site were calculated using GRD estimates from Frederikse et al. (2020) and sterodynamic components from the SODAsi.3 ocean reanalysis model (Giese et al. 2016). The inverse barometer effect was also added using sea-level pressure from the 20th century reanalysis project (Slivinski et al. 2019). Sea-level budgets were computed by Soenke Dangendorf.

Change points in the reconstructions were detected using the change-point model from Caesar et al. (2021) which takes into account both vertical and chronological uncertainties.

This model has been used in other sea-level studies (*e.g.* Gerlach et al. 2017) to quantitatively identify accelerations and decelerations of relative sea-level change. Following Kemp et al. (2013a), the number of change points was chosen based upon the deviance information criterion (DIC; Spiegelhalter et al. 2002) where the lower the DIC, the better the model.

4.8 Sea-level fingerprinting

In order to investigate the Arctic ice melt hypothesis, the new reconstructions need to be considered together with other 19th and 20th century sea-level records in order to determine spatial patterns of sea-level change that can be compared with the barystatic GRD fingerprints (*i.e.* sea-level fingerprints; Gregory et al. (2019)) of melting ice masses. Both proxy-based reconstructions and tide-gauge observations were used (**Table 6; Figure 33**). Site selection for the analysis was based upon both geographic variability (aiming for sites that cover a wide spatial extent), as well as temporal resolution of proxy records over the last 200 years. Proxy records with good coverage of the 19th century were selected from the dataset of Walker et al. (2021). The new reconstruction for the Falkland Islands (Rush, 2021) was added. Whilst the reconstruction from Lutregala would have been valuable to the study, it could not be included due to the limited data in the 19th century (for further details see **Chapter 6**).

Table 6. Sites chosen for comparison to the new Australian records. All proxy records have been updated to IntCal20 or SHCal20 to enable direct comparison between records.

Site	Location	Co-ordinates (Latitude; Longitude)	Reconstruction method	References
Swan Inlet	Falkland Islands	-51.8243; 58.6124	Proxy	Newton (2017); Frederikse et al. (2021); Newton et al. (2021); Rush (2021)
Pounawea	New Zealand	-46.470; 169.700	Proxy	Gehrels et al. (2008) chronology updated by Garrett et al. (2022)
Little Swanport	Tasmania, Australia	-42.344; 147.930	Proxy	Gehrels et al. (2012)
Barn Island	Connecticut, North America	41.338; -71.866	Proxy	Gehrels et al. (2020)
Sand Point	North Carolina, North America	35.885; -75.681	Proxy	Kemp et al. (2011)
Chezzetcook	Nova Scotia, Canada	44.739; -63.260	Proxy	Gehrels et al. (2020)
Brest	France	48.383; -4.495	Instrumental	PSMSL (2021)
Swinoujscie	Poland	53.917; 14.233	Instrumental	PSMSL (2021)

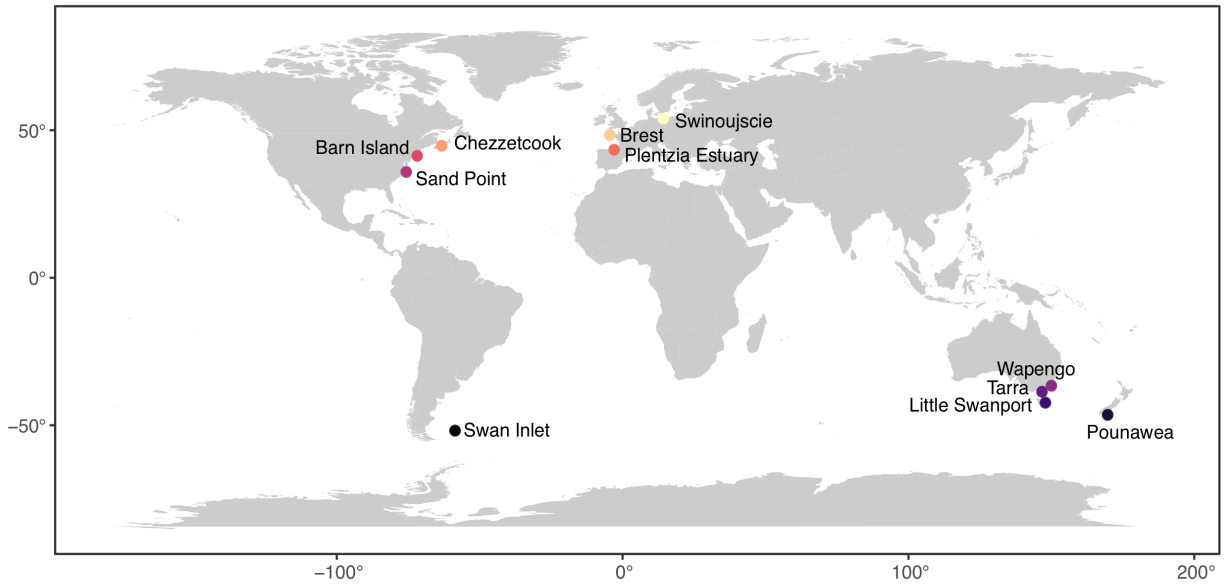

Figure 33. Spatial distribution of the sites used for the fingerprinting investigation.

To compare rates of historical sea-level rise with the new Australian records, all chronologies but Plentzia Estuary (which is based solely on radionuclide data), were updated to IntCal20 or SHCal20 in either *rplum* or *rbacon* (depending on whether the sites had ^{210}Pb data or not; Blaauw, 2021; Blaauw et al. 2021). SLIPs for Swan Inlet were taken from Rush (2021) who updated estimates from Newton (2017) using the transfer function from Newton et al. (2021). The 20th century SLIPs for Swan Inlet were published by Frederikse et al. (2021).

The barystatic component (including GRD and GIA) was isolated from the records by removing the sterodynamic signal that, in turn, was derived from the SODAsi.3 ocean reanalysis model (Giese et al. 2016). A subset of sterodynamic time series corresponding to each SLIP was identified using the mean ± 5 sigma age range of each SLIP. For each of these subsets, a weighted mean (weighted assuming a Gaussian distribution specified by the SLIP mean age and 1 sigma uncertainty) of the sterodynamic contribution was then subtracted

from the mean RSL of the corresponding SLIP. To correct the tide-gauge records, the sterodynamic value was removed from the RSL value for each year. Code for this was written by Fiona Hibbert and analysis undertaken by myself.

For the proxy data, rates of sea-level rise were calculated using error-in-variables regression (EIV; Cahill, 2021). This method of regression accounts for errors in both the vertical and age uncertainties. For the instrumental data, ordinary least squares regression was employed. Data were split into two periods – a ~19th century period 1815 – 1899 (Period 1) and a ~20th century period 1900 – 2013 (Period 2). Separate regressions were run on each period. Period 1 rates were then subtracted from Period 2 rates to obtain the magnitude of the rate of change at each site (see **Chapter 6**) and to remove the influence of GIA which can be discounted due to the linearity of the GIA rate.

The spatial pattern of sea-level change at each site resulting from the mass loss of ice – *i.e.* the barystatic GRD component was computed in order to produce the "sea-level fingerprints". The fingerprints were generated by Soenke Dangendorf using the methods of Dangendorf et al. (2017) whereby ice melt contributions were calculated by solving the sea-level equation (Mitrovica et al. 2005) and the rotational feedback was included following Tamisiea et al. (2010). Fingerprints were based on the sea-level equivalents of 18 major glacier regions (RGI Consortium, 2017) and ice sheet mass balance discharge estimates of the Greenland and Antarctic Ice Sheets. Static fingerprints of 1 mm were generated (equivalent to -362 Gt ice mass change).

The following methodology was written by Fiona Hibbert to describe the optimisation model:

Fingerprint optimisation (to find the combination of fingerprint predictions which most closely matched the sea-level observations) was coded and conducted by Fiona Hibbert using a differential evolution optimisation algorithm (Storn and Price, 1997) to iteratively minimise the distance between the observed rates and predicted relative sea-level rise at each site. The predicted sea-level rise is the sum of different weightings of the individual (n=18) mass loss sea-level fingerprints (f_n) (equation 1).

$$\Delta Rate(\phi, t) = \Sigma(x_0 * f_{GrIS}) + (x_1 * f_{WAIS}) +, \dots (x_n * f_n) \quad (equation\ 1)$$

where,

$\Delta Rate(\phi, t)$ is the difference between the 20th and 19th century rate of sea-level rise,

x_n is the weighting of each fingerprint (f_n)

The upper and lower bounds of contributions from each of the 18 fingerprints were constrained by empirical estimates of 20th century ice mass loss from Malles and Marzeion (2021), except for mass loss from the Greenland and Antarctic Ice Sheets which were taken from Kjeldsen et al. (2015) Adhikari et al. (2018) respectively, **Table 7**). There are no mass balance estimates beyond 1900, therefore it is assumed that the 19th century ice mass loss is zero. Glacier length records from Leclercq et al. (2014) suggest that most glaciers only significantly began losing mass towards the latter decade of the 19th century, therefore the global average will have been close to zero for most of the century. As the West Antarctic

and East Antarctic Ice Sheets have different fingerprints, the Antarctic Ice Sheet total contribution was split into East and West using proportions estimated from the contribution of each to sea level from Rignot et al. (2019).

Table 7. Empirical constraints for the ice mass contribution to sea level over the 20th century from Malles and Marzeion (2021), Kjeldsen et al. (2015) and Adhikari et al. (2018). All units given in mm yr^{-1}.

Ice mass	Mean	Lower (100 % CI)	Upper (100 % CI)
Alaska	0.060	-0.018	0.138
Western Canada & US	0.040	-0.016	0.096
Arctic Canada North	0.080	0.024	0.136
Arctic Canada South	0.060	0.016	0.104
Iceland	0.010	0.001	0.019
Svalbard	0.040	0.029	0.051
Scandinavia	0.003	0.002	0.004
Russian Arctic	0.050	-0.006	0.106
North Asia	0.002	0.001	0.003
Central Europe	0.002	0.001	0.003
Caucasus and Middle East	0.001	0.000	0.002
Central Asia	0.050	0.028	0.072
South Asia	0.060	0.038	0.082
Low Latitudes	0.007	-0.002	0.016
Southern Andes	-0.010	-0.099	0.079
New Zealand	0.003	0.000	0.006
Greenland	0.210	0.166	0.269
West Antarctic	0.050	0.000	0.075
East Antarctic	0.000	0.000	0.034

To find the optimised weighting parameters (*i.e.* x_0, x_1, ..., x_i), the function was evaluated using weighted least squares (*i.e.* to evaluate the goodness of the fit of the predicted sea-level rise at each site compared to the observations).

$$f(x)^2 = \frac{1}{N}\sum_{n=1}^{N}\left(\frac{obs-pred}{\sigma_{obs}}\right)^2 \qquad (equation\ 2)$$

where,

obs is difference between the 19th and 20th century sea-level rates observed at each of the 11 sites,

σ_{obs} is the 1 sigma observation error at each site,

$pred$ is the predicted relative sea level at each of the sites derived from the sum of the weighted GIA fingerprints,

and N is the number of sites.

The global minimum was found using a differential evolution algorithm (Storn and Price, 1997) to search the parameter space. A population of individual candidate solutions was maintained for each iteration, and new potential solutions were generated by combining existing ones according to the "best1bin" scheme (equation 1). The initial population was generated by randomly generating values of each parameter (fingerprint weighting) within the given bounds (**Table 7**), and then evaluating the sum against the observations (*i.e.* $f(x)$, equation 2). From this initial population, each individual was mutated in turn by randomly choosing two of the population members and using their difference to mutate the best population member (equation 3) to create a trial solution. The trial solution was populated by sequentially filling using either the original candidate or the new mutated vector from a binomial distribution (*i.e.* a random number between 0 and 1 was generated for each parameter, and if this was less than the cross-over probability, CR ∈ [0,1], the parameter was loaded from the mutated vector, otherwise it was loaded from the original)

$$v_i = x_{best} + F(x_{r^1} - x_{r^2}) \quad \textit{(equation 3)}$$

where,

v_i is the mutated vector,

x_{best} is the best individual vector (i.e., the individual with the lowest $f(x)$ in the iteration population)

r^i are random integers which are mutually exclusive within the range [1,NP] where NP is the population size, and also different from index *i*,

F is the differential weight (mutation factor, $F \in [0, 2]$)

This trial vector was then evaluated; if the trial was better than the original candidate, then it took its place within the population. Additionally, if the trial was better than the overall solution, it also replaced it. To improve the chances of finding the global solution, a number of factors were implemented into the model including: (i) a large population size (NP=200), as population size has a significant influence on the ability of the algorithm to explore and there is a relative large number of dimensions; (ii) a high mutation factor (F =[0.5, 1.5]) to widen the search radius, as F controls the amplification of the difference vector (equation 3). This included dithering to randomly change the differential weight (mutation factor, F) between 0.5 and 1.5 *(i.e*. how far the model can search within the parameter space) between iterations to help speed convergence and prevent the algorithm overshooting good optima; and (iii) a relatively low crossover probability (recombination, CR = 0.5; *i.e.* how many get carried forward).

The influence of values of these controlling parameters (NP, F, CR), as well as initialisation (*i.e.* vector x_0) was explored, and values chosen to ensure both local and global search capabilities, and that the entirety of the parameter space was explored.

Jackknifing ("leave one site out") was used to evaluate the dependency of the result (*i.e.* fingerprint weighting) on site location. The optimisation algorithm was run 10 times, each time sequentially removing one site from the observations. The bias was calculated as the difference between the mean jackknife result and the original, therefore subtracting this difference from the original result yields a geographic bias-corrected estimate of the contributions of the different ice masses.

4.9 Summary

This chapter has described the methods used to achieve the aims outlined in **Chapter 1**. Sampling of modern and fossil foraminifera was undertaken at three sites in southeastern Australia. Clustering and ordination analyses were used to assess the distribution of modern foraminifera and transfer functions analyses using either PLS or WAPLS (depending on DCCA results) were employed to reconstruct to generate palaeo sea-level estimates. The reconstructive performance of the transfer functions was assessed using the MAT. Site lithology was logged, and representative master cores were taken at each site for further sedimentological and chronological analyses at the University of York and the University of Queensland. Sedimentological analyses included loss on ignition and particle size and chronological analyses included ^{14}C, radiogenic lead, stable lead isotopes, pollen and ITRAX-μXRF analyses.

Bayesian age-depth models were run in *rplum* in order to obtain high-resolution chronologies for each core. Gaussian process regressions were run on the palaeo sea-level estimates in MATLAB. Reconstructions were GIA corrected using the model from Caron et al. (2018). Sea-level fingerprinting analyses were conducted on chosen high-resolution RSL reconstructions and two long-term tide gauge records. The barystatic GRD component was isolated by removing the sterodynamic signal using estimates from Giese et al. (2016). Rates of sea-level rise were calculated using either EIV or simple linear regression. Sea-level fingerprints were generated for sites of interest using the methodology outlined in Dangendorf et al. (2017). A fingerprint optimisation model was employed to assess the contributions of each ice mass to sea level by minimising the difference between observations of sea-level rise from the proxy and tide-gauge records and the predicted fingerprints. Jackknifing was used to assess the dependency of the result on site location.

Chapter 5 of 8

Modern foraminifera and transfer function development

Statement from the author

For the most part, this chapter has been published in Open Quaternary under the citation:

Williams, S., Garrett, E., Moss, P., Bartlett, R. and Gehrels, R., 2021. Development of a Training Set of Contemporary Salt-Marsh Foraminifera for Late Holocene Sea-Level Reconstructions in southeastern Australia. ***Open Quaternary*****, 7(1). doi:10.5334/oq.93**

The majority of the data acquisition, analysis, interpretation and the writing was conducted by S.W with input from E.G, P.M, R.B and R.G. E.G. undertook modelling of tides using the TPXO8-Atlas global tidal model and S.W completed all other analyses. S.W generated all figures for the paper. Further helpful comments were provided by Jason Kirby and two other anonymous reviewers. The majority of this chapter remains unchanged from the published article; however the study sites and methods sections have been removed from this chapter as they are described in **Chapter 3** and **Chapter 4**. Section, figure and table numbers and references have also been changed for consistency with the rest of the thesis.

Some further points: The Tarra local transfer function performance was poor; therefore the decision was made to not include the model in the paper (please see **Appendix I** for further information on the derivation of the transfer function and reasons for not including it in the paper). Furthermore, since the publication of this research article, code to generate Bayesian transfer functions has been made freely available online, therefore **Appendix II** also compares performance statistics between Bayesian transfer functions and the classical models described in this paper. The Bayesian transfer function method is an alternative

way to derive palaeomarsh surface elevation estimates which does not need to assume either a linear or unimodal species response like the classical models do and can incorporate 'prior' information to further constrain elevation.

Abstract

We collected contemporary foraminiferal training sets from two salt marshes to enable more precise and accurate proxy historical sea-level reconstructions from southeastern Australia. Combined with an existing training set from Tasmania, this new regional set consists of 112 samples and 16 species of foraminifera, of which 13 are agglutinated. Cluster analyses group the regional training set into a high–elevation cluster, dominated by *Trochamminita salsa*, a mid–elevation cluster, dominated by *Entzia macrescens* and *Trochammina inflata*, and a mid–low elevation cluster dominated by *Miliammina fusca* and tidal-flat species. We develop transfer functions using local and regional training sets and assess their performance. Our resulting site-specific and chosen regional models are capable of predicting sea level with decimetre-scale precision (95 % confidence intervals of 0.12 – 0.22 m). These results are comparable to other examples from around the world. When developing regional training sets, we advocate that the similarity in the environmental settings (particularly salinity) should be assessed as an alternative way of grouping sites, rather than simply using spatial proximity. We compare our findings with global results and conclude that salt marshes along microtidal coasts yield models with the lowest vertical uncertainties. Studies with the lowest uncertainties are located in the western Pacific and the western Atlantic, whereas those from the eastern Atlantic generally have larger tidal ranges and carry larger vertical uncertainties. Our models expand the

existing region available for sea-level reconstruction and can be used to generate new late Holocene sea-level reconstructions across southeastern Australia.

5.0 Introduction

Proxy-based palaeo sea-level reconstructions usefully complement historical tide-gauge data (Kopp et al. 2016) as they expand our knowledge of sea-level change beyond instrumental records and can be used to validate instrumental records where both overlap. Proxy data are particularly important in the Southern Hemisphere as tide-gauge records are sparse and often short compared to those in the Northern Hemisphere (Holgate et al. 2013). Both proxy and tide-gauge sea-level data have shown that, globally, the 19th to 20th century sea-level acceleration is larger than any acceleration over the preceding 3000 years (Kopp et al. 2016). Proxy records derived from salt-marsh foraminifera in New Zealand and Tasmania have shown that the rise in regional mean sea level in the earlier half of the 20th century may have been anomalously fast in comparison to the global mean (Gehrels et al. 2008; Gehrels et al. 2012). However, the few long tide-gauge records from the region do not show the same early 20th century trends as the proxy records (*e.g.* Gehrels et al. 2012). Compaction has been suggested as a possibility for the discrepancy between the proxy and instrumental data (*e.g.* Grenfell et al. 2012); however, these Southern Hemisphere salt marshes are shallow and are composed of a stratigraphy not very susceptible to compression (Brain et al. 2012). Therefore, this possible discrepancy is still unexplained.

An important first step towards increasing our understanding of long-term sea-level fluctuations is to develop salt marsh sea-level transfer function models from training sets of contemporary salt-marsh micro-organisms (*e.g.* foraminifera and diatoms; Barlow et al.

2013; Kemp and Telford, 2015). This involves quantifying the relationship between elevation and contemporary foraminifera in order to generate palaeomarsh surface elevations. While there are numerous Northern Hemisphere high-resolution salt marsh sea-level reconstructions based on such microfossil proxies, especially from the North Atlantic region (*e.g.* Barlow et al. 2013; Barnett et al. 2019; Gehrels et al. 2020; Kemp et al. 2017a; 2018; Kopp et al. 2015; 2016; Saher et al. 2015), there are very few from the Southern Hemisphere. High-resolution reconstructions are available for Tasmania, (Gehrels et al. 2012), New Zealand (Gehrels et al. 2008; Grenfell et al. 2012), South America (Frederikse et al. 2021) and South Africa (Strachan et al. 2014). However, the potential for salt-marsh based sea-level reconstructions from South Africa, Asia and South America are spatially constrained by the small availability of marsh in these parts of the world, with much greater availability in the Northern Hemisphere (FitzGerald and Hughes, 2019).

Nonetheless, these Southern Hemisphere records are crucial for answering questions about the apparent early 20th century discrepancy in rates of sea-level rise observed between proxy and tide-gauge records (Gehrels et al. 2012; Grenfell et al. 2012), as well as helping to determine the cause of the rapid rise in sea level observed in these records. Gehrels et al. (2012) suggest that the sea-level acceleration observed in the Tasmanian proxy record may be due to the melting of Arctic and Greenland land-based ice, which, as sea-level fingerprinting demonstrates, would result in sea-level rises around Australia (Fleming et al. 2012). Whilst mass loss from the West Antarctic Ice Sheet could also result in sea-level rises along the southeast coast of Australia (Fleming et al. 2012; Gomez et al. 2010), the timing of the apparent sea-level acceleration in the Australian and New Zealand records

appears to correspond with a period of anomalous warming in the Arctic (Hegerl et al. 2018) and subsequent enhanced melt of Arctic glaciers and the Greenland Ice Sheet (*e.g.* Bjørk et al. 2012; Kjeldsen et al. 2015; Parkes and Marzeion, 2018; Vermassen et al. 2020).

It is well established globally that foraminifera occupy specific niches within the tidal frame which reflect both frequency and duration of tidal inundation (*e.g.* Birks, 1995; Gehrels et al. 2012; Kemp et al. 2012a; Scott and Medioli, 1978). As such, modern training sets linking salt-marsh elevation with species assemblages can be used to generate transfer functions for empirically-based numerical estimates of past sea-level change when applied to fossil counterparts in cores (Kemp and Telford, 2015; Sachs, Webb and Clark, 1977). In Australia and New Zealand, studies using transfer functions originating from salt-marsh foraminifera have demonstrated their use as a successful proxy, able to predict sea level with sub-decimetre vertical uncertainties (*e.g.* Callard et al. 2011; Grenfell et al. 2012; Southall, Gehrels and Hayward, 2006). In this paper we develop new local and regional training sets of contemporary salt-marsh foraminifera for southeastern Australia by collecting new samples from Tasmania and New South Wales and combining these with published training sets from Tasmania (Callard et al. 2011). We compare our findings with other microfossil training sets from around the world and assess how transfer function performance is affected by mean tidal range. The training sets presented in this study can be used to establish more salt-marsh based sea-level reconstructions across a wider region in southeastern Australia.

5.1 Results

5.1.1 Modern foraminiferal distributions

5.1.1.1 Lutregala

At Lutregala, transect 1 spanned a distance of 315 m and transect 2 spanned 260 m. Combined, they covered a vertical range of 0.77 m. A total of 51 surface samples were taken. Within the Lutregala training set, we identified 10 agglutinated species and 1 calcareous species (*Ammonia beccarii* - 1 single individual encountered in the training set). Eleven surface samples had total counts lower than 50 individuals (**Figure 34**); therefore, we removed these samples from the training set. In the resulting training set, the total individual count ranged from 56 – 814, with an average total count of 232 individuals per sample.

Along transect 1, the HOF was observed at 0.96 m AHD (0.91 m above MSL). Immediately below HOF, the higher elevation samples were dominated by *T. salsa* and *Haplophragmoides wilberti* (0 – 75 % and 0 – 43 % respectively). Mid-low elevations were dominated by *Trochammina inflata* (1 – 84 %), *Entzia macrescens* (0 – 71 %) and *T. irregularis* (0 – 38 %). Low elevation samples were dominated by *Miliammina fusca* (0 – 97 %), with the largest abundance found in the lowest elevation sample. Along transect 2, *E. macrescens* and *T. inflata* dominated the high-mid elevation samples (0 – 66 % and 12 – 69 % respectively). *Trochamminitia irregularis and H. wilberti* were also found in these samples at lower abundance (0 – 13 % and 0 – 16 % respectively). Low elevation samples were again dominated by *M. fusca* (0 – 75 %) and similarly, to transect 1, the largest abundance was found in the lowest elevation sample. Minor species included *Siphotrochammina lobata*, *Polysaccammina ipohalina*, *Ammobaculites agglutinans* and *Textularia* sp., which each contribute less than 10 % to a sample when present.

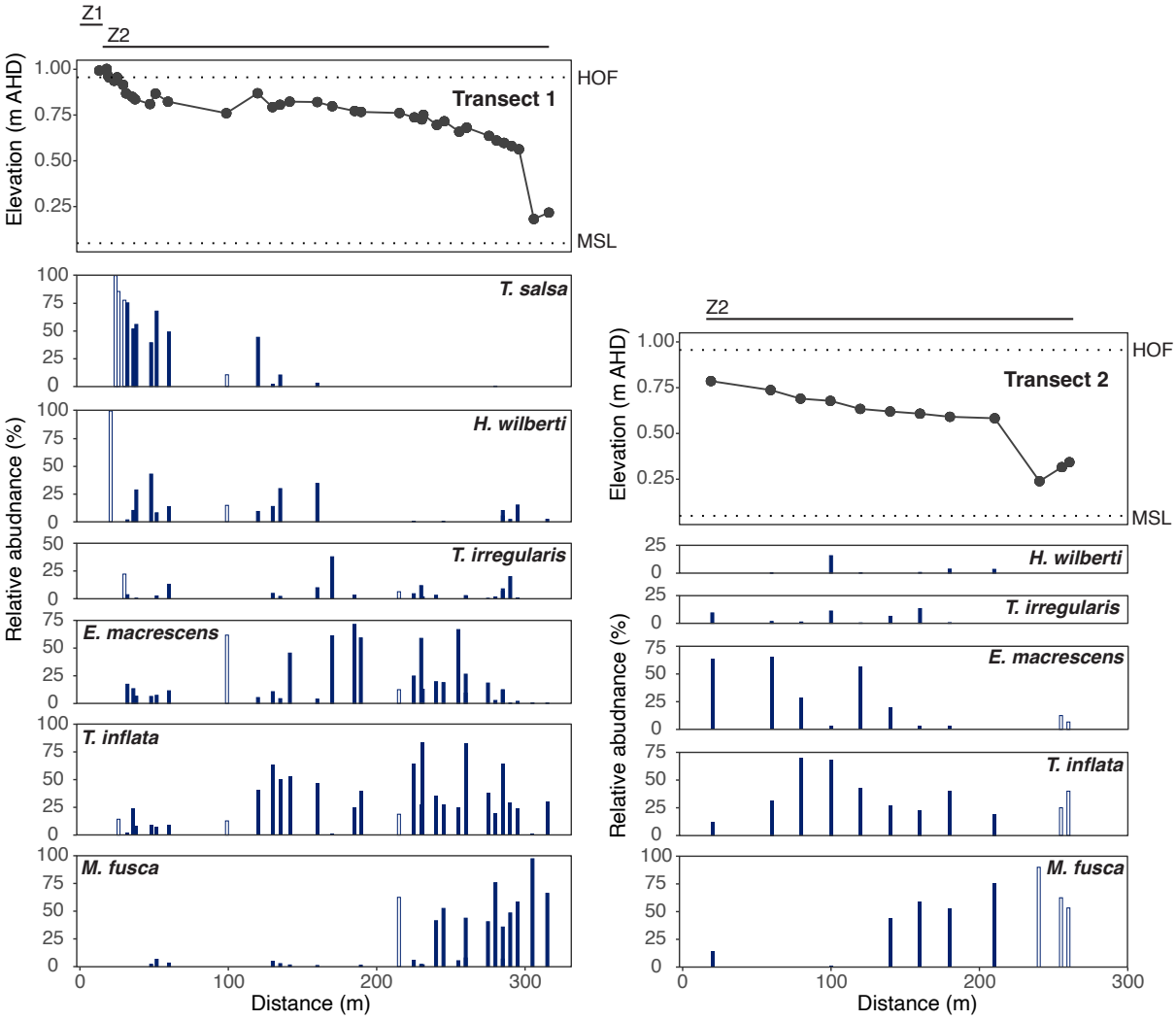

Figure 34. Lateral distribution of surface foraminifera (dead assemblage) along transects 1 and 2 at Lutregala salt marsh. Foraminifera presented represent at least 10 % of the total count in at least one sample. Unfilled bars represent total counts lower than 50. The highest occurrence of foraminifera (HOF) was found at 0.96 m AHD (0.91 m above MSL). Vegetation zones are also shown.

5.1.1.2 Wapengo

At Wapengo, a total of 45 samples were taken. Transect 3 spanned 250 m and transect 4 spanned 60 m. The two surface transects had a total vertical range of 0.71 m. Thirty samples contained total counts greater than 50 (**Figure 35**). Within the resulting training set, we identified 13 agglutinated and 1 calcareous species (*Haynesina germanica* – 1 individual noted within the training set). In the training set, the total count ranged from 55 – 453 and averages 159 individuals per sample.

The HOF was observed at 1.07 m AHD (1.10 m above MSL). Along transect 3, the high-mid elevation samples were dominated by *T. inflata* and *E. macrescens* (0 – 92 % and 0 – 55 % respectively) with low relative abundances of *T. salsa* (0 – 2 %), *H. wilberti* (0 – 9 %) and *T. irregularis* (0 – 5 %). These samples generally had the lowest total counts (<100 individuals). Mid-elevation samples were dominated by *P. ipohalina* (0 – 71 %) and low elevation samples were dominated by *M. fusca* and *Ammobaculites exiguus* (0 – 90 % and 0 – 49 %) with *A. agglutinans* and *Polysaccammina hyperhalina* in low abundance (0 – 7 % and 0 – 9 % respectively). Along transect 4, the high-mid elevation samples were largely dominated by *T. inflata* (0 – 89 %), with a low abundance of *T. salsa* (0 – 5 %) and *Miliammina fusca* (0 – 72 %). *Entzia macrescens* was dominant in the lowest elevation samples (6 – 85 %), with a low abundance of *P. ipohalina* (0 – 17 %). *Siphotrochammina lobata* was also observed in the training set but contributes less than 10 % to a sample when present.

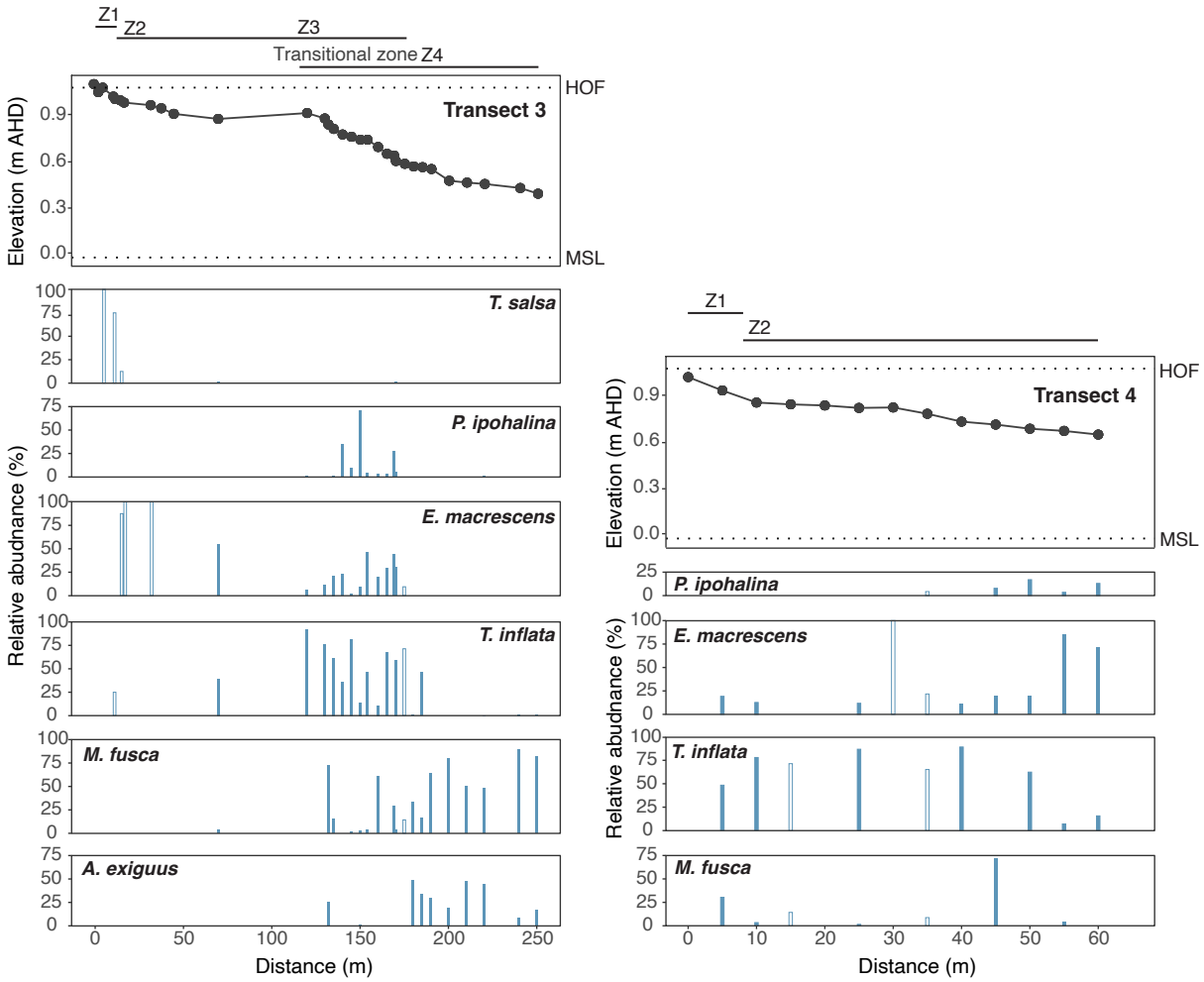

Figure 35. Lateral distribution of surface foraminifera (dead assemblage) along transects 3 and 4 at Wapengo salt marsh. Foraminifera presented represent at least 10 % of the total count in at least two samples and filled bars represent counts greater than 50. The highest occurrence of foraminifera (HOF) was found at 1.07 m AHD (1.10 m above MSL). Vegetation zones are also shown.

5.1.2 Multivariate analyses

5.1.2.1 Partitioning Around Medoids Analysis

Combining samples from Lutregala, Wapengo, and the previously published site at Little Swanport (Callard et al. 2011) into a regional training set, we find that PAM analysis groups samples into three clusters (**Figure 36**). PAM identifies a high-elevation cluster (cluster one), a mid-elevation cluster (cluster two) and a mid-low elevation cluster (cluster three). Cluster one (191 SWLI average) contains large relative abundances of *T. salsa* (average relative

abundance 63 %); the species is principally dominant at the uppermost elevations, but is present from ~200 – 155 SWLI. Cluster one also contains the largest relative abundance of *H. wilberti* (~188 – 156 SWLI; 11 % average). Cluster two (163 SWLI average) comprises the majority of samples and is largely composed of *T. inflata* (~200 – 118 SWLI; 55 % average relative abundance) and *E. macrescens* (~190 – 118 SWLI; 30 % average relative abundance). Both species have wide elevational ranges. Cluster three (155 SWLI average) comprises the majority of low elevation samples and has the largest relative abundance of *M. fusca* (average 59 %). We find that *M. fusca* is generally sparse at high elevations and increases at lower elevations, with a maximum abundance at 114 SWLI. The cluster also contains typical low-marsh species including *A. exiguus*, *A. agglutinans*, *P. hyperhalina* and *Ammobaculites subcatenulatus*. No samples from Little Swanport were classified into cluster three. This is likely due to the near-absence of *M. fusca* at the site.

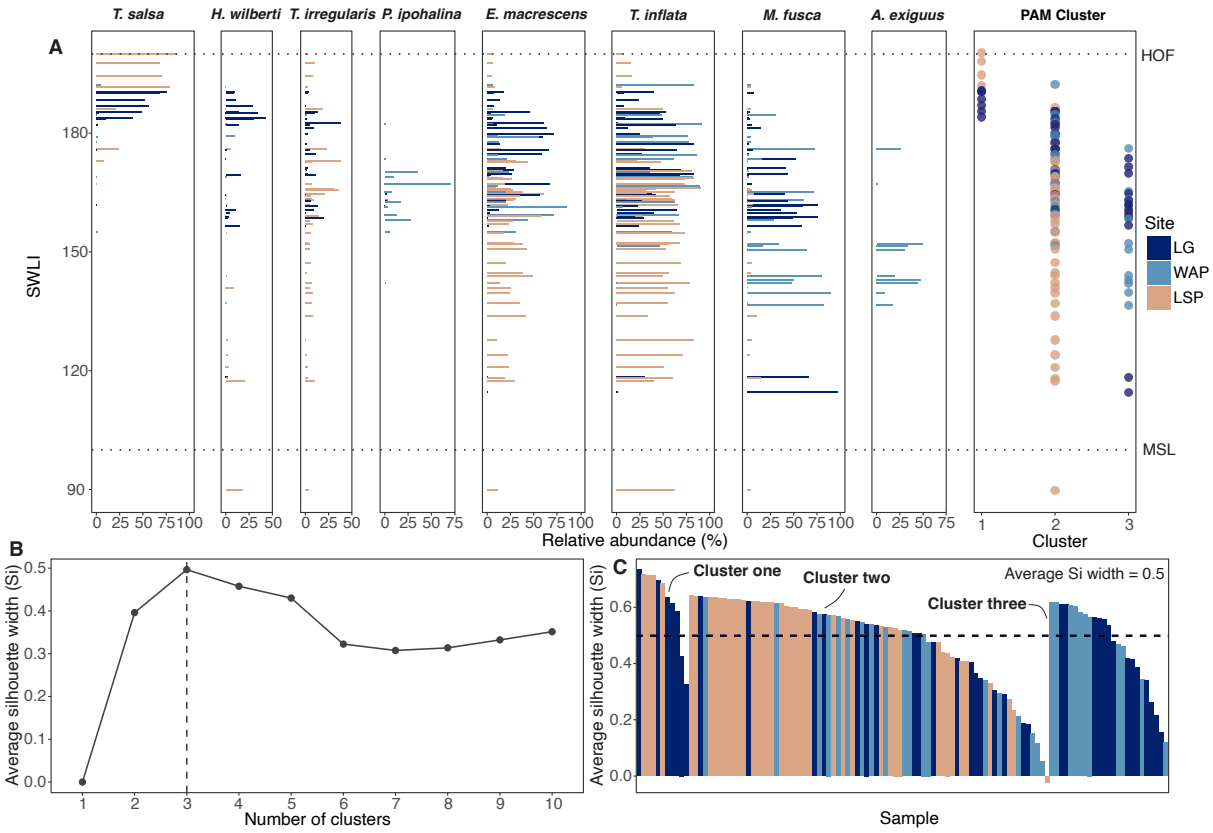

Figure 36. A. Relative abundance of modern foraminifera across the regional training set, showing species exceeding 10 % abundance in at least one sample with total counts greater than 50 individuals. Samples are ordered by Standardised Water-Level Index (SWLI); the highest occurrence of foraminifera (HOF) and mean sea level (MSL) are displayed. Partitioning around medoids (PAM) cluster for each sample is shown. B. Average silhouette method to determine optimal number of clusters across the regional training set. The peak and the dashed line denote that samples are best clustered into three groups. C. Silhouette width of individual samples within the regional training set. The dashed horizontal line indicates the average silhouette width across the entire regional training set. Site key: LG = Lutregala, WAP = Wapengo, LSP = Little Swanport.

5.2.2.2 Detrended Correspondence Analysis

DCA analyses (**Table A2**) indicate that, across all training sets, SWLI is closely aligned with axis 1, although r^2 decreases when samples are combined together with Little Swanport in the regional training set (Lutregala r^2 = 0.60, p= <0.01; Wapengo r^2= 0.52, p= <0.01; Regional r^2 =

0.22, p= <0.01; **Figure 37**). In each ordination plot, high-elevation samples plot furthest away in ordination space from low-elevation samples, suggesting these samples have the most disparate assemblages.

In the Lutregala training set, four clusters are identified - a high-elevation cluster is dominated by *T. salsa*, a mid-elevation cluster is dominated by *E. macrescens* and *T. irregularis* and another mid-elevation cluster is dominated by *T. inflata* (**Figure 37a**). A low-elevation cluster is dominated by *M. fusca*, with influences from *A. exiguus* and *P. ipohalina*. Conversely, in the Wapengo training set, there is no defined high-elevation cluster; high-mid elevation samples form one cluster largely dominated by *T. inflata* and *E. macrescens* and low-elevation samples are dominated by *M. fusca* and *Ammobaculites* spp. (**Figure 37b)**. This may be due to the low abundance of *T. salsa* at the site (~0 – 5 %), compared with ~50 – 85 % in samples near HOF at Lutregala and Little Swanport.

In the regional training set, cluster one is dominated by *T. salsa* and samples with the highest SWLI values and cluster two is dominated by *T. inflata* and *E. macrescens*, with some influence from *T. irregularis* and *S. lobata* (**Figure 37c**). In cluster three, the mid-low elevation samples towards the centre of the plot are also dominated by *T. inflata* and low-elevation samples are dominated by *M. fusca* and *Ammobaculites* spp. Whilst Little Swanport has low-elevation samples, these samples are grouped into the mid-elevation cluster, again, likely due to the absence of low-marsh and tidal-flat species within the training set. Samples from Lutregala generally plot towards the negative side of the DCA triplot, whereas samples from Wapengo plot to the positive side of the DCA triplot, likely reflecting the differences in species assemblages between the sites, with *T. salsa* near absent from Wapengo but prevalent at

Lutregala and *Ammobaculites* spp. and *Polysaccammina* spp. more prevalent at Wapengo but near absent at Lutregala.

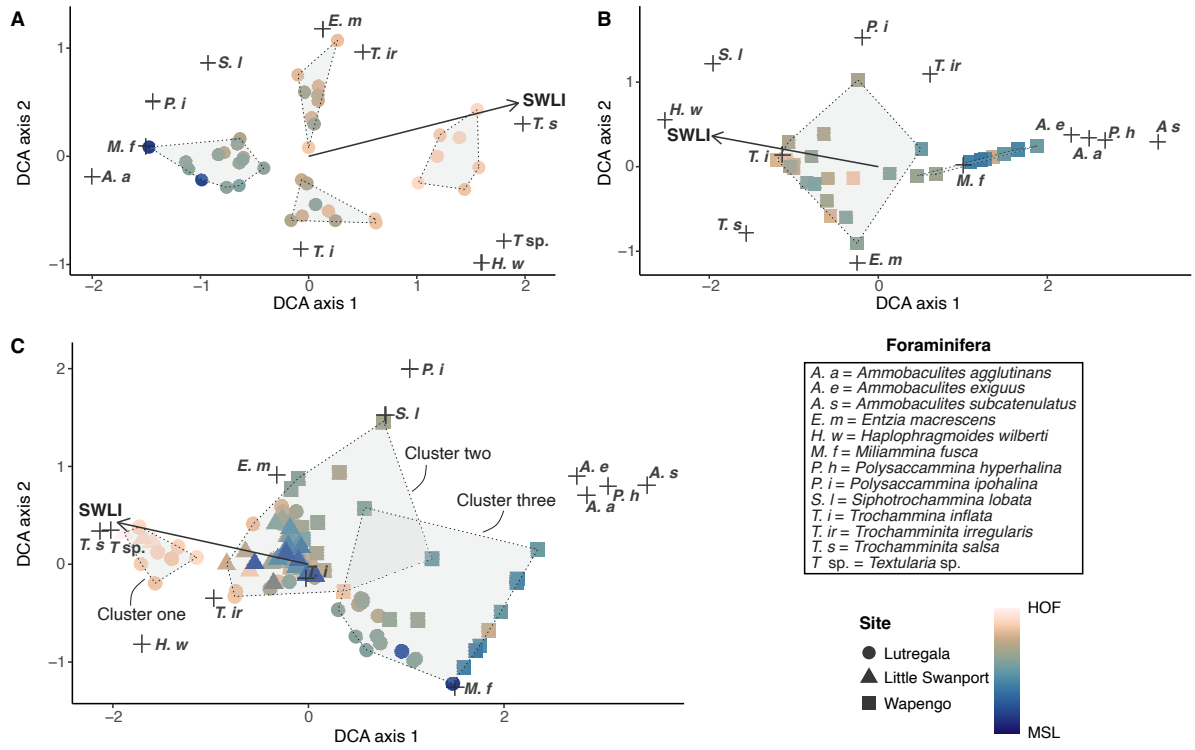

Figure 37. Detrended correspondence analyses of samples from A. the Lutregala training set, B. the Wapengo training set and C. the regional training set (Lutregala, Wapengo and Little Swanport). Cluster number for each detrended correspondence analysis (DCA) plot has been defined by the partitioning around medoids (PAM) algorithm. Samples from varying sites are noted by different symbols. Foraminifera species are denoted by crosses and an associated code. Samples are coloured by Standardised Water-Level Index (SWLI) with samples near mean sea level (MSL; 100 SWLI) in dark blue and samples near highest occurrence of foraminifera (HOF; 200 SWLI) in pink.

5.1.3 Development of a transfer function for southeastern Australia

We develop transfer functions for three local training sets (Lutregala, Wapengo and Little Swanport), a sub-regional training set that comprises the two Tasmanian sites (Lutregala and Little Swanport), a regional training set (I) that includes all samples (Lutregala, Wapengo and Little Swanport), and a regional training set (II) comprising only our new samples (Lutregala and Wapengo). Data are expressed as percentage abundance (**Figure 38**).

Both the Lutregala and Wapengo local training sets, as well as the regional II training set, have axis one lengths greater than two standard deviations (2.05, 2.06 and 2.34 respectively; **Table 8**) therefore, we apply WAPLS models in these sites. The sub-regional and regional I training sets have axis one lengths less than two standard deviations (1.48 and 1.52 respectively; **Table 8**); therefore, we apply PLS models. Callard et al. (2011) had previously used a WAPLS and a PLS model on the Little Swanport training set as the axis one gradient length was close to two standard deviations (1.68; **Table 8**); however, we employ a PLS model (Birks, 1995).

Table 8. Detrended canonical correspondence analysis results for the local, sub-regional and regional training sets.

Training set	Axis 1 Length	Axis 1 Eigenvalue	Axis 2 Eigenvalue	Axis 3 Eigenvalue	Axis 4 Eigenvalue	Cumulative % variance of species data	Eigenvalue (λ1/λ2) ratio
Lutregala	2.05	0.36	0.27	0.15	0.07	24.0	1.33
Wapengo	2.06	0.39	0.30	0.11	0.07	21.7	1.29
Little Swanport	1.68	0.29	0.12	0.05	0.02	28.9	2.51

Sub-regional	1.48	0.19	0.37	0.13	0.09	12.7	0.53
Regional I	1.52	0.19	0.56	0.33	0.16	7.7	0.33
Regional II	2.34	0.39	0.34	0.22	0.13	16.0	1.16

The local training sets from Lutregala and Wapengo perform well, with model performance comparable to, or better than, that of the final Little Swanport model reported by Callard et al. (2011) (**Table 9**). The Lutregala model has the lowest RMSEP, demonstrating an ability to predict sea level within ± 6.4 SWLI units (equivalent to ± 0.06 m at Lutregala at 68 % confidence or ± 0.12 m at 95 % confidence). The Wapengo model prediction error is larger at ± 9.7 SWLI units (equivalent to ± 0.11 m at Wapengo at 68 % confidence or ± 0.22 m at 95 % confidence). No models exhibit a 5 % improvement from component one, therefore we cannot justify the addition of a second component.

Table 9. Summary statistics for cleaned model data across local, sub-regional and regional training sets. Rows highlighted in bold indicate the chosen model for each training set.

Training set	Scale	Sites included in the model	Number of samples	Number of species	Model type and component number	RMSEP (SWLI)	RMSEP (m AHD)	r^2_{boot}	Average bias (SWLI)	Maximum bias (SWLI)
Lutregala	**Local**	**Lutregala**	**37**	**9**	**WAPLS C1**	**6.42**	**0.06**	**0.65**	**-0.01**	**7.86**
					WAPLS C2	6.57	0.06	0.65	0.13	7.42
					WAPLS C3	7.40	0.07	0.60	0.14	8.62
Wapengo	**Local**	**Wapengo**	**29**	**12**	**WAPLS C1**	**9.73**	**0.11**	**0.56**	**0.12**	**20.32**
					WAPLS C2	10.80	0.12	0.53	0.50	18.14
					WAPLS C3	12.49	0.14	0.50	1.02	18.77
Little Swanport	**Local**	**Little Swanport**	**41**	**6**	**PLS C1**	**15.23**	**0.11**	**0.42**	**0.11**	**32.74**
					PLS C2	15.55	0.11	0.44	-0.03	32.95
					PLS C3	14.88	0.11	0.53	-0.38	28.23

Sub-regional	Sub-regional	Lutregala and Little Swanport	76	9	PLS C1	12.64	–	0.41	0.00	32.83
					PLS C2	12.71	–	0.41	0.11	33.86
					PLS C3	12.91	–	0.40	0.21	33.67
Regional I	Regional	Lutregala, Wapengo and Little Swanport	105	13	PLS C1	12.91	–	0.34	0.06	35.12
					PLS C2	12.40	–	0.36	0.06	34.34
					PLS C3	12.39	–	0.37	0.06	34.68
Regional II	Regional	Lutregala and Wapengo	65	13	WAPLS C1	7.66	–	0.69	0.07	9.15
					WAPLS C2	8.49	–	0.65	0.29	8.54
					WAPLS C3	9.68	–	0.63	0.50	8.18

Comparison of the sub-regional and regional model I performance with those of the local models highlights that the inclusion of Little Swanport into the models results in a decrease in performance, measured by an increase in RMSEP and a decrease in r^2_{boot} (Sub-regional RMSEP SWLI units = 12.64, r^2_{boot} = 0.41; Regional I RMSEP SWLI units = 12.91, r^2_{boot} = 0.34; **Table 9**). The residuals are much larger for the sub-regional and regional I model than for the local models, suggesting a poor fit to the observed elevations. Removing Little Swanport from the regional training set (regional II model) results in a ~40 % improvement in RMSEP over regional I. Regional II exhibits the best performance of the multi-site models (RMSEP = 7.66 SWLI units, r^2_{boot}=0.69) and has the second lowest vertical uncertainty after the Lutregala local model (**Table 9**).

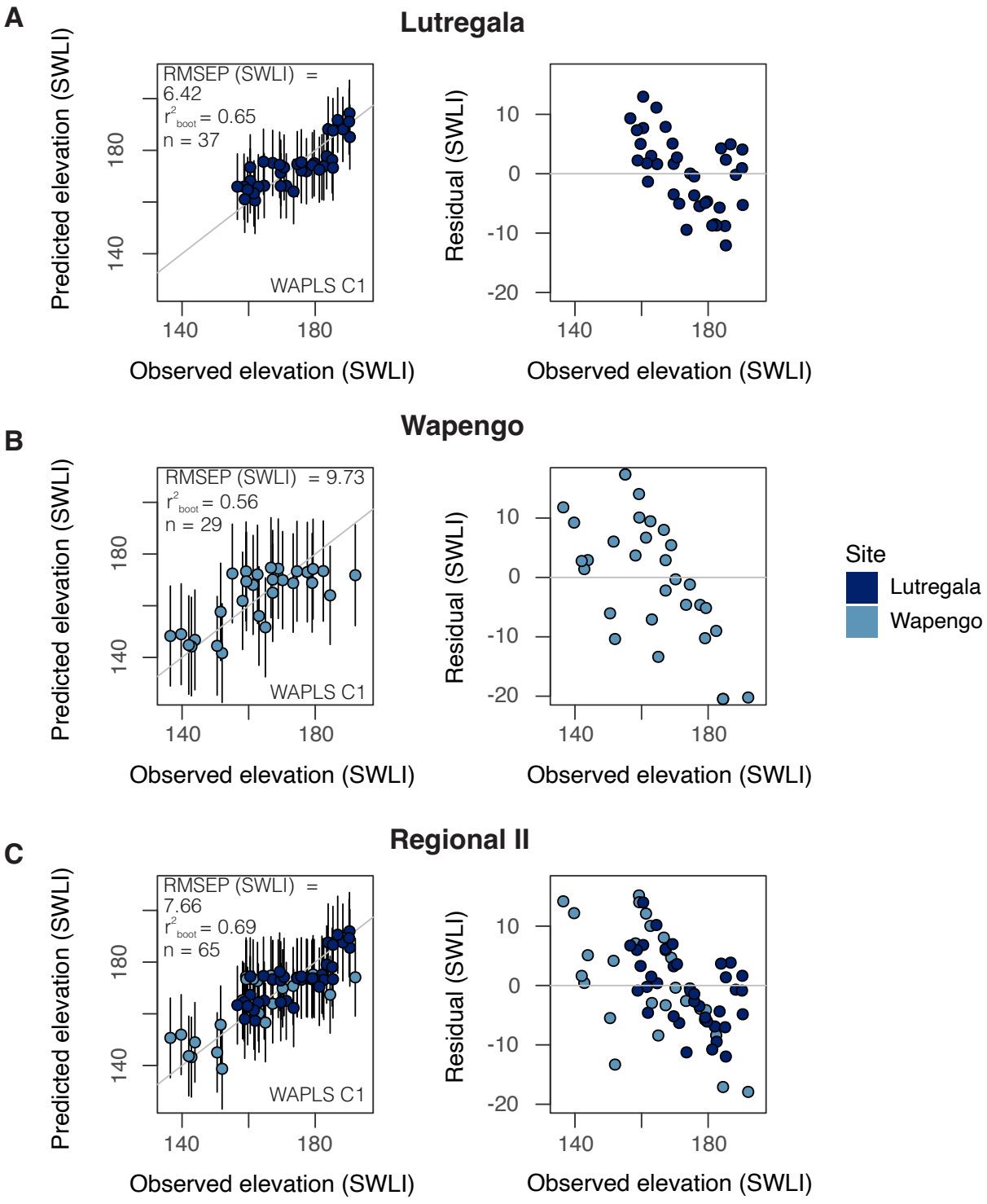

Figure 38. Transfer function performance for local training set models Lutregala (**A**) and Wapengo (**B**), as well as our chosen regional model (**C**; Lutregala and Wapengo combined). Data are presented with elevation converted to Standardised Water-Level Index (SWLI). 95 % prediction uncertainties are given for each sample.

We analyse species optima and tolerance across the Lutregala and Wapengo local transfer functions and the regional II transfer function. We find that species optima and tolerances are largely similar between the models (**Figure 39**). The largest discrepancy is in the predicted optima of *M. fusca*; Lutregala and regional II predict the species optima 13 and 6 SWLI units higher respectively than the Wapengo model. We note this pattern is also replicated with *T. salsa*, *T. irregularis* and *E. macrescens*, with higher predicted species optima in the Lutregala and regional II model in comparison to Wapengo. The tolerance of *T. salsa* is also larger in the Wapengo model than in the Lutregala or regional II model. The species with the closest optima between all models is *T. inflata*, with a difference of only 0.95 SWLI units. *Haplophragmoides wilberti* and *P. ipohalina* optima are also predicted at very similar SWLI values across all models (within 1.7 SWLI units or less). The tight vertical optima and tolerance of *P. ipohalina* across all three models highlights the usefulness of this rare species in sea-level reconstruction.

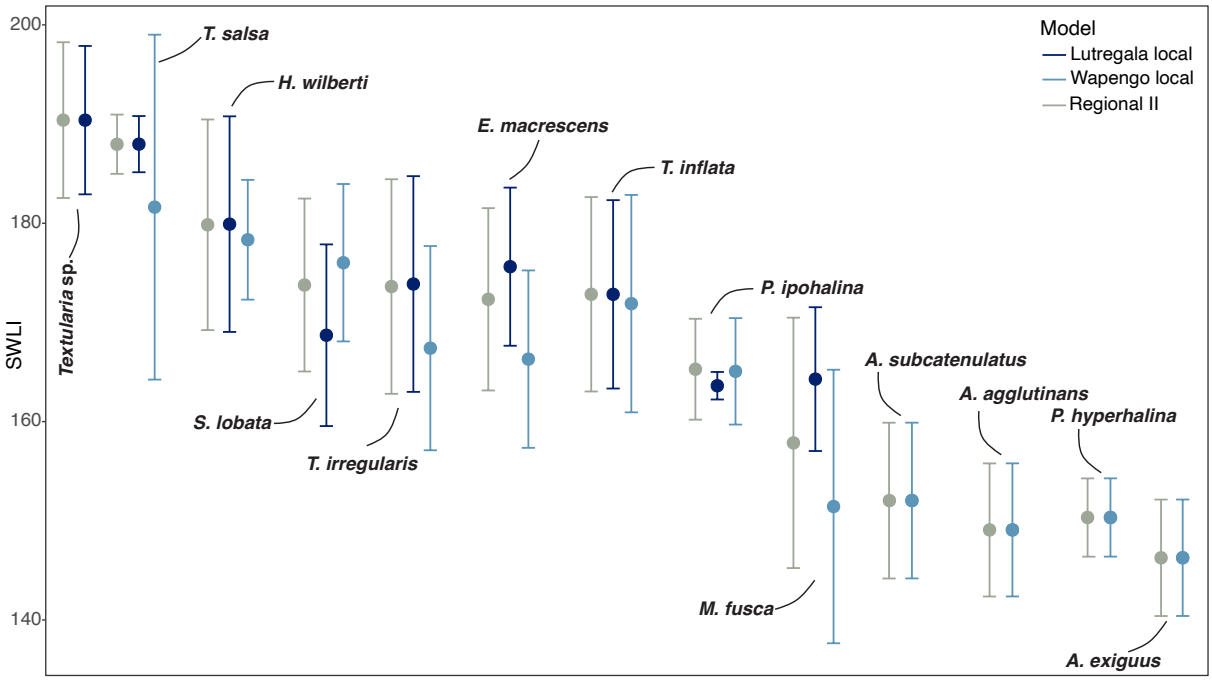

Figure 39. Species optima and tolerances from the local Lutregala and Wapengo models and the regional II model.

5.2 Discussion

5.2.1 Controls on foraminiferal distribution and diversity

Multivariate analyses demonstrate that elevation (as a proxy for duration and frequency of tidal inundation, or hydroperiod) has an influence on foraminiferal distribution, and supports findings reported across the literature (*e.g.* Avnaim-Katav et al. 2017; Barnett, Garneau and Bernatchez, 2016; Edwards, Wright and van de Plassche, 2004; Gehrels, 2000; Horton and Edwards, 2006; Kemp, Horton and Culver, 2009, Milker et al. 2015a). The ratio of the first constrained DCCA eigenvalue ($\lambda 1$) to the second unconstrained eigenvalue ($\lambda 2$) indicates the importance of an environmental variable as a determinant of species distribution (*e.g.* Juggins, 2013). Across all three sites, we find that the ratio exceeds 1 ($\lambda 1/\lambda 2$ = 1.33, 1.29 and 2.51 at Lutregala, Wapengo and Little Swanport respectively; **Table 8**), further suggesting that elevation is an important environmental variable in explaining species distribution at all sites. DCCA axis 1 values suggest elevation is responsible for 24 %, 22 % and 29 % of the cumulative variance of species data at Lutregala, Wapengo and Little Swanport respectively (**Table 8**); however, these values are generally lower than those typically reported in other foraminiferal studies (*e.g.* Hawkes et al. 2010; Horton and Edwards, 2006). Barnett, Garneau and Bernatchez (2016) show that for *M. fusca* and *T. inflata*, some of the most dominant species in our training set, the amount of taxa variation accounted for by axis 1 is low. Furthermore, the values are not out of ranges reported elsewhere in the literature - Avnaim-Katav et al. (2017) report elevation influences 17.1 % of species distribution in their training set. Our values may therefore suggest other environmental variables also influence species distribution at the sites.

We find that the vertical distribution of species varies spatially, with foraminifera at Little Swanport having the widest vertical distributions (**Figure 36a**). For example, *H. wilberti*, *T. irregularis* and *E. macrescens* are generally observed at SWLI values above 150 at Lutregala and Wapengo, but are present at 89 SWLI at Little Swanport, a difference of ~61 SWLI units. Freshwater flooding events (Pearce et al. 2005) and variable rainfall (Hedge and Kriwoken, 2000) in the Little Swanport estuary have periodically lowered the salinity in the estuary to values lower than 10 ppt (Crawford and Mitchell, 1999). We suggest this may cause a non-uniform salinity gradient across the salt marsh, which can cause poorly defined vertical distributions (de Rijk and Troelstra, 1997). Low and variable salinity at the site may also explain the low abundance of *M. fusca* site in comparison to Lutregala and Wapengo.

Salinity may also influence species diversity; Wapengo has the highest species diversity, followed by Lutregala. Foraminifera have higher species diversities at salinities of 32 – 27 ppt (Murray, 2006), and both the Lutregala and Wapengo estuaries have salinity values in this range (Crawford and Mitchell, 1999; Garside et al. 2014; Parsons, 2012). The average salinity in the Little Swanport estuary is ~27 ppt and decreases to ~20 ppt in the salt marsh and mudflat (Sakabe and Lyle, 2010); therefore, the weaker and variable salinity in the Little Swanport estuary may also explain the lower species diversity of this site. The higher species diversity at Wapengo is a result of the presence of a greater number of *Ammobaculites* species. Lal et al. (2020) suggest that high abundances of *Ammobaculites* spp. are correlated with a transition from mangrove to mixed mangrove and salt-marsh vegetation at the mid-elevations of the upper intertidal zone. *Ammobaculites exiguus* has been noted to often reside within mangroves and in unvegetated muddy tidal and sand flats, which we find at Wapengo (Hayward and Hollis, 1994; Schröder-Adams,Boyd and Tran, 2014). Vegetation is influenced

by elevation and salinity (Lal et al. 2020); therefore we suggest that a combination of tidal frequency and duration as well as salinity and vegetation type exert influence on species distribution and diversity at our sites.

5.2.2 Foraminiferal distributions and diversity in southeastern Australia and New Zealand

Modern foraminiferal distributions at Lutregala and Wapengo are broadly similar to those observed in other studies from southeastern Australia and New Zealand. At four sites located near Wollongong, New South Wales, *M. fusca*, *E. macrescens* and *T. inflata* also dominate surface sample assemblages (Lal et al. 2020). *Trochammina inflata* is especially dominant, which is also a common occurrence in New Zealand salt marshes (Hayward, 2014), with the species noted to often be found from pasture and salt meadow to mangroves (Hayward, Grenfell and Scott, 1999).

We find *T. salsa* present from ~155 – 200 SWLI (the upper half of the range between MSL and HOF), which is broadly similar to previous work conducted in New Zealand, where *T. salsa* is largely found in the upper third of the intertidal zone (Hayward and Hollis, 1994). The species can often extend into the upper reaches of estuaries, and is common in brackish settings with significant freshwater input (Hayward, 2014; Hayward, Grenfell and Scott, 1999; Hayward and Hollis, 1994). The species has previously been noted both in Tasmania (Callard et al. 2011) and Victoria (Apthorpe, 1980), and, in agreement with our findings, often occurs as a near-monospecific fauna (Hayward, 2014). However, the species is not documented in lower latitude Australian sites (Berkeley et al. 2008, 2009; Cann et al. 1993; Haslett, 2001; Haslett et al. 2010; Horton et al. 2003; Lal et al. 2020; Strotz, 2015; Wang and Chappell, 2001;

Woodroffe, 2005), which may suggest that the species has a preference for temperate salt marshes in Australia.

Of the dominant agglutinated taxa noted in Lal et al. (2020) (*i.e.* those found at all of their Northern NSW sites), which includes *Ammobaculites* spp., *Ammotium directum*, *E. macrescens*, *M. fusca*, *S. lobata* and *T. inflata*, we note the presence of all but *A. directum* in our regional training set. Furthermore, Lal et al. (2020) encounter *H. wilberti,* but do not find it at every site. Previous literature shows *A. exiguus* can tolerate a wider range of salinities, usually around 20 – 32 ppt (Ostrognay and Haig, 2012; Schröder-Adams, Boyd and Tran, 2014), with preferences for mangrove and tidal flat environments (Hayward and Hollis, 1994; Schröder-Adams, Boyd and Tran, 2014). We find *A. exiguus* in one creek sample at Lutregala, and the species is absent from Little Swanport, supporting evidence of the species' preference for mangrove and muddy substrate.

Rarer species encountered by both Lal et al. (2020) and this study include *Textularia* sp., and *P. ipohalina*. *Polysaccammina ipohalina* is noted to be rare in temperate salt marshes, but has also been documented in New Zealand (Hayward, Grenfell and Scott, 1999). Whilst the species is found both at Lutregala and Wapengo, it is more prevalent at the latter site. *Polysaccammina ipohalina* has been associated as often subdominant to *E. macrescens* and *T. inflata* environments (Camacho et al. 2015), which is replicated also at our sites.

Haslett et al. (2010) observed modern distributions at Minnamurra Inlet, one of the four sites studied by Lal et al. (2020) and note the presence of *T. inflata, Ammobaculites* spp., and *Haplophragmoides* spp., but also encountered species not found at our sites, with the site

reflecting a higher species diversity. However, they find only very low total counts in all surface samples (mean 3.27 specimens/g sediment), with single occurrences common. Furthermore, at Smiths Lake located north of Sydney (Strotz, 2015), species diversity of benthic foraminifera is also markedly higher than at our sites. Species common to our sites include *M. fusca, T. inflata, Textularia* sp., and *A. agglutinans.* We find species diversity tends to be higher at these lower latitude sites as calcareous foraminifera are far more prevalent.

We do not include the samples from Haslett et al. (2010), Lal et al. (2020), and Strotz (2015) in our regional training set due to the site and sample selection criteria outlined in this paper. Lal et al. (2020) employ both living and dead foraminifera in their relative abundance counts, whereas our training set uses only dead assemblages. The Haslett et al. (2010) training set has insufficient total counts (<50 individuals) and the Strotz (2015) training set does not comply with our site selection guidelines, as the training set is derived from an artificially managed system. Other benthic foraminiferal studies from Australia (*i.e.* Berkeley et al. 2008; Cann et al. 1993; Dean and De Deckker, 2013; Haslett, 2001; Horton et al. 2003; Wang and Chappell, 2001; Woodroffe, 2005) are either located outside of the region of interest, lack elevation data, or use grab samples that are not representative of the surface assemblages.

5.2.3 Implications of environmental variability on regional transfer function performance

Whilst the role of frequency of tidal inundation as a primary driver of the vertical distribution of foraminifera has long been established (*e.g.* Scott and Medioli, 1978), other abiotic and biotic factors such as food availability, oxygen, organic matter, grain size, salinity, vegetation and temperature can also influence species distributions (*e.g.* Murray, 2006). Multivariate analyses

of contemporary salt-marsh foraminifera from salt marshes on the Atlantic coast of North America have directly indicated that elevation does not exclusively control foraminiferal distribution (Edwards, Wright and van de Plassche, 2004; Wright, Edwards and van de Plassche, 2011). Whilst regional models can be advantageous due to the fact that they combine sites with differing physiographical and environmental parameters, making them applicable to a larger range of palaeoenvironments (Kemp and Telford, 2015), we find that the differing vertical foraminiferal distribution between species at Little Swanport and the two new sites greatly affects model performance. In both the sub-regional and regional I transfer functions, nearly all Little Swanport samples have predicted elevations ~158 SWLI (see **Figure A6**). This is likely due to the near absence of *M. fusca* and dominance of *T. inflata* at the site. As such, while the regional II transfer function is appropriate for reconstructing sea level from fossil assemblages at both Lutregala and Wapengo, this model is likely not suitable for reconstructions at sites with low (*i.e.* less than ~30 ppt) or variable salinity. We suggest that in such cases, a local model is currently more suitable and further modern samples should be collected to extend the training set. In line with other studies (*e.g.* Watcham et al. 2013; Hocking, Garrett and Cisternas, 2017), we suggest that when employing regional models, a wide spatial extent beyond a sub-region may be needed for good model performance.

5.2.4 The use of transfer-function models in relative sea-level reconstruction

5.2.4.1 Comparison with other local and regional sea-level transfer-function models

Transfer function approaches are now widely employed in palaeoenvironmental research as they provide a quantitative and largely objective method by which reconstructions of palaeoenvironmental conditions can be directly compared and replicated by other studies

(Kemp and Telford, 2015). We compare our transfer-function model performance with other proxy-based transfer functions from the literature, updating a global database of transfer function performance versus mean tidal range (MTR; Barlow et al. 2013; Barnett et al. 2017; Callard et al. 2011; Mills et al. 2013). The updated database integrates data from multiple proxies used in sea-level reconstruction: diatoms, benthic foraminifera, testate amoebae and pollen (**Table 10**).

Table 10. Comparisons of model performance and mean tidal range from multiple regions across the globe. Good model performance is recognised by a lower root mean squared error of performance (RMSEP). N – number of samples within training set. WA - Weighted Averaging regression, WA-Tol — Tolerance Down-Weighted Weighted Averaging regression, WAPLS — Weighted-Average Partial-Least-Squares regression, PLS — Partial-Least-Squares regression, ML – Maximum Likelihood. Table updated from those published by Barlow et al. (2013), Barnett et al. (2017), Callard et al. (2011) and Mills et al. (2013) combining and adding studies that utilise either diatoms, benthic foraminifera, testate amoebae, pollen or multiproxy (diatoms, foraminifera and testates combined) for sea-level reconstruction. We omit the Horton et al. (2007) subtidal transfer function from the analysis as this represents a large outlier in the dataset.

Region	Site	Ref	Model	Microfossil	N	RMSEP	MTR	RMSEP/MTR
Adriatic	Croatia - Values given relative to Split tide gauge	Shaw et al. (2016)	WA-PLS	Foraminifera	60	0.08	0.19	42.1
Eastern Atlantic	Brancaster Marsh, UK	Gehrels, Roe and Charman (2001)	WA-Tol	Diatoms	88	0.21	3.81	1.4
Eastern Atlantic	Brancaster Marsh, UK	Gehrels, Roe and Charman (2001)	PLS	Foraminifera	90	0.08	3.81	2.2
Eastern Atlantic	Brancaster Marsh, UK	Gehrels, Roe and Charman (2001)	PLS	Testate	52	0.08	3.81	2.2
Eastern Atlantic	UK – Values given relative to Cowpen Marsh	Horton, Edwards and Lloyd (1999)	WA-Tol	Foraminifera	131	0.12	3.37	3.4
Eastern Atlantic	Mersey River UK	Mills et al. (2013)	WA-PLS	Foraminifera	56	0.13	5.93	2.2

Eastern Atlantic	Ho Bugt Denmark	Szkornik, Gehrels and Kirby (2006)	WA-PLS	Diatoms	40	0.14	1.5	9.3
Eastern Atlantic	UK- Values given relative to Cowpen Marsh	Zong and Horton (1999)	WA-Tol	Diatoms	88	0.21	3.37	6.3
Eastern Atlantic	Scotland (average of 9 locations)	Barlow et al. (2013)	WA-PLS	Diatoms	215	0.4	4.3	9.3
Eastern Atlantic	Scotland (average of 9 locations)	Barlow et al. (2013)	WA-PLS	Diatoms	121	0.21	4.3	4.9
Eastern Atlantic	Scotland	Barlow et al. (2013)	WA-PLS	Diatoms	73	0.16	4.3	3.7
Eastern Atlantic	Scotland	Barlow et al. (2013)	WA-PLS	Diatoms	53	0.1	4.3	2.3
Eastern Atlantic	Norway - Values given relative to Lødingen	Barnett (2013)	WA-PLS	Testate	29	0.09	1.92	4.7
Eastern Atlantic	Western Denmark	Gehrels and Newman (2004)	WA-Tol	Foraminifera	16	0.16	1.5	10.7
Eastern Atlantic	Florida, USA - Values given relative to Little Manatee River	Gerlach et al. (2017)	WA-PLS	Foraminifera	66	0.07	0.47	14.9
Eastern Atlantic	Bristol Channel, England	Hill et al. (2007)	WA-Tol	Diatoms	61	0.88	11.66	7.5
Eastern Atlantic	Norfolk, England (average of 2 locations)	Horton and Edwards (2005)	WA-PLS	Foraminifera	47	0.25	4.8	5.2

Eastern Atlantic	Southern Portugal	Leorri et al. (2010)	PLS	Foraminifera	22	0.14	2	7
Eastern Atlantic	Northern Portugal	Leorri et al. (2011)	WA-PLS	Foraminifera	30	0.1	1.95	5.1
Eastern Atlantic	Brittany, France	Leorri et al. (2010)	PLS	Foraminifera	43	0.22	2.59	8.5
Eastern Atlantic	Northern Spain (average of 4 sites)	Leorri, Horton and Cearreta (2008)	WA-PLS	Foraminifera	30	0.19	2.5	7.6
Eastern Atlantic	South Devon	Massey et al. (2006)	WA-PLS	Foraminifera	85	0.29	4.65	6.2
Eastern Atlantic	Schedlt estuary, Belgium	Ooms, Beyens and Temmerman (2012)	WA-PLS	Testate	37	0.24	4.98	4.8
Eastern Atlantic	Brittany, France (average of 2 sites)	Rossi et al. (2011)	PLS	Foraminifera	36	0.07	3	2.3
Eastern Atlantic	Brittany, France - Values given relative to Bay of Brest	Stéphan et al. (2014)	WA-PLS	Foraminifera	29	0.2	3.89	5.1
Eastern Pacific	Upper Cook Inlet, Alaska USA (average of 4 locations)	Barlow, Shennan and Long (2012)	WA-PLS	Diatoms	149	0.3	7.98	3.8
Eastern Pacific	California, USA - Values given relative to Tijuana River Estuary	Avnaim-Katav et al. (2017)	WA-PLS	Foraminifera	55	0.09	1.13	8.4

Eastern Pacific	Alaska, USA	Hamilton and Shennan (2005)	WA-PLS	Diatoms	154	0.11	7.98	1.4
Eastern Pacific	Oregon (average of 5 sites)	Hawkes et al. (2010)	WA-PLS	Foraminifera	91	0.2	1.81	11
Eastern Pacific	Chile, South America - Values given relative to Chaihuín	Hocking, Garrett and Cisternas (2017)	WA-PLS	Diatoms	176	0.23	0.95	24
Eastern Pacific	Alaska, USA - Values given relative to Anchorage	Watcham, Shennan and Barlow (2013)	WA-PLS	Diatoms	255	0.66	8	8.3
Northern Atlantic	Viðarholmi Iceland	Gehrels et al. (2006)	WA-Tol	Foraminifera	21	0.2	2.1	9.5
Northern Atlantic	Viðarholmi Iceland	Saher et al. (2015)	WA-PLS	Diatoms	53	0.09	2.1	4.3
Northern Atlantic	Aasiaat, Greenland	Woodroffe and Long (2010)	WA-PLS	Diatoms	64	0.16	2.7	5.9
Northern Atlantic	Sisimut, Greenland	Woodroffe and Long (2010)	WA-PLS	Diatoms	70	0.19	4.5	4.2
Red Sea	Shuaiba Lagoon	Abu-Zied and Bantan (2013)	WA-PLS	Foraminifera	29	0.16	0.06	266.7
South Atlantic	Galpins salt-marsh – Values given relative to Port Elizabeth	Strachan et al. (2015)	PLS	Foraminifera	37	0.17	1.12	15.2
South Atlantic	Swan Inlet	Newton et al. (2021)	WA-Tol	Testate amoebae	28	0.13	0.07	0.19
South Atlantic	Swan Inlet	Newton et al. (2021)	WA-PLS	Diatoms	37	0.06	0.07	0.09

South Atlantic	Swan Inlet	Newton et al. (2021)	WA-PLS	Multiproxy	46	0.09	0.07	0.13
Western Atlantic	Magdalen Islands - Values given relative to Cap-aux-Meules	Barnett, Garneau and Bernatchez (2016)	PLS	Foraminifera	39	0.12	0.29	41.4
Western Atlantic	Magdalen Islands	Barnett, Garneau and Bernatchez (2016)	Wa-Cla	Testate	62	0.08	0.29	27.6
Western Atlantic	Newfoundland	Wright, Edwards and van de Plassche (2011)	WA-PLS	Foraminifera	37	0.07	0.83	8.4
Western Atlantic	Pattagansett River, Connecticut, USA	Wright, Edwards and van de Plassche (2011)	WA-PLS	Foraminifera	26	0.1	1.16	8.6
Western Atlantic	Maine and Nova Scotia, North America - Values given relative to the Chezzetook Inlet	Charman et al. (2010)	WA-Tol	Testate	29	0.05	1.25	4.2
Western Atlantic	Connecticut USA (average of 4 sites)	Edwards, Wright and van de Plassche (2004)	WA-PLS	Foraminifera	91	0.18	1.36	13.2
Western Atlantic	Maine USA (average of 4 sites)	Gehrels (2000)	WA-PLS	Foraminifera	68	0.25	3.11	8
Western Atlantic	Nova Scotia	(Gehrels et al. 2005)	WA-Tol	Foraminifera	46	0.06	1.86	3.2

Western Atlantic	New Brunswick, Canada	Gehrels, Hendon and Charman (2006)	WA	Testate	12	0.08	5.8	1.4
Western Atlantic	Maine, USA	Gehrels, Hendon and Charman (2006)	WA	Testate	17	0.07	2.6	2.7
Western Atlantic	Delaware, USA	Gehrels, Hendon and Charman (2006)	WA	Testate	9	0.07	1.75	4
Western Atlantic	Outer Banks North Carolina USA (average of 3 sites)	Horton et al. (2006)	WA-PLS	Diatoms	46	0.08	0.35	22.9
Western Atlantic	Outer Banks North Carolina USA (average of 10 sites)	Kemp et al. 2009)	WA-PLS	Foraminifera	46	0.04	0.27	14.8
Western Atlantic	New Jersey - Values given relative to Leeds Point	Kemp et al. (2012a)	WA-PLS	Foraminifera	62	0.14	1.16	11.8
Western Atlantic	New Jersey - Values given relative to Leeds Point	Kemp et al. (2013b)	WA	Foraminifera	175	0.15	1.16	13.2
Western Atlantic	Elizabeth River, North Carolina, USA	Wright, Edwards and van de Plassche (2011)	WA-PLS	Foraminifera	53	0.14	1.34	10.4
Western Pacific	Kaledupa	Engelhart et al. (2007)	ML	Pollen	63	0.22	1.13	19.6
Western Pacific	Central Great Barrier Reef –	Horton et al. (2007)	WA-PLS	Foraminifera	43	3.5	1.51	231.1

	values given relative to Cleveland Bay							
Western Pacific	Hokkaido Japan (average of 2 sites)	Sawai, Horton and Nagumo (2004)	WA-PLS	Diatoms	78	0.29	1.05	27.6
Western Pacific	Caitlins Coast	Southall, Gehrels, and Hayward (2006)	WA-Tol	Foraminifera	31	0.05	1.5	3.3
Western Pacific	Little Swanport	Callard et al. (2011)	WA-PLS	Foraminifera	43	0.1	0.6	16.7
Western Pacific	New Zealand - Values given relative to Mokomoko	Garrett et al. (Unpublished)	PLS	Foraminifera	77	0.08	1.89	4.2
Western Pacific	Manukau Harbour	Grenfell et al. (2012)	WA-Tol	Foraminifera	25	0.11	1.84	6
Western Pacific	Cocoa Creek, Great Barrier Reef Coastline, Australia	Horton et al. (2003)	WA-PLS	Foraminifera	34	0.07	1.48	4.7
Western Pacific	**Lutregala**	**This study**	**WA-PLS**	**Foraminifera**	**37**	**0.06**	**0.47**	**12.8**
Western Pacific	**Wapengo**	**This study**	**WA-PLS**	**Foraminifera**	**28**	**0.11**	**0.95**	**11.6**
Western Pacific	**Regional II – Values given relative to Lutregala**	**This study**	**WA-PLS**	**Foraminifera**	**65**	**0.07**	**0.47**	**14.9**

We find a positive and significant correlation between MTR and model performance (both local and regional models) assessed using RMSEP ($r^2 = 0.44$, n = 67, p = <0.01; **Figure 40a**). Our results suggest that microtidal ranges, such as those seen at Lutregala and Wapengo, provide the optimal environments for sea-level reconstructions as they yield models with low vertical uncertainties. We find that, due to generally smaller MTR, sites in the western Pacific (*e.g.* Callard et al. 2011; Horton et al. 2003; Southall, Gehrels and Hayward, 2006), western Atlantic, (*e.g.* Barnett, Garneau and Bernatchez, 2016; Horton et al. 2006; Kemp, Horton and Culver; Wright, Edwards and van de Plassche, 2011) and South Atlantic (*e.g.* Newton et al. 2021), have lower vertical uncertainties, whereas those from the eastern Atlantic, with larger tidal ranges, have larger vertical uncertainties (*e.g. B*arlow et al. 2013; Horton and Edwards, 2005; Massey et al. 2006; Mills et al. 2013). This supports findings previously described in the literature. When our regional model is compared to other regional models from across the world (**Figure 40b**), we note that our model performs well, with similarly small vertical uncertainties to western Atlantic regional models from Barnett, Garneau and Bernatchez (2016), Charman et al. (2010), Horton et al. (2006) and Kemp, Horton and Culver (2009). Spatially, the closest regional training set to ours currently is located in Japan (Sawai, Horton and Nagumo, 2004); most regional training sets come from the East and West Atlantic; therefore, future work should concentrate on developing more training sets for the western Pacific (Oceania) region in order to better resolve recent sea-level histories for this region of the world.

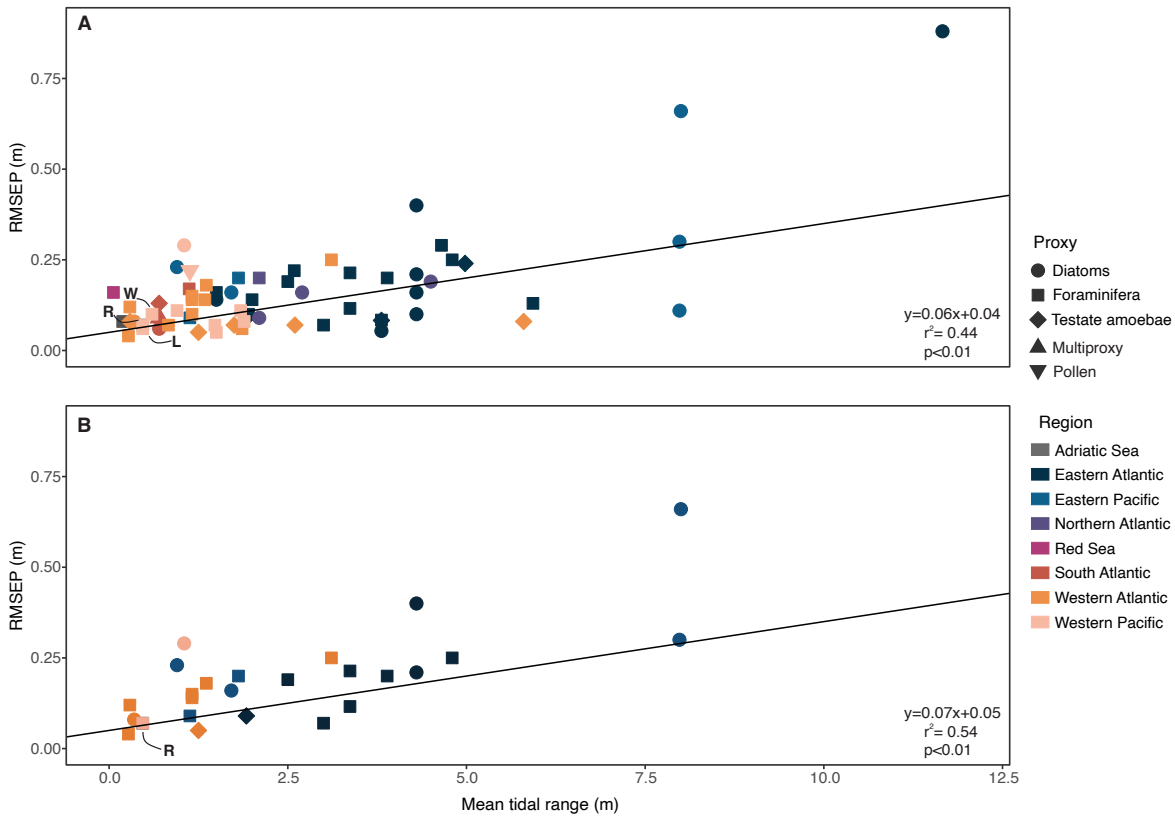

Figure 40. A. Relationship between model performance (root mean squared error of prediction; RMSEP) and mean tidal range (MTR) across 67 models (**Table 10**) including the Lutregala (L) and Wapengo (W) local training sets and the regional II model (R). The updated dataset integrates training sets that use diatoms, benthic foraminifera, testate amoebae, pollen and multiproxy (diatoms, foraminifera and testates combined) approaches for sea-level reconstruction from multiple regions of the world**. B.** Relationship between model performance and mean tidal range showing only regional models.

5.2.4.2 Alternative methods for paleoenvironmental reconstruction

An alternative to the transfer-function approach is a 'visual assessment' (VA; Long et al. 2010). VAs may be used to assess key changes in microfossil taxa, whilst incorporating environmental data. Variables such as stratigraphy, loss on ignition and particle size, which cannot be incorporated into traditional transfer-function analyses, can be considered with a VA approach. VAs may also be used where the

modern training set yields no good modern analogues for fossil material (*e.g.* Barnett et al. 2015). This method is not used widely, but may be utilised at sites with microtidal ranges, particularly in the upper marsh where species are mostly constrained to a small vertical range. However, the VA method has been criticised as it considers elevation as a discrete variable which can result in step changes in relative sea-level reconstructions, whereas transfer-function approaches produce sample-specific errors as elevation is treated as a continuous variable (Kemp et al. 2017b). Furthermore, generally, transfer-function approaches will yield models with lower vertical uncertainties (Kemp and Telford, 2015). The recent use of Bayesian transfer functions in relative sea-level reconstruction provides an alternative to both of these methods and may incorporate the best aspects of both approaches (*e.g.* Cahill et al. 2016; Kemp et al. 2017a; Walker et al. 2021). Future relative-sea level studies may choose to use this approach over the more traditional transfer-function method.

5.3 Conclusions

This study is the first to collate salt-marsh foraminifera into a regional training set for southeastern Australia and produces new transfer functions that will underpin future late Holocene sea-level reconstructions in the region. We report assemblages from two new sites: Lutregala salt marsh located on Bruny Island, Tasmania and Wapengo salt marsh located in southern New South Wales, and combine these with a previously published training set from Little Swanport, Tasmania (Callard et al. 2011), successfully expanding the available region for reconstruction north and southwards of the previous site. Multivariate analyses identify three clusters within the combined regional foraminiferal training set, comprising a high elevation biozone, a mid-elevation biozone and a mid to low elevation biozone. Similar to

contemporary foraminiferal distributions reported elsewhere in Australia and New Zealand, *T. inflata* is dominant at all sites and found along the majority of the sampled elevation gradient. No samples from Little Swanport are classified into the mid to low elevation cluster; we attribute this to the low and variable salinity in the Little Swanport estuary.

New local transfer functions for Lutregala and Wapengo perform well, with an ability to predict sea level within ± 0.06 m (68 % confidence) or ± 0.12 m (95 % confidence), and ± 0.11 m (68 % confidence) or ± 0.22 m (95 % confidence), respectively. The dominance of *T. inflata* and near-absence of *M. fusca* at Little Swanport complicates the development of a transfer function model that incorporates all three sites. Rather, a model combining the two higher salinity sites provides improved performance (RMSEP = 7.66 SWLI units) despite the large distance between these sites. When developing regional training sets, we advocate that the similarity in the environmental settings (particularly salinity) should be assessed as an alternative way of grouping sites, rather than simply using spatial proximity.

Our transfer functions provide comparable predictive ability to other transfer functions reported elsewhere in Australia and New Zealand (*e.g.* Callard et al. 2011; Southall et al. 2006). By updating a global database of transfer function model performance we also show that our models are comparable with studies in distant regions, namely those from the western Atlantic. Our revised database of studies that use diatoms, benthic foraminifera, testate amoebae and pollen for sea-level reconstruction demonstrates that model performance is superior in locations with

microtidal regimes. Future sea-level reconstructions from the microtidal coasts of New South Wales and Tasmania underpinned by the work presented here offer the potential for sea-level reconstructions with low vertical uncertainties that will help to refine understanding of late Holocene sea-level change in Australia as well as shed light on the discrepancy in rates of sea-level rise observed in proxy and instrumental records in the western Pacific, and help to elucidate the causes of the early 20th century sea-level acceleration.

Supplementary materials

See Appendix III

Chapter 6 of 8

Reconstructing sea level in southeastern Australia

6.0 Introduction

This chapter presents the site stratigraphy, fossil foraminifera, palaeomarsh surface elevations (using transfer functions from **Chapter 5**), modern analogue evaluations, age-depth models, and the sea-level reconstructions of the master cores taken at each site. It also updates the previously published reconstruction from Little Swanport, Tasmania (Gehrels et al. 2012) to SHCal20. The aim of this chapter is to create three sea-level reconstructions to investigate the timing and magnitude and of sea-level change in southeastern Australia. The sea-level reconstructions are compared to nearby tide gauges and a modelled sea-level budget (Frederikse et al. 2020; Giese et al. 2016; Slivinski et al. 2019).

N.B. Stratigraphy presented in the cross-section figures vary slightly to the master core descriptions, as the cross-sections detail field descriptions of the stratigraphy, whereas the master cores detail the re-described laboratory descriptions.

6.1 Results

6.1.1 Lutregala

6.1.1.1 Stratigraphy and foraminiferal assemblages

At Lutregala, two coring transects were established (**Figure 41**). At the base of the sequence at Lutregala (Unit 3) is a beige medium silty sand unit which extends down to at least –1.24 m AHD. Overlying this unit is a brown-grey tidal-flat silt (Unit 2) is thickest towards the seaward and landward sides of the salt marsh. At the surface of the sequence is a salt-marsh peat (Unit 1). At its thickest, the peat extends from 0.48 m to 0.76 m AHD. This unit can be further subdivided into a very dark brown silty salt-marsh peat at the bottom (1b; 17 – 28 cm), and a fibrous brown salt-marsh peat at the

top (1a; 0 – 17 cm). The contact between these two sub-units is gradual in nature. Unit 2 is found between 28 – 31 cm and contains some rootlets. Unit 3 can be sub-divided into a beige medium silty sand (31 – 40 cm; Unit 3a) and a beige medium sand (41 – 60 cm; Unit 3b) (**Table 11**).

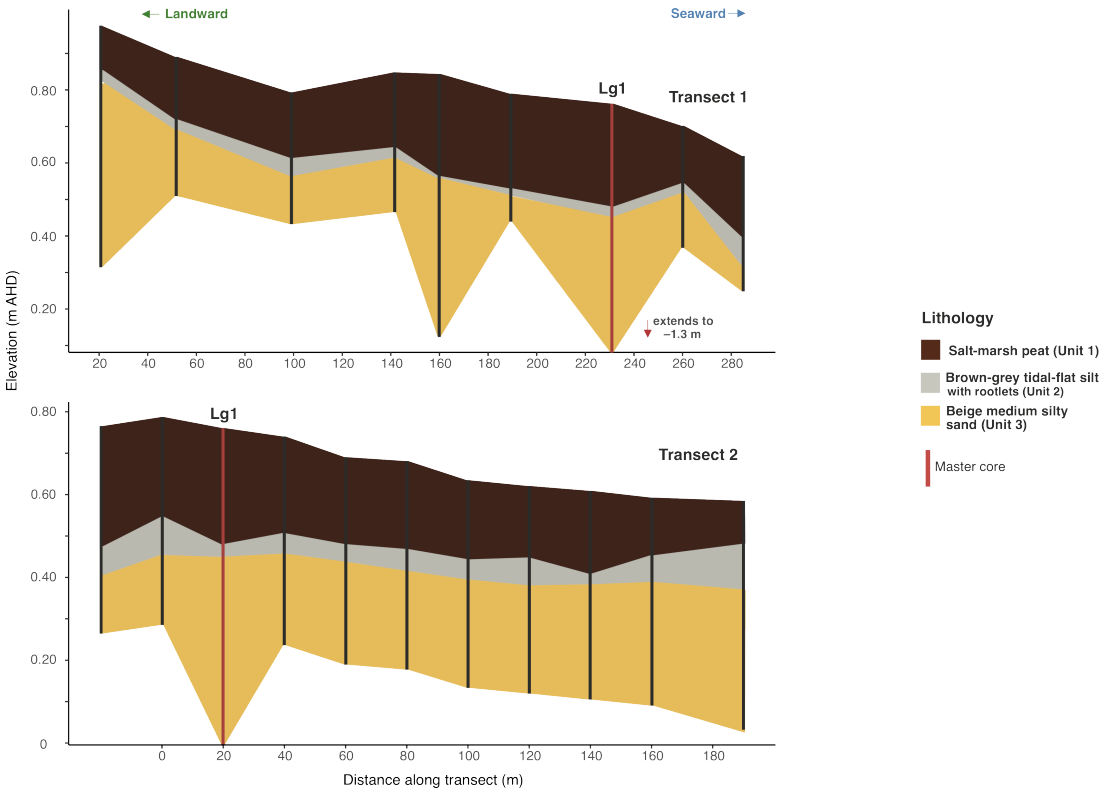

Figure 41. Cross section of both coring transects at Lutregala showing variations in stratigraphy across the site. The locality of the master core (LG-1) is highlighted in red in both transects. Both transects exhibit a salt-marsh peat unit, underlain by a brown-grey tidal-flat silt and a beige medium silty sand.

Table 11. Description of the main sediment units identified within the master core sequence from LG-1 and associated Troels-Smith (1955) classification.

Unit	Unit depth (cm)	Description	Troels-Smith log
1a	0 – 17	Fibrous brown peat	Th3 Ag1 + dar 2 + strat 2 + sicc 0 + elas 0 + lm -
1b	17 – 28	Very dark brown silty peat	Th2 Ag2 + dar 3 + strat 2 + sicc 0 + elas 0 + lm 1
2	28 – 31	Brown/grey silt with rootlets	Ag1 Th^{+} + dar 1^{+} + strat 2 + sicc 0 + elas 0 + lm 1
3a	31 – 40	Beige medium silty sand	Ga3 Ag1 Th^{+} + dar 1 + strat 2 + sicc 0 + elas 0 + lm 0
3b	41 – 60	Beige medium sand	Ga4 + dar 1 + strat 2 + sicc 0 + elas 0 + lm 0

Total counts of dead foraminifera are high throughout the core, with only two samples at 30 and 32 cm having fewer than 50 foraminifera (3 and 13 individuals; **Figure 42**). Excluding these samples, total counts range from 69 – 665, with an average of 359 individuals per sample. Foraminifera are consistently found with total counts exceeding 100 individuals from 28 cm. Core samples contain eight species of foraminifera: *Trochamminita salsa*, *Haplophragmoides wilberti*, *Entzia macrescens*, *Polysacammina ipohalina*, *Trochamminita irregularis*, *Trochammina inflata*, *Siphotrochammina lobata* and *Milliamina fusca*. *Trochammina inflata* remains largely prevalent throughout the core (1 – 100 % relative abundance). The foraminifera in the silty sand unit of the core are inconsistent with the lithology and are mainly comprised of the high to mid marsh species *Trochammina inflata* (average relative abundance 96 %), with a low abundance of *Trochamminita salsa* and *Entzia macrescens.* Total counts are low in the unit (average of 19 specimens per sample). Foraminifera in the silt unit are largely comprised of *T. inflata* (average 96 % relative abundance),

and average total counts are higher (56 individuals per sample). Within the silty salt-marsh peat unit of the core, *T. salsa* is more prevalent (average 39 % relative abundance, up to a maximum of 75 % relative abundance). Into the fibrous salt-marsh peat, the relative abundance of *T. salsa* declines and the assemblages diversify, with *T. inflata, E. macrescens* and *M. fusca.* Total counts are largest in this unit (average 219 individuals per sample).

In general, both inorganic and organic carbon content increase upcore (range: 10 – 64 % organic and 2 – 17 % inorganic; **Figure 42**). Both start increasing significantly from 28 cm, which corresponds with the consistent large total counts of foraminifera, as well as the silt/peat boundary. Particle size data show silt and sand sized particles dominate the majority of the core. Increases in clay are noted at 28 cm, 24 cm and 18 cm. Significant rises in sand percentages are noted in the upper 3 cm of the core, which corresponded to small decreases in the carbon content, especially around 2 cm where organic carbon content decreases to 35 %.

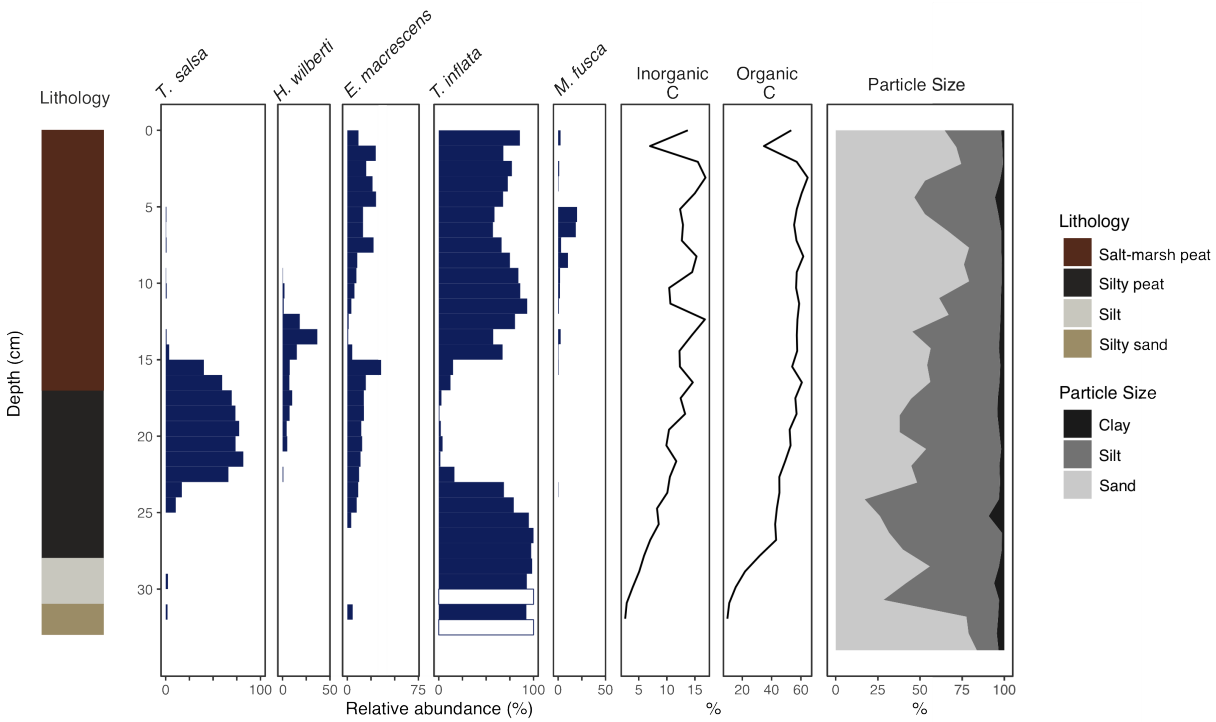

Figure 42. Litho-biostratigraphy of core LG-1 showing the relative abundance of foraminifera found exceeding 10 % in at least one sample. Unfilled bars represent samples with a total count <50. Core lithology, inorganic and organic carbon percentage change downcore (loss on ignition) and particle size are also shown.

The greatest number of live individuals are found in the top centimetre (107 individuals per cm^3) and decline downcore, with 15 individuals per cm^3 between 1 – 2 cm and 14 individuals per cm^3 between 2 – 3 cm (**Figure 43**). Species that occur infaunally include *E. macrescens*, *T. inflata*, *T. irregularis*, *S. lobata* and *M. fusca*. Live foraminifera are found as deep as 10 cm, and as such their limit has not been found. However, they occur in very low numbers (~4 live individuals per cm^3 in comparison to ~80 dead individuals per cm^3). Similarly to the dead assemblage, *T. inflata* dominates the live assemblage throughout the top 10 cm.

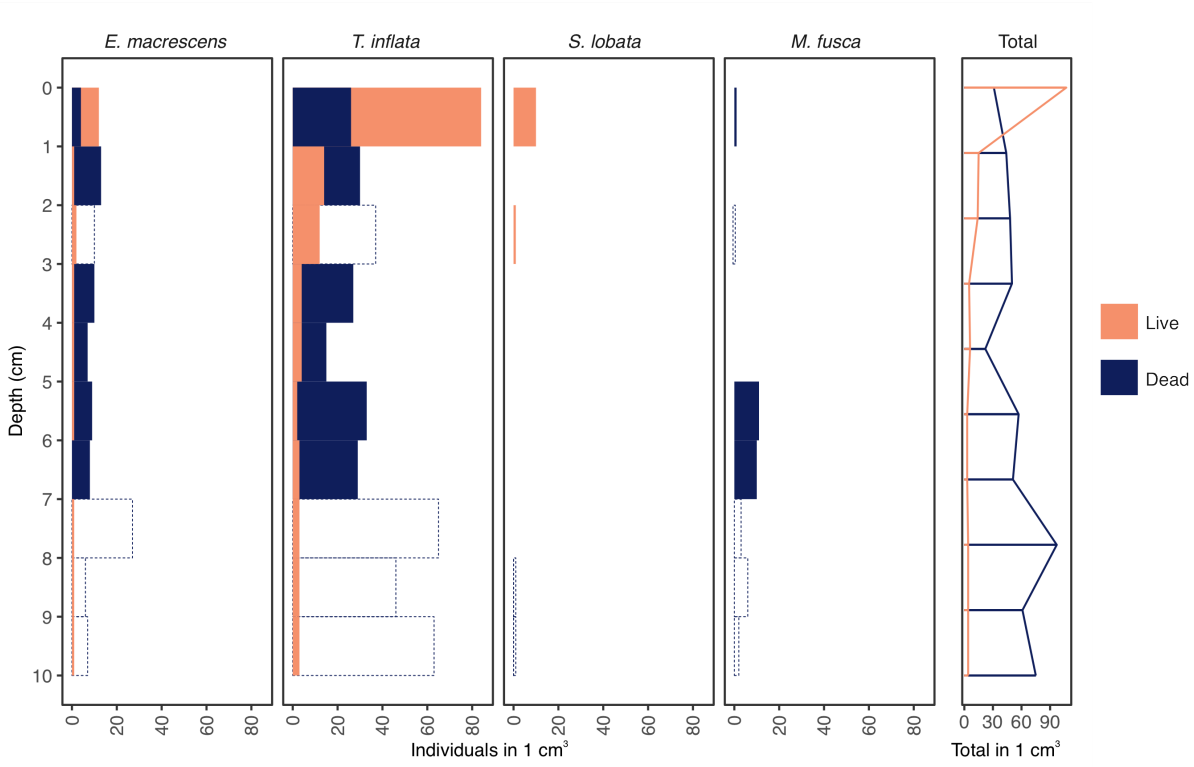

Figure 43. Live and dead foraminiferal densities (1cm³) in core LG-1 showing species with at least 5 individuals per cm³. Dotted bars denote where the death assemblage density has been estimated as they were not enumerated in the sample.

6.1.1.2 Modern analogue evaluation and palaeomarsh surface elevation reconstruction

In line with recommendations from Kemp and Telford (2015), the 20th percentile is chosen as the threshold for analogy as the diversity of the modern training sets are low (**Chapter 5**). This is because the dissimilarity amongst samples is relatively low and so the absolute distance for a particular percentile threshold is small, therefore a relatively high upper threshold is needed. Following Watcham, Shennan and Barlow (2013), "good" and "fair" analogues are defined as those with MinDC less than the 5th and 20th percentiles respectively.

Modern analogue results (**Figure 44**) show that both the regional and local transfer functions provide at least fair modern analogues for all fossil samples, suggesting that modern assemblages are mostly representative of fossil assemblages. The regional model results in 29 good analogues and 2 fair, whereas the local model results in 22 good analogues and 9 fair. In the local model most fair analogues are found in the lower section of the core, suggesting that samples become more analogous to the surface samples upcore. The larger number of fair rather than good analogues in the lower third of the core (**Figure 44**) is due to the relative abundance of *T. inflata* being higher in the core compared to the modern surface samples (Williams et al. 2021). Whilst the regional model results in a larger number of good modern analogues compared to the local model, there is very little difference in PMSE estimates between the two models (**Figure 44**). As such, the local transfer function model is employed for the reconstruction.

Only one sample from the silty sand unit provided in excess of 50 specimens; the resulting PMSE estimate suggests the sample accumulated at 0.71 m elevation, an elevation corresponding to the modern mid to high marsh, suggesting incongruence between the foraminifera and sediment, which could be a result of infaunality in the core or reworking of material following deposition. Similarly, PMSE estimates in this silt suggest that the marsh elevation remained largely unchanged from the silty sand, and foraminifera remain indicative of a mid-high salt-marsh environment. In the silty salt-marsh peat, corresponding with the increase in *T. salsa*, PMSE increases by 0.21 ± 0.08 m, reaching a maximum of 0.91 m AHD, suggesting an increase in the marsh elevation. Into the fibrous salt-marsh peat, there was a fall in PMSE to

0.70 m AHD which corresponds with the diversification of the assemblages to include more mid-low marsh species. In total, the local PMSE estimates range from 0.68 to 0.91 m AHD with an average uncertainty of ± 0.06 m (1 σ).

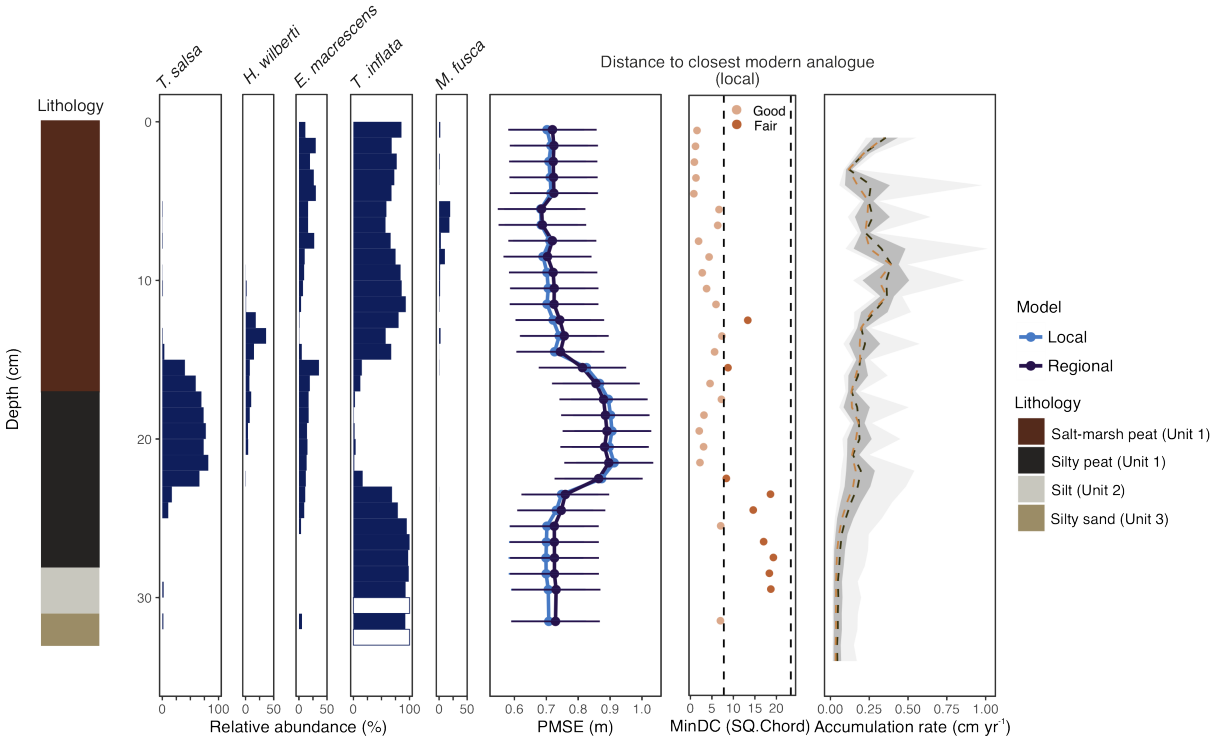

Figure 44. Fossil foraminifera, palaeomarsh surface elevation (PMSE) estimations, modern analogue results and sedimentation rate for core LG-1. Unfilled bars represent samples with total counts <50 individuals where PMSE estimates were not generated due to low numbers of individuals (Kemp, Wright and Cahill, 2020). Modern analogue results for the Lutregala local model are shown with light orange showing samples classed as "good" and dark orange showing samples classed as "fair". Dashed lines show 5th and 20th percentile boundaries. Both the Lutregala local transfer function PMSE estimates and regional PMSE estimates are shown. In the accumulation rate plot, the orange dotted line = median accumulation rate, dark green dotted line = mean accumulation rate, dark grey ribbon = 68 % confidence interval, light grey ribbon = 95 % confidence interval. The accumulation rate has been derived from age-depth modelling (see section 6.1.1.3).

6.1.1.3 Chronology

High-resolution sea-level reconstructions must be underpinned by a robust and well-dated chronology. This can be difficult to obtain over the Common Era due to the radiocarbon plateau and the limited chronometer of ^{210}Pb (Kemp et al. 2012b); therefore, a combination of radiocarbon ^{14}C AMS dating, radionuclide, stable lead ratios and pollen and charcoal data were used to generate chronologies for each core.

In total 11 ^{210}Pb samples were obtained from core LG-1. Samples show a decline in unsupported Pb downcore (**Table 12**). A comparison between the CRS-derived age estimates and *rplum* age estimates (**Figure 45**) demonstrate that the ages agree well between the two models at the top of the core and diverge downcore, with uncertainty also becoming larger downcore. In the upper section there is a difference of ~2 – 3 years between the means of the *rplum* and CRS model age estimates, which increases to ~10 – 20 years towards the bottom of the profile. The uncertainties of *rplum* are also larger towards the bottom of the core, which is a common feature of the *rplum* model, but have largely been postulated to yield more accurate age uncertainties than the CRS model (Aquino-López et al. 2020).

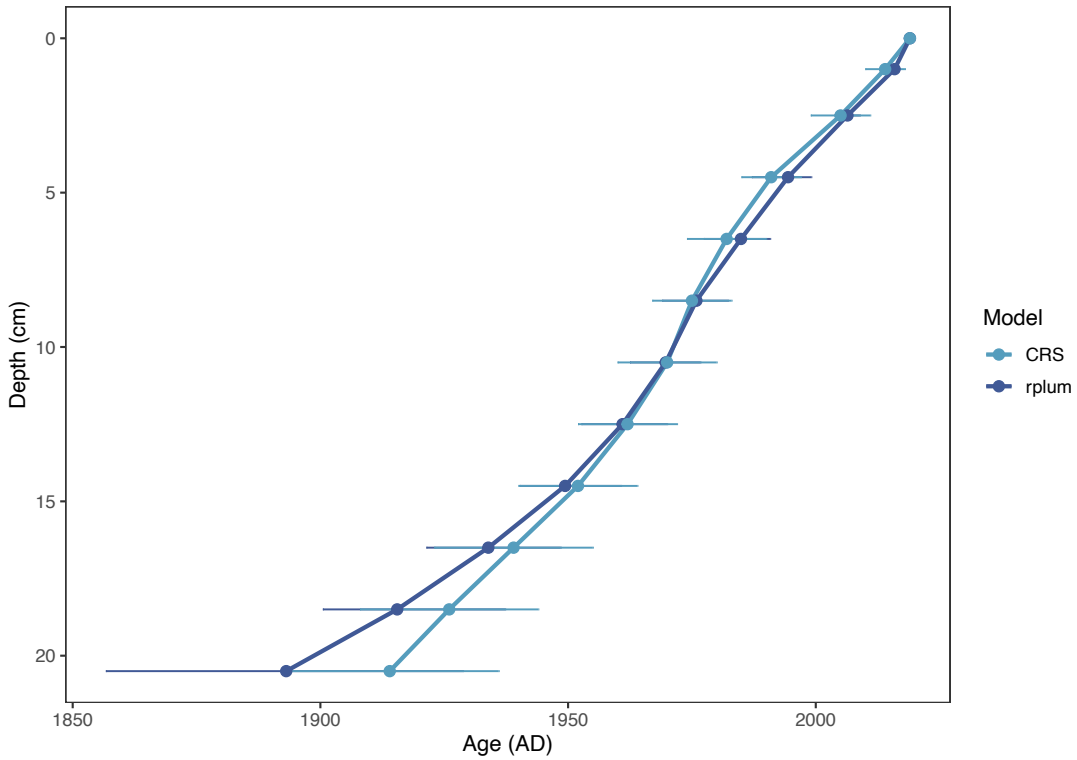

Figure 45. Comparison of the ^{210}Pb age estimates from the Constant Rate of Supply model (CRS) and the Bayesian *rplum* model in core LG-1.

Table 12. ^{210}Pb results from core LG-1.

ANSTO ID	Depth (cm)			Dry Bulk Density (g/cm^3)	Cumulative Dry Mass (g/cm^2)			Count Date	Total ^{210}Pb (Bq/kg)			Supported ^{210}Pb (Bq/kg)			Unsupported ^{210}Pb Decay corrected 11-Mar-20 (Bq/kg)		
X133	0	-	2	0.14	0.17	±	0.17	16-Feb-21	158.53	±	8.37	1.54	±	0.23	161.63	±	8.62
W622	2	-	3	0.19	0.44	±	0.08	16-Mar-20	216.38	±	11.27	1.15	±	0.21	215.31	±	11.27
W623	4	-	5	0.10	0.72	±	0.08	16-Mar-20	131.73	±	6.58	0.54	±	0.16	131.24	±	6.59
W624	6	-	7	0.12	0.94	±	0.07	16-Mar-20	88.21	±	4.06	2.73	±	0.38	85.52	±	4.08
W625	8	-	9	0.10	1.16	±	0.07	16-Mar-20	47.33	±	2.33	0.74	±	0.17	46.61	±	2.33
W626	10	-	11	0.08	1.34	±	0.06	16-Mar-20	54.54	±	2.55	5.21	±	0.58	49.35	±	2.61
W627	12	-	13	0.13	1.55	±	0.06	16-Mar-20	48.14	±	2.29	0.62	±	0.15	49.35	±	2.29
X134	14	-	15	0.14	1.82	±	0.06	16-Feb-21	32.83	±	1.53	0.76	±	0.18	33.02	±	1.59
X135	16	-	17	0.18	2.14	±	0.06	16-Feb-21	24.81	±	1.23	1.18	±	0.25	24.33	±	1.29
X136	18	-	19	0.17	2.49	±	0.07	16-Feb-21	13.05	±	0.67	0.71	±	0.18	12.71	±	0.71
X137	20	-	21	0.17	2.83	±	0.07	16-Feb-21	11.09	±	0.60	1.48	±	0.22	9.90	±	0.65

Stable Pb isotope data (**Appendix VI**) show samples become increasingly less radiogenic and diverging from the Tasmania background signature to more polluted isotopic ratios from ~25 cm, with a large excursion ~23 cm. This is attributable to the mining of the Broken Hill lead-zinc-silver ore deposits (~1895; **Figure 46**). A pollution maximum is reached at 10.5 cm (~1974 following a peak in petrol consumption and subsequent Pb emissions; Kristensen, 2015) after which samples reverse back to more radiogenic values following the introduction of unleaded petrol (1985) and potentially also the removal of leaded petrol (2002) in Australia (Kristensen, 2015).

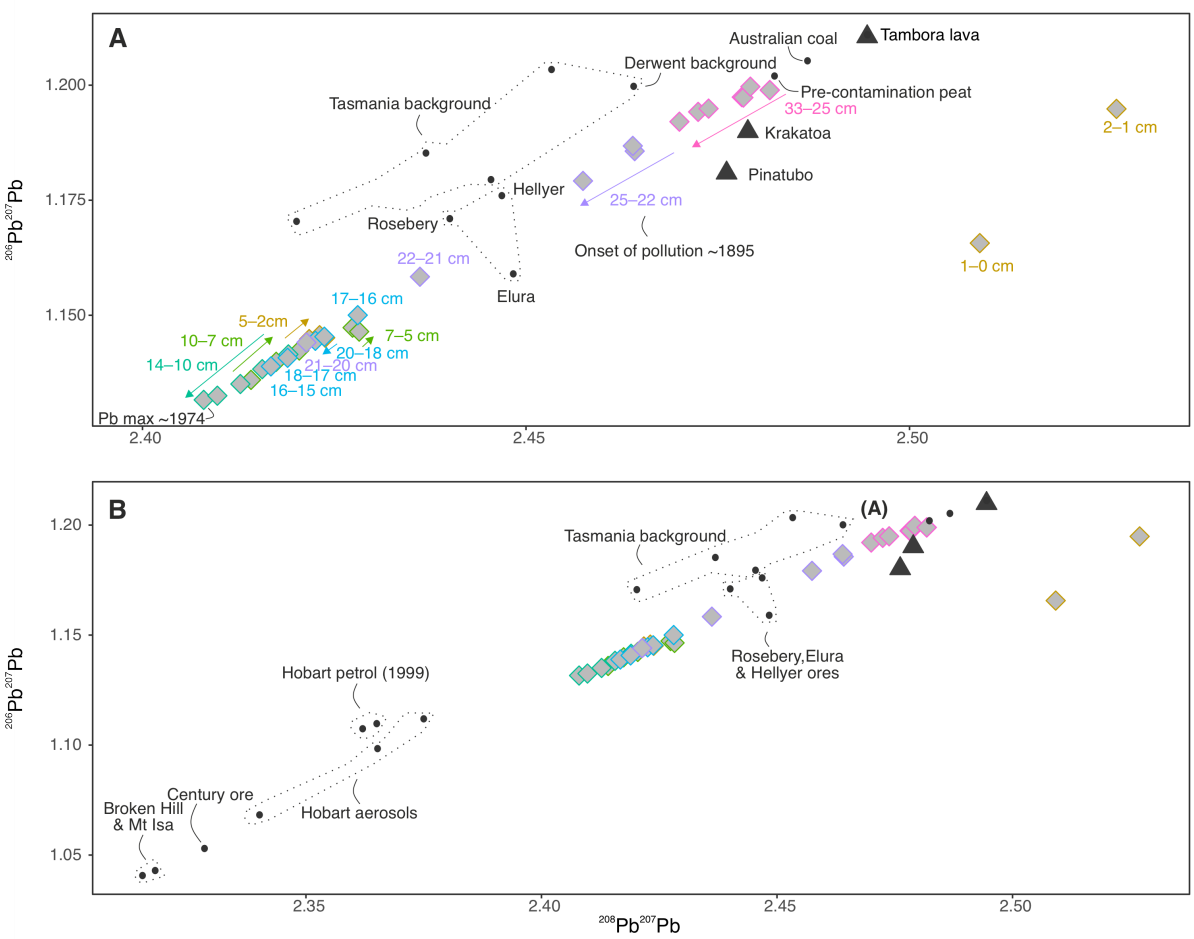

Figure 46. A. Source plot for samples from core LG-1 (coloured markers) as well as volcanic, pollution and background isotopic signatures (black markers). **B.** A zoom out of plot **A** showing also the isotopic signatures of the Hobart aerosols and petrol, the Century ore and the Broken Hill and Mt Isa ores (black markers). Data are available in **Appendix IX.**

Exotic pollen does not appear until 13 cm (which stable lead isotopes and calibrated ^{14}C dates suggest is mid – late 20th century) and no discernible chronohorizons can be identified in the trace metal record (**Figure 47**). As such, there are two identifiable chronohorizons in LG-1 (**Table 13**).

Table 13. Calendar dates obtained from core LG-1.

Chronostratigraphic Marker	Depth (cm)	Calendar Year (AD)	Date given in model (AD)	Reference
Pb maximum	10.5	1964 – 1984	1974 ± 10	Kristensen (2015)
Broken Hill smelting	23.5	1890 – 1900	1895 ± 5	Van de Velde et al. (2005)

In total, nine AMS ^{14}C samples were obtained from ANSTO, SUERC and UCI (**Table 14**). However, after considering stratigraphic ordering and comparing calibrated dates to established chronohorizons, two dates were removed prior to age-depth modelling (UCIAMS-26610 and UCIAMS-236611). These dates were deemed too young for their stratigraphic position; this could be a result of root contamination or misidentification of material.

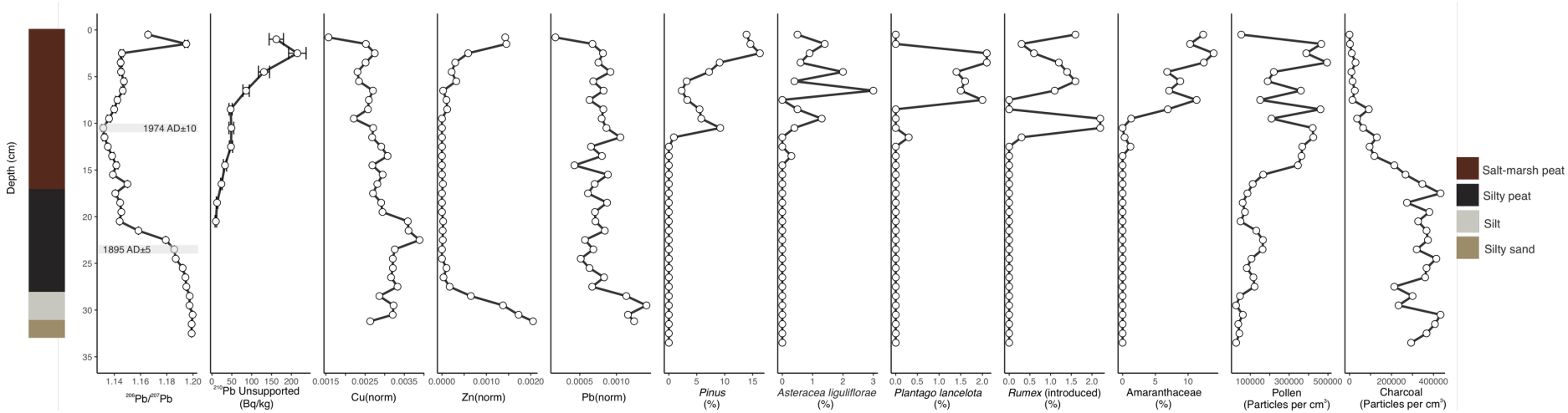

Figure 47. Stable lead ($^{206}Pb/^{207}Pb$), ^{210}Pb, pollen and charcoal data for core LG-1. Identified chronohorizons are highlighted by the grey boxes.

Table 14. ^{14}C results from core LG-1 calibrated using SHCal20 (Hogg et al. 2020) and Bomb13 SH1 – 2 (Hua, Barbetti and Rakowski, 2013). Dates removed prior to age-depth modelling are highlighted by an asterisk. Depths given in the table represent the mid points of the samples.

Publication Code	Material	Depth (cm)	Percent modern ^{14}C (pMC) and error (1 σ)	Calibrated radiocarbon age 2 σ (AD)	$\delta^{13}C$-VPDB‰
SUERC-93775	Grass	5	110.99 ± 0.48	1958 – 2000	-26.9
UCIAMS-236604	Grass	7	116.59 ± 0.19	1959 – 1992	n.d
UCIAMS-236607	Grass	9	111.04 ± 0.18	1958 – 1998	n.d
OZZ407	Bulk sediment	15	137.51 ± 0.35	1963 – 1976	-27.7 +/- 0.1
UCIAMS-236608	Grass	16	116.77 ± 0.18	1959 – 1992	n.d
UCIAMS-236609	Grass	19	98.75 ± 0.18	1711 – 1956	n.d
UCIAMS-236610 *	Grass	26	99.42 ± 0.18	1954 – 1956	n.d
UCIAMS-236611 *	Grass	29	100.45 ± 0.17	1955 – 1956	n.d
OZZ408	Bulk sediment	34	95.39 ± 0.23	1463 – 1628	-26.3 +/- 0.2

The resulting ^{14}C, ^{210}Pb and calendar ages were combined in a Bayesian age-depth model to produce age estimates and uncertainties downcore. The prior for accumulation rate (acc.mean) was selected using that suggested by *rplum* from initial data analysis. The prior for memory (how much the accumulation rate can vary) was kept at the default of 0.5. The accumulation shape (*i.e.* accumulation smoothness *c.f.* Blaauw and Christen, 2011) was set at 0.5 in order to better constrain model iterations through the Broken Hill (23.5 cm) calendar date. The model was run with a setting of ra.case=1 where the model assumes constant radium (*i.e* background Pb). Thickness was kept at the default of 1. A minimum core age of 2019 was set, and this was also given as the sampling date.

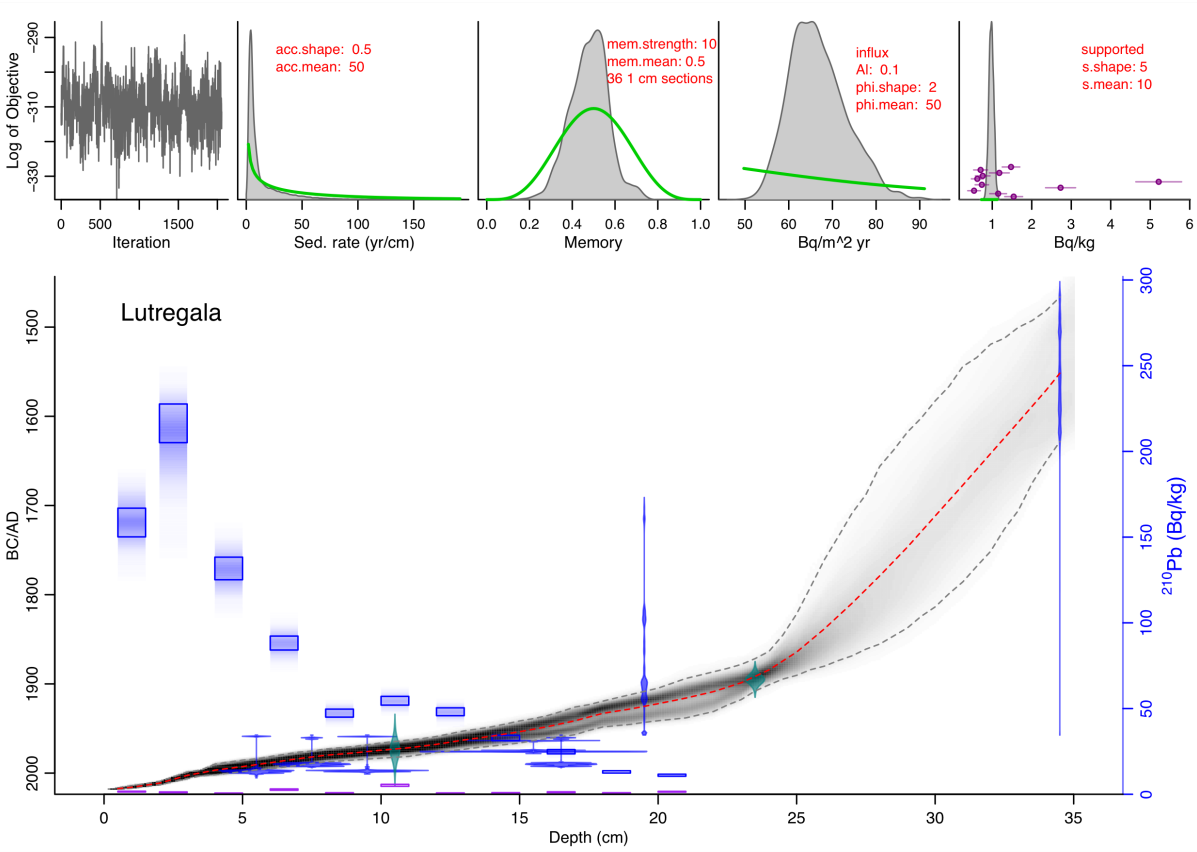

Figure 48. Upper panels: Prior (light green) and posterior distributions (light grey) as well as Markov Chain Monte Carlo iterations (dark grey). **Lower panel:** Age-depth model for core LG-1. Blue dotted squares show measured ^{210}Pb and columns show modelled ^{210}Pb. Purple squares show supported ^{210}Pb. Calendar dates (teal) and calibrated radiocarbon dates (dark blue) are also shown. Mean ages are denoted by the dotted red line and 95 % confidence interval (*i.e.* age range) is denoted by the grey dotted lines.

MCMC iterations indicate that that the model run was successful, with no visible structure seen. The model suggests variability in sedimentation rate from ~40 yr cm^{-1} – <10 yr cm^{-1} from the base to the top of the core. In the sand and silt units, the average accumulation rate was 0.03 cm yr^{-1}; this increased in the salt-marsh peat unit to an average of 0.19 cm yr^{-1}. The model generates a mean age for each depth in the core alongside a 95 % confidence interval to yield

a minimum and maximum range. Model uncertainty is well constrained throughout the upper section of the core but increases between the final calendar date and basal radiocarbon date due to a lack of dateable material.

A comparison of prior (calibrated ^{14}C dates) and posterior age probability distribution functions shows that the posterior age distributions cover a larger chronological range than the prior age distributions as they are combined with the other dating methods (**Figure 49**). The posterior ages are estimated older than prior ages. Posterior probability distribution functions fit a near-Gaussian profile (**Figure 50**); therefore, a Gaussian-process model was deemed suitable for the sea-level reconstruction.

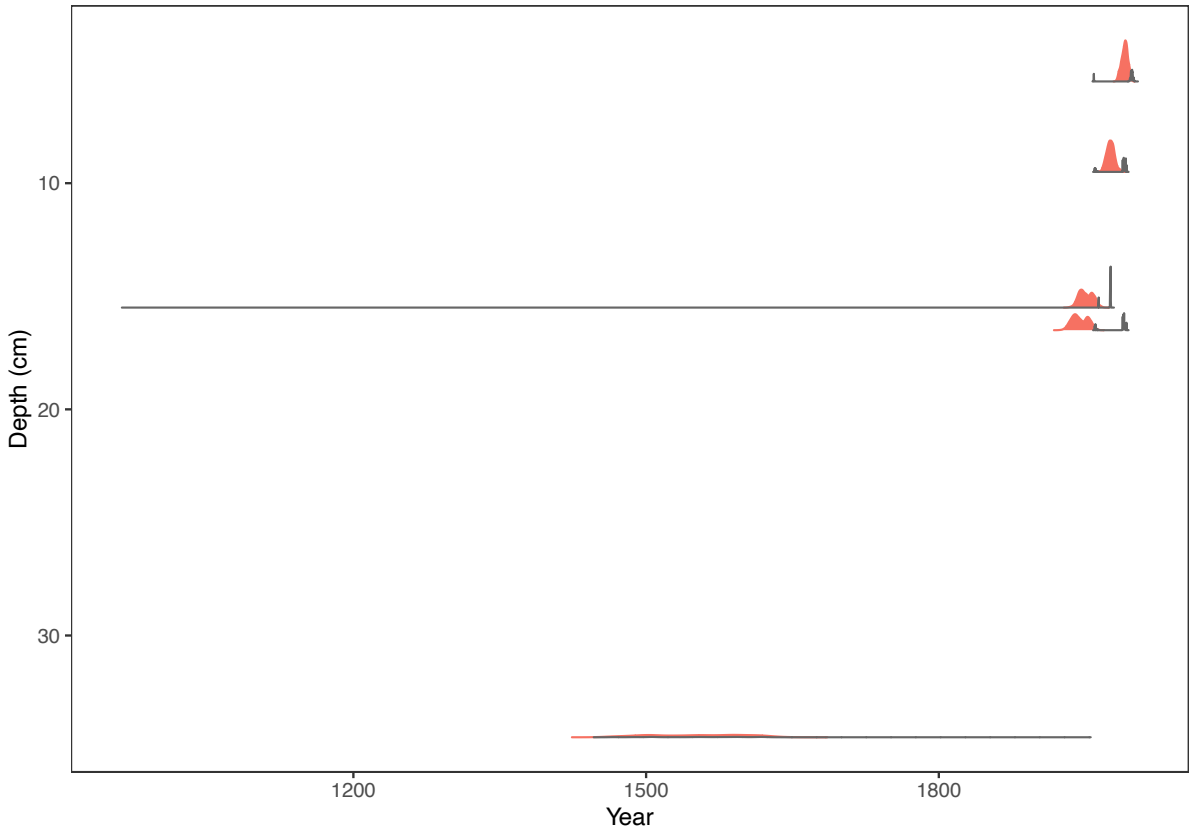

Figure 49. Probability distribution functions (PDFs) of prior ^{14}C dates (grey) and posterior *rplum* distributions (orange).

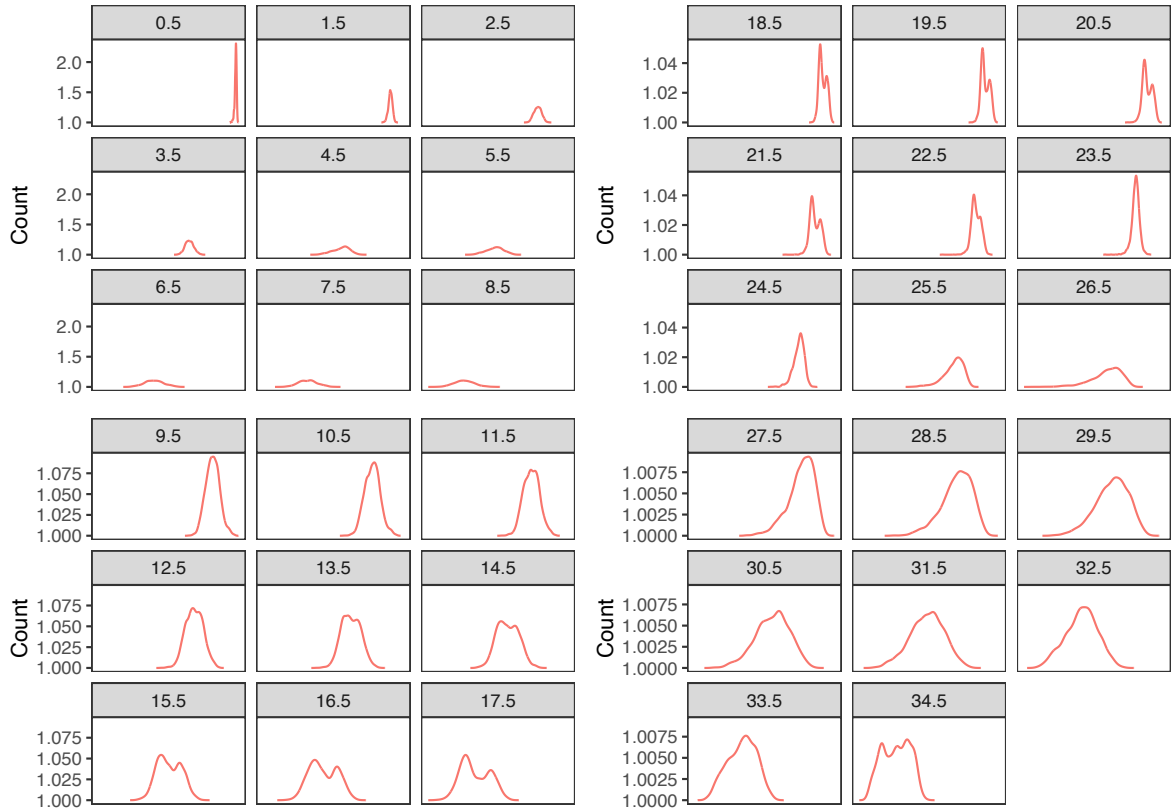

Figure 50. Probability distribution functions (PDFs) of the posterior age ranges from the Lutregala age-depth model. Numbers in the grey box indicate the depth that the PDF has been extracted from in centimetres.

6.1.1.4 Sea-level reconstruction and change-point analysis

Due to a lack of chronological constraint in the deeper part of the core, as well as incongruent foraminifera in the silt units, only data from above 23.5 cm (*i.e.* from the silty peat) are included in the Gaussian process model. The reconstruction was GIA-corrected at a rate of - 0.01 (-0.41 – 0.51; 95 % Confidence interval (CI)), mm yr^{-1} (Caron et al. 2018). The reconstruction suggests GIA-corrected sea level (GCSL) was ~0.31 m below present in the late 19th century (**Figure 51**). The rate of sea-level rise during the first half of the 20th century

(1900 – 1949) was 1.7 (-4.0 – 6.5) mm yr^{-1}. Change-point analysis detects a change point between 1904 – 1930 (95 % credible interval) and yields a mean change-point estimate of 1918, but it is not until 1953 that maximum rates of 8.3 (4.4 – 16.8) mm yr^{-1} were reached, showing a very fast acceleration over the first half of the century. Detrending by the minimum, maximum and mid GIA rate indicates that the timing of emergence above 0 mm yr^{-1} (Ea0; *i.e.* when the rate of sea-level rise exceeds 0 mm yr^{-1}) of the modern acceleration in sea level was between ~1900 – 1940, and broadly coincides with the first change point. Timings of Ea0 are largely similar for each correction, varying no more than a few years between the median and lower 95 % CI for each. However, the upper 95 % CI of the maximum GIA rate shows a later onset (~10 years) than the upper 95 % limit of the mid and minimum GIA rates. Over the second half of the 20^{th} century (1950 – 1999), rates remained high at an average of 4.6 (0.9 – 8.7) mm yr^{-1}, although rates do decline over the century. A second change point is detected in 1977 which may reflect the decrease in the rate of sea-level rise from the 1960s to present.

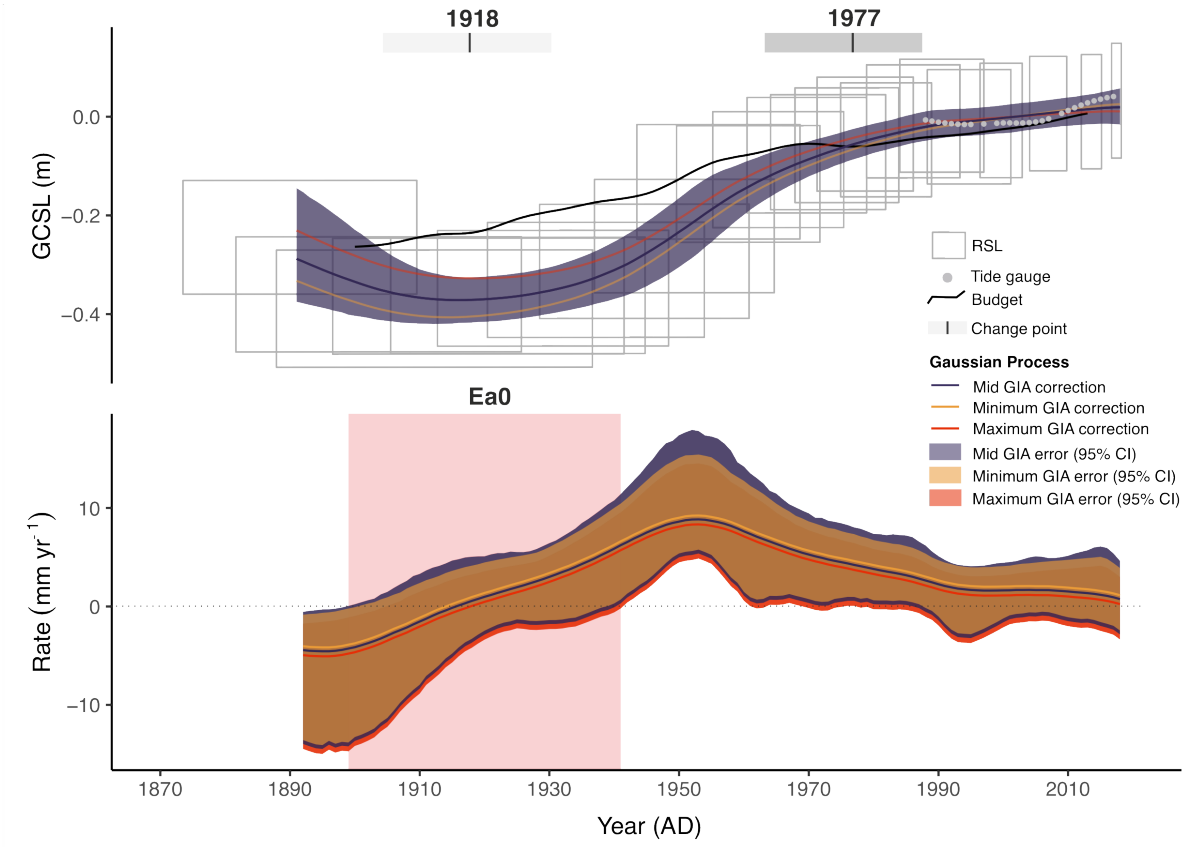

Figure 51. Upper panel. GIA-corrected sea-level (GCSL) reconstruction for Lutregala salt marsh. Grey parallelograms show palaeo sea-level estimates (*i.e.* sea-level index points) from core LG-1 with 2 σ vertical and age uncertainties. A GIA-corrected Gaussian process regression has been fitted to the index points showing the median (purple line) and 95 % confidence intervals (purple shading) of the mid-range GIA correction. Also shown are the median gaussian process regression curves after detrending using the minimum (yellow line) and maximum (red line) GIA corrections. The filled grey bars denote identified change points from the change-point model (Caesar et al. 2021) showing 95% credible intervals and mean change point (black lines). Also plotted are local tide-gauge data and the sea-level budget (barystatic gravity, rotation and deformation, sterodynamic and the inverse barometer components - both have been 15-yr smoothed). **Lower panel.** The rate of sea-level change calculated from the Gaussian process regression showing the median (purple line) and 95 % confidence intervals (purple shading) of the mid-range GIA correction. Also shown are the rates after detrending using the minimum (yellow line and shading) and maximum (red line and shading) GIA corrections. The timing of emergence above 0 (Ea0) of the acceleration in sea level is denoted by the red box.

6.1.2 Wapengo

6.1.2.1 Stratigraphy and foraminiferal assemblages

At Wapengo three coring transects were established (**Figure 52**). The deepest core (WAP-100), located at 100 m along Transect 3, reached −1.03 m AHD. The basal unit is characterised by a silty sandy unit (Unit 3). Overlying Unit 3 is a brown-grey tidal-flat silt with yellow pebbles and rootlets (Unit 2), and above this is a salt-marsh peat unit (Unit 1). The area of thickest peat is observed from 0.73 to 0.97 m AHD. In core WAP-100, Unit 1 can be subdivided into a fibrous brown peat unit (0 – 16 cm; Unit 1a), and a very dark brown silty peat (16 – 24 cm; Unit 1b). Unit 2 (24 – 41 cm) is homogenous and contains some roots. Unit 3 can be subdivided into two units: a beige silty coarse sand (41 – 78 cm; Unit 3a) and a fine-medium sandy silt with yellow mottles (78 – 125 cm; Unit 3b; **Table 15**).

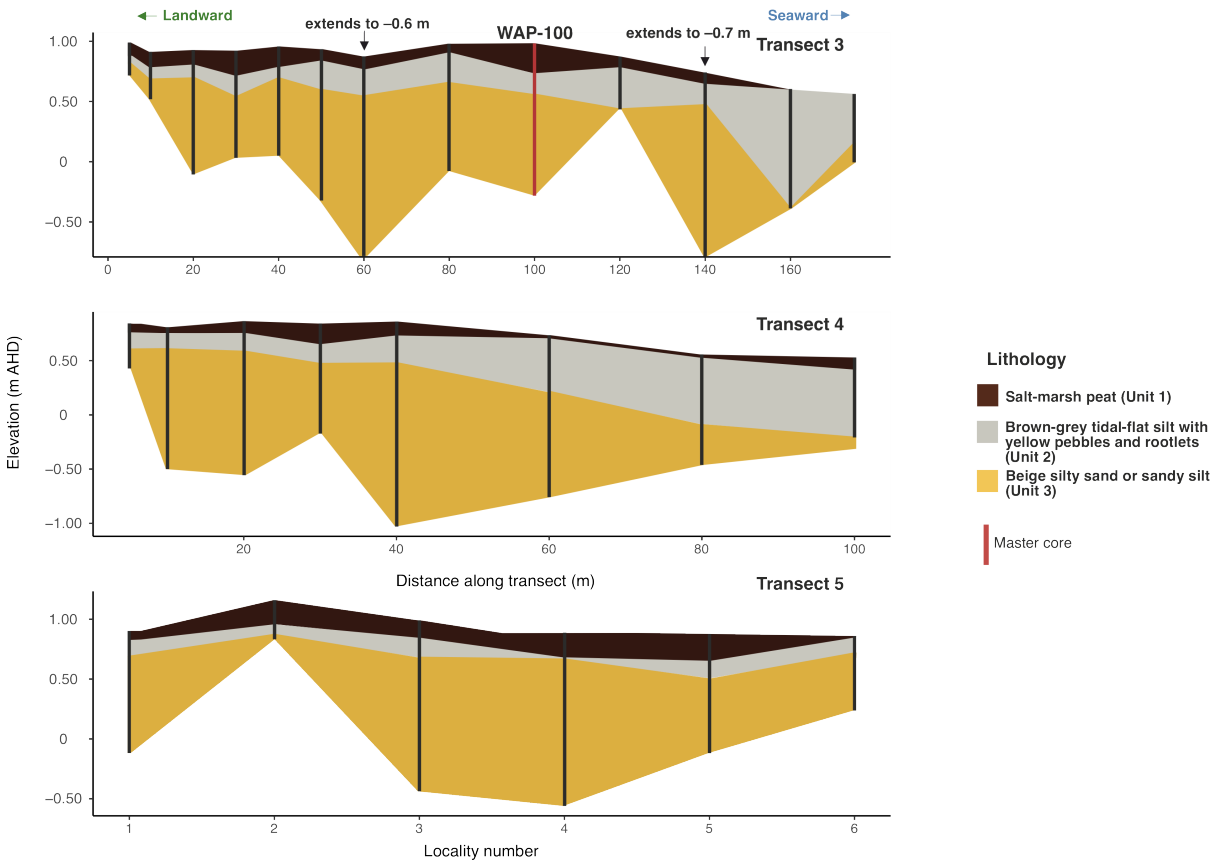

Figure 52. Cross section of coring transects at Wapengo showing variations in stratigraphy across the site. The locality of the master core (WAP-100) is highlighted in red in Transect 3. All transects exhibit a salt-marsh peat unit, underlain by a brown-grey tidal-flat silt with yellow pebbles and rootlets and a silty sand/ sandy silt unit.

Table 15. Description of the main sediment units identified within the master core sequence from WAP-100 and associated Troels-Smith (1955) classification.

Unit	Unit depth (cm)	Description	Troels-Smith log
1a	0 – 16	Fibrous brown peat	Th3 Ag1 + dar 2^+ + strat 0 + sicc 2 + elas 0 + lm -
1b	16 – 24	Very dark brown silty peat	Th2 Ag2 Sh^+ + dar 3 + strat 0 + sicc 2 + elas 0 + lm 2
2	24 – 41	Brown/grey silt with yellow pebbles and rootlets	Ag3 Ga1 Th^+ Gg^+ + dar 1 + strat 0 + sicc 2^- + elas 0 + lm 2
3a	41 – 78	Beige silty coarse sand	Ag1Gs3 Th^+ + dar 1 + strat 0 + sicc 1 + elas 0 + lm 2
3b	78 – 125	Fine-medium sandy silt with yellow mottles	As3Ga1Th^+ + dar 1 + strat 0 + sicc 2 + elas 0 + lm 3

In core WAP-100 total counts of dead foraminifera are consistently high above ~20 cm (**Figure 53**). The lowest counts are generally found in the lower quarter of the core and are especially sparse between in the silt between 29 – 41 cm, exceeding no more than 9 individuals. In total, 22 samples contain less than 50 individuals. The average dead total count for the core is 194 individuals per sample with a range across the core of 0 – 1420. Foraminiferal assemblages consist of *T. salsa*, *H. wilberti*, *E. macrescens*, *P. ipohalina*, *T. irregularis*, *T. inflata*, *S. lobata* and *M. fusca*. However, both *T. irregularis* and *S. lobata* are only found in low abundance (≤11 %). The silty sand unit is largely comprised of *T. inflata, E. macrescens* and *H. wilberti* (averages 69 %, 11 % and 9 % respectively), although total counts are low (average 26 individuals), again suggesting incongruence between the foraminiferal assemblages and the sedimentology. In the core, the silt unit includes primarily *T. inflata* and *M. fusca*; however, again, foraminiferal counts are low (average of 15 individuals). *Trochamminita salsa* and *T. inflata* become dominant

towards the top of the silt unit. The base of the silty peat contains a fairly high proportion of *T. salsa* (average 23 %), although this decreases up the unit and is replaced by high counts of *T. inflata* (average 70 %). Into the fibrous salt-marsh peat, the relative abundance of *M. fusca* and *P. ipohalina* increase and *T. inflata* remained fairly prevalent (averages 33 %, 8 % and 36 % respectively).

Both inorganic and organic carbon content increase upcore (range: 2 – 48 % organic and 0.4 – 8 % inorganic). Organic carbon increases substantially from ~18 cm and inorganic from ~8 cm. The organic carbon content increases are ~2 cm further upcore than the substantial increases in foraminifera. The top 5 cm of the core represents the most organic section of the core. Particle size data indicate that the core is largely composed of silt and sand. Sand is most prevalent in the lower section of the core with silt increasing marginally upcore.

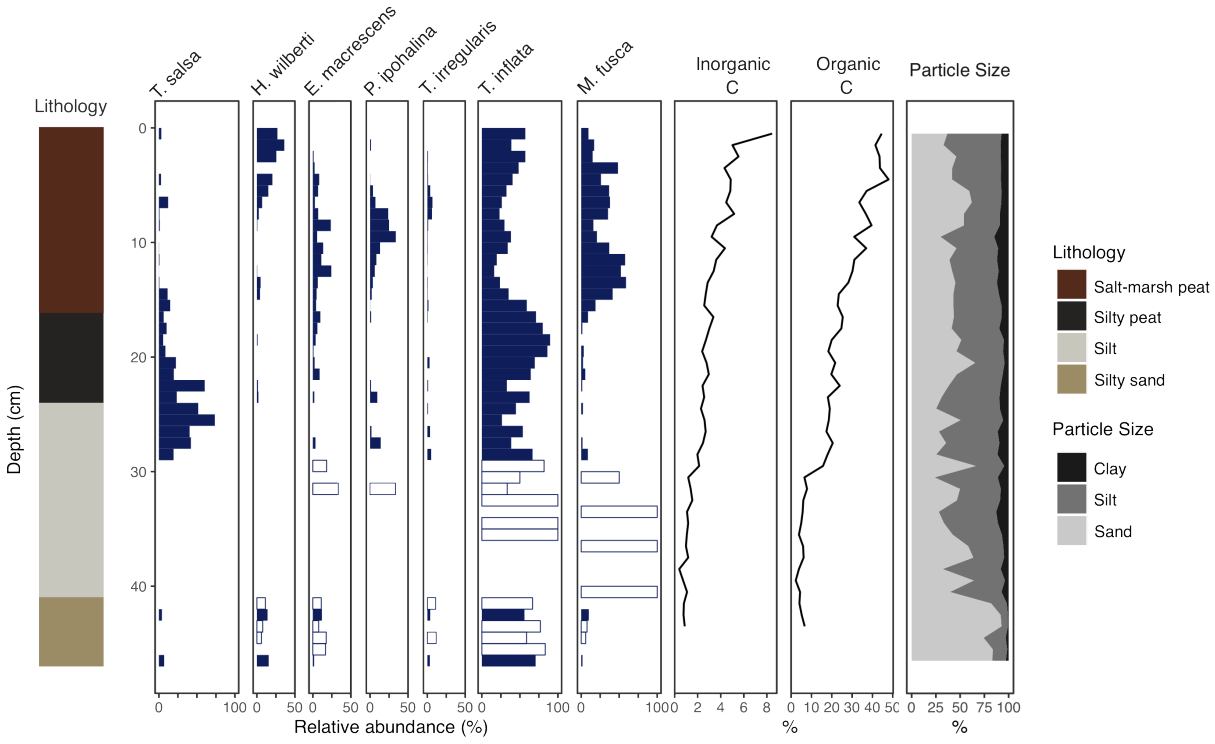

Figure 53. Litho-biostratigraphy of core WAP-100 showing the relative abundance of foraminifera found exceeding 10 % in at least one sample. Unfilled bars represent samples with a total count <50. Core lithology, inorganic and organic carbon percentage change downcore (loss on ignition) and particle size are also shown.

All species noted in the dead assemblages are found infaunally (**Figure 54**). Live foraminifera show that the greatest total numbers of live individuals are found between 2 – 3 cm (11 individuals per cm^3), with the next highest densities found in the uppermost centimetre of the core (9 individuals per cm^3). Live densities are very low in comparison to dead assemblage densities; the average dead density is 159 individuals per cm^3 in the upper 3 cm. After 3 cm, live foraminifera exceed no more than 5 individuals per cm^3. Mirroring death assemblages, *T. inflata* is the most dominant. *Trochammina inflata* is noted as deep as 10 cm.

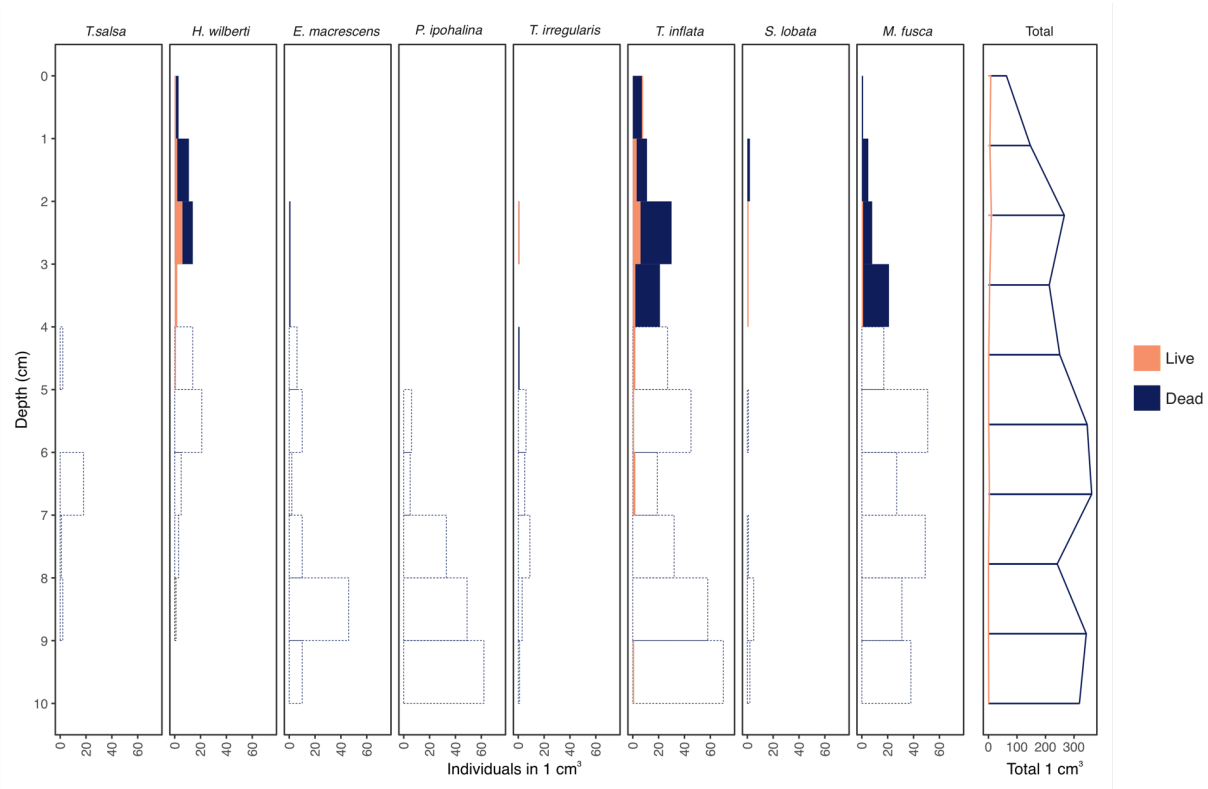

Figure 54. Live and dead foraminiferal densities (1cm³) in core WAP-100 showing species with at least 5 individuals per cm³. Dotted bars denote where the death assemblage density has been estimated as they were not enumerated in the sample.

6.1.2.2 Modern analogue evaluation and palaeomarsh surface elevation reconstruction

Modern analogue results indicate that the regional transfer function provides 13 good analogues and 18 fair analogues, as well as no poor analogues. The local model results in 14 samples with poor analogues, 11 with fair and 6 with good analogues. This is due to the fairly high relative abundance of *T. salsa* in the fossil assemblages, but low abundance of *T. salsa* in the local modern training set. *Trochamminita salsa* was often found in low count samples at Wapengo near the limit of the highest occurrence of foraminifera or highest astronomical tide, and so these samples were not included in the training set after screening by count size (**Chapter 5**; Williams et al. 2021). However, the species was more abundant in the regional training set due to the higher abundance in high total count samples at Lutregala. Williams et

al. (2021) compared the modern species optima between the Wapengo local model and the regional model. As optima were consistent between models, the regional transfer function is employed for the Wapengo reconstruction.

From the sandy silt to the silt, PMSE increases by 0.19 ± 0.11 m, reaching a maximum of 0.98 m. This elevation is associated with high-marsh environments in the modern environment, again potentially suggesting some infaunality or other post-depositional alteration of the assemblages. In line with the foraminifera, PMSE estimates decline from the silty peat to the fibrous peat by 0.13 ± 0.11 m to reach the core-top value of 0.81 m. Overall, PMSEs estimates from the regional transfer function range from 0.64 – 0.98 m AHD, with an average uncertainty of ± 0.08 m ($1\ \sigma$).

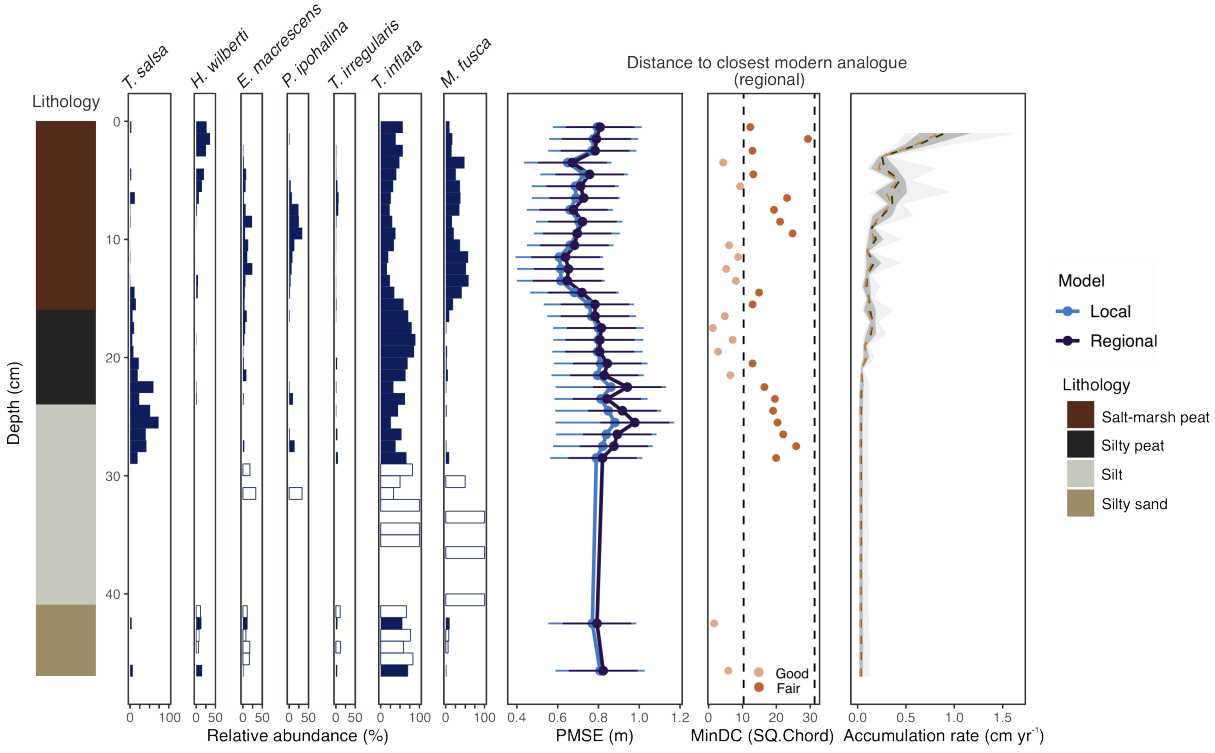

Figure 55. Fossil taxa**,** palaeomarsh surface elevation (PMSE) estimations, modern analogue results and sedimentation rate for core WAP-100 using both the Wapengo local model and regional model. Unfilled bars represent counts <50 individuals where PMSE estimates were not calculated due to low total counts (Kemp, Wright and Cahill, 2020). Both the Wapengo local transfer function PMSE estimates and regional PMSE estimates are shown. Modern analogue results for the regional model are shown with light orange showing samples classed as "good" and dark orange showing samples classed as "fair". Dashed lines show the 5th and 20th percentiles respectively. In the accumulation rate plot, the orange dotted line = median accumulation rate, dark green dotted line = mean accumulation rate, dark grey ribbon = 68 % confidence interval, light grey ribbon = 95 % confidence interval. The accumulation rate has been derived from age-depth modelling (see section 6.1.2.3).

6.1.2.3 Chronology

Sixteen samples were taken for ^{210}Pb analyses. Samples show a decline in unsupported Pb downcore (**Figure 56; Table 16**). Two samples, X127 and X130, did not have detectable unsupported ^{210}Pb and so these samples were removed prior to modelling. A comparison of

the *rplum* model age estimations with the CRS model (**Figure 56**) shows that the *rplum* and CRS ages agree well within the top 8 cm of the core; age estimations are within a year of each other. After 10 cm, the difference between the means of the models increases to ~10 – 30 years. At this point, the *rplum* model predicts younger ages than the CRS model.

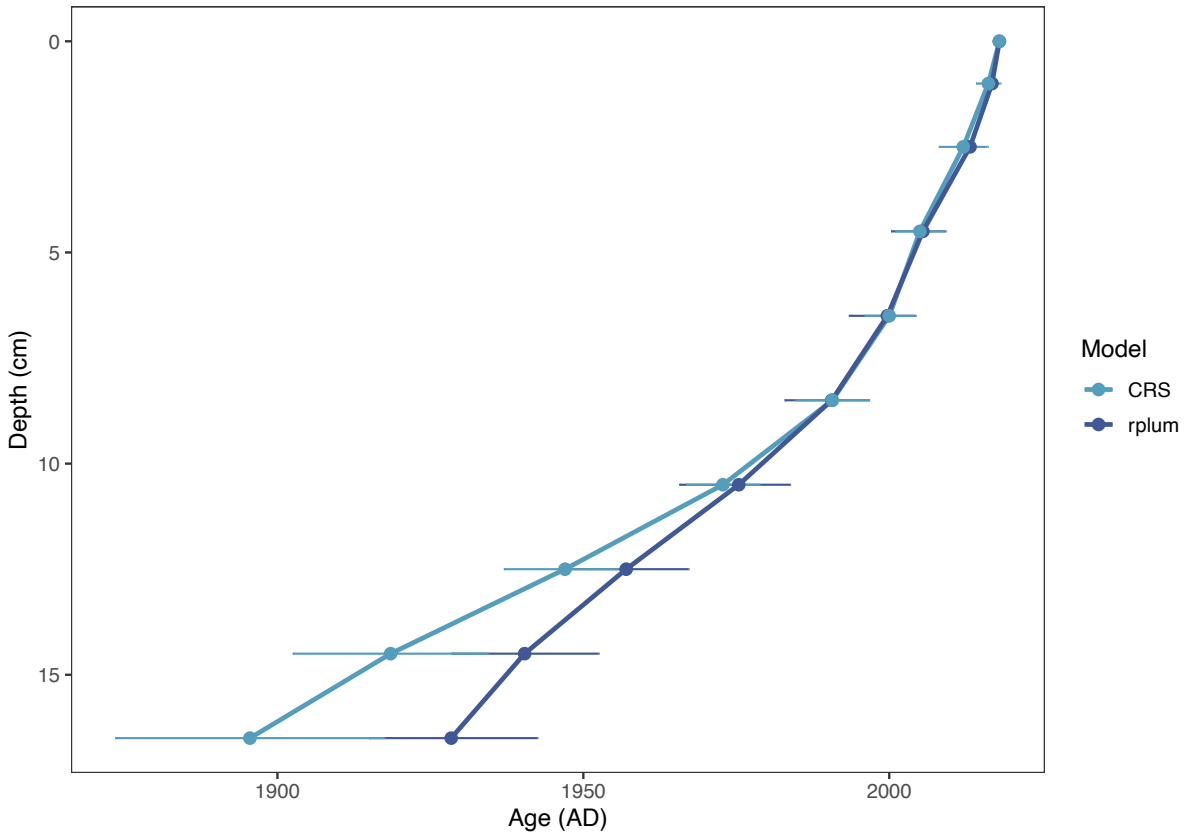

Figure 56. Comparison of the ^{210}Pb age estimates from the Constant Rate of Supply model (CRS) and the Bayesian *rplum* model in core WAP-100.

Table 16. ^{210}Pb results from core WAP-100.

ANSTO ID	Depth (cm)			Dry Bulk Density (g/cm^3)	Cumulative Dry Mass (g/cm^2)			Count Date	Total ^{210}Pb (Bq/kg)			Supported ^{210}Pb (Bq/kg)			Unsupported ^{210}Pb Decay corrected 11-Mar-20 (Bq/kg)		
X123	0	-	2	0.11	0.12	±	0.12	18-Feb-21	167.0	±	6.9	9.5	±	1.0	162.2	±	7.1
W608	2	-	3	0.15	0.31	±	0.06	16-Mar-20	303.1	±	19.1	6.3	±	0.6	297.0	±	19.1
W609	4	-	5	0.10	0.56	±	0.06	16-Mar-20	203.1	±	10.5	7.9	±	0.7	195.3	±	10.6
W610	6	-	7	0.11	0.77	±	0.06	16-Mar-20	177.5	±	9.7	5.6	±	0.6	172.0	±	9.7
W611	8	-	9	0.20	1.08	±	0.06	16-Mar-20	188.0	±	9.8	9.7	±	0.9	178.3	±	9.8
W612	10	-	11	0.22	1.50	±	0.07	16-Mar-20	161.6	±	7.6	6.8	±	0.6	154.8	±	7.6
W613	12	-	13	0.16	1.88	±	0.08	16-Mar-20	127.2	±	6.3	7.8	±	0.7	119.5	±	6.4
W614	14	-	15	0.21	2.25	±	0.08	16-Mar-20	43.2	±	2.3	12.1	±	1.1	31.1	±	2.5
X124	16	-	17	0.20	2.66	±	0.08	18-Feb-21	24.0	±	1.2	10.9	±	1.1	13.5	±	1.6
X125	18	-	19	0.42	3.28	±	0.09	18-Feb-21	17.8	±	0.8	11.4	±	1.0	6.6	±	1.3
X126	20	-	21	0.42	4.12	±	0.10	18-Feb-21	15.6	±	0.7	11.0	±	0.9	4.7	±	1.2
X127	22	-	23	0.52	5.06	±	0.11	18-Feb-21	14.5	±	0.7	16.5	±	1.5		not detected	
X128	24	-	25	0.63	6.20	±	0.13	18-Feb-21	15.4	±	0.8	12.9	±	1.1	2.5	±	1.4

X129	26	-	27	0.50	7.33	±	0.14	18-Feb-21	19.1	±	0.9	13.3	±	1.2	6.0	±	1.5
X130	28	-	29	0.45	8.28	±	0.15	18-Feb-21	14.0	±	0.7	15.3	±	1.4		not detected	
X131	30	-	31	0.70	9.42	±	0.15	18-Feb-21	16.0	±	0.8	11.3	±	1.0	4.8	±	1.3

$^{206}Pb/^{207}Pb$ data (**Appendix VII**) show the onset of Pb pollution from 17.5 cm from mining of the Broken Hill ore (~1895) and samples rapidly become less radiogenic. A pollution maximum is reached at 7.5 cm (~1974) after which samples reverse back to more radiogenic values **Figure 57**). Exotic pollen indicative of European settlement appears and increases after 21.5 cm alongside increases in *Sporormiella* (dung fungus) which is associated with European settlement (*i.e.* pastoralisation of the land) from this depth (**Figure 58**). The pollen record also shows increases in pine *(Pinus)* pollen from around the same depth as the Pb maximum. As documented in **Chapter 3,** pine plantations across southern NSW over the late 1960s and early 1970s, with a peak in 1985 (Keith and Bedward, 1999). Due to the lag time of pine trees to produce pollen, this may suggest the pollution maximum date (*i.e.* 1974±10) may be towards the younger age range (*i.e.* 1980 and beyond). In total, three chronohorizons are identified in WAP-100 (**Table 17**).

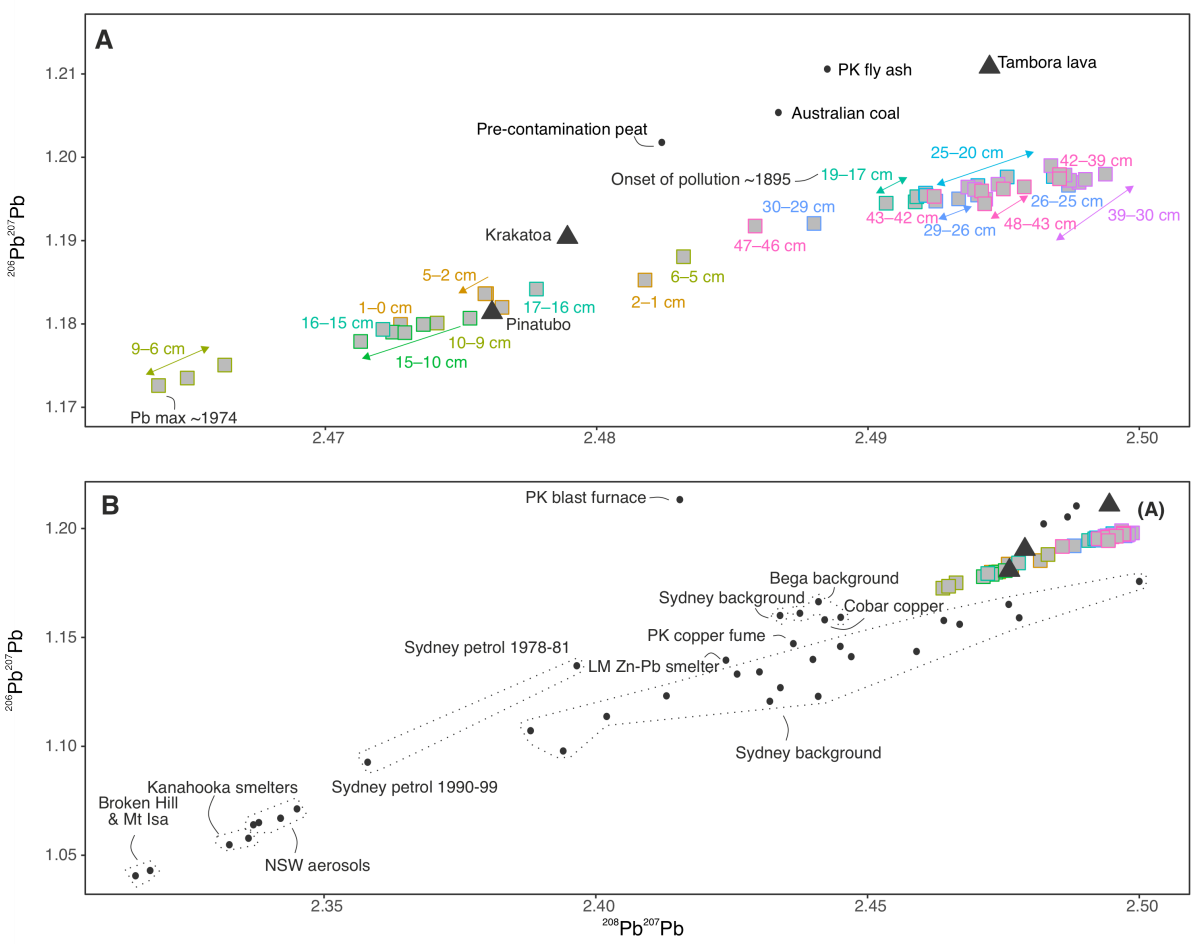

Figure 57. A. Source plot for samples from core WAP-100 (coloured markers) as well as volcanic, pollution and background isotopic signatures (black markers). **B.** A zoom out of plot A showing also the isotopic signatures of the New South Wales aerosols and Sydney petrol, New South Wales smelters and the Broken Hill and Mt Isa ores (black markers). Data available in **Appendix IX.** PK= Port Kembla, LM= Lake Macquarie.

Table 17. Calendar dates obtained from core WAP-100.

Chronostratigraphic Marker	Depth (cm)	Calendar Year (AD)	Date given in model (AD)	Reference
Pb pollution maximum and introduction of pine plantations near Eden and Bermagui	7.5	1964 – 1984	1974 ± 4	Australian Bureau of Agricultural and Resource Economics (2000); Keith and Bedward (1999); Kristensen (2015)
Broken Hill smelting	17.5	1890 – 1900	1895 ± 5	Van de Velde et al. (2005)
European settlement (exotic pollen introduction, peaks in charcoal and increase in *Sporormiella*)	21.5	1830 – 1840	1835 ± 5	Lunney and Leary (1988)

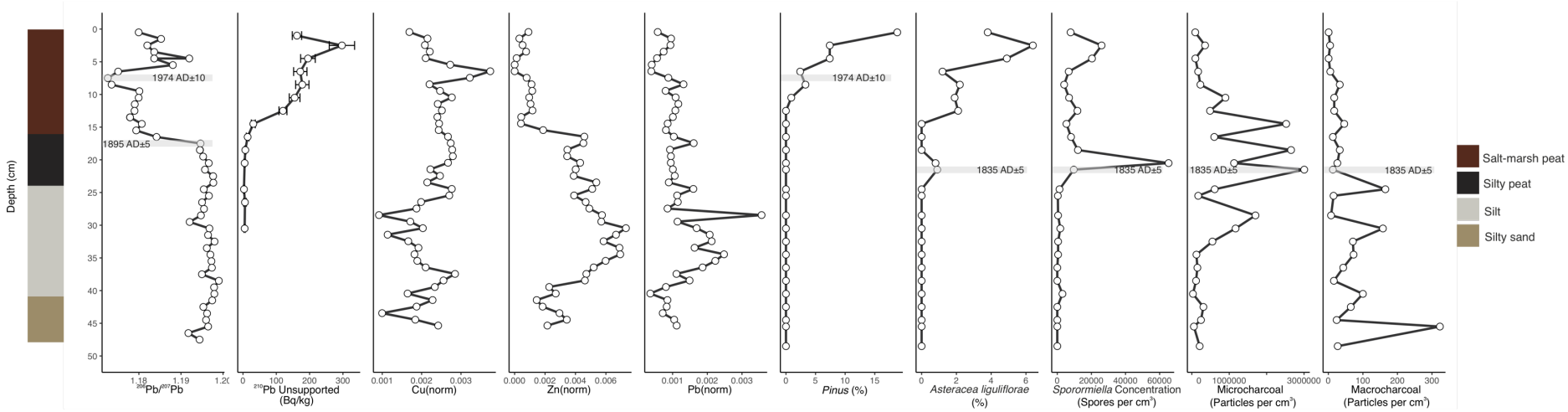

Figure 58. Stable lead (^{206}Pb/^{207}Pb), ^{210}Pb, pollen and charcoal data for core WAP-100. Identified chronohorizons are highlighted by the grey boxes.

In total, eight AMS ^{14}C samples were obtained from ANSTO, SUERC and UCI (**Table 18**). However, a visual inspection based on stratigraphic ordering, and taking into account chronohorizons from the stable lead and pollen data, suggests that samples UCIAMS-236617, UCIAMS-236618 and UCIAMS-236619 have calibrated ages that are too young for their stratigraphic position and sample OZZ403 is too old for its stratigraphic position. Sample OZZ403 was a bulk sediment sample which may have contained older material and could have resulted in an older date and the younger dates may have been contaminated by root penetration. As clear outliers, these dates were removed from the age-depth model.

Table 18. ^{14}C results from core WAP-100 calibrated using SHCal20 (Hogg et al. 2020) and Bomb13 SH1 – 2 (Hua, Barbetti and Rakowski, 2013). Dates removed prior to age-depth modelling are highlighted by an asterisk. Depths given in the table represent the mid points of the samples.

Publication Code	Material	Depth (cm)	Percent modern ^{14}C (pMC) and error (1 σ)	Calibrated radiocarbon age 2 σ (AD)	$\delta^{13}C$-VPDB‰
UCIAMS-236612	Plant macrofossil	3.5	108.10 ± 0.19	1958 – 2005	n.d
UCIAMS-236615	Plant macrofossil	7.5	119.87 ± 0.21	1960 – 1987	n.d
UCIAMS-236616	Plant macrofossil	12.5	126.71 ± 0.23	1962 – 1982	n.d
UCIAMS-236617 *	Plant macrofossil	17.5	110.91 ± 0.19	1958 – 1998	n.d
OZZ403 *	Bulk sediment	20	95.93 ± 0.28	1504 – 1649	-26.5 +/- 0.1
UCIAMS-236618 *	Plant macrofossil	24.5	108.40 ± 0.19	1958 – 2004	n.d
UCIAMS-236619 *	Plant macrofossil	32.5	104.03 ± 0.18	1956 – 1957	n.d
SUERC-93777	Bulk sediment	46.5	84.05 ± 0.39	638 – 772	-25.9

The resulting ^{14}C, ^{210}Pb and calendar ages were combined in the age-depth model to produce age estimates and uncertainties downcore (**Figure 59**). Accumulation rate was established using that suggested by *rplum* from initial data analysis. Model memory was kept at the default of 0.5. The model was ran with a setting of ra.case=1. Thickness was kept at the default of 1 to allow flexibility in the model. A minimum core age of 2018 was set, and this was also given as the sampling date.

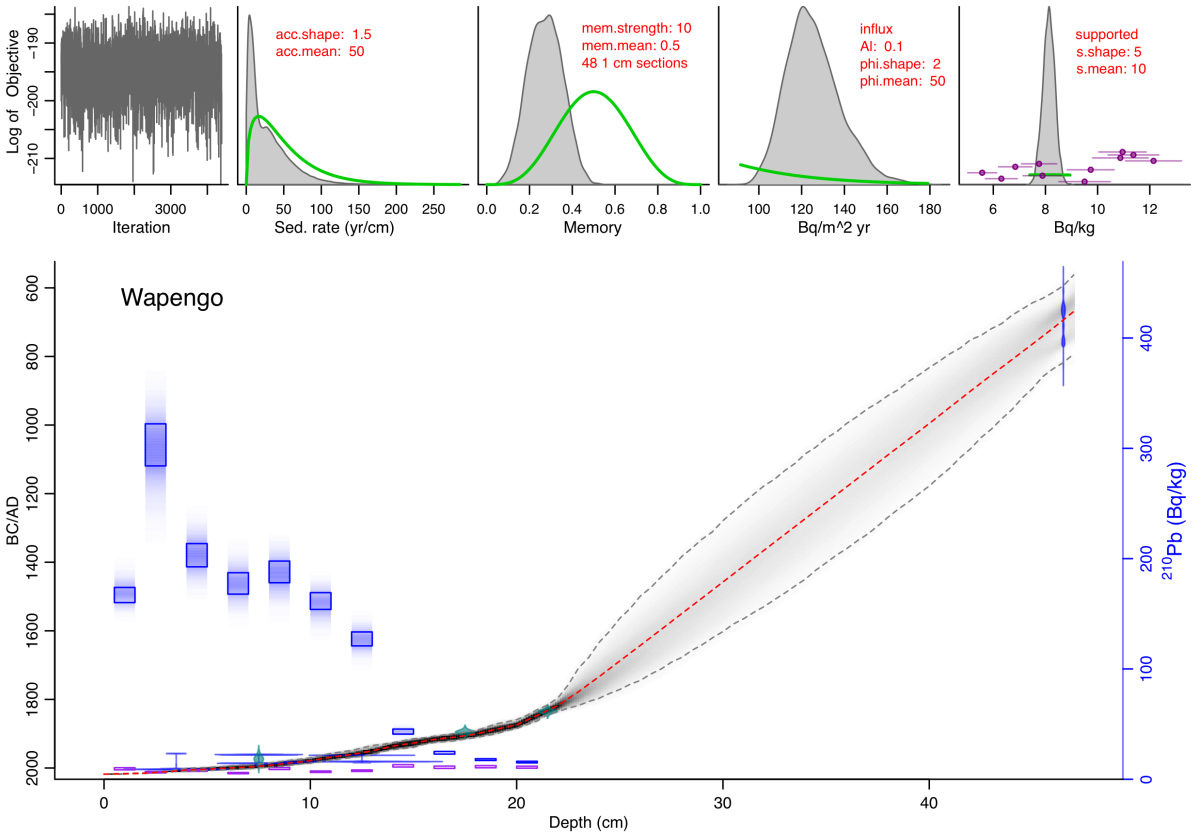

Figure 59. Upper panels: Prior (light green) and posterior distributions (light grey) as well as Markov Chain Monte Carlo iterations (dark grey). **Lower panel:** Age-depth model for core WAP-100. Blue dotted squares show measured ^{210}Pb and columns show modelled ^{210}Pb. Purple squares show supported ^{210}Pb. Calendar dates (teal) and calibrated radiocarbon dates (dark blue) are also shown. Mean ages are denoted by the dotted red line and 95 % confidence interval (*i.e.* age range) is denoted by the grey dotted lines.

MCMC iterations indicate that that the model run was successful, with no visible structure seen. The sedimentation rate varies from ~50 yr cm^{-1} – <10 yr cm^{-1} with significant increases from ~22 cm. Accumulation rate in the sand and silt units is ~0.02 cm yr^{-1}; this increases to ~0.18 cm yr^{-1} in the salt-marsh peat. Model uncertainty is well constrained between ~1800 – 2018, but error increases after this period until it is constrained by the final basal date.

A comparison of prior (calibrated ^{14}C dates) and posterior age probability distribution functions shows that the posterior post-bomb ages are better constrained than the prior ^{14}C dates. The post-bomb dates are estimated to be younger than their prior calibrated ages; however, dates between 10 – 20 cm are predicted to be older than their prior ages (**Figure 60**). Interrogations of the probability function distributions shows that dates largely follow a Gaussian distribution aside from depths 45.5 and 46.5 cm which are close to the depth of a ^{14}C date and therefore have bi-modal distributions (**Figure 61**). As most probability distribution functions fit a near-Gaussian shape, a Gaussian-process model was deemed suitable for the sea-level reconstruction.

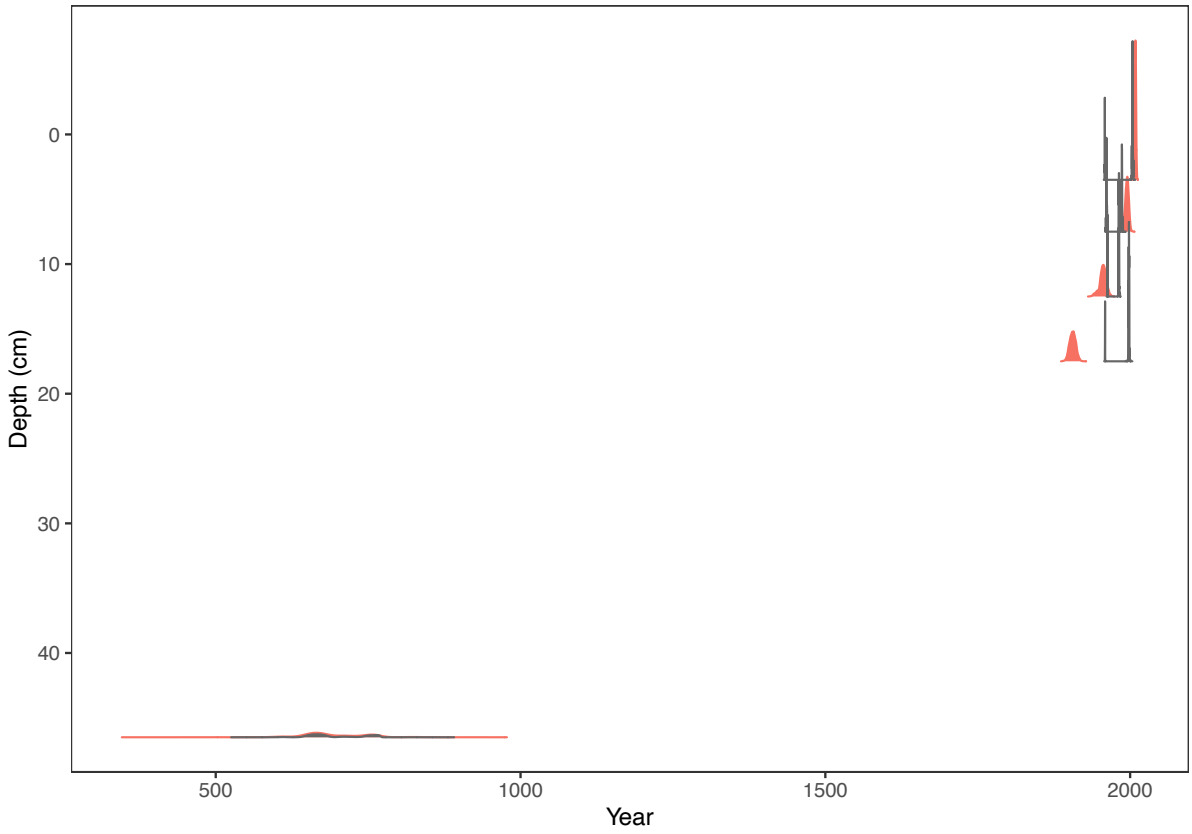

Figure 60. Probability distribution functions (PDFs) of prior ^{14}C dates (grey) and posterior *rplum* distributions (orange).

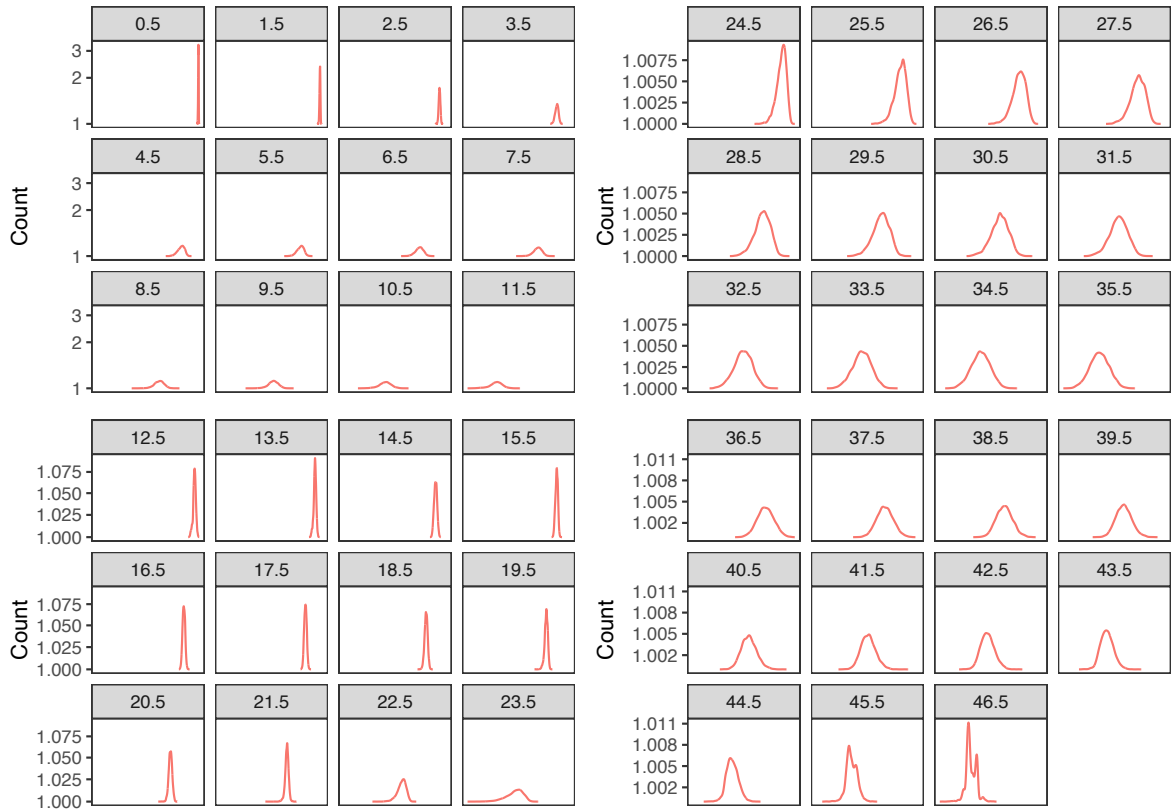

Figure 61. Probability distribution functions (PDFs) from the Wapengo age-depth model. Numbers in the grey box indicate the depth that the PDF has been extracted from in centimetres.

6.1.2.4 Sea-level reconstruction

Due to a lack of chronological constraint below 21.5 cm as well as incongruent foraminifera in the silt units, only data from 21.5 cm upcore (*i.e.* from the silty peat) are included the Gaussian process model. The reconstruction was GIA-corrected at a rate of -0.14 (-0.52 – 0.28) mm yr^{-1} (Caron et al. 2018). GIA-corrected sea-level (GCSL) was ~0.25 m below present in the 19th century (**Figure 62**). The rate of sea-level rise was gradual over the century at 0.9 (- 2.2 – 3.5; 95 % CI) mm yr^{-1} (1833 – 1899), it then increased significantly over the 20th century to 4.0 (1.2 – 7.1) mm yr^{-1}. Change-point analysis detects a change point in RSL in 1892 (1836 – 1935; 95 % credible interval), likely detecting the onset of the acceleration. Varying the GIA rate to assess the timing of Ea0 shows good agreement with the change point estimation,

suggesting an emergence sometime between ~1832 – 1908. Timings of Ea0 remain largely similar between all three corrections, especially between the mid and minimum GIA rates. The median values of the mid, maximum and minimum GIA rates indicate a lag of ~15 years in the Ea0 of the maximum GIA correction behind the mid and minimum rates, however, the upper and lower 95 % CIs remain largely consistent between all three. Maximum rates of sea-level rise were reached in 1931, with rates of up to 5.4 (2.1 – 8.9) mm yr^{-1}. Over the second half of the 20th century (1950 – 1999), the rate of sea-level rise decreased to 0.9 (- 2.1 – 2.8) mm yr^{-1}. A second change point is detected in 1957 which may reflect the decrease in the rate of sea-level rise over this period.

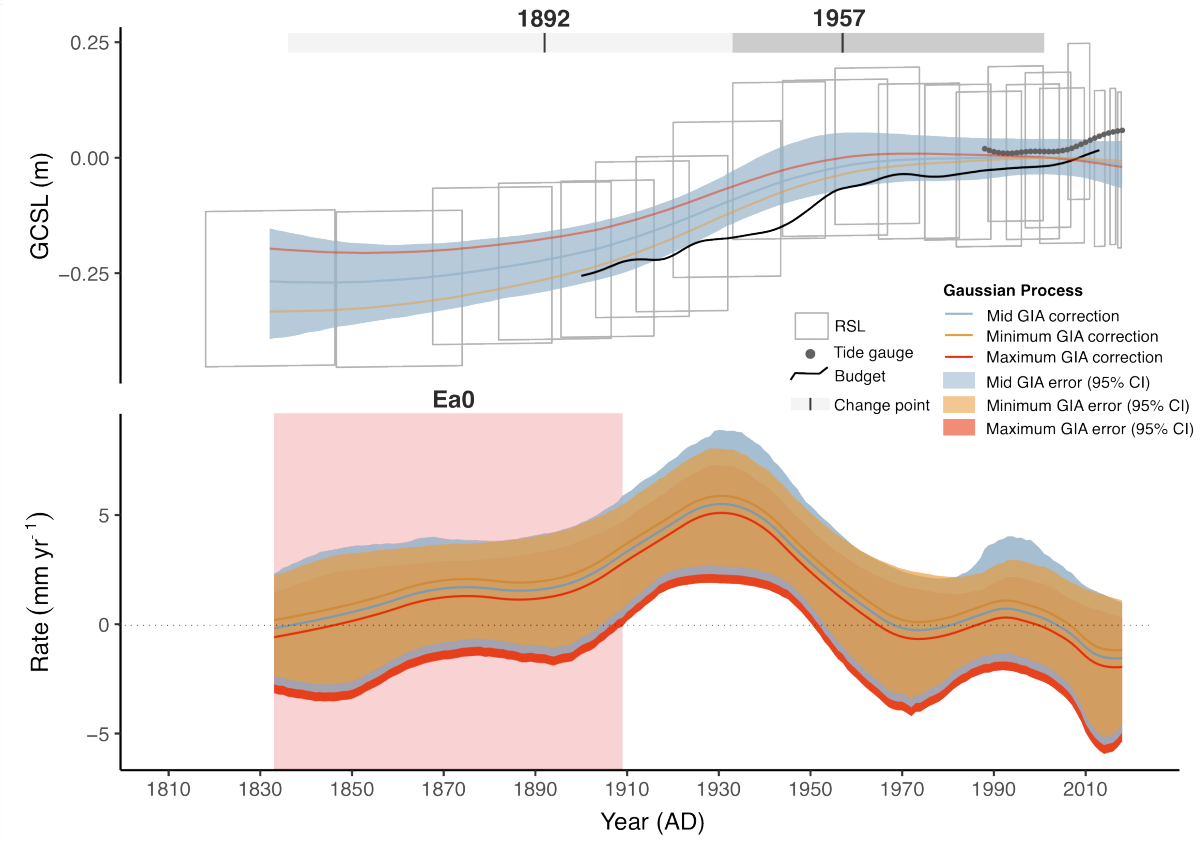

Figure 62. Upper panel. GIA-corrected sea-level (GCSL) reconstruction for Wapengo salt marsh. Grey parallelograms show proxy sea-level estimates (*i.e.* sea-level index points) from core WAP-100 with 2 σ vertical and age uncertainties. A GIA-corrected Gaussian process regression has been fitted to the index points showing the median (blue line) and 95 % confidence intervals (blue shading) of the mid-range GIA correction. Also shown are the median gaussian process regression curves after detrending using the minimum (yellow line) and maximum (red line) GIA corrections. The filled grey boxes denote identified change points from the change-point model (Caesar et al. 2021) showing 95 % credible intervals and mean change point (black lines). Also shown are local tide-gauge data and sea-level budget data (barystatic gravity, rotation and deformation, sterodynamic and inverse barometer effect components – both have been 15-yr smoothed). **Lower panel.** The rate of sea-level change calculated from the Gaussian process regression showing the median (blue line) and 95 % confidence intervals (blue shading) of the mid-range GIA correction. Also shown are the rates after detrending using the minimum (yellow line and shading) and maximum (red line and shading) GIA corrections. The timing of emergence above 0 (Ea0) of the acceleration in sea level is denoted by the red box.

6.1.3 Tarra

6.1.3.1 Stratigraphy and foraminiferal assemblages

At Tarra four coring transects were established. The deepest core extends to - 0.41 m AHD and is characterised by a yellow mottled grey silt with rootlets (Unit 3). Unit 3 is overlain by a brown-grey tidal-flat silt with fine red sand (Unit 2). The marsh is topped with salt-marsh peat. The area of thickest peat is found from 0.91 m to 1.08 m AHD. A master core was taken at 40 m along Transect 6 (TAR-40; **Figure 63**). Unit 1 can be sub-divided into two units: a fibrous brown peat unit (0 – 10 cm; Unit 1a), and a very dark brown silty peat (10 – 17 cm; Unit 1b). Unit 2 (17 – 29 cm) is comprised of a brown-grey tidal-flat silt with small proportions of fine red sand, and Unit 3 (29 – 74 cm) is comprised of a grey silt with yellow mottles and rootlets (**Table 19**).

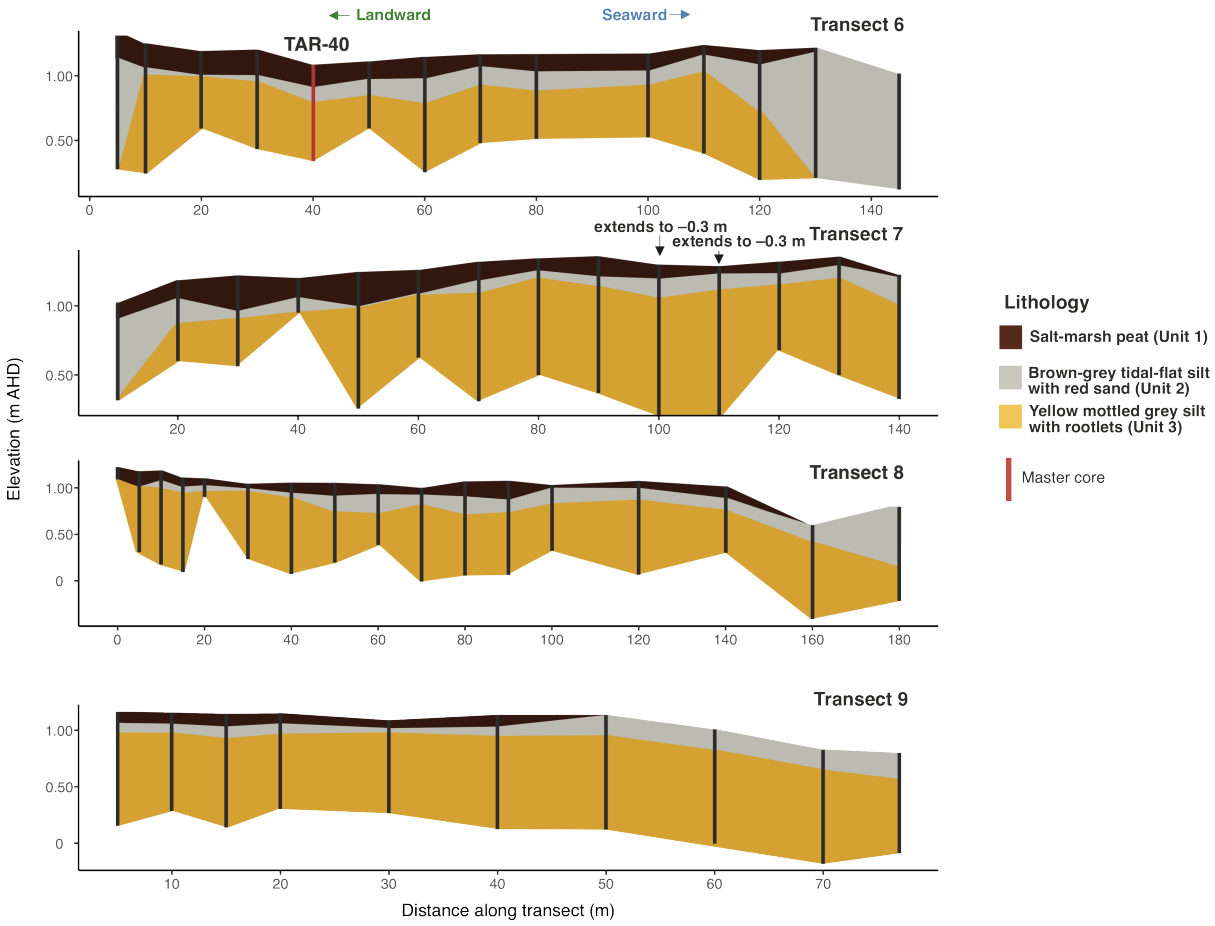

Figure 63. Cross section of coring transects at Tarra showing variations in stratigraphy across the site. The locality of the master core (TAR-40) is highlighted in red in Transect 6. All transects exhibit a salt-marsh peat unit, underlain by a brown-grey tidal-flat silt with red sand and a yellow mottled grey silt with rootlets.

Table 19. Description of the main sediment units identified within the master core sequence from TAR-40 and associated Troels-Smith (1955) classification.

Unit	Unit depth (cm)	Description	Troels-Smith log
1a	0 – 10	Fibrous brown peat	Th3 Ag1 + dar 2^{+} + strat 0 + sicc 2 + elas 0 + lm -
1b	10 – 17	Red brown silty peat with roots	Th2 Ag2 + dar 2 + strat 0 + sicc 2 + elas 0 + lm 2
2	17 – 29	Brown/grey silt with red sand	As3 Ga1 Th^{+} + dar 1 + strat 0 + sicc 2^{-} + elas 0 + lm 2
3	29 – 74	Yellow mottled grey silt with roots	As3 Th1 + dar 1 + strat 0 + sicc 3 + elas 0 + lm 2

In core TAR-40, total counts of dead foraminifera increase from ~26 cm (**Figure 64**). Below 26 cm, total counts of individuals are ≤17 individuals and foraminifera are especially sparse below 29 cm, exceeding no more than 8 individuals per sample. Throughout the whole core, total counts of dead foraminifera range from 0 – 611, with an average of 150 individuals. Foraminiferal assemblages consist of *T. salsa*, *H. wilberti*, *E. macrescens*, *P. ipohalina*, *T. irregularis*, *T. inflata*, *S. lobata* and *M. fusca*. *Trochammina inflata* is prevalent in the core, representing at least ¼ of the sample in the majority of samples. The yellow mottled silt unit of the core contains very sparse foraminifera (average total count is two specimens). The brown-grey silt unit of the core largely contains *T. salsa*, *T. inflata* and *M. fusca* (average relative abundances 19 %, 51 % and 15 % respectively). Total counts of foraminifera in the unit are higher (average 163 individuals per sample). In the silty peat, *T. salsa* and *M. fusca* decrease and the relative abundance of typical mid marsh species *T. inflata* and *E. macrescens* increases, with *T. inflata* becoming especially dominant, reflecting modern assemblages (average relative abundance 68 %). Into the fibrous organic salt-marsh peat, assemblages remain largely similar to the silty peat, although there is an increase in the relative abundance of *E. macrescens* (average relative abundance 25 %).

Inorganic and organic carbon content increases upcore (range: 4 – 47 % organic and 2 – 11 % inorganic). Organic carbon increases substantially from ~16 cm and inorganic from ~13 cm. The top 4 cm of the core represents the most organic section of the core. Particle size data showed the core matrix is largely uniform in sorting, consisting mainly of silt and sand. However, there is also clay throughout the core (reaching 32 % at its maximum).

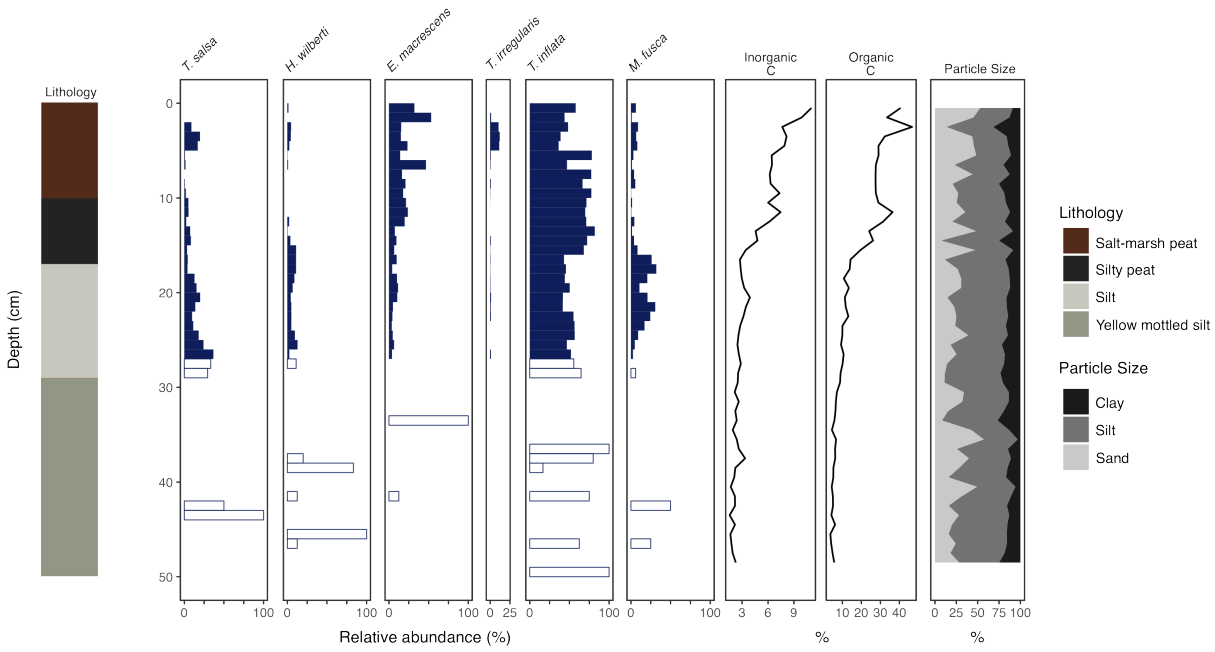

Figure 64. Litho-biostratigraphy of core TAR-40 showing the relative abundance of foraminifera found within the core exceeding 10 % in at least one sample. Unfilled bars represent samples with a total count <50. Core lithology, inorganic and organic carbon percentage change downcore (loss on ignition) and particle size are also shown.

Infaunal species found in TAR-40 include *H. wilberti*, *E. macrescens*, *P. ipohalina*, *T. irregularis*, *T. inflata*, *M. fusca* and *Ammobaculites* sp. (**Figure 65**). Total counts of live foraminifera are highest in the uppermost centimetre (28 individuals per cm^3) and generally decline downcore, however this does fluctuate, with higher densities of live foraminifera noted between 4 – 6 cm, mirroring dead totals. In the lowest sample, there are 4 live foraminifera per cm^3 compared to an estimated 83 dead foraminifera per cm^3. Similar to the dead assemblage, *T. inflata* dominate the live counts, followed by *E. macrescens*.

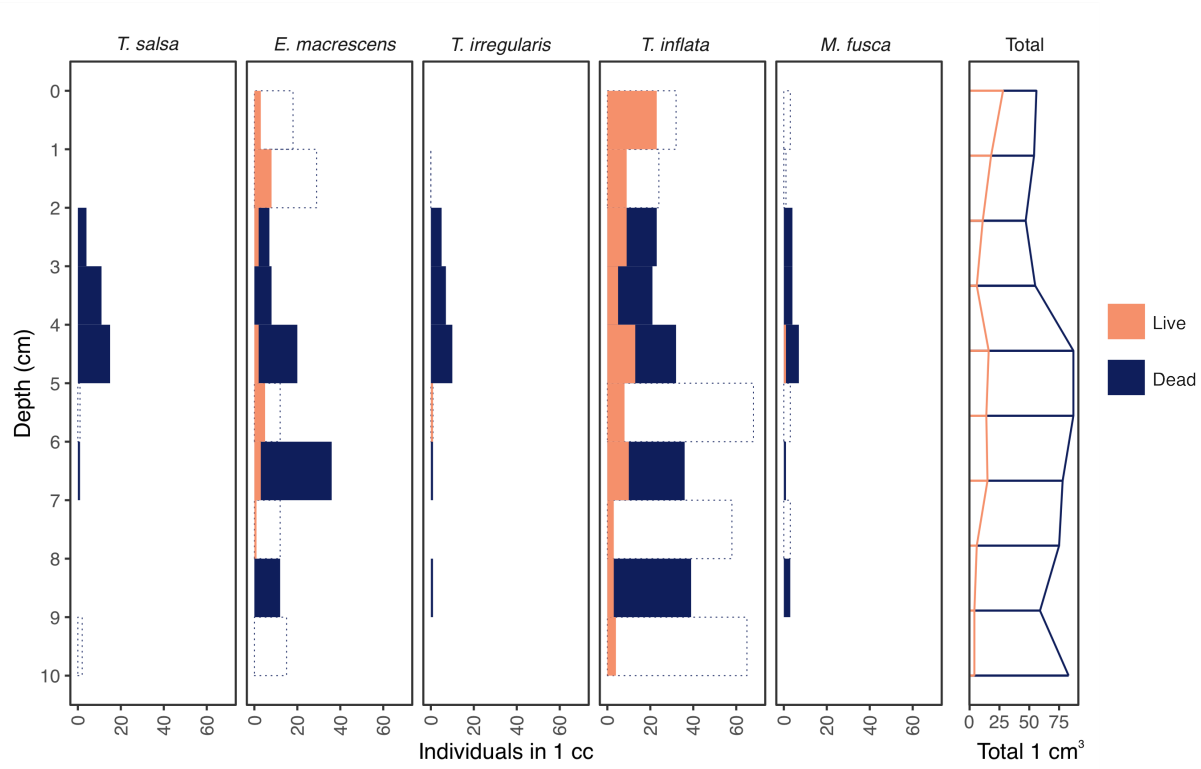

Figure 65. Live and dead foraminiferal densities (1cm^3) in core TAR-40 showing species with at least 5 individuals per cm^3. Dotted bars denote where the death assemblage density has been estimated as they were not enumerated in the sample.

6.1.3.2 Modern analogue evaluation and palaeomarsh surface elevation reconstruction

For Tarra a local transfer function was created; however, as documented in **Appendix I**, the resulting transfer function performed very poorly in terms of the relationship between observed and predicted elevations. Comparison of the species optima shows the regional model is appropriate for the Tarra reconstruction (**Appendix I**); therefore, there are several options: 1. use the existing regional II training set for the Tarra reconstruction, 2. include the Tarra samples in a regional training set with existing samples, or 3: follow, for example, Long et al. (2014) and assign conservative semi-quantitative indicative ranges based on stratigraphy and common species. When samples are incorporated into the existing southeastern Australia regional transfer function (Williams et al. 2021), the model r^2_{boot} reduces from 0.69 to 0.54 as

many of the samples, like in the local transfer function, are predicted at the same elevation. Furthermore, the Tarra surface samples do not provide a wider range of analogues than the existing regional training set, therefore there is little reason to include them. The present day salt marsh extends between 1.35 and 1.01 m AHD, which yields an indicative range of 1.18 ± 0.17 m. Narrower vertical ranges cannot be assigned, as foraminifera found at the upper and lower elevation limits in the modern environment at Tarra are present in the core. Using the regional II training set to estimate PMSE results in ranges of 1.12 ± 0.12 to 1.33 ± 0.12 m AHD, with an average of 1.20 ± 0.12 m AHD. Therefore, both approaches result in very similar outputs. Finally, the poorly performing local transfer function PMSE estimates were compared with the regional PMSE estimates; data show that estimates are predicted within error between both models, further suggesting that the regional model is appropriate. The regional II training set is employed for the reconstruction due to the varying relative abundances of *M. fusca*, *T. salsa* and *E. macrescens* in the core which can be accurately modelled by the regional II training set, as well as the lower vertical uncertainty.

Modern analogue results show that the regional training set provides good analogues for 14 samples from the Tarra core and fair analogues for 13 samples (**Figure 66**). The majority of good analogues are found towards the top of the core where *E. macrescens* and *T. inflata* (common species in the modern training set) increase in abundance. No samples are classified as having a poor analogue, suggesting that the regional training set is fairly representative of fossil material in the Tarra core.

PMSE estimates were not calculated for the yellow mottled silt unit of the core due to the low total counts. In the brown-grey silt PMSE estimates decline by 0.22 ± 0.18 m from 1.33 m AHD, suggesting a decrease in the marsh surface. In the peat units, PMSE estimates remained largely uniform, suggesting the marsh kept pace with sea-level rise, with a small decline at the top of the core, reaching a core-top value of 1.16 m. In total, PMSE estimates range from 1.12 to 1.33 m with an average uncertainty of ± 0.12 m (1 σ).

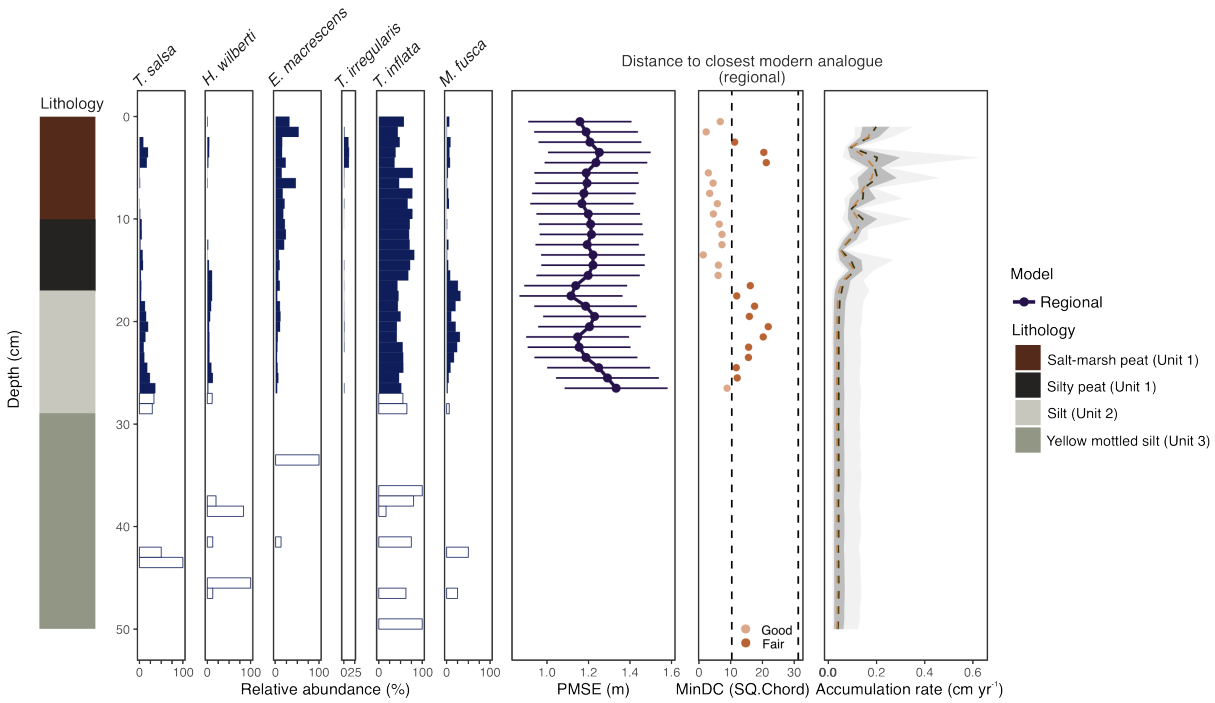

Figure 66. Fossil foraminifera, palaeomarsh surface elevation (PMSE) estimations, modern analogue results and sedimentation rate for core TAR-40. Unfilled bars represent counts <50 individuals where PMSE estimates were not calculated due to low total counts of individuals (Kemp, Wright and Cahill, 2020). PMSE estimates from the regional model are shown. Modern analogue results for the regional model are shown with light orange showing samples classed as "good" and dark orange showing samples classed as "fair". Dashed lines show 5th and 20th percentile boundaries. In the accumulation rate plot, the orange dotted line = median accumulation rate, dark green dotted line = mean accumulation rate, dark grey ribbon = 68 % confidence interval, light grey ribbon = 95 % confidence interval. The accumulation rate has been derived from age-depth modelling (see section 6.1.3.3).

6.1.3.3 Chronology

In total eight ^{210}Pb samples were obtained from TAR-40. ^{210}Pb samples show a decline in unsupported Pb downcore, reaching near background levels at 14 – 15 cm (**Table 20**). A comparison between the *rplum* and CRS model (**Figure 67**) show that the *rplum* model estimates younger ages than the CRS model. Both *rplum* and CRS uncertainties are small

towards the top of the core but increase downcore. Means are closer towards the surface (~3 years difference between the *rplum* and CRS model at 1 cm) and diverge downcore (to a maximum of ~16 years difference in the lowest sample).

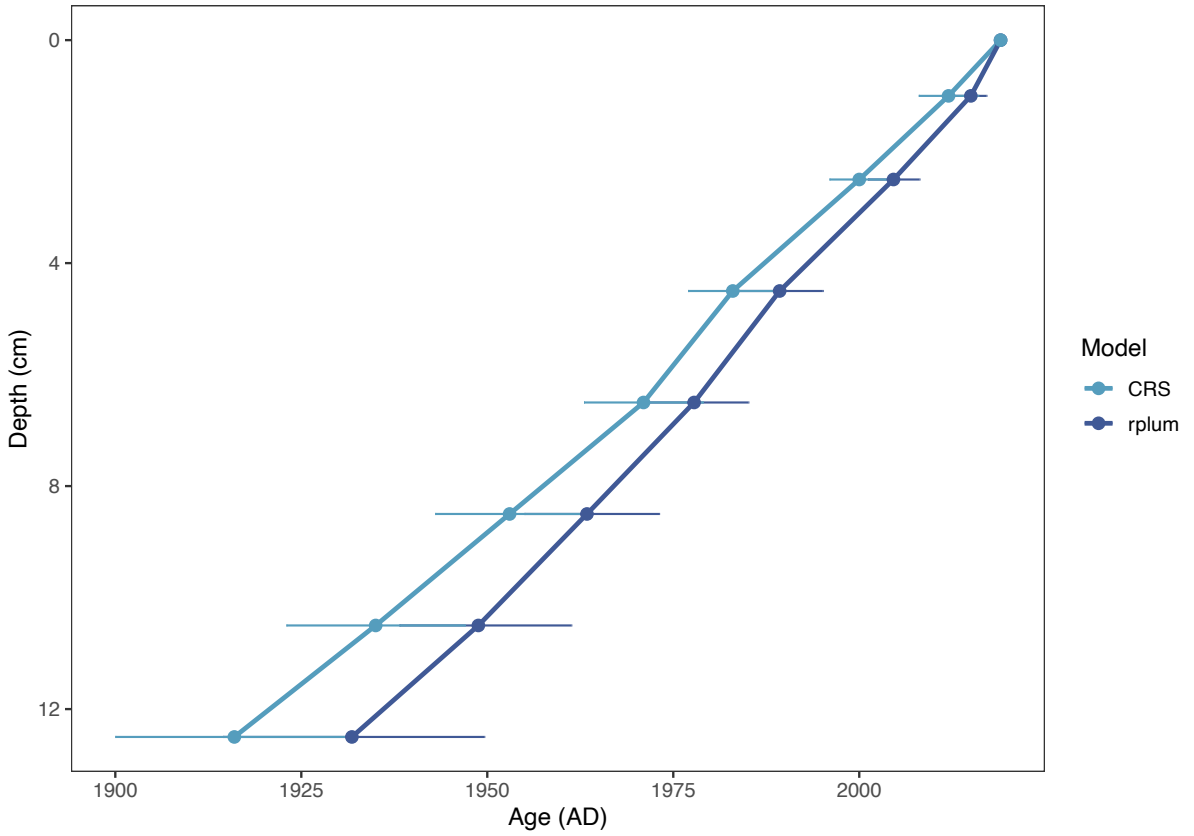

Figure 67. Comparison of the ^{210}Pb age estimates from the Constant Rate of Supply model (CRS) and the Bayesian *rplum* model in core TAR-40.

Table 20. ^{210}Pb results from core TAR-40.

ANSTO ID	Depth (cm)			Dry Bulk Density (g/cm^3)	Cumulative Dry Mass (g/cm^2)			Count Date	Total ^{210}Pb (Bq/kg)			Supported ^{210}Pb (Bq/kg)			Uncorrected ^{210}Pb (Bq/kg)			Unsupported ^{210}Pb Decay corrected 11-Mar-20 (Bq/kg)		
X132	0	–	2	0.30	0.30	±	0.30	18-Feb-21	201.32	±	7.96	4.27	±	0.46	197.05	±	7.97	202.92	±	8.21
W615	2	–	3	0.25	0.71	±	0.14	16-Mar-20	320.07	±	15.83	3.46	±	0.36	316.61	±	15.83	316.74	±	15.84
W616	4	–	5	0.26	1.22	±	0.14	16-Mar-20	94.69	±	5.04	5.01	±	0.47	89.68	±	5.06	89.72	±	5.07
W617	6	–	7	0.28	1.76	±	0.14	16-Mar-20	81.36	±	4.26	10.63	±	0.96	70.74	±	4.37	70.77	±	4.37
W618	8	–	9	0.36	2.40	±	0.14	16-Mar-20	58.80	±	2.94	6.50	±	0.57	52.30	±	3.00	52.32	±	3.00
W619	10	–	11	0.28	3.04	±	0.14	16-Mar-20	37.24	±	1.95	14.49	±	1.31	22.75	±	2.35	22.76	±	2.35
W620	12	–	13	0.37	3.69	±	0.15	16-Mar-20	31.64	±	1.65	14.21	±	1.27	17.43	±	2.08	17.44	±	2.09
W621	14	–	15	0.14	4.20	±	0.14	16-Mar-20	16.96	±	0.83	10.24	±	0.92	6.73	±	1.24	6.73	±	1.24

$^{206}Pb/^{207}Pb$ data (**Appendix VIII**) show the onset of Broken Hill Pb pollution from 14.5 cm and samples rapidly become less radiogenic after this depth (**Figure 68**). The Pb maximum (1974 ± 10) is placed at 4.5 cm.

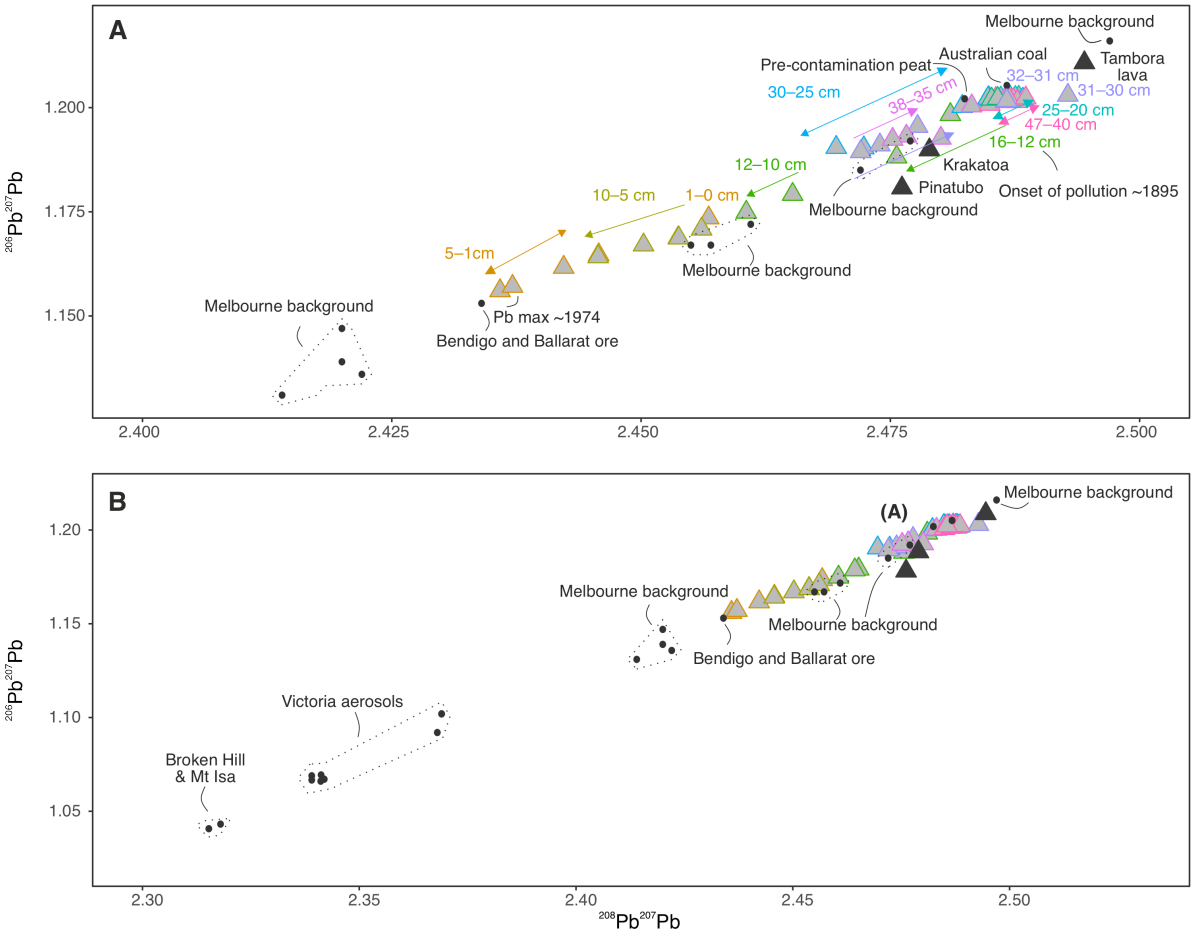

Figure 68. A. Source plot for samples from core TAR-40 (coloured markers) as well as volcanic, pollution and background isotopic signatures (black markers). **B.** A zoom out of plot A showing also the isotopic signatures of the Victoria aerosols, Bendingo and Ballarat ores, the Melbourne background and the Broken Hill and Mt Isa ores (black markers). Data available in **Appendix IX.**

Exotic pollen indicative of European settlement appears at 46.5 cm and 22.5 cm, however the occurrences are isolated (**Figure 69**) and do not increase significantly until 15.5 cm, therefore European settlement is placed at 15.5 cm where pine and Asteraceae (Liguliflorae, introduced

European daisy) have sustained increases. Following Gehrels et al. (2008), a 20-year lag period with a ± 10 year error is added to account for the time taken for pine trees to produce pollen. In total, three chronostratigraphic horizons can be identified within the core from pollen and stable lead data (**Table 21**).

Table 21. Calendar dates obtained from core TAR-40.

Chronostratigraphic Marker	Depth (cm)	Calendar Year (AD)	Date given in model (AD)	Reference
Pb pollution maximum	4.5	1964 – 1984	1974 ± 10	Kristensen (2015)
Broken Hill smelting	14.5	1890 – 1900	1895 ± 5	Van de Velde et al. (2005)
European settlement	15.5	1841 – 1851	1861 ± 10 (20-year lag added for pollen marker and error increased)	Caldow (2003)

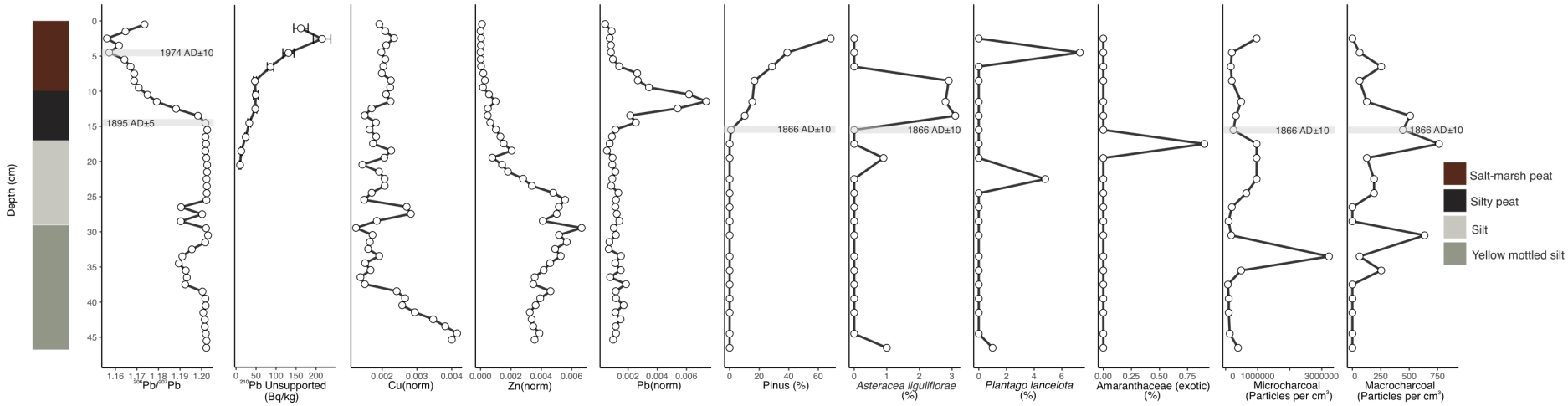

Figure 69. Stable lead (^{206}Pb/^{207}Pb), ^{210}Pb, pollen and charcoal data for core TAR-40. Identified chronohorizons are highlighted by the grey boxes.

A visual inspection using prior information from the identified chronohorizons and pollen data suggests that OZZ405, SUERC-93778 and SUERC-93779 are too old for their stratigraphic position. All three of the samples were bulk sediment and may have been contaminated by older material. UCIAMS-236625 is too young as it occurs at the same chronohorizon as the Broken Hill smelting and therefore place precedence on this marker over the ^{14}C date due to the clarity of the signal. This may have been misidentified or subject to root penetration. Therefore, these dates were removed from the age-depth model prior to analysis.

Table 22. ^{14}C results from core TAR-40 SHCal20 (Hogg et al. 2020) and SH Zone 1 – 2 (Hua, Barbetti and Rakowski, 2013). Dates removed prior to age-depth modelling are highlighted by an asterisk. Depths given in the table represent the mid points of the samples.

Publication/ Lab Code	Material	Depth in core (cm)	Percent modern ^{14}C (pMC) and error (1 σ)	Calibrated radiocarbon age 2 σ (AD)	$\delta^{13}C$-VPDB‰
UCIAMS-236620	Plant macrofossil	4.5	115.74 ± 0.20	1959 – 1993	n/a
SUERC-93776	Plant macrofossil	6.5	125.06 ± 0.57	1962 – 1983	-20.2
UCIAMS-236624	Plant macrofossil	11.5	130.45 ± 0.23	1963 – 1980	n/a
UCIAMS-236625 *	Plant macrofossil	14.5	101.98 ± 0.18	1956 – 1957	n/a
OZZ405 *	Bulk sediment	20	93.77 ± 0.30	1412 – 1454	-27.1 +/- 0.1
SUERC-93778 *	Bulk sediment	24	95.85 ± 0.42	1485 – 1654	-25.0
SUERC-93779 *	Bulk sediment	26	93.47 ± 0.43	1330 – 1455	-25.1
OZZ406	Bulk sediment	50	84.80 ± 0.21	676 – 825	-26.4 +/- 0.1

The resulting ^{14}C, ^{210}Pb and calendar ages were combined in the age-depth model to produce age estimates and uncertainties downcore (**Figure 70**). The accumulation rate was established using that suggested by *rplum* from initial data analysis. Model memory was kept at the default of 0.5. The model was ran with a setting of ra.case=1. Thickness was kept at the default of 1 to allow flexibility in the model. A minimum core age of 2019 was set, and this was also given as the sampling date.

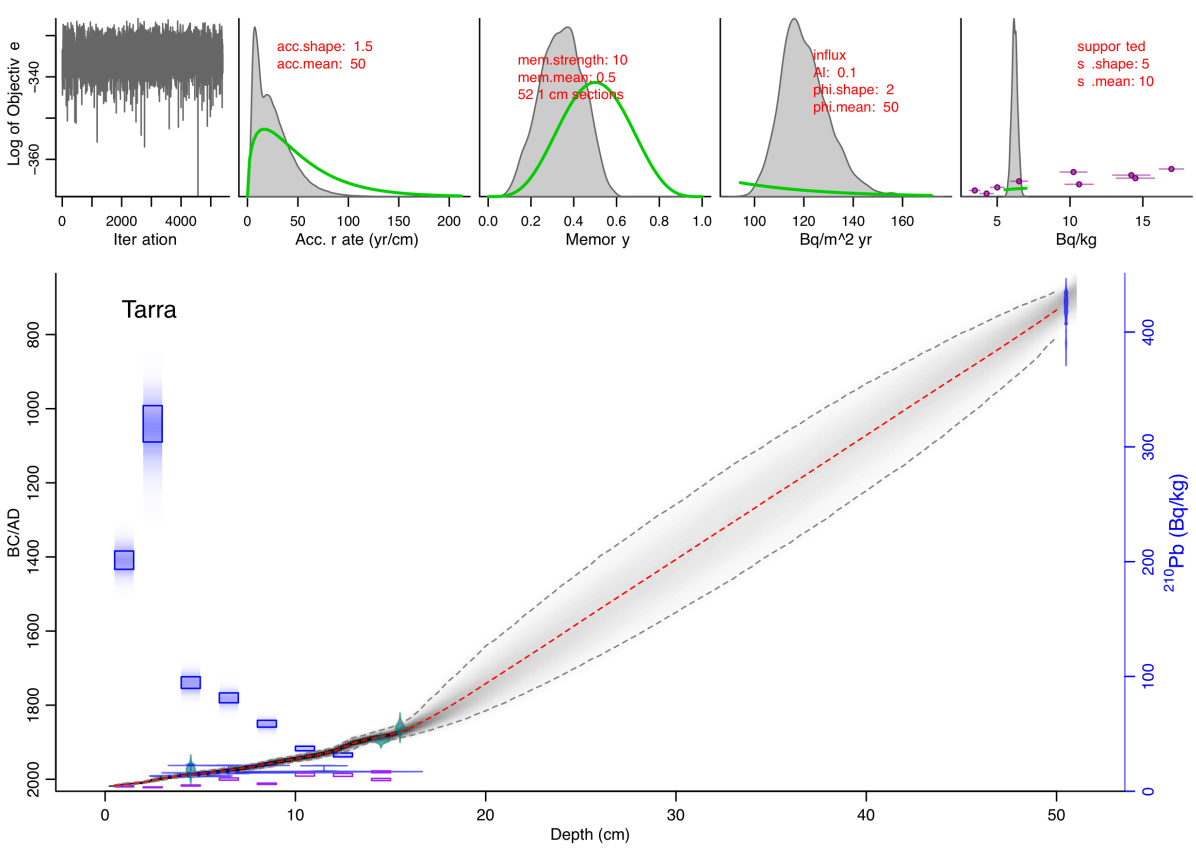

Figure 70. Upper panel: Prior (light green) and posterior distributions (light grey) as well as Markov Chain Monte Carlo iterations (dark grey). **Lower panel:** Age-depth model for core TAR-40. Blue dotted squares show measured ^{210}Pb and columns show modelled ^{210}Pb. Purple squares show supported ^{210}Pb. Calendar dates (teal) and calibrated radiocarbon dates (dark blue) are also shown. Mean ages are denoted by the dotted red line and 95 % confidence interval (*i.e.* age range) is denoted by the grey dotted lines.

MCMC iterations indicate that that the model run was successful, with no visible structure seen. The sedimentation rate varies from ~40 yr cm^{-1} – <10 yr cm^{-1} with significant increases from ~18 cm. The accumulation rate in the sand and silt units is ~0.03 cm yr^{-1} in both units; this increases to ~0.11 cm yr^{-1} in the salt-marsh peat, suggesting slightly slower accumulation at Tarra than the other two sites. Model uncertainty is well constrained between ~1800 – 2019, but error increases before this period until it is constrained slightly by the final basal date.

A comparison of prior and posterior probability distribution functions shows that when combined with the other dating methods, the dates between 0 – 11.5 cm are estimated to be marginally older than the ^{14}C prior ages and the date at 20 cm is modelled younger (**Figure 71**). Interrogations of the posterior age distributions show most fit a near-Gaussian profile (**Figure 72**) and so Gaussian-process model was deemed suitable for the sea-level reconstruction.

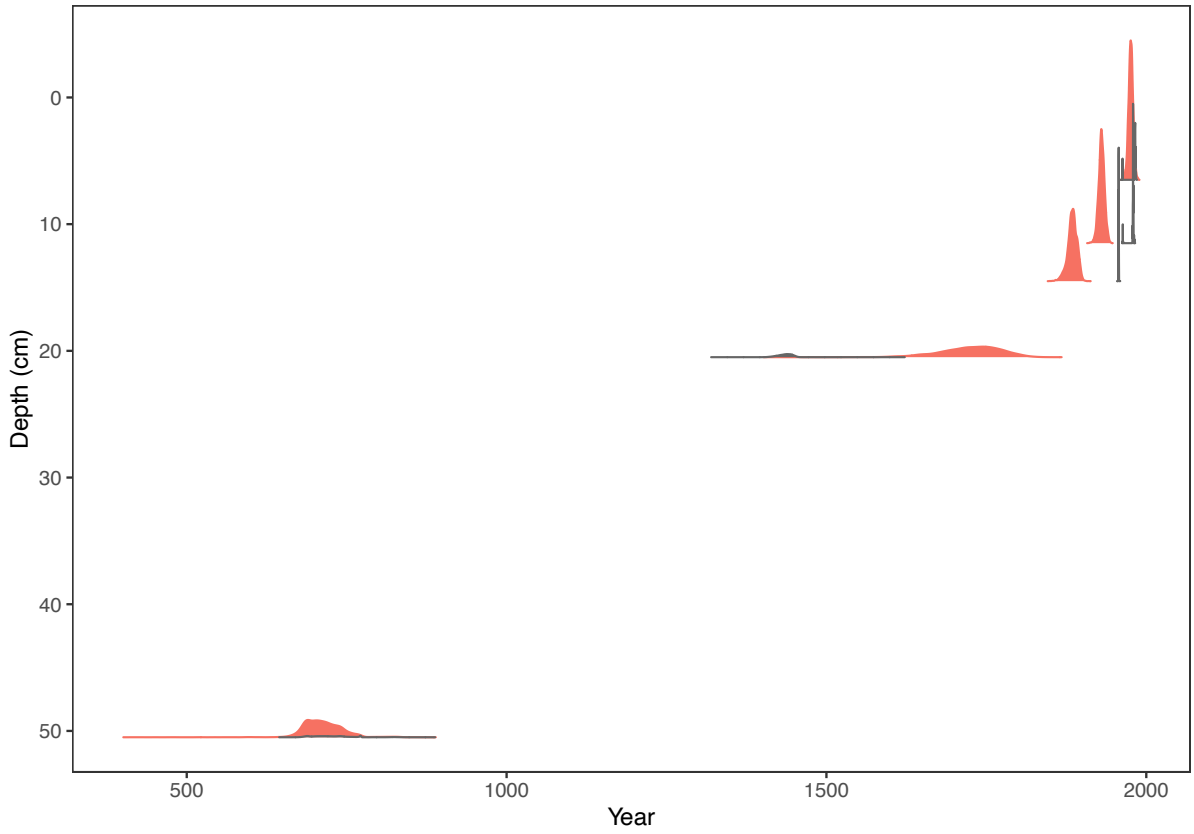

Figure 71. Probability distribution functions (PDFs) of prior ^{14}C dates (grey) and posterior *rplum* distributions (orange).

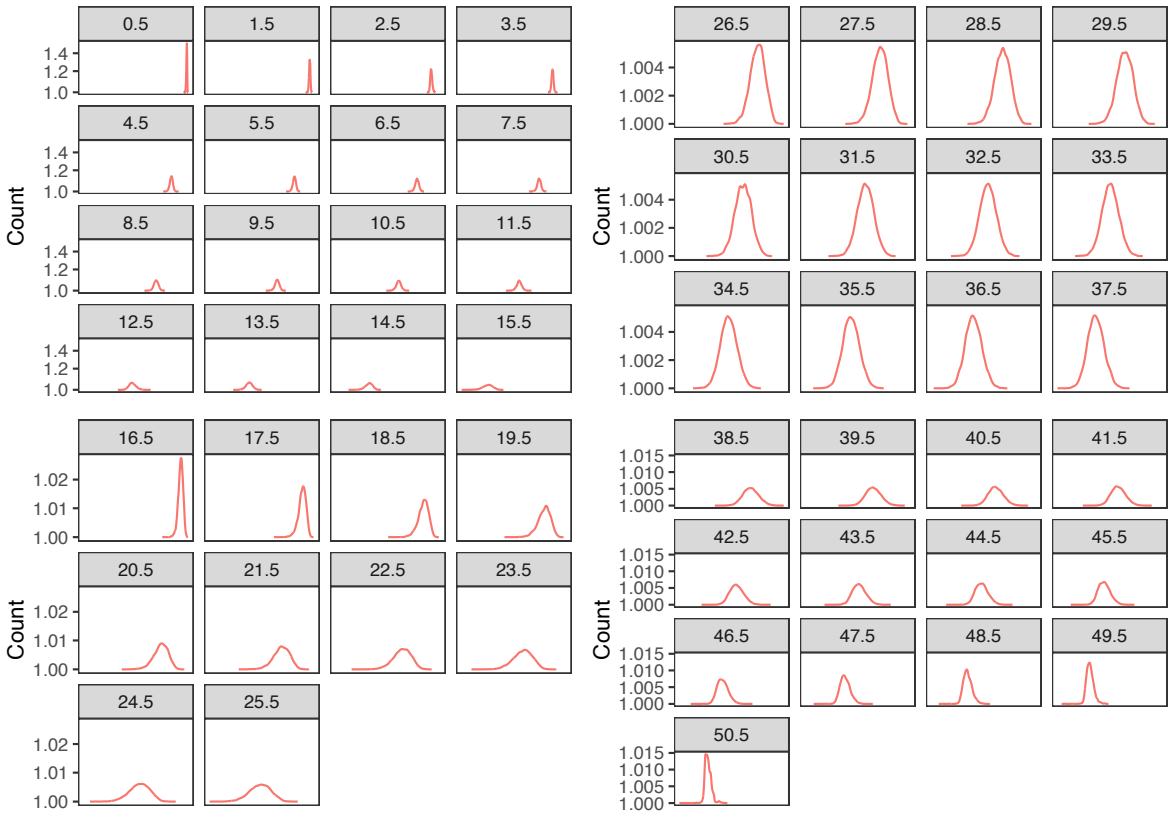

Figure 72. Probability distribution functions (PDFs) from the Tarra age-depth model. Numbers in the grey box indicate the depth that the PDF has been extracted from in centimetres.

6.1.3.4 Sea-level reconstruction

Due to a lack of chronological constraint beyond 15.5 cm as well as foraminifera not being consistent with the sedimentology in the silt units, only data from 15.5 cm upcore are included the Gaussian process model. The reconstruction was corrected for GIA at a rate of -0.25 (-1.16 – 0.30) mm yr^{-1}. GCSL was 0.19 m below present in the late 19th century (**Figure 73**). For the last two decades of the 19th century, sea level rose gradually at a rate of 0.3 (-8.0 – 7.8) mm yr^{-1} (1871 – 1899). The rate of sea-level rise increased over the 20th century to rates of 1.4 (-2.0 – 4.7) mm yr^{-1} (1900 – 1949). Change-point analysis detects one change point in the Tarra reconstruction in 1942, although the credible intervals are extremely large

(1873 – 2015). This is likely due to the slower rate of sea-level rise at Tarra as well as the larger vertical uncertainties. Varying the GIA rate to assess Ea0 constrains this somewhat, with the Ea0 estimated sometime between ~1870 – 1950. Whilst the median values of all three corrections remain largely similar (varying on the order of a few years), the lower 95 % uncertainty varies the Ea0 quite significantly depending on which correction is used. The mid and minimum GIA corrections suggest emergence as early as ~1900, however, the maximum correction does not suggest emergence until the mid-20th century. The rate of sea-level rise fell over the second half of the century (1950 – 1999), with average rates of 1.2 (-2.5 – 4.3) mm yr^{-1}. Maximum rates of sea-level rise were not reached until the early 21st century, with rates of up to 5.5 (0.9 – 9.8) mm yr^{-1} witnessed in 2002.

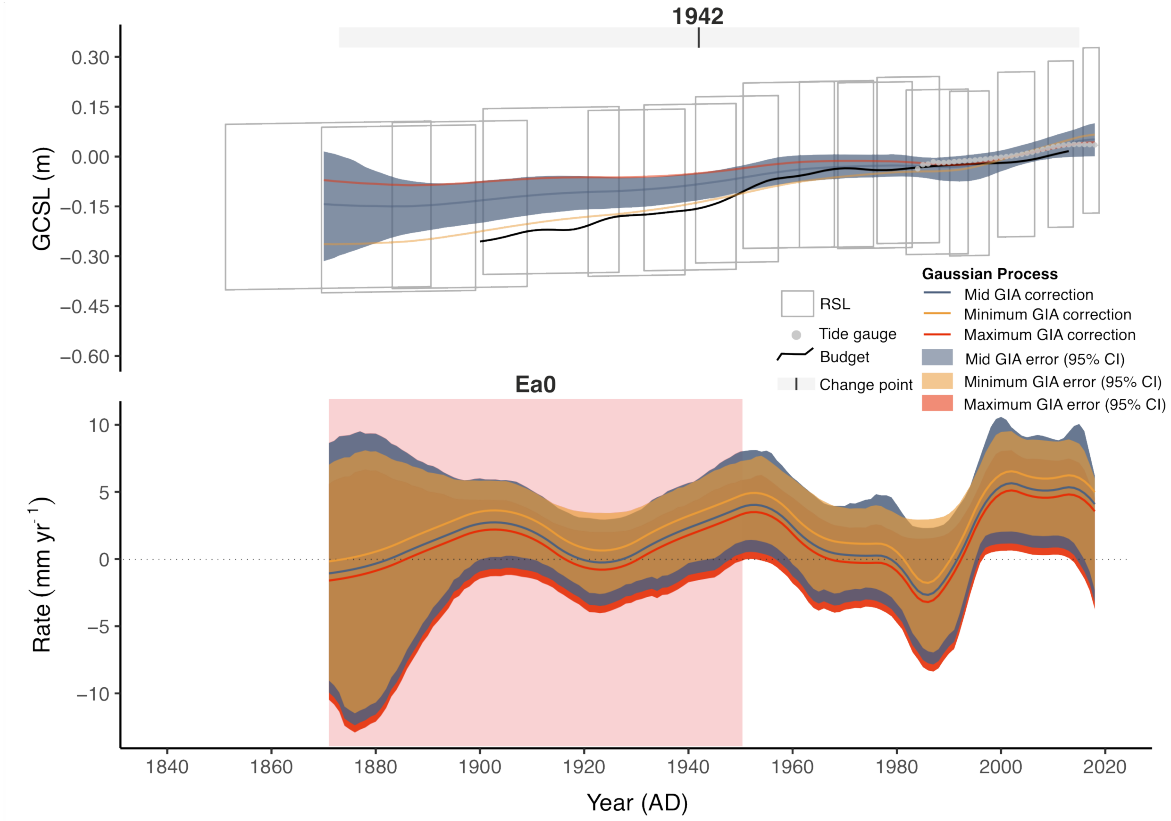

Figure 73. Upper panel. GIA-corrected sea-level (GCSL) reconstruction for Tarra salt marsh. Grey parallelograms show proxy sea-level estimates (*i.e.* sea-level index points) from core TAR-40 with 2 σ vertical and age uncertainties. A GIA-corrected Gaussian process regression has been fitted to the index points showing the median (blue line) and 95 % confidence intervals (blue shading) of the mid-range GIA correction. Also shown are the median gaussian process regression curves after detrending using the minimum (yellow line) and maximum (red line) GIA corrections. The filled grey boxes denote identified change points from the change-point model (Caesar et al. 2021) showing 95% credible intervals and mean change point (black line). Also shown are local tide-gauge data and the sea-level budget (barystatic gravity, rotation and deformation, sterodynamic and the inverse barometer components - both have been 15-yr smoothed). **Lower panel.** The rate of sea-level change calculated from the Gaussian process regression showing the median (blue line) and 95 % confidence intervals (blue shading) of the mid-range GIA correction. Also shown are the rates after detrending using the minimum (yellow line and shading) and maximum (red line and shading) GIA corrections. The emergence above 0 (Ea0) of the acceleration in sea level is denoted by the red box.

6.1.4 Update of Little Swanport, Tasmania

The Little Swanport age-depth model (Gehrels et al. 2012) was updated to the latest radiocarbon calibration curve, SHCal20 (Hogg et al. 2020) and run through the same Gaussian process analyses as the new reconstructions to provide a regional comparison to the new reconstructions (see **Chapter 7**). The reconstruction was corrected for GIA at a rate of -0.05 (-0.70 – 0.46) mm yr^{-1}. The reconstruction shows that GCSL was ~0.31 m below present around the start of the 19th century (1822; **Figure 74**). The rate of sea-level rise was steady over the 19th century (1822 – 1899) at 1.0 (- 2.3 – 4.3) mm yr^{-1}. The first change point was detected in the mid 19th century (mean change point 1869; 1838 – 1891 95 % credible interval). The Ea0 is estimated at ~1820 – 1880, agreeing well with the first change point. The lower 95 % CIs of all three rates suggest similar timings in the onset of Ea0, however the median rates differ fairly substantially, with the maximum GIA correction suggesting an onset ~15 years later than the minimum correction and ~5 years later than the mid correction. The rate of sea-level rise then increased over the first half of the 20th century (1900 – 1949) to rates of 4.0 (1.6 – 7.1) mm yr^{-1}. Maximum rates of sea-level rise were reached in 1907 (5.4 (3.0 – 8.4)) mm yr^{-1}. Following a peak in the early 20th century, rates of sea-level rise then slowed over the second half of the 20th century to 0.4 (-2.6 – 3.3) mm yr^{-1}.

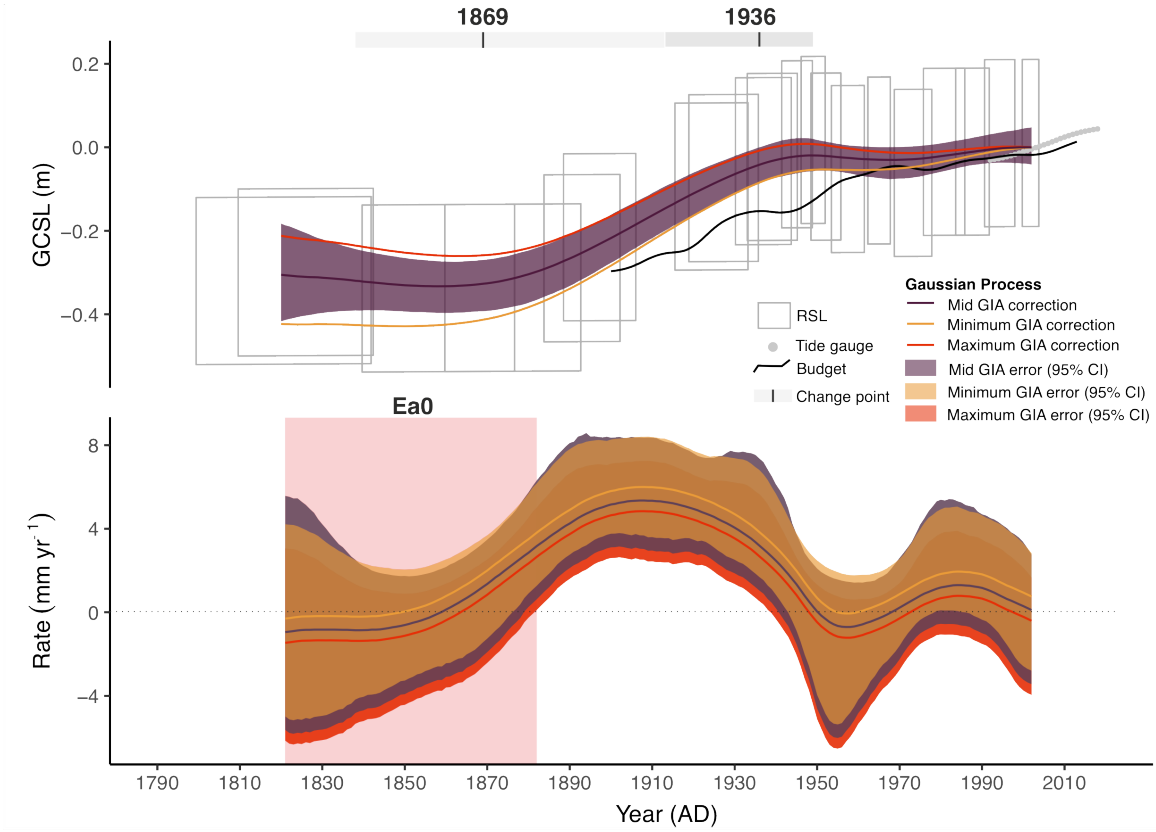

Figure 74. Upper panel. GIA-corrected sea-level (GCSL) reconstruction for Little Swanport salt marsh. Grey parallelograms show proxy sea-level estimates (*i.e.* sea-level index points) with 2 σ vertical and age uncertainties. A GIA-corrected Gaussian process regression has been fitted to the index points showing the median (plum-coloured line) and 95 % confidence intervals (plum-coloured shading) of the mid-range GIA correction. Also shown are the median gaussian process regression curves after detrending using the minimum (yellow line) and maximum (red line) GIA corrections. The filled grey boxes denote identified change points from the change-point model (Caesar et al. 2021) showing 95% credible intervals and mean change point (black line). Also shown are local tide-gauge data and the sea-level budget (barystatic gravity, rotation and deformation, sterodynamic and the inverse barometer components - both have been 15-yr smoothed). **Lower panel.** The rate of sea-level change calculated from the Gaussian process regression showing the median (plum line) and 95 % confidence intervals (plum shading) of the mid-range GIA correction. Also shown are the rates after detrending using the minimum (yellow line and shading) and

maximum (red line and shading) GIA corrections. The emergence above 0 (Ea0) of the acceleration in sea level is denoted by the red box.

6.2 Summary

This chapter has presented the site stratigraphy, fossil foraminifera, palaeomarsh surface elevation estimates, chronologies, and subsequent relative sea-level reconstructions for three master cores taken from Lutregala, Wapengo and Tarra, as well as an update to the previously published record from Little Swanport. All sites consist of a similar lithology, with a basal unit comprised of a silt or sandy silt unit which is often characterised by yellow mottling; this is overlain by a thin brown-grey silt. Overlying each marsh is a unit that is comprised of ~30 cm of salt-marsh peat, which the chronology suggests formed in ~80 – 100 years.

Core samples primarily contained eight species of foraminifera: *T. salsa*, *H. wilberti*, *E. macrescens*, *P. ipohalina*, *T. irregularis*, *T. inflata*, *S. lobata* and *M. fusca*. *Trochammina inflata* was the most abundant species across all three cores, which mirrors the modern data (see **Chapter 5**). In all cores, live foraminifera were found infaunally in the top 10 cm; however, their densities were much lower than dead foraminifera, especially downcore of the top 3 cm. A visual inspection suggests that foraminiferal assemblages in the inorganic units of the cores are indicative of a mid-high marsh environment, which is not analogous with the sediment. However, total counts of foraminifera in the sands and silts are low - frequently below 50 individuals. Upcore, foraminiferal assemblages diversify to those indicative of mid-low marsh environments.

Using the modern analogue technique, the reconstructive performance of the transfer functions was assessed. For Lutregala, whilst the regional II model resulted in more "good" modern analogues, there were no poor analogues and so little justification could be made to employ the regional model over the local. However, for the Wapengo reconstruction, the modern analogue technique showed that using the local model resulted in 14 poor analogues, whereas the regional model resulted in no poor analogues. This is likely due to the low abundance of *T. salsa* in the modern surface samples (due to removal during data screening), but higher abundance in the core. Similarly for Tarra, as the local transfer function performance was extremely poor, multiple methods of obtaining palaeomarsh surface elevation estimates were considered. Species-elevation relationships were comparable between the local and regional training set and results were similar to assuming a constant indicative range, and so and the regional model was also employed for this reconstruction. Across the models, PMSE estimates range from 0.64 – 1.33 m AHD with 1 σ uncertainties of 0.06 – 0.12 m.

Three chronologies were developed using multiple dating approaches. $^{206}Pb/^{207}Pb$ ratios were analysed down each core and the profiles were used to identify chronohorizons in the cores. Two distinct signals were apparent in each core: the mining of the Broken Hill ore and the late 20th century pollution maximum resulting from peak petrol consumption. Pollen and charcoal in the cores were used to identify the European settlement at Wapengo and Tarra which was dated using the archival information in **Chapter 3**; however, no evidence of initial European settlement was found in the Lutregala core. Bayesian modelling using MCMC simulations in *rplum* were used to establish age-depth models. The

models combined the raw ^{210}Pb and ^{14}C data with the calendar ages to provide downcore age estimates at 1 cm resolution with corresponding uncertainties. Age-depth models show sediment accumulation in the silt and sand units was low ~0.02 – 0.03 cm yr^{-1}, but this increased rapidly in the peat to ~0.11 – 0.19 cm yr^{-1} .

New reconstructions were only generated from the 19th century onwards (in the organic units of the cores) due to the poor dating resolution in the silt and sandy units, as well as the inconsistent foraminiferal assemblages in these sections of the cores. The previously published reconstruction from Little Swanport, Tasmania (Gehrels et al. 2012) was updated to SHCal20 to enable a regional comparison (see **Chapter 7**) and run through the same Gaussian process analyses as the new reconstructions. The GCSL reconstructions demonstrate that sea level was ~0.2 – 0.3 m below present in the 19th century. Rates of 19th century sea level rise were gradual at Wapengo, Tarra and Little Swanport at 0.9 (- 2.2 – 3.5) mm yr^{-1} (1833 – 1899), 0.3 (-8.0 – 7.8) mm yr^{-1} (1871 – 1899) and at 1.0 (- 2.3 – 4.3) mm yr^{-1} (1822 – 1899) respectively. Trends could not be derived for Lutregala over this period as the record only begins in the last decade of the 19th century.

The rate of sea-level rise increased during the first half of the 20th century to 1.7 (- 4.0 – 6.5) mm yr^{-1}, 4.0 (1.2 – 7.1) mm yr^{-1}, 1.4 (-2.0 – 4.7) mm yr^{-1} and 4.0 (1.6 – 7.1) mm yr^{-1} at Lutregala, Wapengo, and Tarra and Little Swanport respectively. Maximum rates of sea-level rise were reached at Lutregala, Wapengo and Little Swanport in the early-mid 20th century, but at Tarra did not peak until the early 21st century. Varying the GIA rate does change the Ea0 at each site, especially at Tarra, although the overall uncertainty in the Ea0 is similar to that predicted by change-point analysis and differences

in Ea0 vary largely on the order of years. For these reconstructions, a mid-range value is appropriate as there is little difference in the magnitude of RSL change between the different GIA rates. Rates decreased over the second half of the 20th century at Wapengo 0.9 (-2.1 – 2.8) mm yr^{-1}, Tarra 1.2 (-2.5 – 4.3) mm yr^{-1} and Little Swanport 0.4 (-2.6 – 3.3) mm yr^{-1}; however, the average rate of sea-level rise was high at Lutregala at 4.6 (0.9 – 8.7) mm yr^{-1} (although rates did fall over the century). Therefore, the reconstructions suggest considerable regional variability. Reasons for this variability are explored further in **Chapter 7**.

Chapter 7 of 8

Discussion

7.0 Introduction

This chapter first undertakes a regional comparison of the proxy reconstructions with tide-gauge data from Australia and the wider western Pacific, as well as to the global average over the 20th century. Second, it discusses the drivers of 20th century sea-level change in the region, considering both the barystatic and sterodynamic contributions to RSL over this period. Third, it presents the sea-level fingerprinting analyses to consider the likely sources of barystatic sea-level rise over the 20th century.

7.1 Discussion

7.1.1 Regional and global comparison

Overall, the two longest records from Wapengo and Little Swanport show that rates of sea-level rise were similar over the 19th century at ~0.9 – 1.0 mm yr^{-1}. The records then suggest the rate of sea-level rise increased to ~4.0 mm yr^{-1} over the first half of the 20th century. These two records suggest faster rates of sea-level rise than at Lutregala and Tarra over the same period of the 20th century (~1.4 – 1.7) mm yr^{-1}.

Varying each reconstruction by its maximum, minimum and mid GIA correction (*i.e.* the upper 95 % CI, lower 95 % CI and median) does marginally affect the Ea0 (typically on the order of years, but up to decades in some cases) and may, in part, explain some of the differences between the onset of modern acceleration in each of the records. There is clear overlap in the Ea0 at Wapengo and Tarra and each of the Tasmanian sites (**Figure 75**), but Lutregala and Little Swanport differ significantly in their Ea0's (~80 – 120 years) despite

being in closest proximity to each other spatially. This suggests that there are other drivers responsible for the differences between the RSL histories at each site.

There may be several reasons for the discrepancies in the pattern and magnitude of RSL change between the records: firstly the earliest SLIPs in the Little Swanport record derive from a tidal-flat mud (Gehrels et al. 2012). This study has demonstrated that owing to a low accumulation rate (suggesting removal and dispersal of material), low preservation of foraminifera, and age reversals in the chronology, these tidal-flat deposits may be subject to re-working. This may be the same for the tidal-flat deposit at Little Swanport. Similarly, there is also a possibility of infaunality within this unit of the core. Future work may seek to only run Gaussian process analyses on the organic unit of the Little Swanport reconstruction to re-analyse the Ea0 and change-point analysis and compare to the other three reconstructions to see if this affects Ea0.

Secondly, all reconstructions have been derived from salt marshes along coastlines with microtidal tidal ranges. Whilst this is advantageous due to the resulting smaller vertical errors (Williams et al. 2021), this could also mean that the foraminifera are responding to other localised processes such as wave and wind-induced changes in tidal range (Woodroffe and Long, 2010). Changes in the tidal range along the coastline may also be affected by pressure-induced changes owing to changing atmospheric conditions. A more detailed discussion on the effect of these pressure-induced changes on 20th century sea level in Australia is considered in section 7.1.3.

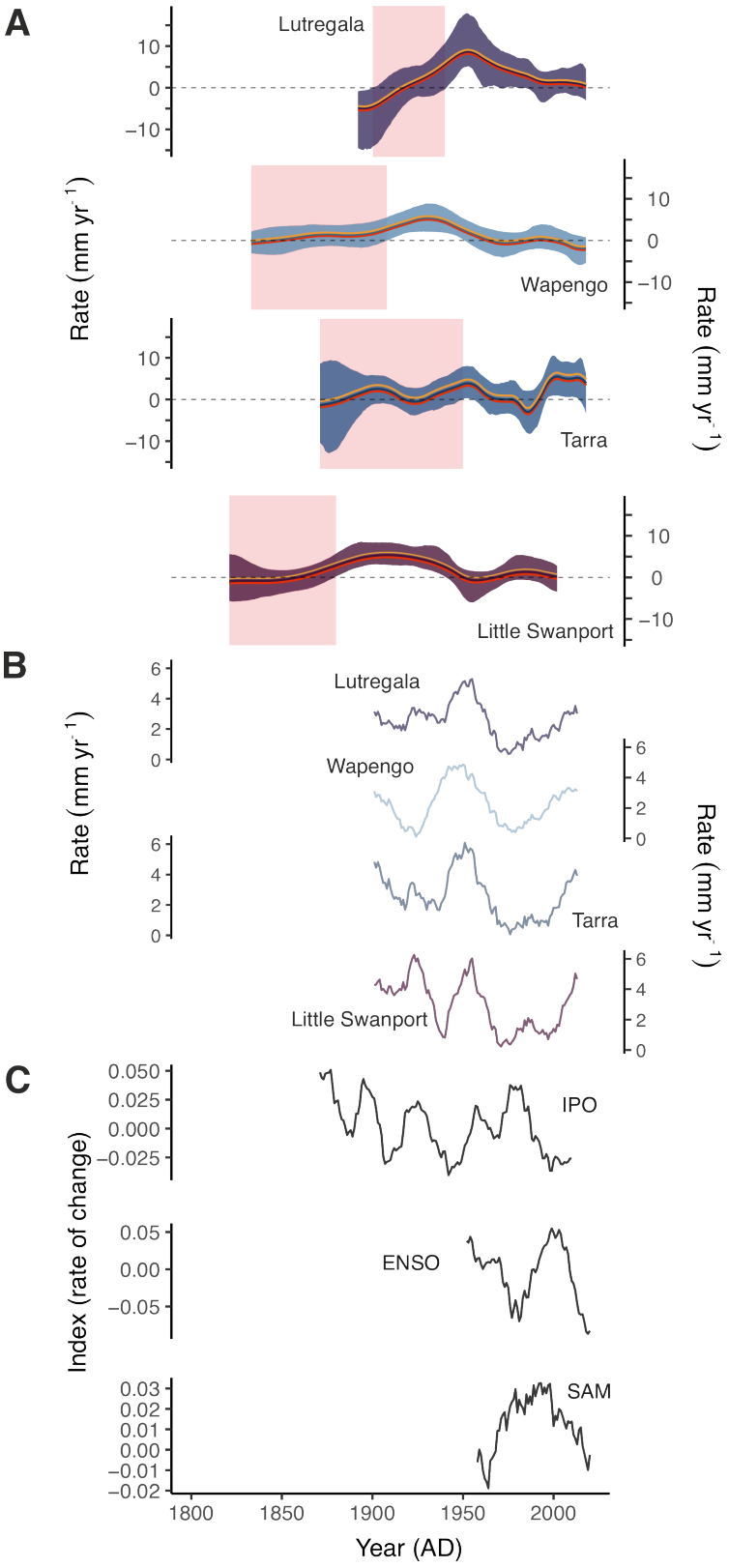

Figure 75. Comparison of **A**. the rate of relative sea-level rise at the salt marshes, **B.** full budget at each of the sites (15-yr smoothed) and **C**. dominant climate indices (Interdecadal Pacific Oscillation IPO; El Niño Southern Oscillation ENSO; and Southern Annular Mode SAM - all 15-yr smoothed) from 1900 – 2020. Red boxes denote the emergence above 0 mm yr^{-1} (Ea0) of the modern acceleration in sea level. Data for the climate indices are from Marshall (2003); Henley et al. (2015) and NOAA (2021) updated by NOAA (2021).

Thirdly, the Tarra salt marsh is located up-estuary and perhaps may be better characterised as a fluvially-dominated salt marsh, as opposed to an embayment marsh (which Lutregala, Wapengo and Little Swanport may be described as). At Tarra there is little vertical range between the landward and seaward ends of the marsh, and also a distinct lack of vertical zonation in both the flora (across the salt marsh until entering the mangrove zone) and in the foraminifera (both modern and fossil). Foraminifera (namely *T. salsa* and *M. fusca*) which are typically found at the upper and lower ends of the elevation gradient in other marshes (*e.g.* Williams et al. 2021), often co-exist at the same elevation. This may suggest a weak environmental gradient across the marsh, and the presence of *Phragmites* in the southern end of the marsh (not sampled in this study) may suggest significant freshwater inputs to the marsh. The near-linearity of the reconstruction therefore may be an artefact of the age-depth model, and future work therefore should derive more reconstructions from the southern Australian coastline to verify the Tarra reconstruction. It should consider location of the marsh in terms of its position in the estuary and should seek to sample from marshes located in closer proximity to the open ocean.

Therefore, currently, it is difficult to ascertain the reason(s) for the discrepancies of both the onset of the acceleration and the pattern of RSL change between the local reconstructions. Whilst varying the GIA rate does change the Ea0 and magnitude of RSL (to a degree), there remain differences which are unrelated to a long-term linear signal. Several reasons presented could include: infaunality and re-working of foraminifera, response of foraminifera to localised changes in the tidal range (which may be augmented as a result of the salt marshes being located on microtidal coastlines) and or the response of foraminifera to secondary variables other than tidal inundation such as salinity changes, freshwater

input, vegetation and organic matter content of the sediment. Finally, another factor causing the variability could be the result of localised sterodynamic changes in sea level. As previously mentioned, this will be considered further in the resulting sections.

At Lutregala, a comparison of the proxy record with the instrumental data over the last three decades shows good agreement, with the Hobart tide-gauge data falling entirely within the Gaussian process range (**Figure 51**). Similarly, tide-gauge data from Stony Point agree very well with the Tarra proxy record, falling within the Gaussian process range over the entire reconstruction (**Figure 73**). There is little cross over between available instrumental data and the Little Swanport proxy record, although where data do overlap, the tide-gauge data fall in the lower uncertainty of the Gaussian process range (**Figure 74**). Tide-gauge data from Eden also lie within the Gaussian process range over the late 1980s, 1990s and early 2000s, but predict faster rates of sea-level rise than the Wapengo Gaussian process range from the mid 2000s to present. Differences between the tide-gauge data and the proxy data cannot be attributed to GIA uncertainty, but may reflect small localised changes in sea level due to the distance between the two sites (~65 km). Tide-gauge data are however still within the error of the SLIPs (**Figure 62**).

Estimates of global mean sea level from 1900 – 1949 suggest an average rate of 1.4 (0.8 – 1.8) mm yr^{-1} and rates from the Indo-Pacific are 1.0 (0.1 – 1.9) mm yr^{-1} (Frederikse et al. 2020). Therefore, the global average is comparable to that estimated at Lutregala and Tarra, but far slower than those reconstructed at Wapengo and Little Swanport. Similarly, in the Indo-Pacific, rates of sea-level rise are slower than those observed in our records from southeastern Australia (Frederikse et al. 2020). Over the second half of the 20th century, rates

at Wapengo, Tarra and Little Swanport are closer to the global average 1.0 (- 0.4 – 0.3) mm yr^{-1} and the Indo-Pacific average 0.4 (- 0.5 – 0.6) mm yr^{-1}, whereas the rates from Lutregala are far higher owing to the exceptionally fast rates in the 1950s and 1960s.

Unfortunately, the few long-term tide gauges in southeastern Australia such as Sydney Fort Denison, Newcastle, and Williamstown (**Figure 32**) have large data gaps, subsidence issues and datum shifts, especially over the late 19th and early 20th century which can make them problematic (Hogarth, 2014a, 2014b; White et al. 2014). In the longest record, Fort Denison, there were issues with the digitisation of the record which may have led to errors in the earlier part of the record (Hamon, 1988; White et al. 2014). White et al. (2014) state that individual Australian tide-gauge records are too short and too variable for the detection of statistically significant accelerations in sea-level rise.

7.1.2 Comparison to the sea-level budget

An alternative approach to a comparison of the proxy records and the tide-gauge data is to compare the reconstructions to a sea-level budget at each site. As previously mentioned, the sea-level budget uses barystatic GRD estimates from Frederikse et al. (2020) and sterodynamic sea-level estimates from the SODAsi.3 ocean reanalysis model (Giese et al. 2016). The inverse barometer effect (IBE) is added using sea-level pressure from the 20th Century Reanalysis V3 model (20CRv3; Slivinski et al. 2019). All components are taken from nearest neighbour estimates to the proxy sites. An advantage of this method is that the data are also continuous in time from 1900 – 2013, so have higher temporal resolution than the

tide-gauge data over the early 20th century. A disadvantage however is that data density in the model is sparse prior to ~1950 (owing to lack of observational data) and therefore earlier sterodynamic estimates may be less precise.

As documented in **Chapter 6**, at all sites, the budget falls within the uncertainty of the GIA-corrected SLIPs during the first half of the 20th century and largely lies within the Gaussian process range from ~1950 – present, thus suggesting that sterodynamic, barystatic GRD, and IBE contributions can explain the observed RSL rise at the sites. At Lutregala however, the budget falls within the very upper limits of the SLIP uncertainty over the early 20th century, which may suggest an over-estimation of the acceleration at this site or an under-estimation of the budget. The discrepancy between the two may be better resolved by using an ensemble of sterodynamic estimates to evaluate the sterodynamic contribution to sea level over this period.

There was an increase in the rate of the barystatic GRD contribution to sea level at all of the sites from ~1920, and a marked increase in the sterodynamic component from ~1930 – 1940 (**Figure 76**). The IBE declined from 1900 – 1930 but increased rapidly from ~1930 – 1960 before falling again, where it remained low to present. The full budget suggests that from ~1950 – 1975, the rate of the contribution from sterodynamic, barystatic and the IBE components to RSL slowed, which agrees with the proxy records. The barystatic GRD contribution remained at a record low over the century until ~1975, when the contribution increased rapidly until present. The contribution from the sterodynamic component, however, did not increase again significantly until ~2000. Increases in the rate of RSL are not observed in the Lutregala, Little Swanport or Wapengo record over the latter decades

of the 20th century but are apparent in the Tarra record from ~1975. This may be due to the fact that the density of index points are not particularly large at the time series boundaries, which may have also added additional uncertainty to the Gaussian process at the start and end of the records.

It is important to note that sterodynamic changes are the only component that show significant regional variability between individual locations. Variability is especially large over the first half of the 20th century, after which sterodynamics become more comparable between sites (**Figure 76**).

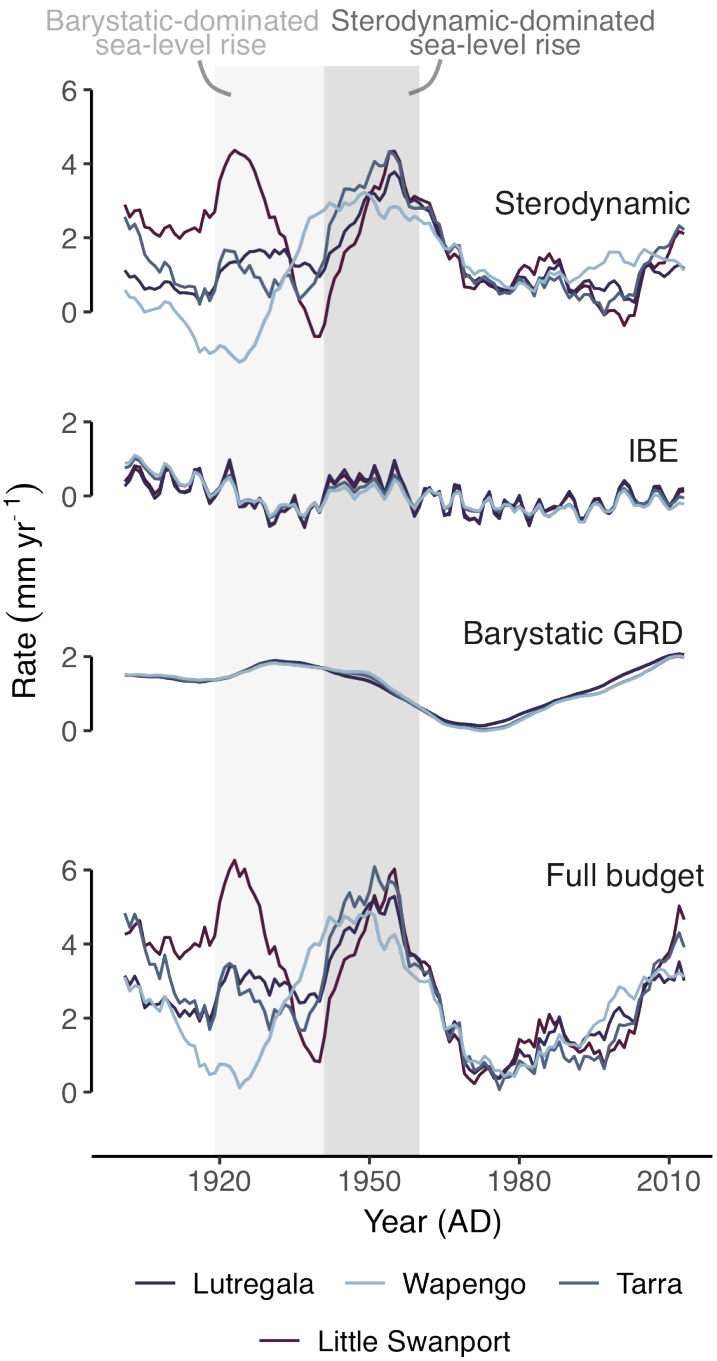

Figure 76. Contribution from the sterodynamic component, inverse barometer effect (IBE) and barystatic gravity, rotation and deformation (GRD) component (all 15-yr smoothed) to sea level at Lutregala, Wapengo, Tarra and Little Swanport from 1900 – 2013.

7.1.3 Drivers of 20th century sea-level change in southeastern Australia and the wider western Pacific

Both the barystatic GRD and sterodynamic components have contributed to the rapid rates of sea-level rise at the sites. The barystatic GRD component contribution was high over the first half of the 20th century. Overall, it contributed an average of 1.6 mm yr^{-1} between 1900 – 1949 to sea level at the sites, with substantial contributions of ~2 mm yr^{-1} especially between 1920 and 1940. The barystatic component also dominated early 20th century global mean sea-level rise (*e.g.* Parkes and Marzeion, 2018; Frederikse et al. 2020; Malles and Marzeion, 2021), with contributions primarily from land-based glaciers, as well as and the Greenland and Antarctic Ice Sheets (Frederikse et al. 2020).

The sterodynamic component then amplified the rapid rates and subsequently drove the acceleration from ~1930 – 1940, contributing up to ~4 mm yr^{-1} at its peak in the mid 20th century. The increase in sterodynamic sea level may have been driven by strengthening of ocean gyres (including the East Australian Current; Cai and Cowan, 2007; Giese et al. 2016), increases in sea surface temperature (especially from ~1920), changes in wind stress (Giese et al. 2016) and phase changes of several key climate modes. For example, over the early 20th century, the Interdecadal Pacific Oscillation (IPO) index declined (*e.g.* Salinger et al. 2001; Parker et al. 2007), changing from a positive to a negative phase. The IPO modulates the impacts of the El Niño Southern Oscillation (ENSO) in Australia by controlling the position of the South Pacific Convergence Zone and influencing sea surface temperature (and thus sea level) (*e.g.* Power et al. 1999; Henley et al. 2015; Kelly et al. 2019). This rapid decline in the IPO (marked by a positive increase in the rate of change of the index) is

coincident with our rapid rates of sea-level rise (**Figure 75**). Additionally, an upward trend of the Southern Annular Mode (SAM) due to the depletion of ozone has resulted in higher rates of sea-level rise in the subtropical southern oceans over the late 20th century and early 21st century (Duan et al. 2021).

A common feature of the Australian records and the New Zealand proxy record (Garrett et al. 2022; Gehrels et al. 2008) is a plateauing or falling of sea level over the latter few decades of the 20th century to present (except Tarra which begins to rise again from ~2000), and the change point-model identifies secondary change points in the Lutregala and Wapengo reconstructions over this time period (mean change points 1977 and 1957 respectively). This trend has also been found in tide-gauge records around Australia and New Zealand. For example, White et al. (2014) noted a sea-level depression of ~0.2 mm yr^{-1} for the majority of the east Australian coast from 1966 – 2010. The records from Wapengo and Lutregala show an average depression with rates of ~0.0 – 0.1 mm yr^{-1} over the same period. Similarly, Haigh et al. (2011) also observed a period of stability in tide-gauge records from Western Australia between 1950 – 1990, with a rise in the early 21st century.

The stabilisation in sea level in the western Pacific over the latter half of the 20th century has also been attributed to phase changes and an intensification of climate modes (*e.g.* Goring and Bell, 1999; Church et al. 2004; Sasaki et al. 2008; Woodworth et al. 2009; Haigh et al. 2011; Holbrook et al. 2011; Watson, 2011; White et al. 2014). An El Niño (negative ENSO) phase depresses sea level around Australia (Goring and Bell, 1999) and the index became progressively more negative after ~1960, resulting in more El Niño phases. The (sterodynamic) budget reconstruction estimates a decline in the rate from ~1960 – 2000

coinciding with a trend of more frequent high-pressure events over Australia (**Figure 75**; **Figure 76**).

However, the fall or plateau in the rate of sea-level change occurs at different times amongst the reconstructions (which does not suggest a synchronous response to climatic events) and therefore warrants further investigation into the discrepancy between the patterns of RSL rise. This may be achieved through addition of new reconstructions in the region, and or by undertaking a more robust statistical analysis to better decipher the regional and local non-linear and linear signals in the RSL records such as that undertaken by Walker et al. (2022).

Whilst the modelled budget suggests increased contributions from the barystatic GRD and sterodynamic components over the early 21st century, only the proxy data from Tarra reflect the increase in the rate of sea-level rise over this period. Currently, other reconstructions from the region (*i.e.* Little Swanport, Pounawea, Mokomoko) are too old to capture 21st century sea-level trends (Garrett et al. 2022; Gehrels et al. 2008, 2012).

7.1.4 Sea-level fingerprinting

To better quantify the barystatic GRD contribution to RSL over the 20th century, a set of sea-level records from around the world was used (see **Chapter 4**; **Figure 33**). Each site was corrected for sterodynamic sea-level changes prior to analysis (**Figure 77**). As sterodynamic sea level was and is, in general, much higher in the Southern Hemisphere compared to the

Northern (**Figure 78; Figure 79**), the sterodynamic corrections are greater for the Australian sites than for those located in North America and Europe (**Figure 77**).

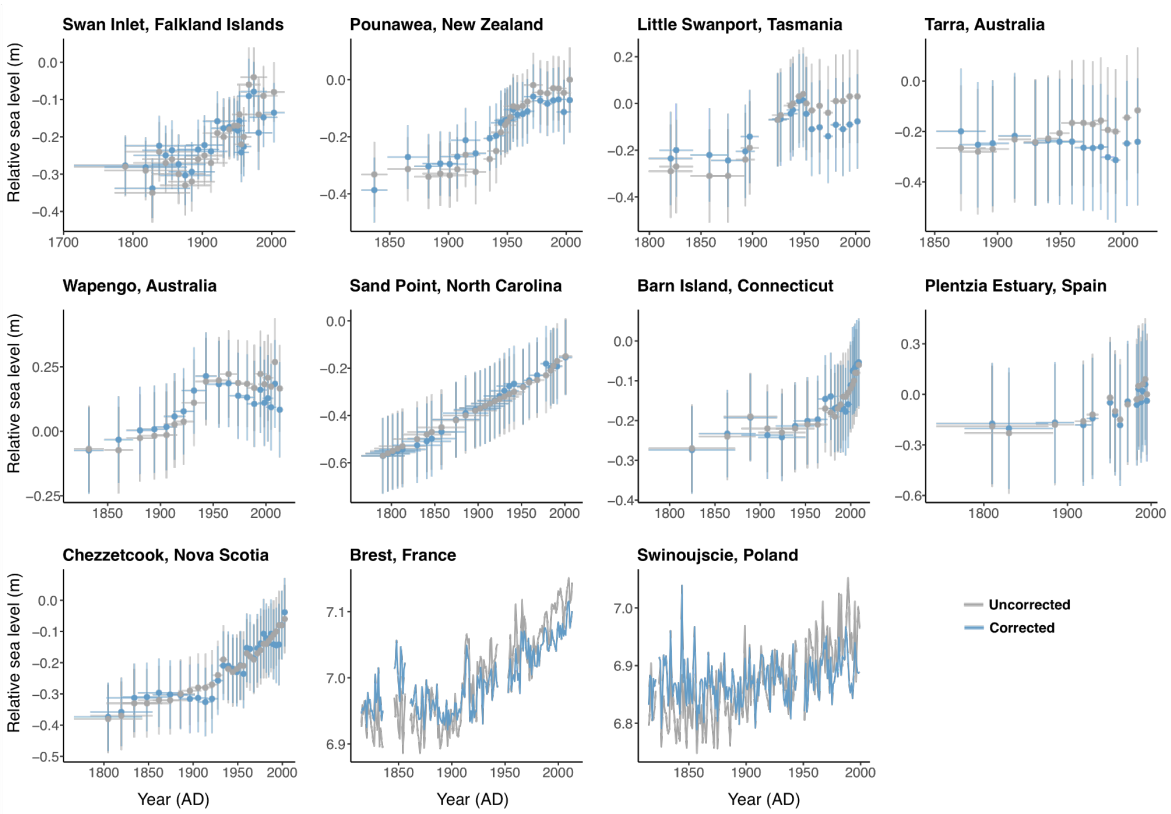

Figure 77. Comparison of sterodynamic uncorrected (grey) and corrected (blue) relative sea-level reconstructions at the salt marsh and tide-gauge sites.

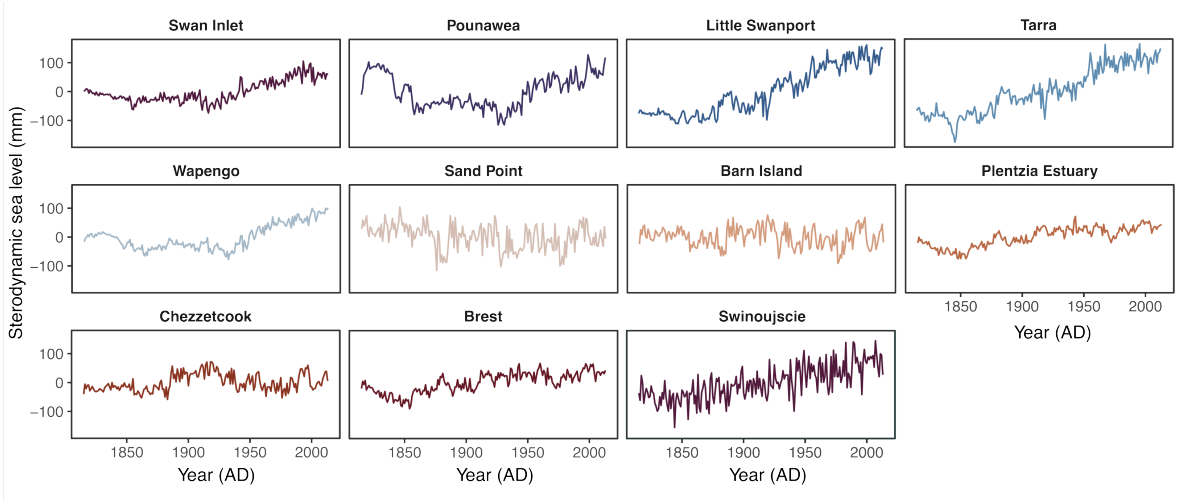

Figure 78. Time series of sterodynamic sea level at the fingerprinting sites from 1815 – 2013 from the SODAsi.3 ocean reanalysis model (Giese et al. 2016).

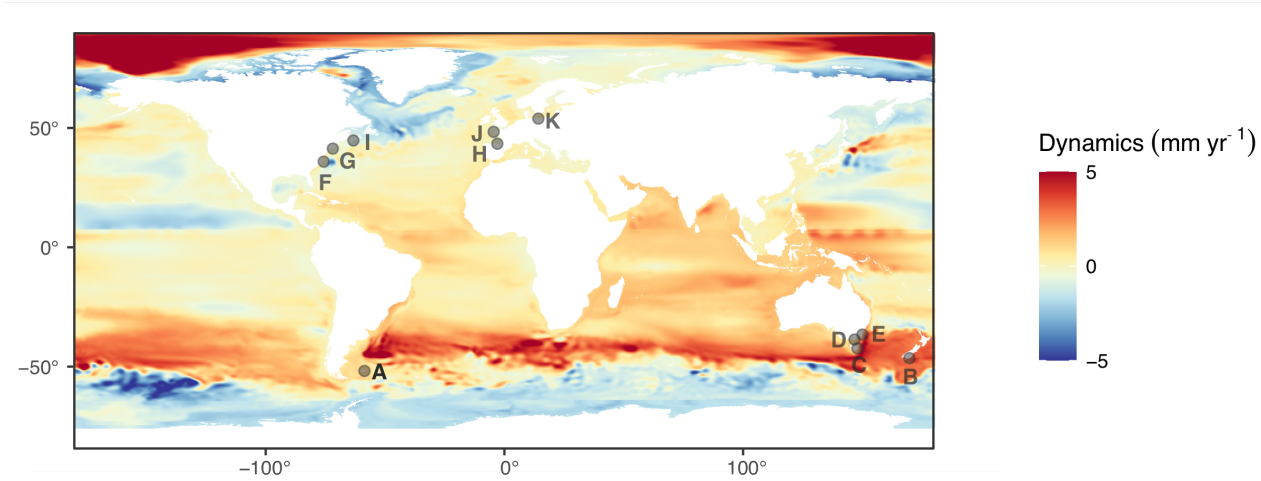

Figure 79. Global sterodynamic sea level from the SODAsi.3 ocean reanalysis model from 1815 – 2013 (Giese et al. 2016) showing linear trend differences between Period 1 (1815 – 1899) and Period 2 (1900 – 2013). Highlighted are **A.** Swan Inlet, **B.** Pounawea, **C.** Little Swanport, **D.** Tarra, **E.** Wapengo, **F.** Sand Point, **G.** Barn Island, **H.** Plentzia Estuary, **I.** Chezzetcook, **J.** Brest, **K.** Swinoujscie.

Sterodynamic-corrected RSL shows positive increases in sea level at the majority of sites over the 19th century, although there is a mean negative trend at Brest, Swinoujscie and Tarra (**Figure 80**). It must be noted that at Tarra the error is large over this period due to the

limited number of SLIPs in the 19th century, as well as the large vertical uncertainty of the available SLIPs. The corrected records from the Plentzia Estuary, Chezzetcook and Brest exhibit the greatest increases in sea-level rates from Period 1 (1815 – 1899) to Period 2 (1900 – 2013) (**Table 23**). This is followed by New Zealand and Swan Inlet in the Southern Hemisphere (**Table 23**). In the 20th century, the mean trend at the Little Swanport and Tarra sites is negative, although uncertainties are large.

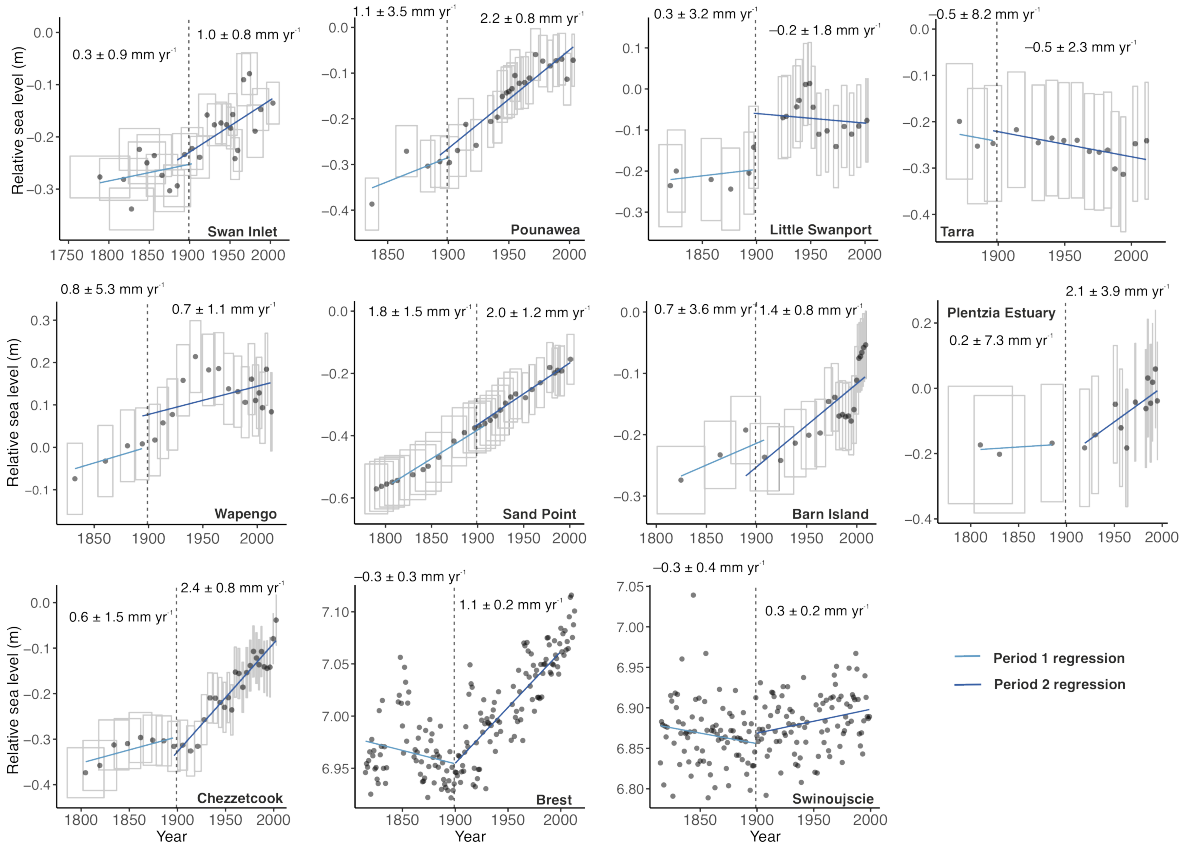

Figure 80. Comparison of Period 1 (1815 – 1899) and Period 2 (1900 – 2013) sterodynamic-corrected rates using error-in-variables regression or least squares regression for proxy records from Swan Inlet, Pounawea, Little Swanport, Tarra, Wapengo, Sand Point, Barn Island, Plentzia Estuary, Chezzetcook, Brest and Swinoujscie. Mean rates are denoted by the blue lines, 1 σ sea-level index point errors are denoted by the grey boxes and the mean of each index point is denoted by the grey dots. Rates are given to 2 σ.

Table 23. Calculated rates of sea-level rise at the sites using error-in-variables regression or linear least squares regression (marked by an asterisk) for Period 1 (1800 – 1899) and Period 2 (1900 – 2013). All units are given in mm yr^{-1}.

Site	Period 1 rate	Period 1 error (1 σ)	Lower (95 % uncertainty)	Upper (95 % uncertainty)	Period 2 rate	Period 2 error (1 σ)	Lower (95 % uncertainty)	Upper (95 % uncertainty)	Rate difference (P2-P1)	Error (1 σ)
Swan Inlet	0.3	0.5	-0.6	1.3	1.0	0.4	0.2	1.7	0.7	0.6
Pounawea	1.1	1.7	-2.6	4.4	2.2	0.4	1.4	3.0	1.1	1.8
Little Swanport	0.3	1.6	-2.9	3.5	-0.2	0.9	-1.9	1.6	-0.5	1.9
Tarra	-0.5	4.1	-8.6	7.6	-0.5	1.2	-2.8	1.6	0.0	4.2
Wapengo	0.8	2.7	-4.9	6.0	0.7	0.6	-0.4	1.7	-0.1	2.7
Sand Point	1.8	0.8	0.4	3.4	2.0	0.6	0.8	3.1	0.1	1.0
Barn Island	0.7	1.8	-3.1	4.6	1.4	0.4	0.6	2.2	0.7	1.8
Plentzia Estuary	0.2	3.7	-7.3	7.6	2.1	1.9	-1.7	6.1	1.9	4.2
Chezzetcook	0.6	0.7	-0.9	2.0	2.4	0.4	1.6	3.2	1.8	0.8
Brest *	-0.3	0.1	-0.5	0.0	1.1	0.1	0.9	1.2	1.3	0.2
Swinoujscie *	-0.3	0.2	-0.6	0.1	0.3	0.1	0.1	0.5	0.6	0.2

Using the empirical estimates and uncertainties of the contribution of glaciers and Ice Sheets to sea level over the 20th century from glaciers (Malles and Marzeion, 2021), Greenland (Kjeldsen et al. 2015) and Antarctica (Adhikari et al. 2018), an optimisation model was run to establish the likely contribution from each ice mass. The proportion of each ice masses' contributions were produced by evaluating the goodness of the fit of the predicted sea-level rise at each site, compared to the observations (*i.e.* minimising the difference between the predicted rates of sea-level rise and the observed rates of sea-level rise; **Figure 81**).

To understand the influence of each site on the ice-mass contributions (*i.e.* the geographic bias) jackknifing (leave-one-site-out) was employed. Jackknifing suggests that there is little difference between the optimised fingerprints and the bias-corrected fingerprints, implying that no one site has a dominant influence on the contribution estimates (**Table 24**). Where there are marginally larger differences between the optimisation results and the cross-validated results (as denoted by the orange values in **Table 24**), the ice-mass contribution estimates (*i.e.* the fingerprint weightings) tend to be influenced by the removal of the most southerly and northerly RSL sites, and it is generally the ice masses located furthest north that are affected, likely reflecting the effects of GRD.

Table 24. Fingerprinting results showing the mean contribution (*i.e.* the empirically derived mean contribution from each ice mass to sea level over the 20th century from the literature); Optimised contribution (*i.e.* the weighted fingerprint prediction (where population=200, F=[0.5,1.5], CR=0.5)); Jackknife results, X = Excluding, SI = Swan Inlet, PW = Pounawea, LSP = Little Swanport, TAR = Tarra, WAP = Wapengo, SP = Sand Point, BI = Barn Island, PE = Plentzia Estuary, CZ = Chezzetcook, B = Brest, S = Swinoujscie; Jackknife = the average of all jackknifing results; Diff = the difference between optimised fingerprint and the average jackknifed fingerprint for each ice mass and Corrected = the bias-corrected result (*i.e.* the difference between Diff and Optimised). f(x) is the difference between the observed and predicted values at each site. All values are given in mm yr^{-1}. Orange values show fingerprints with marginally larger differences which are more affected by the removal of a particular site.

Ice mass	Mean	Optimised	X-SI	X-PW	X-LSP	X-TAR	X-WAP	X-SP	X-BI	X-PE	X-CZ	X-B	X-S	Jackknife	Diff	Corrected
Alaska	0.06	0.14	0.14	0.14	0.14	0.14	0.14	0.14	0.14	0.14	0.14	0.08	0.14	0.13	0.01	**0.13**
Western Canada & US	0.04	0.10	0.10	0.10	0.10	0.10	0.10	0.10	0.10	0.10	0.10	-0.02	0.10	0.07	0.02	**0.07**
Arctic Canada North	0.08	0.04	0.10	0.04	0.06	0.04	0.05	0.07	0.04	0.04	0.02	0.02	0.14	0.05	-0.02	**0.05**
Arctic Canada South	0.06	0.02	0.02	0.02	0.02	0.02	0.02	0.02	0.02	0.02	0.02	0.02	0.07	0.03	-0.01	**0.03**
Iceland	0.01	0.00	0.00	0.00	0.00	0.00	0.00	0.00	0.00	0.00	0.00	0.00	0.00	0.00	0.00	**0.00**
Svalbard	0.04	0.05	0.05	0.05	0.05	0.05	0.05	0.05	0.05	0.05	0.03	0.03	0.03	0.04	0.01	**0.04**
Scandinavia	0.00	0.00	0.00	0.00	0.00	0.00	0.00	0.00	0.00	0.00	0.00	0.00	0.00	0.00	0.00	**0.00**

Russian Arctic	0.05	0.11	0.11	0.11	0.11	0.11	0.11	0.11	0.11	0.11	0.11	-0.01	0.11	0.08	0.02	**0.08**
North Asia	0.00	0.00	0.00	0.00	0.00	0.00	0.00	0.00	0.00	0.00	0.00	0.00	0.00	0.00	0.00	**0.00**
Central Europe	0.00	0.00	0.00	0.00	0.00	0.00	0.00	0.00	0.00	0.00	0.00	0.00	0.00	0.00	0.00	**0.00**
Caucasus and Middle East	0.00	0.00	0.00	0.00	0.00	0.00	0.00	0.00	0.00	0.00	0.00	0.00	0.00	0.00	0.00	**0.00**
Central Asia	0.05	0.07	0.07	0.07	0.07	0.07	0.07	0.07	0.07	0.07	0.07	0.07	0.07	0.07	0.00	**0.07**
South Asia	0.06	0.08	0.08	0.08	0.08	0.08	0.08	0.08	0.08	0.08	0.08	0.08	0.08	0.08	0.00	**0.08**
Low Latitudes	0.01	0.02	0.02	0.02	0.02	0.02	0.02	0.02	0.02	0.02	0.02	0.02	0.02	0.02	0.00	**0.02**
Southern Andes	-0.01	0.08	0.08	0.08	0.08	0.08	0.08	0.08	0.08	0.08	0.08	0.08	0.08	0.08	0.00	**0.08**
New Zealand	0.00	0.01	0.01	0.01	0.01	0.01	0.01	0.01	0.01	0.01	0.01	0.01	0.01	0.01	0.00	**0.01**
Greenland	0.21	0.17	0.17	0.17	0.17	0.17	0.17	0.17	0.17	0.17	0.17	0.17	0.17	0.17	0.00	**0.17**
West Antarctic	0.05	0.08	0.08	0.08	0.08	0.08	0.08	0.08	0.08	0.08	0.08	0.08	0.08	0.08	0.00	**0.08**
East Antarctic	0.00	0.03	0.03	0.03	0.03	0.03	0.03	0.03	0.03	0.03	0.03	0.03	0.03	0.03	0.00	**0.03**
	f(x)	*0.83*	*0.85*	*0.87*	*0.81*	*0.86*	*0.85*	*0.80*	*0.87*	*0.87*	*0.82*	*0.55*	*0.78*			

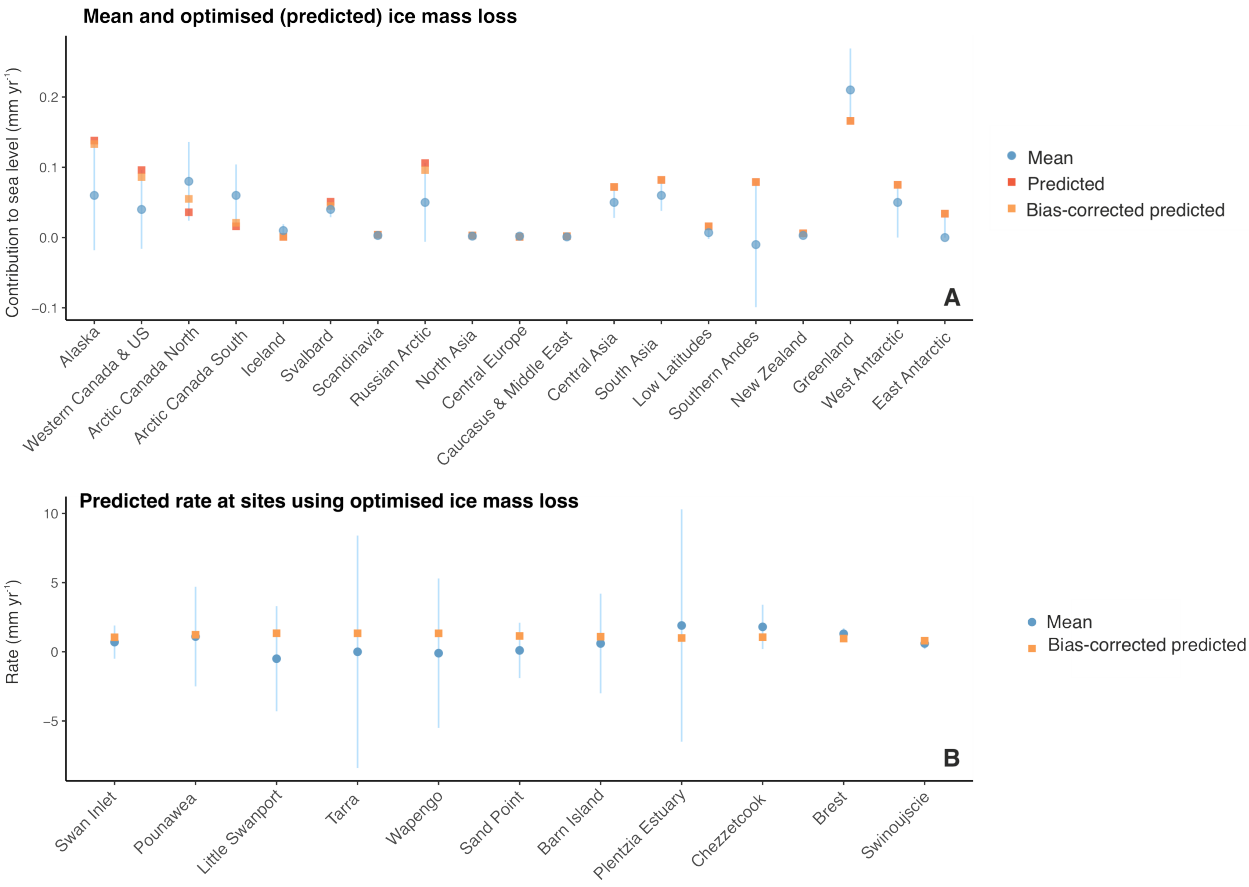

Figure 81. A. Mean ice mass loss (in sea-level equivalent to show contribution to sea level) from glaciers and the ice sheets over the 20th century. Blue circles and error bars show mean estimates and uncertainty from the literature (100 % confidence intervals), orange squares show the fingerprint optimisation (*i.e.* the predicted contribution) and yellow squares show the Jackknifed bias-corrected optimisation. **B.** Rates of sea-level rise at the global sites showing observed rates of sea-level rise calculated from error-in-variables analysis (blue circles and error bars - 2 σ) and Jackknifed bias-corrected predicted rates of sea-level rise using the optimised ice mass loss (yellow squares).

The results suggest that the largest contributions from glaciers have come from Alaska, western Canada and the US, the Russian Arctic, central and southern Asia as well as the southern Andes (**Figure 81; Table 24**). Large contributions from Alaskan glaciers to mid-late 20th century sea level are well documented in the literature showing ~30 % of glacier contributions to sea level came from Alaska between the 1960s – early 2000s (*e.g.* Box et al. 2018; Zemp et al. 2019). Empirical estimates suggest a contribution of Alaskan glaciers of ~8 % (equivalent to 0.06 mm yr^{-1}) from 1901 – 1990 (Malles and Marzeion, 2021). The optimised results suggest that Alaska contributed above the mean empirical estimates of Malles and Marzeion (2021), indicating Alaska was responsible for ~14 % of the rise (equivalent to ~0.13 mm yr^{-1} 1901 – 1990). Large mass losses from Alaska over the second half of the 20th century were associated with increasing summer temperatures (Arendt Luthcke and Hock, 2009; Bieniek et al. 2014; Winski et al. 2018), which may be related to both internal climate variability and increased sea surface temperatures (Christian et al. 2016).

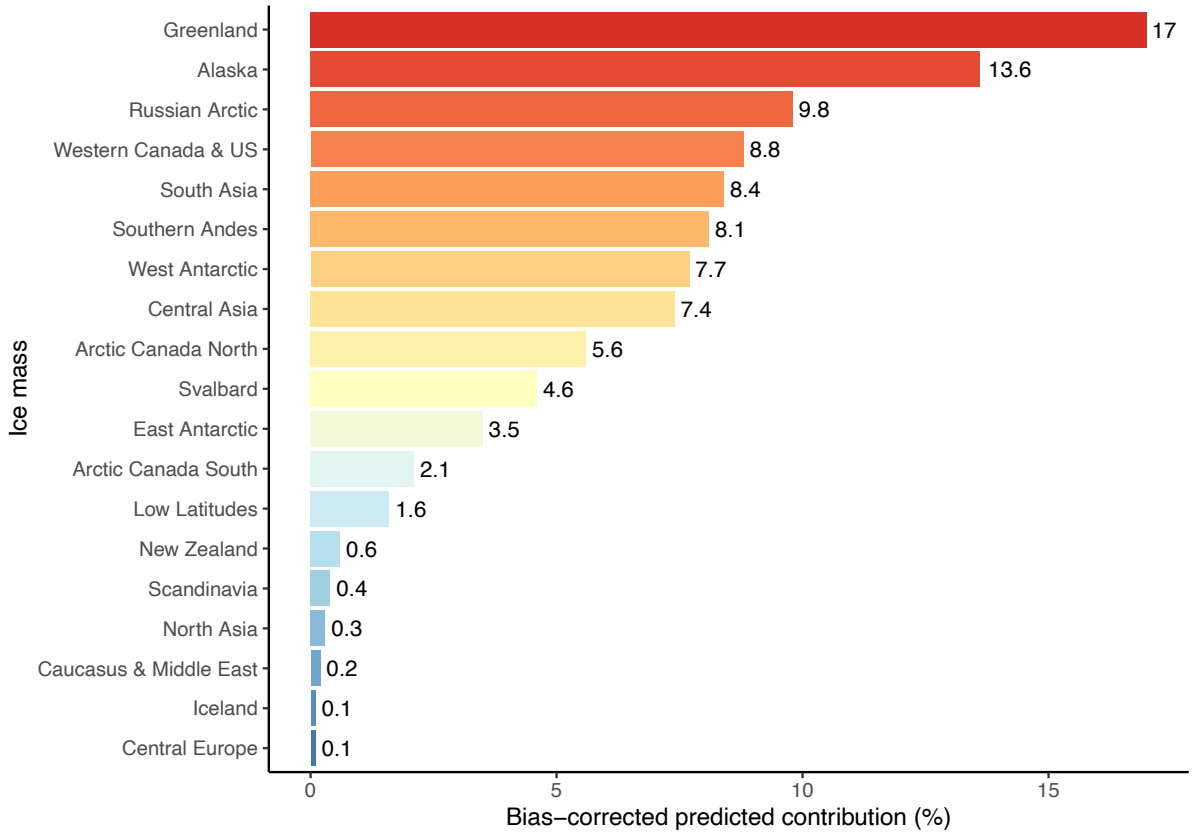

Figure 82. Bias-corrected predicted contribution from the ice masses to sea level over the 20th century estimated from the optimisation model.

The results also indicate ~10 % (0.10 mm yr^{-1}) of the observed sea-level rise came from the Russian Arctic, which is marginally more than empirical data suggest (~7 %; Malles and Marzeion, 2021). This region has been proposed as a large contributor to 20th century sea-level change in the literature after Alaska and Arctic Canada (Box et al. 2018; Malles and Marzeion, 2021; Zemp et al. 2019). For example, Box et al. (2018) states that, over 1971 – 2017, barystatic sea-level contributions from land north of ~55° were largest from Greenland (10.6 ± 7.3 mm), followed by Alaska (5.7 ± 2.2 mm), Arctic Canada (3.2 ± 0.7 mm) and the Russian Arctic (1.5 ± 0.4 mm). However, in comparison to Alaska and Canada, mass balance records from the Russian Arctic are sparse (Box et al. 2018), being limited both temporally as well as spatially due to the inaccessible nature of the environment.

In contrast to findings from the literature (Box et al. 2018; Gardner et al. 2011; Malles and Marzeion, 2021; Noël et al. 2018), the results do not suggest a significant input from Arctic Canada. Results suggest a contribution of only ~8 % when Arctic Canada North and South are combined which is ~0.08 mm yr^{-1}. This is 0.06 mm yr^{-1} less than the mean empirical estimate (Malles and Marzeion, 2021). However, Parkes and Marzeion (2018) found that there was poor agreement between estimates of the Arctic Canada contribution to sea level, and Malles and Marzeion (2021) note that the uncertainty for this region in their model is high. This may be because the region has a large number of marine-terminating glaciers for which statistical modelling does not take into account frontal ablation (therefore producing a discrepancy between statistically modelled estimates and observational estimates of ice mass loss (Hanna et al. 2020)).

For the Southern Hemisphere an 8 % contribution is estimated from the southern Andes. Glacier mass balance observations from the southern Andes are also temporally and spatially limited (with most mass loss histories only quantified over the 21st century; *e.g.* Bamber et al. 2018; Braun et al. 2019; Dussaillant et al. 2019; Wouters, Gardner and Moholdt, 2019). Furthermore, the different reconstruction methods produce variable results as this region, like Arctic Canada, has many marine-terminating glaciers (Hanna et al. 2020). Currently, evidence suggests that over the last few decades, most ice loss has come from the Patagonian Ice Fields (~0.05 ± 0.00 mm yr^{-1} Braun et al. 2019), but a 35-year long record has suggested the wider Andean Cordillera has lost mass, contributing on average ~0.10 mm yr^{-1} to sea level between 1979 – 2013 (Mernild et al. 2017). Zemp et al. (2019) suggests that relative mass changes were largest from the southern Andes from 1961 – 2016 out of any glaciated region on Earth.

The data also suggest above average contributions from central and south Asia (combined ~16 % equivalent to 0.15 mm yr^{-1}). Glaciers in the mountains of Asia have been losing mass since at least the 1960s and 70s (Bhattacharya et al. 2021; Dehecq et al. 2019; Farinotti et al. 2015; King et al. 2019; Zhou et al. 2018). The largest amount of mass loss in this region has occurred in the central-eastern Himalayas (Bhattacharya et al. 2021; Zhou et al. 2018) and Malles and Marzeion (2021) estimate a mean contribution of 0.11 mm yr^{-1} to sea level from glaciers in central and south Asia over the 20th century. Since the LIA, Himalayan glaciers have lost 0.92 – 1.38 mm SLE and Lee et al. (2021) state that the centennial-scale rates of change in mass exceed those observed anywhere else in the world. However, the large weighting of the Asian ice masses may also be a result of using the empirical estimates from Malles and Marzeion (2021) which are higher for central and south Asia than the previously published literature (*e.g.* Wouters, Gardner and Moholdt, 2019; Zemp et al. 2019).

The model shows the largest single barystatic contributor to sea-level rise over the 20th century was the GrIS (17 % equivalent to 0.17 mm yr^{-1}; **Figure 81**), which is largely consistent with observational estimates (Kjeldsen et al. 2015) which predict a ~0.21 mm yr^{-1} contribution over the 20th century. Greenland mass loss has been driven by atmospheric warming (Hanna et al. 2020) and reconstructions of Arctic temperatures suggest that significant warming occurred in the 19th century (Neukom et al. 2019). Trusel et al. (2018) reconstructed past melt rates from Greenland using refrozen melt layers in ice cores. They demonstrated that GrIS run off occurred from the mid 19th century in response to weakening of the Atlantic meridional overturning circulation and a shift to a negative North Atlantic Oscillation phase. The results from this study are furthermore supported by global sea-level data as Frederikse et al. (2020)

have attributed melting from the GrIS as a primary driver of global sea-level rise, especially from the 1940s.

Finally, the results also indicate an above average contribution from the Antarctic Ice Sheet (AIS) to sea level (~11 %). It had been thought until fairly recently that the East Antarctic Ice Sheet (EAIS) had been largely stable, contributing 0.01 ± 0.13 mm yr^{-1} between 1992 – 2017 (Shepherd et al. 2018). It was suggested that most mass loss had come from the West Antarctic Ice Sheet (WAIS; Shepherd et al. 2018). However, subsequent evidence using improved high-resolution datasets and updated SMB estimates has suggested that, whilst most of the acceleration has indeed come from the WAIS (0.13 mm SLE yr^{-1} $decade^{-1}$), contributions from the EAIS have also accelerated at 0.08 mm SLE yr^{-1} $decade^{-1}$ (Rignot et al. 2019). Rignot et al. (2019) stated that over the last four decades, the cumulative contribution to sea level from the EAIS is close to that of the WAIS, and that their observations challenge the conventional view that the EAIS is/has been stable. This study also challenges this view and suggests more melt may have come from the AIS than previously assumed.

Over the 20th century, most of the mass loss of the AIS has been dominated by dynamic ice loss (Bamber et al. 2018; Hanna et al. 2020), with increased sea-surface temperatures and the upwelling of saline deep circumpolar water likely drivers (Rignot et al. 2019). Rignot et al. (2019) found evidence of dynamic ice loss from as early as the 1970s, as well as periglacial retreat from the 1960s. Furthermore, significant warming trends have been found over much of the AIS since at least the 1950s (Abram et al. 2013; Bromwich et al. 2013; Steig et al. 2009). Like Greenland, this warming has also been attributed to early greenhouse gas emissions as well as internal climate variability (namely strengthening of the SAM) which has been driven

by atmospheric circulation changes resulting from ozone depletion (Abram et al. 2013). This therefore suggests future work may seek to further constrain AIS mass loss over the recent past to better understand the contributions of the WAIS, EAIS and Antarctic Peninsular to sea level over the 20th century.

7.1.5 Limitations to the fingerprinting study and improving estimates of the barystatic GRD contribution to sea level

Despite recent improvements to quantify mass loss of the AIS over the late 20th century, it remains very poorly constrained in comparison to the GrIS (largely due to its considerable extent which increases the uncertainty of SMB and GIA estimates (Shepherd et al. 2018). Unfortunately, there are only a few approaches available to constrain the mass loss history prior to the satellite era (*e.g.* sea-level fingerprinting and ice cores) and, currently, mass balance data only extend back the last four decades (Rignot et al. 2019). This is a large limitation to this study, as it was assumed that the late 20th century contribution of Antarctica was representative of the whole century.

Furthermore, some evidence has pointed to an underestimation of both mass balance and SMB of the AIS even over the last few decades. For example, Agosta et al. (2019) stated that AIS SMB may have been miscalculated due to underestimating continental-scale sublimation and Sutterley et al. (2014) found that satellite altimetry was underestimating mass loss of the WAIS when compared to observational data. Hanna et al. (2020) suggested that the difference in mean mass loss estimates of 62 Gt yr^{-1} between Shepherd et al. (2018) and Rignot et al. (2019) likely arose from uncertainties in ice thickness and modelled SMB, as well as uncertainty in

GIA when processing GRACE data. Hanna et al. (2020) further noted that the range of mass loss estimations from the AIS does not seem to be reducing with time, and state that there is a lack of advancement in the mass balance determination methods, which is hindering a good understanding of AIS mass balance over the recent past. Shepherd et al. (2018) stated that further SMB model improvements, validations and intercomparisons are needed for EAIS mass balance and Rignot et al. (2019) suggested that more focus be placed on understanding mass loss of the EAIS.

There are several ongoing developments which are improving estimates of historical ice sheet mass balance over the 20th century. For both the AIS and the GrIS, there are efforts to improve estimates of SMB via the SMB Model Intercomparison Project (SMB_MIP (Fettweis et al. 2020)). This project aims to standardise model comparisons and evaluation using *in situ* and satellite data (Hanna et al. 2020) which will help to inform which model outputs are the most reliable/realistic. Another solution as mentioned in **Chapter 2** is to downscale regional climate models to more accurately model ice sheet mass balance (Noël et al. 2018). The Randolph Glacier Inventory and the Greenland Ice Mapping Project have recently produced high-resolution digital elevation models and glacier outlines of the GrIS (and its peripheral glaciers) which better represent boundary conditions for numerical modelling and statistical downscaling (van den Broeke et al. 2017). Expanding the long-term glaciological measurement programmes and glacier front observations in space and time will also aid with quantifying contributions to sea level over the recent past.

Additionally, extending ice sheet mass-balance histories by incorporating empirical evidence from ice cores into mass balance models has recently been shown to be highly effective (Trusel

et al. 2018) and could be used to inform models in the future (*e.g.* Abram et al. 2013; Briner et al. 2020; Das and Alley, 2008; Trusel et al. 2018). Furthermore, the use of high-resolution RSL reconstructions in close proximity to the ice sheets may also help to inform about past barystatic GRD contributions (*e.g.* Long et al. 2010). Ongoing improvements to GIA models (*i.e.* shifting from 1D models which assume a uniform lateral rheology to 3D models that more accurately model the different rheologies) and allowing the GIA rate to vary through time (rather than assuming a temporally constant rate) will also improve estimates as currently, GIA models are large sources of uncertainty in AIS mass balance models (*e.g.* Gomez, Latychev and Pollard, 2018; Hanna et al. 2020; Whitehouse et al. 2019).

Whilst glacier mass-balance histories are largely better resolved than those for the ice sheets, there are still issues with the spatial distribution of mass balance records which are biased to easily accessible regions such as western North America, central Europe, New Zealand, Scandinavia and Iceland (Zemp et al. 2015). As mentioned in section 7.1.4, there is a paucity of data in more inaccessible regions such as the peripheral glaciers of the AIS, Arctic Canada, Arctic Russia and the low latitudes (Zemp et al. 2015). The mass-balance histories of these understudied regions will likely be better resolved as improvements are made to modelling techniques and reconciling statistical, observational and altimetry data.

This study used estimates of glacier contribution to sea level from Malles and Marzeion (2021) as these modelled results extend furthest back into the 20th century (from 1900) and because they are the most recent estimates with the most up-to-date validation data and Randolph Glacier Inventory version. As previously mentioned, there are some differences between the mass balance estimates of individual glacier regions over the late 20th century between Malles

and Marzeion (2021) and previously published literature (Bamber et al. 2018; Wouters, Gardner and Moholdt, 2019; Zemp et al. 2019; see Table 4 in Malles and Marzeion, 2021) which will bias the optimisation model; however, the authors note their estimates do mostly lie in the uncertainty of the global estimations (with a maximum of ~0.2 mm yr^{-1} difference between their estimations and other estimations from the literature over the same time periods). Furthermore, many of the fingerprints are predicted at their lower or upper empirical uncertainty **(Figure 81**), which suggests that the bounds should either be extended, or that probabilities could be placed on the mean and confidence intervals to reconcile this. This may, however, significantly increase computational time, which may necessitate the removal of and or combination of ice masses to reduce the number of observations.

Finally, the optimisation model would greatly benefit from more sea-level observations, specifically from those in locations from which the fingerprinting source can be more easily identified as the results tend to underpredict contributions from Arctic Canada and perhaps overpredict for some of the regions such as the southern Andes and western Canada and the US. For example, to better quantify AIS mass loss, we should reconstruct sea level for sites located in areas sensitive to Southern Hemisphere ice loss where we can use gradients of RSL rise to distinguish the ice mass. An area of particular interest would be the east coast of South America (taking into account the effect of localised GRD; **Figure 83**). Whilst the fingerprint of WAIS mass loss would be also observed along the Chilean coast, it would there be overprinted by earthquake deformation cycles, which cannot currently be sufficiently accounted for to provide tectonically corrected reconstructions (Garrett et al. 2020; Wesson et al. 2015). Some sections of the coastline are also affected by the Patagonian Ice Fields **(Figure 83**).

Other areas of interest to better quantify AIS loss would also be the southern tip of South Africa and southwestern Australia. Whilst there are a couple of RSL reconstructions in South Africa (Compton, 2001; Strachan et al. 2014), they are not at a high enough temporal resolution to study 20th century ice mass contributions, and there are currently no high-resolution RSL records from Western Australia. Also of interest would be an investigation into sites in the low latitudes, where both the GrIS and AIS signals should be present. For example, some high-resolution coral records have been used to reconstruct Holocene sea level in the Pacific (Goodwin and Harvey, 2008; Hallmann et al. 2018; Majewski et al. 2022; Woodroffe et al. 2012) and future work could seek to quantify the barystatic contribution from both sources, which in theory, should be greatest in this region.

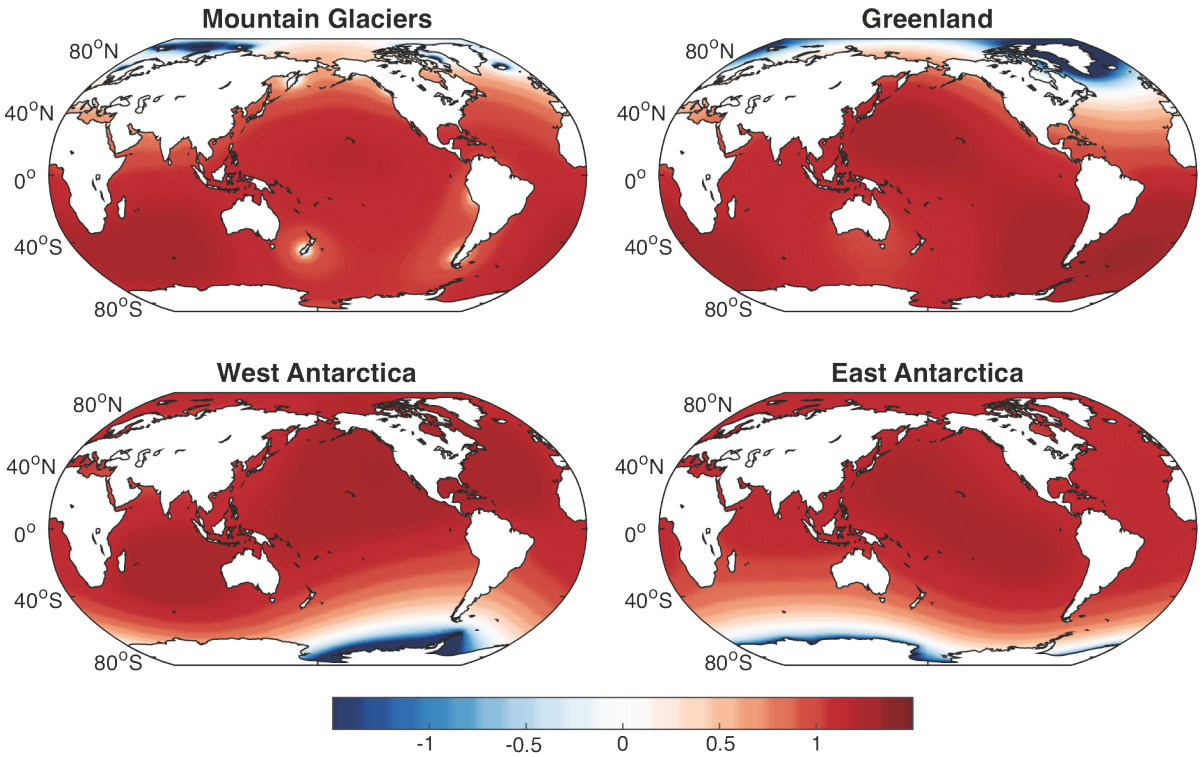

Figure 83. The gravitational, rotational and deformational effects (or "fingerprints") of Mountain Glaciers, the Greenland Ice Sheet, West Antarctic Ice Sheet and East Antarctic Ice Sheet (all excluding peripheral glaciers).

7.2 Summary

This chapter has assessed the magnitude and rate of sea-level rise in the new RSL records from southeastern Australia and compared them with instrumental data from the wider Indo-Pacific, as well the global average and a modelled sea-level budget. Over the early 20th century, rates of sea-level rise from Lutregala and Tarra agree more with tide-gauge data from the Indo-Pacific and the global average. However, over the second half of the 20th century, the rates of sea-level rise at Wapengo and Little Swanport decrease, which agrees better with the instrumental data, but the average rates of sea-level rise at Lutregala are far higher. The differences in both the magnitude of sea-level rise, as well as the timing of the onset in the RSL records may be attributable to a variety of linear and non-linear processes.

Varying the GIA rate does marginally change the onset of the acceleration in each reconstruction (especially for Tarra), and can account for, in part, some of the discrepancy between the onset of the acceleration between the records. However, assessing the Ea0 shows that even when accounting for uncertainty in GIA, the timing of the Ea0 is different for each site, and is especially disparate between the Lutregala and Little Swanport records (despite them being located in close spatial proximity). This suggests that there are other non-linear drivers of change causing the regional variability in sea level witnessed in the reconstructions. It remains unclear whether the variability has been driven by the foraminifera themselves (*i.e.* as a result of issues regarding re-working and infaunality), whether it is the response of the foraminifera to more localised changes in tidal range driven by waves, wind or atmospheric pressure changes, or whether it is a result of varying sterodynamic contributions to sea level.

Currently, the budget shows that initially, the rapid rates were driven by the barystatic component ~1920 – 1940, but that rates were subsequently amplified and driven by the sterodynamic component where maximum rates were reached in the mid 20th century. Future work may seek to employ an ensemble of sterodynamic estimates to better estimate the sterodynamic contribution over the 20th century and or may seek to assess the timing of emergence of the modern acceleration in sea level using a more robust statistical approach such as that employed by Walker et al. (2022).

To assess the contribution of the barystatic component to sea-level rise over the 20th century, the new records (excluding Lutregala as the record only starts in the last decade of the 19th century), together with published sea-level reconstructions and long tide-gauge records, were compared with sea-level fingerprints from melting ice masses. To find the combination of ice

masses that best fit the sea-level observations, an optimisation model was employed. The results suggest that the GrIS was the single largest barystatic contributor to sea-level rise over the 20th century, followed by Alaska, the Russian Arctic and western Canada and the US. This largely agrees with results found in the literature (*e.g.* Bamber et al. 2018; Box et al. 2018; Kjeldsen et al. 2015; Noël et al. 2018; Zemp et al. 2019), but the fingerprinting results suggest a bigger contribution from western Canada and the US, and a smaller contribution from Arctic Canada than is suggested in the literature from glaciological records and models (Box et al. 2018; Malles and Marzeion, 2021; Noël et al. 2018). Results also suggest a significant contribution from Southern Hemisphere land-based ice such as the southern Andes and the AIS. The contributions from these ice masses to 20th century sea level are more uncertain in the glaciological literature (*e.g.* Braun et al. 2019; Dussaillant et al. 2019; Rignot et al. 2019; Shepherd et al. 2018; Wouters, Gardner and Moholdt, 2019; Zemp et al. 2019), and this suggests that the optimisation model would benefit from further sea-level observations, especially in areas sensitive to Southern Hemisphere ice loss.

The model used in this study is especially limited by empirical estimates of the AIS contribution to sea level due to the poorly constrained mass loss history. Future work will rely on a better constraint of AIS mass loss over the 20th century, especially that before the satellite era. Whilst the study uses the most up-to-date and longest term estimations of glacier contribution to sea level over the 20th century, Malles and Marzeion (2021) note that mass loss estimates of some glacier regions are different to those previously estimated in the literature (*e.g.* Wouters, Gardner and Moholdt, 2019; Zemp et al. 2019), and the results from this study are biased towards the empirical estimations from that study. It is clear that more work is needed to better constrain the ice mass loss history of glaciers in more remote locations and

the ice sheets over the 20th century and into the 19th century and beyond. Future work therefore may seek to combine modelling with proxy records such as has been done by Trusel et al. (2018) for the GrIS in order to quantify ice loss over longer time scales.

Chapter 8 of 8

Conclusions

8.0 Introduction

This thesis has generated RSL reconstructions for three sites in southeastern Australia: Lutregala salt marsh (Bruny Island, Tasmania), Wapengo salt marsh (New South Wales) and Tarra salt marsh (Victoria) (**Chapter 3**). The sites were chosen because previous work from Little Swanport, Tasmania (Gehrels et al. 2012) suggested that the sea-level acceleration between ~1850 and ~1950 was more rapid in southeastern Australia than from comparable records from the North Atlantic (**Chapter 1**). Instrumental records from tide gauges from the region are too short to capture the acceleration, and so further records were needed to confirm the rapid rates of the Little Swanport reconstruction.

Therefore, this study set out to test the hypotheses that:

(i) *Sea-level rise between ~1850 and ~1950 was faster in southeastern Australia than in the North Atlantic region.*

If confirmed, geophysical theory predicts that far-field (*i.e.* Northern Hemisphere) ice melt could explain the difference. Therefore, a second hypothesis to be tested in this study was that:

(ii) *Arctic land-based ice melt was responsible for the global sea-level acceleration(s) between ~1850 and ~1950.*

The new sea-level reconstructions for southeastern Australia were established to test these hypotheses (**Chapter 6**) in conjunction with a comprehensive review of land-ice contributions

to regional and global sea-level change during the 20th century (**Chapters 2 and 7**). This was achieved through the following objectives:

1. Record and analyse the distribution of modern foraminiferal assemblages from salt marshes in southeastern Australia to create new sea-level transfer function models for the region (**Chapter 5**).
2. Document the stratigraphy of the sites and undertake foraminiferal analyses on representative salt-marsh cores (**Chapter 6**).
3. Establish a chronology for each core using a multiple dating approach (**Chapter 6**).
4. Reconstruct the timing and magnitude of sea-level rise across southeastern Australia at three sites (**Chapter 6**).
5. Compare the novel sea-level records to sea-level fingerprint models, ocean dynamic models and historical records of ice melt (**Chapter 7**).

This chapter summarises the main findings of this study.

8.1 Sea-level transfer functions

Chapter 5 presented two new local training sets for southeastern Australia from Lutregala and Wapengo, as well as (sub)regional training sets which both included and excluded samples from the previously published Little Swanport site. The local training set for Tarra was excluded from the regional model because the local transfer function model performed poorly, with samples largely predicted at the same elevation. When samples from Tarra were

combined with samples from Wapengo and Lutregala, it also reduced model precision and did not provide a wider range of potential analogues for fossil samples.

PAM and silhouette analysis showed samples were clustered into three distinct biozones, grouped by elevation (*i.e.* frequency of tidal inundation). The local transfer functions for Lutregala and Wapengo performed well and were able to predict sea level with decimetre-scale precision; however, when Little Swanport samples were included in a regional model with the Lutregala and Wapengo samples, it reduced the vertical precision of the model. Again, including the samples did not provide a wider range of analogues than the training set comprised of samples from Lutregala and Wapengo, therefore they were not included in the final regional training set (Regional II).

The performance of the classical models were compared with Bayesian transfer functions. The comparison showed that the Bayesian transfer functions had marginally higher vertical precision for the local training sets, and marginally lower precision for the regional training set. Overall, analysis showed that using the Bayesian models for the RSL reconstructions would not result in significantly different reconstructions to those generated using the classical models.

8.2 Sea-level reconstructions

Chapter 6 presented the stratigraphy, fossil foraminifera, PMSE estimates, chronologies and RSL reconstructions for Lutregala, Wapengo and Tarra (as well as a RSL reconstruction for Little Swanport updated using the SHCal20 radiocarbon calibration curve). At all sites, the

stratigraphy of the marshes were comprised of three main units, containing a basal unit of a Holocene sand or silt (often characterised by yellow mottling), overlain by a brown-grey tidal flat silt and topped by a unit of salt-marsh peat. PMSE estimates ranged from 0.64 – 1.33 m with uncertainties of 0.6 – 0.12 m (1 σ). The reliability of the modern foraminifera as sea-level indicators was assessed using the MAT. This showed that all fossil samples had at least a fair modern analogue using either a local or the regional II training set.

Chronologies were established using multiple dating methods including ^{14}C AMS, radiogenic lead (^{210}Pb), stable lead isotopes and pollen. The dating resolution was high from present back to ~1830 but decreased significantly below this depth due to a lack of dateable organic material in the cores, as well as there being no further anthropogenic chronohorizons. As the dating resolution declined significantly before ~1830 and because foraminifera in the silt and sand units of the cores were incongruous with the sedimentology (perhaps suggesting reworking and or issues with test preservation) sea level was only reconstructed from the organic units of the core. In total, records span from ~1830 – 2018.

The new reconstructions suggest that sea level has risen by ~0.2 – 0.3 m over the last 200 years. Although both the timings and magnitudes differ between sites, all sites showed evidence of a sea-level acceleration in either the late 19th century or early 20th century, in agreement with the Little Swanport reconstruction (Gehrels et al. 2012) and thus confirming the first hypothesis of this study.

8.3 Drivers of sea-level change in southeastern Australia

Inter-site variability in southeastern Australian RSL in the early 20th century may be attributed to a variety of both linear and non-linear processes. The influence of GIA uncertainty on the timing of the acceleration was ascertained by observing how detrending by the minimum (lower 95 % CI), median and maximum (upper 95 % CI) rate affected the timing of Ea0 (*i.e.* the onset of acceleration). Whilst detrending the records using different GIA rates did affect the timing of the Ea0, the effect was minimal (typically on the order of years), especially for Lutregala, Wapengo and Little Swanport. This suggests that non-linear processes are primarily responsible for the variability in the RSL reconstructions. Currently, it remains unclear what is causing this disparity. Differences could be a result of the foraminifera themselves (re-working and/or infaunality), the response of the foraminifera to changes in the local tidal range (perhaps as a result of wind, wave or atmospheric pressure-induced changes) and/or changes in RSL driven by local sterodynamic sea level.

The barystatic GRD and IBE components remained largely consistent between sites. Maximum average rates of sea-level rise were high in the early 20th century, reaching up to 4.0 (-0.4 – 7.1) mm yr^{-1} between 1900 – 1949. The budget showed that initially, the barystatic GRD component drove the acceleration, contributing ~1.6 mm yr^{-1} to sea level between 1900 – 1949. However, from ~1930 – 1940, the sterodynamic component amplified and subsequently drove sea level, contributing up to ~4.0 mm yr^{-1} at its peak in the mid 20th century. The second hypothesis tested in this thesis suggested that barystatic sea level was the driver of the 1850 – 1950 acceleration; however, the study has brought to light new evidence which indicates that the sterodynamic component (as a result of changes in ocean density and

circulation caused by increased sea surface temperatures, changes in wind stress, increasing overturning circulation and phase changes in dominant climate modes) was the primary driver of the acceleration. Therefore, the hypothesis is rejected and instead, it is proposed that a combination of both sterodynamic and barystatic sea-level rise drove the sea-level acceleration between 1850 and 1950, with sterodynamic sea level the main cause of the acceleration.

8.4 Contributions of melting land ice to 20th century global sea level

Sea-level fingerprinting analyses in **Chapter 7** demonstrated that the largest single barystatic contributor to global sea level in the 20th century was the GrIS (17 %). Observational evidence for the GrIS only extends to 1900, but data suggest significant losses from the early 20th century (especially between 1920 – 1940). Furthermore, melt layers in ice cores suggest mass loss from the GrIS since the mid 19th century (Kjeldsen et al. 2015; Trusel et al. 2018) which suggests melting has occurred since the onset of industrial-era warming.

The fingerprinting results also suggested significant contributions have likely come from Alaska (14 %), the Russian Arctic (10 %), Western Canada and the US (9 %), central and southern Asia (16 % combined) and the southern Andes (8 %). This largely agrees with the literature (*e.g.* Malles and Marzeion, 2021; Wouters, Gardner and Moholdt, 2019; Zemp et al. 2019), although the results do not suggest as large a contribution from Arctic Canada (8 %) which is in contrast to most other recent findings (*e.g.* Noël et al. 2018). This may be a result of using the empirical estimates from Malles and Marzeion (2021) for which Arctic Canada has a large uncertainty due to the high number of marine-terminating glaciers in the region.

The results also suggest significant mass loss from some Southern Hemisphere sources including the AIS (11 %) and southern Andes (8 %). Mass loss from the southern Andes is only really well constrained over the early 21st century, but longer-term evidence suggests that the Andean Cordillera has been losing mass since at least the second half of the 20th century. Mass loss from the AIS remains subject to debate, with large uncertainty between estimates for the late 20th century. Some recent work, however, suggests significant loss from both the WAIS and EAIS since at least the 1960s and 1970s (Rignot et al. 2019). It is clear that further work is still needed in order to quantify loss over the 20th century (Hanna et al. 2020; Rignot et al. 2019; Shepherd et al. 2018).

To conclude, this study has generated three new RSL reconstructions for southeastern Australia. The new records demonstrate that early 20th century sea level was more rapid in southeastern Australia than in comparable records from the Northern Hemisphere. The barystatic component likely initiated the sea-level acceleration, with contributions from the GrIS, AIS and other large, glaciated regions such as Alaska, the Russian Arctic and Asia. It is probable that these ice bodies have lost mass in response to natural climate variability, as well as anthropogenically-induced climate change (driven primarily by greenhouse gas emissions). However, the hypothesis is rejected as this study adds further evidence which suggests that a combination of both barystatic and sterodynamic contributions drove the acceleration in southeastern Australia, with the sterodynamic component primarily responsible for the rapid rates (especially between 1930 – 1950).

8.5 Recommendations for future work

From this study, the following recommendations for future work are drawn:

As documented in **Chapter 7**, it is clear that high-resolution RSL studies can help to better quantify longer-term ice-mass loss beyond the satellite era, but that more observations are needed, in particular from the Southern Hemisphere. Currently, there remains large uncertainties of 19th and early 20th sea level in the South Atlantic Ocean and South Pacific Ocean. Future research efforts should be placed on targeting sites on the west coast of South America, the southern tip of South Africa, southwestern Australia and the low latitudes which would help to better constrain the uncertainties in these regions. Furthermore, the, sites could be chosen to exploit gradients of the barystatic GRD fingerprint of ice mass loss (*i.e.* using transects of sites north to south) which will help to elucidate whether the fingerprint of Northern or Southern Hemisphere ice loss is captured in RSL records.

Additionally, future studies should attempt to better quantify contributions of glaciers and the ice sheets to GMSL over the last two centuries, as currently this represents a large uncertainty. Whilst the 20th century contribution of the GrIS is largely now well quantified, uncertainty remains prior to ~1900. Similarly, for some glaciers (namely those in accessible regions such as North America and Europe), the 20th century contributions are also well understood, but for glaciers in the Russian Arctic and Southern Hemisphere, even the 20th century mass-balance histories are not well determined. Likewise, the AIS mass balance is very poorly constrained over the 20th century due to its considerable size. Therefore, of great importance will be understanding the early-mid 20th century contributions, and ideally the

19th century mass balance history of the ice sheets. Perhaps of primary importance is to better constrain mass losses in more remote locations over the 20th century (a similar issue was highlighted by Parkes and Marzeion (2018) of the importance of including small and disappeared glaciers in the estimation of the contribution to 20th century sea level) and subsequently to try to extend all histories into at least the 19th century to better understand their histories since the LIA. This may be achieved by combining ice-core studies with sea-level fingerprinting studies to quantify mass loss over longer time scales. Both approaches, or the combined approach, may then help to inform statistical models to improve mass balance models and estimates.

This study has also shown that it is valuable to assess the effect of uncertainty in GIA on RSL records and consider how this may affect the timing in the onset of the acceleration and the magnitude of RSL change. Detrending records via the minimum, median and maximum rates may be especially important for RSL reconstructions which reconstruct sea level back through the Common Era and beyond into the late Quaternary where the effect of GIA uncertainty becomes larger.

Finally, the sterodynamic component of 20th century sea-level change needs to be better constrained. Results from **Chapter 6** have demonstrated that using ocean reanalysis models to reconstruct sterodynamic sea level is of crucial importance for understanding the drivers of RSL; however, only one estimate of sterodynamic sea level was used in this study. Therefore, future work should seek to develop and use multiple ocean reanalysis products with ensemble uncertainties that may more accurately model sterodynamic contributions. Furthermore, this study has demonstrated that variability between RSL records is attributable

to differences in dynamic regimes, therefore future work may further assess the role of ocean circulation changes in explaining regional differences between individual locations. It has also shown that comparing RSL reconstructions to a sea-level budget is valuable in regions where there is limited temporal and spatial availability of reliable tide-gauge data. Therefore, studies may seek to compare RSL records to a modelled sea-level budget alongside tide-gauge records to assess the reliability of the proxy data.

References

Abram, N. J., McGregor, H. V., Tierney, J. E., Evans, M. N., McKay, N. P. and Kaufman, D. S. (2016). Early onset of industrial-era warming across the oceans and continents. *Nature*, 536 (7617), 411–418. doi:10.1038/nature19082.

Abram, N. J., Mulvaney, R., Wolff, E. W., Triest, J., Kipfstuhl, S., Trusel, L. D., Vimeux, F., Fleet, L. and Arrowsmith, C. (2013). Acceleration of snow melt in an Antarctic Peninsula ice core during the twentieth century. *Nature Geoscience*, 6 (5), 404–411. doi:10.1038/ngeo1787.

Abu-Zied, R. H. and Bantan, R. A. (2013). Hypersaline benthic foraminifera from the Shuaiba Lagoon, eastern Red Sea, Saudi Arabia: Their environmental controls and usefulness in sea-level reconstruction. *Marine Micropaleontology*, 103, 51–67. doi:10.1016/j.marmicro.2013.07.005.

Adhikari, S., Caron, L., Steinberger, B., Reager, J. T., Kjeldsen, K. K., Marzeion, B., Larour, E. and Ivins, E. R. (2018). What drives 20th century polar motion? *Earth and Planetary Science Letters*, 502, 126–132. doi:10.1016/j.epsl.2018.08.059.

Agosta, C., Amory, C., Kittel, C., Orsi, A., Favier, V., Gallée, H., van den Broeke, M. R., Lenaerts, J. T. M., van Wessem, J. M., van de Berg, W. J., et al. (2019). Estimation of the Antarctic surface mass balance using the regional climate model MAR (1979–2015) and identification of dominant processes. *The Cryosphere*, 13 (1), 281–296. doi:10.5194/tc-13-281-2019.

Alley, R.B., Clark, P.U., Huybrechts, P. and Joughin, I., (2005). Ice-sheet and sea-level changes. *Science*, *310* (5747), 456-460 doi:10.1126/science.1114613.

Andresen, C. S., Kokfelt, U., Sicre, M.-A., Knudsen, M. F., Dyke, L. M., Klein, V., Kaczmar, F., Miles, M. W. and Wangner, D. (2017). Exceptional 20th century glaciological regime of a major SE Greenland outlet glacier. *Scientific reports*, 7 (1), 1–8. doi: 10.1038/s41598-017-13246-x.

Andresen, C. S., Straneo, F., Ribergaard, M. H., Bjørk, A. A., Andersen, T. J., Kuijpers, A., Nørgaard-Pedersen, N., Kjær, K. H., Schjøth, F., Weckström, K., et al. (2012). Rapid response of Helheim Glacier in Greenland to climate variability over the past century. *Nature Geoscience*, 5 (1), 37–41. doi:10.1038/ngeo1349.

Appleby, P. G. and Oldfield, F. (1978). The calculation of lead-210 dates assuming a constant rate of supply of unsupported ^{210}Pb to the sediment. *Catena*, 5 (1), 1–8. doi: 10.1016/S0341-8162(78)80002-2.

Apthorpe, M. (1980). *Foraminiferal distribution in the estuarine Gippsland Lakes system, Victoria*. Proceedings of the Royal Society of Victoria.

Aquino-López, M. A., Ruiz-Fernández, A. C., Blaauw, M. and Sanchez-Cabeza, J.-A. (2020). Comparing classical and Bayesian ^{210}Pb dating models in human-impacted aquatic environments. *Quaternary Geochronology*, 60, 101106. doi:10.1016/j.quageo.2020.101106.

Arendt, A. A., Luthcke, S. B. and Hock, R. (2009). Glacier changes in Alaska: can mass-balance models explain GRACE mascon trends? *Annals of Glaciology*, 50 (50), 148–154. doi:10.3189/172756409787769753.

Augustinus, P., Barton, C. E., Zawadzki, A. and Harle, K. (2010). Lithological and geochemical record of mining-induced changes in sediments from Macquarie Harbour, southwest Tasmania, Australia. *Environmental Earth Sciences*, 61 (3), 625–639. doi:10.1007/s12665-009-0377-x.

Australian Bureau of Agricultural and Resource Economics, State Forests of New South Wales, Australia and Bureau of Rural Sciences. (2000). *Identification of commercial timber plantation expansion opportunities in New South Wales: upper and lower north east CRA regions*. Canberra, A.C.T. Bureau of Rural Sciences. https://www.awe.gov.au/sites/default/files/sitecollectiondocuments/rfa/regions/nsw-southern/resources/nsw_sthn_na07es.pdf

Australian Bureau of Statistics. (2021). *2011 Census QuickStats*. https://quickstats.censusdata.abs.gov.au/census_services/getproduct/census/2011/quickstat/GL_TAS608?opendocument [Accessed 9 April 2021].

Australian Government Bioregional Assessments. (2015). *Geology of the Gippsland Basin bioregion including faults and structural elements. Locations of cross-sections A1–A2 and B1–B2 are delineated | Bioregional Assessments*. https://www.bioregionalassessments.gov.au/data/geology-gippsland-basin-bioregion-including-faults-and-structural-elements-locations-cross-sections [Accessed 7 June 2021].

Australian Government Bioregional Assessments. (2018). *1.2.1.1.1 Black coal | Bioregional Assessments*. https://www.bioregionalassessments.gov.au/assessments/12-resource-assessment-gippsland-basin-bioregion/12111-black-coal [Accessed 29 June 2021].

Australian Government, Department of Defence. (2020). *Australian National Tide Tables 2020*.

Australian Government, Department of Sustainability, Environment, Water, Population and Communities. (2011). *Corner Inlet Ramsar site. Ecological Character Description*. https://rsis.ramsar.org/RISapp/files/525/documents/AU261ECD.pdf

Avnaim-Katav, S., Gehrels, W.R., Brown, L. N., Fard, E. and MacDonald, G. M. (2017). Distributions of salt-marsh foraminifera along the coast of SW California, USA: Implications for sea-level reconstructions. *Marine Micropaleontology*, 131, 25–43. doi:10.1016/j.marmicro.2017.02.001.

Bacon, C., A. (1986). *The Adventure Bay coalfield*. http://www.mrt.tas.gov.au/mrtdoc/dominfo/download/UR1986_03/UR1986_03.pdf.

Bamber, J. L., Westaway, R. M., Marzeion, B. and Wouters, B. (2018). The land ice contribution to sea level during the satellite era. *Environmental Research Letters*, 13 (6), 063008. doi:10.1088/1748-9326/aac2f0.

Bamber, J. and Riva, R. (2010). The sea level fingerprint of recent ice mass fluxes. *The Cryosphere*, 4, 621–627. doi:10.5194/tc-4-621-2010.

Barlow, N. L., Long, A. J., Saher, M. H., Gehrels, W. R., Garnett, M. H. and Scaife, R. G. (2014). Salt-marsh reconstructions of relative sea-level change in the North Atlantic during the last 2000 years. *Quaternary Science Reviews*, 99, 1–16. doi: 10.1016/j.quascirev.2014.06.008.

Barlow, N. L. M., Shennan, I. and Long, A. J. (2012). Relative sea-level response to Little Ice Age ice mass change in south central Alaska: Reconciling model predictions and geological evidence. *Earth and Planetary Science Letters*, 315–316, 62–75. doi:10.1016/j.epsl.2011.09.048.

Barlow, N. L. M., Shennan, I., Long, A. J., Gehrels, W. R., Saher, M. H., Woodroffe, S. A. and Hillier, C. (2013). Salt marshes as late Holocene tide gauges. *Global and Planetary Change*, 106, 90–110. doi:10.1016/J.GLOPLACHA.2013.03.003.

Barnett, R. L. (2013). Testate amoebae as sea-level indicators in northwestern Norway: developments in sample preparation and analysis. *Acta Protozoologica*, 52 (3). 115–128. doi:10.4467/16890027AP.13.0012.1109.

Barnett, R. L., Bernatchez, P., Garneau, M., Brain, M. J., Charman, D. J., Stephenson, D. B., Haley, S. and Sanderson, N. (2019). Late Holocene sea-level changes in eastern Québec and potential drivers. *Quaternary Science Reviews*, 203, 151–169. doi:10.1016/j.quascirev.2018.10.039.

Barnett, R. L., Garneau, M. and Bernatchez, P. (2016). Salt-marsh sea-level indicators and transfer function development for the Magdalen Islands in the Gulf of St. Lawrence, Canada. *Marine Micropaleontology*, 122, 13–26. doi:10.1016/j.marmicro.2015.11.003.

Barnett, R. L., Gehrels, W. R., Charman, D. J., Saher, M. H. and Marshall, W. A. (2015). Late Holocene sea-level change in Arctic Norway. *Quaternary Science Reviews*, 107, 214–230. doi:10.1016/j.quascirev.2014.10.027.

Barnett, R. L., Newton, T. L., Charman, D. J. and Gehrels, W.R. (2017). Salt-marsh testate amoebae as precise and widespread indicators of sea-level change. *Earth-Science Reviews*, 164, 193–207. doi:10.1016/j.earscirev.2016.11.002.

Barrows, T. T., Stone, J. O., Fifield, L. K. and Cresswell, R. G. (2001). Late Pleistocene Glaciation of the Kosciuszko Massif, Snowy Mountains, Australia. *Quaternary Research*, 55 (2), 179–189. doi:10.1006/qres.2001.2216.

Barrows, T. T., Stone, J. O., Fifield, L. K. and Cresswell, R. G. (2002). The timing of the Last Glacial Maximum in Australia. *Quaternary Science Reviews*, 21 (1), 159–173. doi:10.1016/S0277-3791(01)00109-3.

Bayley, W. A. (1942). *The story of the settlement and development of Bega*. Bega Historical Society.

Bazley, S. (2015). A brief history of the Merimbila-Imlay district. *Anglican Historical Society Journal*, 59, 13–21.

Beitsch, A., Jungclaus, J. H. and Zanchettin, D. (2014). Patterns of decadal-scale Arctic warming events in simulated climate. *Climate dynamics*, 43 (7–8), 1773–1789. doi:10.1007/s00382-013-2004-5.

Bell, P. and McCarthy, J. (2011). The evolution of early copper smelting technology in Australia. *Journal of Australian Mining History*. 9, 20–35.

Berkeley, A., Perry, C. T., Smithers, S. G. and Horton, B. P. (2008). The spatial and vertical distribution of living (stained) benthic foraminifera from a tropical, intertidal environment, north Queensland, Australia. *Marine Micropaleontology*, 69 (2), 240–261. doi:10.1016/j.marmicro.2008.08.002.

Berkeley, A., Perry, C. T., Smithers, S. G., Horton, B. P. and Cundy, A. B. (2009). Foraminiferal biofacies across mangrove-mudflat environments at Cocoa Creek, north Queensland, Australia. *Marine Geology*, 263 (1), 64–86. doi:10.1016/j.margeo.2009.03.019.

Bhattacharya, A., Bolch, T., Mukherjee, K., King, O., Menounos, B., Kapitsa, V., Neckel, N., Yang, W. and Yao, T. (2021). High Mountain Asian glacier response to climate revealed by multi-temporal

satellite observations since the 1960s. *Nature Communications*, 12 (1), 4133. doi:10.1038/s41467-021-24180-y.

Bieniek, P. A., Walsh, J. E., Thoman, R. L. and Bhatt, U. S. (2014). Using Climate Divisions to Analyze Variations and Trends in Alaska Temperature and Precipitation. *Journal of Climate*, 27 (8), 2800–2818. doi:10.1175/JCLI-D-13-00342.1.

Bird, E. (2010). *Encyclopedia of the World's Coastal Landforms*. Dordrecht, London, New York: Springer Science & Business Media.

Birks, H.J.B. (1995). Chapter 6: Quantitative Palaeoenvironmental Reconstructions In: Maddy, D., and Brew, J.S., (Eds.), *Statistical Modelling of Quaternary Science Data, Technical Guide*. 5. Cambridge: Quaternary Research Association. 161–254.

Bjørk, A. A., Aagaard, S., Lütt, A., Khan, S. A., Box, J. E., Kjeldsen, K. K., Larsen, N. K., Korsgaard, N. J., Cappelen, J., Colgan, W. T., et al. (2018). Changes in Greenland's peripheral glaciers linked to the North Atlantic Oscillation. *Nature Climate Change*, 8 (1), 48–52. doi:10.1038/s41558-017-0029-1.

Bjørk, A. A., Kjær, K. H., Korsgaard, N. J., Khan, S. A., Kjeldsen, K. K., Andresen, C. S., Box, J. E., Larsen, N. K. and Funder, S. (2012). An aerial view of 80 years of climate-related glacier fluctuations in southeast Greenland. *Nature Geoscience*, 5 (6), 427–432. doi:10.1038/ngeo1481.

Björnsson, H., Pálsson, F., Gudmundsson, S., Magnússon, E., Adalgeirsdóttir, G., Jóhannesson, T., Berthier, E., Sigurdsson, O. and Thorsteinsson, T. (2013). Contribution of Icelandic ice caps to sea level rise: Trends and variability since the Little Ice Age. *Geophysical Research Letters*, 40 (8), 1546–1550. doi: 10.1002/grl.50278.

Blaauw, M. (2021). *rplum*. https://cran.r-project.org/web/packages/rplum/rplum.pdf.

Blaauw, M. and Christen, J. A. (2011). Flexible paleoclimate age-depth models using an autoregressive gamma process. *Bayesian analysis*, 6 (3), 457–474.

Blaauw, M., Christen, J. A., Lopez, M. A.., Vazquez, J. E., Gonzalez, O. M., Belding, T., Theiler, J., Gough, B. and Karney, C. (2021). *rbacon: Age-Depth Modelling using Bayesian Statistics*. https://CRAN.R-project.org/package=rbacon [Accessed 25 October 2021].

Błaszczyk, M., Jania, J. A. and Kolondra, L. (2013). Fluctuations of tidewater glaciers in Hornsund Fjord (Southern Svalbard) since the beginning of the 20th century. *Polish Polar Research*, 34 (4), 327–352. doi:10.2478/popore-2013-0024.

Bokuchava, D. D. and Semenov, V. A. (2020). Factors of natural climate variability contributing to the Early 20th Century Warming in the Arctic. *IOP Conference Series: Earth and Environmental Science*, 606, p.012008. doi:10.1088/1755-1315/606/1/012008.

Boreland, F. and Lyle, D. (2009). Using performance indicators to monitor attendance at the Broken Hill blood lead screening clinic,. *Environmental Research*, 109 (3), 267–272. doi:10.1016/J.ENVRES.2008.11.009.

Box, J. E. (2013). Greenland Ice Sheet Mass Balance Reconstruction. Part II: Surface Mass Balance (1840–2010). *Journal of Climate*, 26 (18), 6974–6989. doi:10.1175/JCLI-D-12-00518.1.

Box, J.E., Bromwich, D.H., Veenhuis, B.A., Bai, L.S., Stroeve, J.C., Rogers, J.C., Steffen, K., Haran, T. and Wang, S.H., (2006). Greenland Ice Sheet surface mass balance variability (1988–2004) from calibrated polar MM5 output. *Journal of Climate*, *19* (12), 2783-2800. doi: /10.1175/JCLI3738.1

Box, J. E., Colgan, W. T., Wouters, B., Burgess, D. O., O'Neel, S., Thomson, L. I. and Mernild, S. H. (2018). Global sea-level contribution from Arctic land ice: 1971–2017. *Environmental Research Letters*, 13 (12), 125012. doi:10.1088/1748-9326/aaf2ed.

Brain, M. J., Long, A. J., Woodroffe, S. A., Petley, D. N., Milledge, D. G. and Parnell, A. C. (2012). Modelling the effects of sediment compaction on salt marsh reconstructions of recent sea-level rise. *Earth and Planetary Science Letters*, 345–348, 180–193. doi:10.1016/j.epsl.2012.06.045.

Braun, M. H., Malz, P., Sommer, C., Farías-Barahona, D., Sauter, T., Casassa, G., Soruco, A., Skvarca, P. and Seehaus, T. C. (2019). Constraining glacier elevation and mass changes in South America. *Nature Climate Change*, 9 (2), 130–136. doi:10.1038/s41558-018-0375-7.

Brennan, M. K., Hakim, G. J. and Blanchard-Wrigglesworth, E. (2020). Arctic Sea-Ice Variability During the Instrumental Era. *Geophysical Research Letters*, 47 (7), e2019GL086843. doi:10.1029/2019GL086843.

Briner, J. P., Cuzzone, J. K., Badgeley, J. A., Young, N. E., Steig, E. J., Morlighem, M., Schlegel, N.-J., Hakim, G. J., Schaefer, J. M., Johnson, J. V., et al. (2020). Rate of mass loss from the Greenland Ice Sheet will exceed Holocene values this century. *Nature*, 586 (7827), 70–74. doi:10.1038/s41586-020-2742-6.

Bromwich, D. H., Nicolas, J. P., Monaghan, A. J., Lazzara, M. A., Keller, L. M., Weidner, G. A. and Wilson, A. B. (2013). Central West Antarctica among the most rapidly warming regions on Earth. *Nature Geoscience*, 6 (2), 139–145. doi:10.1038/ngeo1671.

Brooke, B. P., Nichol, S. L., Huang, Z. and Beaman, R. J. (2017). Palaeoshorelines on the Australian continental shelf: Morphology, sea-level relationship and applications to environmental management and archaeology. *Continental Shelf Research*, 134, 26–38. doi:10.1016/j.csr.2016.12.012.

Brooks, A., Lawrence, S. and Lennon, J. (2011). The Parsonage of the Reverend Willoughby Bean: Church, State and Frontier Settlement in Nineteenth-Century Colonial Australia. *Historical Archaeology*, 45 (4), 1–19.

Bryant, S., L. (2018). *Mammals on Lutregala Marsh Reserve, Bruny Island 2015 - 2017*. Tasmanian Land Conservancy, Lower Sandy Bay, Tasmania 7005. https://tasland.org.au/content/uploads/2015/06/Mammals-on-Lutregala-Marsh-Reserve-2015-2017.pdf.

Burgette, R. J., Watson, C. S., Church, J. A., White, N. J., Tregoning, P. and Coleman, R. (2013). Characterizing and minimizing the effects of noise in tide gauge time series: relative and geocentric sea level rise around Australia. *Geophysical Journal International*, 194 (2), 719–736. doi:10.1093/gji/ggt131.

Burn, M. J. and Palmer, S. E. (2014). Solar forcing of Caribbean drought events during the last millennium. *Journal of Quaternary Science*, 29 (8), 827–836. doi:10.1002/jqs.2660

Byrne, D. R. (1983). *The Five Forests: An Archaeological and Anthropological Investigation*. Syndey: National Parks and Wildlife Service of New South Wales.

Caesar, L., McCarthy, G. D., Thornalley, D. J. R., Cahill, N. and Rahmstorf, S. (2021). Current Atlantic meridional overturning circulation weakest in last millennium. *Nature Geoscience*, 14 (3), 118–120. 10.1038/s41561-021-00699-z.

Cahill, N. (2021). *ncahill89/CPModel*. https://github.com/ncahill89/CPModel [Accessed 6 July 2021].

Cahill, N., Kemp, A. C., Horton, B. P. and Parnell, A. C. (2016). A Bayesian hierarchical model for reconstructing relative sea level: from raw data to rates of change. *Climate of the Past*, 12 (2), 525–542. doi:10.5194/cp-12-525-2016.

Cai, W. and Cowan, T. (2007). Trends in Southern Hemisphere Circulation in IPCC AR4 Models over 1950–99: Ozone Depletion versus Greenhouse Forcing. *Journal of Climate*, 20 (4), 681–693. doi:10.1175/JCLI4028.1.

Calafat, F. M., Chambers, D. P. and Tsimplis, M. N. (2014). On the ability of global sea level reconstructions to determine trends and variability. *Journal of Geophysical Research: Oceans*, 119 (3), 1572–1592. doi:10.1002/2013JC009298.

Caldow, W. (2003). The Commercial Inn, Tarraville: maritime trade and the early settlement of Gippsland. *Victorian Historical Journal*, 74 (1), 23–45.

Callard, S.L, Gehrels, W.R, Morrison, B.V, Grenfell, H. R. (2011). Suitability of salt-marsh foraminifera as proxy indicators of sea level in Tasmania. *Marine Micropaleontology*, 79 (3–4), 121–131. doi:10.1016/J.MARMICRO.2011.03.001.

Camacho, S. G., Moura, D. M. de J., Connor, S., Scott, D. B. and Boski, T. (2015). Taxonomy, ecology and biogeographical trends of dominant benthic foraminifera species from an Atlantic-Mediterranean estuary (the Guadiana, southeast Portugal). *Palaeontologia Electronica*, 18 (1), 1–27. doi:0.26879/512.

Cann, J. H., Belperio, A. P., Gostin, V. A. and Rice, R. L. (1993). Contemporary benthic foraminifera in Gulf St Vincent, South Australia, and a refined Late Pleistocene sea-level history. *Australian Journal of Earth Sciences*, 40 (2), 197–211. doi:10.1080/08120099308728074.

Caron, L., Ivins, E. R., Larour, E., Adhikari, S., Nilsson, J. and Blewitt, G. (2018). GIA Model Statistics for GRACE Hydrology, Cryosphere, and Ocean Science. *Geophysical Research Letters*, 45 (5), 2203–2212. doi:10.1002/2017GL076644.

Carslaw, K. S., Lee, L. A., Reddington, C. L., Pringle, K. J., Rap, A., Forster, P. M., Mann, G. W., Spracklen, D. V., Woodhouse, M. T., Regayre, L. A., et al. (2013). Large contribution of natural aerosols to uncertainty in indirect forcing. *Nature*, 503 (7474), 67–71. doi:10.1038/nature12674.

Charman, D. J., Gehrels, W. R., Manning, C. and Sharma, C. (2010). Reconstruction of recent sea-level change using testate amoebae. *Quaternary Research*, 73 (2), 208–219. doi:10.1016/j.yqres.2009.11.009.

Chen, H., Shaw, T. A., Wang, J., Engelhart, S., Nikitina, D., Pilarczyk, J. E., Walker, J., García-Artola, A. and Horton, B. P. (2020). Salt-Marsh Foraminiferal Distributions from Mainland Northern Georgia, USA: An Assessment of Their Viability for Sea-Level Studies. *Open Quaternary*, 6 (1), p.6. doi:10.5334/oq.80.

Chiaradia, M., Chenhall, B. E., Depers, A. M., Gulson, B. L. and Jones, B. G. (1997). Identification of historical lead sources in roof dusts and recent lake sediments from an industrialized area: indications

from lead isotopes. *Science of The Total Environment*, 205 (2–3), 107–128. doi:10.1016/S0048-9697(97)00199-X.

Christian, J. E., Siler, N., Koutnik, M. and Roe, G. (2016). Identifying Dynamically Induced Variability in Glacier Mass-Balance Records. *Journal of Climate*, 29 (24), 8915–8929. doi:10.1175/JCLI-D-16-0128.1.

Church, J. A., Clark, P. U., Cazenave, A., Gregory, J. M., Jevrejeva, S., Levermann, A., Merrifield, M. A., Milne, G. A., Nerem, R. S., Nunn, P. D., et al. (2013). Sea level change. In: Stocker, T.F., Qin, D., Plattner, G.-K., Tignor, M., Allen, S.K., Boschung, J., Nauels, A., Xia, Y., Bex, V., Midgley, P. M. (Eds.), *Climate Change 2013: The Physical Science Basis. Contribution of Working Group I to the Fifth Assessment Report of the Intergovernmental Panel on Climate Change.* Cambridge: Cambridge University Press. 1137–1216. http://drs.nio.org/drs/handle/2264/4605.

Church, J. A. and White, N. J. (2011). Sea-Level Rise from the Late 19th to the Early 21st Century. *Surveys in Geophysics*, 32 (4–5), 585–602. doi:10.1007/s10712-011-9119-1.

Church, J. A., White, N. J., Coleman, R., Lambeck, K. and Mitrovica, J. X. (2004). Estimates of the regional distribution of sea level rise over the 1950–2000 period. *Journal of climate*, 17 (13), 2609–2625. doi:10.1175/1520-0442(2004)017<2609:EOTRDO>2.0.CO;2.

Chylek, P., Klett, J. D., Dubey, M. K. and Hengartner, N. (2016). The role of Atlantic Multi-decadal Oscillation in the global mean temperature variability. *Climate Dynamics*, 47 (9), 3271–3279. doi:10.1007/s00382-016-3025-7.

Clark, J. A., Farrell, W. E. and Peltier, W. R. (1978). Global Changes in Postglacial Sea Level: A Numerical Calculation. *Quaternary Research*, 9 (3), 265–287. doi:10.1016/0033-5894(78)90033-9.

Clark, K., Cochran, U. and Mazengarb, C. (2011). Holocene coastal evolution and evidence for paleotsunami from a tectonically stable region, Tasmania, Australia. *The Holocene*, 21 (6), 883–895. doi:10.1177/0959683610391317.

Clark, P. U., Shakun, J. D., Marcott, S. A., Mix, A. C., Eby, M., Kulp, S., Levermann, A., Milne, G. A., Pfister, P. L., Santer, B. D., et al. (2016). Consequences of twenty-first-century policy for multi-millennial climate and sea-level change. *Nature Climate Change*, 6 (4), 360–369. doi:10.1038/nclimate2923.

Cogley, J.G., (2009). Geodetic and direct mass-balance measurements: comparison and joint analysis. *Annals of Glaciology*, *50* (50), 96-100. doi:10.3189/172756409787769744

Colgan, W., Box, J.E., Andersen, M.L., Fettweis, X., Csatho, B., Fausto, R.S., Van As, D. and Wahr, J., (2015). Greenland high-elevation mass balance: inference and implication of reference period (1961–90) imbalance. *Annals of Glaciology*, *56* (70), 105-117. doi:10.3189/2015AoG70A967.

Colhoun, E. A. and Barrows, T. T. (2011). Chapter 74 - The Glaciation of Australia. In: Ehlers, J., Gibbard, P. L. and Hughes, P. D. (Eds.), *Developments in Quaternary Sciences*. Quaternary Glaciations - Extent and Chronology. 15. Elsevier. 1037–1045. doi:10.1016/B978-0-444-53447-7.00074-X.

Compton, J. S. (2001). Holocene sea-level fluctuations inferred from the evolution of depositional environments of the southern Langebaan Lagoon salt marsh, South Africa. *The Holocene*, 11 (4), 395–405. doi:10.1191/095968301678302832.

Corbett, K. D. (2001). *The geology of the Mount Lyell mines area, Tasmania re-interpretation based on studies at Lyell Comstock, North Lyell and the iron blow area.* PhD Thesis, University of Tasmania. https://eprints.utas.edu.au/19127/1/whole_CorbettKeithDouglas2001_thesis.pdf.

Crawford, C. and Mitchell, I. (1999). *Physical and chemical parameters of several osyter growing areas in Tasmania*. Technical, Tasmanian Aquaculture & Fisheries Institute. https://eprints.utas.edu.au/6653/1/Tech_Report_4_PhysicalChemicall.pdf.

Creese, R. G., Glasby, T. M., West, G. and Gallen, C. (2009). *Mapping the habitats of NSW estuaries*. 97. http://www.friendsoftuggerahlakes-cen.org.au/SEAGRASS/2009%2009%2000%20Industry%20and%20Investment%20HabitatMapping-Final-Report.pdf

Csatho, B., Schenk, T., Van Der Veen, C. J. and Krabill, W. B. (2008). Intermittent thinning of Jakobshavn Isbræ, West Greenland, since the Little Ice Age. *Journal of Glaciology*, 54 (184), 131–144. doi:10.3189/002214308784409035.

Dangendorf, S., Hay, C., Calafat, F. M., Marcos, M., Piecuch, C. G., Berk, K. and Jensen, J. (2019). Persistent acceleration in global sea-level rise since the 1960s. *Nature Climate Change*, 9 (9), 705–710. doi:10.1038/s41558-019-0531-8.

Dangendorf, S., Marcos, M., Wöppelmann, G., Conrad, C. P., Frederikse, T. and Riva, R. (2017). Reassessment of 20th century global mean sea level rise. *Proceedings of the National Academy of Sciences*, 114 (23), 5946–5951. doi:10.1073/pnas.1616007114.

Das, S. B. and Alley, R. B. (2008). Rise in frequency of surface melting at Siple Dome through the Holocene: Evidence for increasing marine influence on the climate of West Antarctica. *Journal of Geophysical Research: Atmospheres*, 113 (D2). doi:10.1029/2007JD008790.

Davies, B. (2021). *Calculating glacier ice volumes and sea level equivalents*. http://www.antarcticglaciers.org/glaciers-and-climate/estimating-glacier-contribution-to-sea-level-rise/ [Accessed 18 November 2021].

Davis, B. (1990). *Guide to Bruny Island history*. 2nd ed. Bruny Island, Tas: Bruny Island Historical Society.

Dean, L. F. and De Deckker, P. (2013). Recent benthic foraminifera from Twofold Bay, Eden NSW: community structure, biotopes and distribution controls. *Australian Journal of Earth Sciences*, 60 (4), 475–496. doi:10.1080/08120099.2013.792294.

DECCW. (2011). *Mimosa Rocks National Park Plan of Management*. NSW National Parks and Wildlife Service, Department of Environment, Climate Change and Water. https://www.environment.nsw.gov.au/-/media/OEH/Corporate-Site/Documents/Parks-reserves-and-protected-areas/Parks-plans-of-management/mimosa-rocks-national-park-plan-of-management-110246.pdf

Dehecq, A., Gourmelen, N., Gardner, A. S., Brun, F., Goldberg, D., Nienow, P. W., Berthier, E., Vincent, C., Wagnon, P. and Trouvé, E. (2019). Twenty-first century glacier slowdown driven by mass loss in High Mountain Asia. *Nature Geoscience*, 12 (1), 22–27. doi:10.1038/s41561-018-0271-9.

Denys, P. H., Beavan, R. J., Hannah, J., Pearson, C. F., Palmer, N., Denham, M. and Hreinsdottir, S. (2020). Sea Level Rise in New Zealand: The Effect of Vertical Land Motion on Century-Long Tide Gauge Records in a Tectonically Active Region. *Journal of Geophysical Research: Solid Earth*, 125 (1), e2019JB018055. doi:10.1029/2019JB018055.

de Rijk, S. and Troelstra, S. R. (1997). Salt marsh foraminifera from the Great Marshes, Massachusetts: environmental controls. *Palaeogeography, Palaeoclimatology, Palaeoecology*, 130 (1), 81–112. doi:10.1016/S0031-0182(96)00131-9.

Donnelly, J. P., Cleary, P., Newby, P. and Ettinger, R. (2004). Coupling instrumental and geological records of sea-level change: Evidence from southern New England of an increase in the rate of sea-level rise in the late 19th century. *Geophysical Research Letters*, 31 (5). doi:10.1029/2003GL018933.

Dougherty, A. J., Thomas, Z. A., Fogwill, C., Hogg, A., Palmer, J., Rainsley, E., Williams, A. N., Ulm, S., Rogers, K., Jones, B. G., et al. (2019). Redating the earliest evidence of the mid-Holocene relative sea-level highstand in Australia and implications for global sea-level rise. *PLOS ONE*, 14 (7), e0218430. doi:10.1371/journal.pone.0218430.

Duan, J., Li, Y., Wang, F., Hu, A., Han, W., Zhang, L., Lin, P., Rosenbloom, N. and Meehl, G. A. (2021). Rapid Sea-Level Rise in the Southern-Hemisphere Subtropical Oceans. *Journal of Climate*, 34 (23), 9401–9423. doi:10.1175/JCLI-D-21-0248.1.

Dussaillant, I., Berthier, E., Brun, F., Masiokas, M., Hugonnet, R., Favier, V., Rabatel, A., Pitte, P. and Ruiz, L. (2019). Two decades of glacier mass loss along the Andes. *Nature Geoscience*, 12 (10), 802–808. doi:10.1038/s41561-019-0432-5.

Edwards, R. J. and Horton, B. P. (2000). Reconstructing relative sea-level change using UK salt-marsh foraminifera. *Marine Geology*, 169 (1), 41–56. doi:10.1016/S0025-3227(00)00078-5.

Edwards, R. J., Wright, A. J. and van de Plassche, O. (2004). Surface distributions of salt-marsh foraminifera from Connecticut, USA: modern analogues for high-resolution sea level studies. *Marine Micropaleontology*, 51 (1), 1–21. doi:10.1016/j.marmicro.2003.08.002.

Edwards, R. and Wright, A. (2015). Chapter 13: Foraminifera. In: Shennan, I., Long, A.J., and Horton, B.P., (Eds.), *Handbook of Sea-Level Research*. Chichester, UK : John Wiley & Sons, Ltd. 191–217. doi:10.1002/9781118452547.ch13.

Egbert, G. D. and Erofeeva, S. (2010). OSU Tidal Data Inversion. *Oregon State University*.

Egorova, T., Rozanov, E., Arsenovic, P., Peter, T. and Schmutz, W. (2018). Contributions of Natural and Anthropogenic Forcing Agents to the Early 20th Century Warming. *Frontiers in Earth Science*, 6, 206. doi:10.3389/feart.2018.00206.

Ekblom Johansson, F., Wangner, D. J., Andresen, C. S., Bakke, J., Støren, E. N., Schmidt, S. and Vieli, A. (2020). Glacier and ocean variability in Ata Sund, west Greenland, since 1400 CE. *The Holocene*, 30 (12), 1681–1693. doi:10.1177/0959683620950431.

Eklund, E. (2002). *Steel town : the making and breaking of Port Kembla*. Melbourne University Press.

Engelhart, S. E., Horton, B. P., Douglas, B. C., Peltier, W. R. and Törnqvist, T. E. (2009). Spatial variability of late Holocene and 20th century sea-level rise along the Atlantic coast of the United States. *Geology*, 37 (12), 1115–1118. doi:10.1130/G30360A.1.

Engelhart, S. E., Horton, B. P., Roberts, D. H., Bryant, C. L. and Corbett, D. R. (2007). Mangrove pollen of Indonesia and its suitability as a sea-level indicator. *Marine Geology*, 242 (1), 65–81. doi:10.1016/j.margeo.2007.02.020.

Faivre, S., Bakran-Petricioli, T., Barešić, J., Horvatić, D. and Macario, K. (2019). Relative sea-level change and climate change in the Northeastern Adriatic during the last 1.5 ka (Istria, Croatia). *Quaternary Science Reviews*, 222, p.105909. doi:10.1016/j.quascirev.2019.105909.

Farinotti, D., Longuevergne, L., Moholdt, G., Duethmann, D., Mölg, T., Bolch, T., Vorogushyn, S. and Güntner, A. (2015). Substantial glacier mass loss in the Tien Shan over the past 50 years. *Nature Geoscience*, 8 (9), 716–722. doi:10.1038/ngeo2513.

Farmer, N. & Forsyth, S.M. *Dover Sheet. Geological Atlas 1:50,000*. Tasmania Department of Mines.

Fatela, F. and Taborda, R. (2002). Confidence limits of species proportions in microfossil assemblages. *Marine Micropaleontology*, 45 (2), 169–174. doi:10.1016/S0377-8398(02)00021-X.

Fettweis, X., Box, J. E., Agosta, C., Amory, C., Kittel, C., Lang, C., van As, D., Machguth, H. and Gallée, H. (2017). Reconstructions of the 1900–2015 Greenland Ice Sheet surface mass balance using the regional climate MAR model. *The Cryosphere*, 11 (2), 1015–1033. doi:10.5194/tc-11-1015-2017.

Fettweis, X., Hanna, E., Gallée, H., Huybrechts, P. and Erpicum, M. (2008). Estimation of the Greenland Ice Sheet surface mass balance for the 20th and 21st centuries. *The Cryosphere*, *2* (2), 117-129. doi:10.5194/tc-2-117-2008.

Fettweis, X., Hofer, S., Krebs-Kanzow, U., Amory, C., Aoki, T., Berends, C. J., Born, A., Box, J. E., Delhasse, A., Fujita, K., et al. (2020). GrSMBMIP: intercomparison of the modelled 1980–2012 surface mass balance over the Greenland Ice Sheet. *The Cryosphere*, 14 (11), 3935–3958. doi: 0.5194/tc-14-3935-2020.

Figueira, B. and Hayward, B. W. (2014). Impact of reworked foraminifera from an eroding salt marsh on sea-level studies, New Zealand. *New Zealand Journal of Geology and Geophysics*, 57 (4), 378–389. doi:10.1080/00288306.2014.924971.

FitzGerald, D. M. and Hughes, Z. (2019). Marsh Processes and Their Response to Climate Change and Sea-Level Rise. *Annual Review of Earth and Planetary Sciences*, 47 (1), 481–517. doi:10.1146/annurev-earth-082517-010255.

Fleming, K. M., Tregoning, P., Kuhn, M., Purcell, A. and McQueen, H. (2012). The effect of melting land-based ice masses on sea-level around the Australian coastline. *Australian Journal of Earth Sciences*, 59 (4), 457–467. doi:10.1080/08120099.2012.664828.

Fletcher, M.-S. and Thomas, I. (2010). A Holocene record of sea level, vegetation, people and fire from western Tasmania, Australia. *The Holocene*, 20 (3), 351–361. doi:10.1177/0959683609351903.

Fox-Kemper, B., Hewitt, H. T., Xiao, C., Aðalgeirsdóttir, G., Drijfhout, S. S., Edwards, T. L., Golledge, N. R., Hemer, M., Kopp, R. E., Krinner, G., Mix, A., Notz, D., Nowicki, S., Nurhati, I.S, Ruiz, L., Sallée, J-B., Slangen, A. B. A., Yu, Y. 2021. Ocean, Cryosphere and Sea Level Change. In: Masson-Delmotte, V., Zhai, P., Pirani, A., Connors, S. L., Péan, C., Berger, S., Caud, N., Chen, Y., Goldfarb, L., Gomis, M. I., Huang, M., Leitzell, K., Lonnoy, E., Matthews, J.B.R., Maycock, T. K., Waterfield, T., Yelekçi, O., Yu, R., and Zhou, B. (Eds.), *Climate Change 2021: The Physical Science Basis. Contribution of Working Group I to the Sixth Assessment Report of the Intergovernmental Panel on Climate Change*. Cambridge University Press. In Press.

Frederikse, T., Adhikari, S., Daley, T. J., Dangendorf, S., Gehrels, R., Landerer, F., Marcos, M., Newton, T. L., Rush, G., Slangen, A. B. A., et al. (2021). Constraining 20th-Century Sea-Level Rise in

the South Atlantic Ocean. *Journal of Geophysical Research: Oceans*, 126 (3), e2020JC016970. doi: 10.1029/2020JC016970.

Frederikse, T., Landerer, F., Caron, L., Adhikari, S., Parkes, D., Humphrey, V. W., Dangendorf, S., Hogarth, P., Zanna, L., Cheng, L., et al. (2020). The causes of sea-level rise since 1900. *Nature*, 584 (7821), 393–397. doi:10.1038/s41586-020-2591-3.

Freund, M. B., Henley, B. J., Karoly, D. J., McGregor, H. V., Abram, N. J. and Dommenget, D. (2019). Higher frequency of Central Pacific El Niño events in recent decades relative to past centuries. *Nature Geoscience*, 12 (6), 450–455. doi:10.1038/s41561-019-0353-3.

Friedman, A. R., Hegerl, G. C., Schurer, A. P., Lee, S.-Y., Kong, W., Cheng, W. and Chiang, J. C. H. (2020). Forced and Unforced Decadal Behavior of the Interhemispheric SST Contrast during the Instrumental Period (1881–2012): Contextualizing the Late 1960s–Early 1970s Shift. *Journal of Climate*, 33 (9), 3487–3509. doi:10.1175/JCLI-D-19-0102.1.

Frost, W. (1997). Farmers, government, and the environment: the settlement of Australia's 'wet frontier', 1870-1920. *Australian Economic History Review*, 37 (1), 19–38. doi:10.1111/1467-8446.00002.

Fyfe, J. C., von Salzen, K., Gillett, N. P., Arora, V. K., Flato, G. M. and McConnell, J. R. (2013). One hundred years of Arctic surface temperature variation due to anthropogenic influence. *Scientific Reports*, 3 (1), 2645. doi:10.1038/srep02645.

Gardner, A. S., Moholdt, G., Wouters, B., Wolken, G. J., Burgess, D. O., Sharp, M. J., Cogley, J. G., Braun, C. and Labine, C. (2011). Sharply increased mass loss from glaciers and ice caps in the Canadian Arctic Archipelago. *Nature*, 473 (7347), 357–360. doi:10.1038/nature10089.

Garrett, E., Gehrels, W.R., Hayward, B.W., Newnham, R., Gehrels, M.J., Morey, C.J. and Dangendorf, S., 2022. Drivers of 20th century sea-level change in southern New Zealand determined from proxy and instrumental records. *Journal of Quaternary Science*.

Garrett, E., Melnick, D., Dura, T., Cisternas, M., Ely, L. L., Wesson, R. L., Jara-Muñoz, J. and Whitehouse, P. L. (2020). Holocene relative sea-level change along the tectonically active Chilean coast. *Quaternary Science Reviews*, 236, 106281. doi:10.1016/j.quascirev.2020.106281.

Garside, C. J., Glasby, T. M., Coleman, M. A., Kelaher, B. P. and Bishop, M. J. (2014). The frequency of connection of coastal water bodies to the ocean predicts *Carcinus maena*s invasion. *Limnology and Oceanography*, 59 (4), 1288–1296. doi:10.4319/lo.2014.59.4.1288.

Gehrels, W. R. (2000). Using foraminiferal transfer functions to produce high-resolution sea-level records from salt-marsh deposits, Maine, USA. *The Holocene*, 10 (3), 367–376. doi: 10.1191/095968300670746884.

Gehrels, W. R., Dangendorf, S., Barlow, N. L. M., Saher, M. H., Long, A. J., Woodworth, P. L., Piecuch, C. G. and Berk, K. (2020). A Preindustrial Sea-Level Rise Hotspot Along the Atlantic Coast of North America. *Geophysical Research Letters*, 47 (4), e2019GL085814. doi:10.1029/2019GL085814.

Gehrels, W. R., Hayward, B. W., Newnham, R. M. and Southall, K. E. (2008). A 20th century acceleration of sea-level rise in New Zealand. *Geophysical Research Letters*, 35 (2), p.L02717. doi:10.1029/2007GL032632.

Gehrels, W. R., Hendon, D. and Charman, D. J. (2006). Distribution of testate amoebae in salt marshes along the North American East Coast. *Journal of Foraminiferal Research*, 36 (3), 201–214. doi:10.2113/gsjfr.36.3.201.

Gehrels, W. R., Marshall, W. A., Gehrels, M. J., Larsen, G. N., Kirby, J. R., Eiríksson, J. N., Heinemeier, J. and Shimmield, T. (2006). Rapid sea-level rise in the North Atlantic Ocean since the first half of the nineteenth century. *The Holocene*, 16 (7), 949–965. doi:10.1177/0959683606hl986rp.

Gehrels, W. R. and Newman, S. W. G. (2004). Salt-marsh foraminifera in Ho Bugt, western Denmark, and their use as sea-level indicators. *Geografisk Tidsskrift-Danish Journal of Geography*, 104 (1), 97–106. doi:10.1080/00167223.2004.10649507.

Gehrels, W. R., Roe, H. M. and Charman, D. J. (2001). Foraminifera, testate amoebae and diatoms as sea-level indicators in UK saltmarshes: a quantitative multiproxy approach. *Journal of Quaternary Science*, 16 (3), 201–220. doi:10.1002/jqs.588.

Gehrels, W. R. and Woodworth, P. L. (2013). When did modern rates of sea-level rise start? *Global and Planetary Change*, 100, 263–277. doi:10.1016/j.gloplacha.2012.10.020.

Gehrels, W.R., Callard, S.L., Moss, P.T., Marshall, W.A., Blaauw, M., Hunter, J., Milton, J.A. and Garnett, M.H. (2012). Nineteenth and twentieth century sea-level changes in Tasmania and New Zealand. *Earth and Planetary Science Letters*, 315–316, 94–102. doi:10.1016/J.EPSL.2011.08.046.

Gehrels, W.R., Kirby, J.R., Prokoph, A., Newnham, R.M., Achterberg, E.P., Evans, H., Black, S., Scott, D. B. (2005). Onset of recent rapid sea-level rise in the western Atlantic Ocean. *Quaternary Science Reviews*, 24 (18–19), 2083–2100. doi:10.1016/J.QUASCIREV.2004.11.016.

Gehrels, W.R., Milne, G.A., Kirby, J.R., Patterson, R.T., Belknap, D. F. (2004). Late Holocene sea-level changes and isostatic crustal movements in Atlantic Canada. *Quaternary International*, 120 (1), 79–89. doi:10.1016/J.QUAINT.2004.01.008.

Gerlach, M. J., Engelhart, S. E., Kemp, A. C., Moyer, R. P., Smoak, J. M., Bernhardt, C. E. and Cahill, N. (2017). Reconstructing Common Era relative sea-level change on the Gulf Coast of Florida. *Marine Geology*, 390, 254–269. doi:10.1016/j.margeo.2017.07.001.

Giese, B. S., Seidel, H. F., Compo, G. P. and Sardeshmukh, P. D. (2016). An ensemble of ocean reanalyses for 1815–2013 with sparse observational input. *Journal of Geophysical Research: Oceans*, 121 (9), 6891–6910. doi:10.1002/2016JC012079.

Gill, E. D., Lang, J. G. and Boyd, E. S. (1982). The peak of the Flandrian Transgression in Victoria, S.E. Australia - faunas and sea level changes. *Proceedings of the Royal Society of Victoria*, 94 (1), 23–34.

Gomez, N., Latychev, K. and Pollard, D. (2018). A Coupled Ice Sheet–Sea Level Model Incorporating 3D Earth Structure: Variations in Antarctica during the Last Deglacial Retreat. *Journal of Climate*, 31 (10), 4041–4054. doi:10.1175/JCLI-D-17-0352.1.

Gomez, N., Mitrovica, J. X., Tamisiea, M. E. and Clark, P. U. (2010). A new projection of sea level change in response to collapse of marine sectors of the Antarctic Ice Sheet. *Geophysical Journal International*, 180 (2), 623–634.

Goodwin, I. D. and Harvey, N. (2008). Subtropical sea-level history from coral microatolls in the Southern Cook Islands, since 300 AD. *Marine Geology*, 253 (1), 14–25. doi:10.1016/j.margeo.2008.04.012.

Goring, D. G. and Bell, R. G. (1999). El Niño and decadal effects on sea-level variability in northern New Zealand: A wavelet analysis. *New Zealand Journal of Marine and Freshwater Research*, 33 (4), 587–598. doi:10.1080/00288330.1999.9516902.

Gregory, J. M., Griffies, S. M., Hughes, C. W., Lowe, J. A., Church, J. A., Fukimori, I., Gomez, N., Kopp, R. E., Landerer, F., Cozannet, G. L., et al. (2019). Concepts and Terminology for Sea Level: Mean, variability and change, both local and global. *Surveys in Geophysics*, 40 (6), 1251–1289. doi:10.1007/s10712-019-09525-z.

Grenfell, H. R., Hayward, B. W., Nomura, R. and Sabaa, A. T. (2012). A foraminiferal proxy record of 20th century sea-level rise in the Manukau Harbour, New Zealand. *Marine and Freshwater Research*, 63 (4), 370–384.

Griffiths, T. (2002). How many trees make a forest? Cultural debates about vegetation change in Australia. *Australian Journal of Botany*, 50 (4), 375. doi:10.1071/BT01046.

Grose, M. et al. (2015). *Southern Slopes Cluster Report, Climate Change in Australia Projections for Australia's Natural Resource Management Regions*. https://www.climatechangeinaustralia.gov.au/media/ccia/2.2/cms_page_media/168/SOUTHERN_SLOPES_CLUSTER_REPORT_1.pdf.

Haigh, I. D., Eliot, M., Pattiaratchi, C. and Wahl, T. (2011). Regional changes in mean sea level around Western Australia between 1897 and 2008. In: *Coasts and ports 2011: Diverse and developing: Proceedings of the 20th Australasian coastal and ocean engineering conference and the 13th Australasian Port and Harbour conference*. 280.

Hallmann, N., Camoin, G., Eisenhauer, A., Botella, A., Milne, G. A., Vella, C., Samankassou, E., Pothin, V., Dussouillez, P., Fleury, J., et al. (2018). Ice volume and climate changes from a 6000 year sea-level record in French Polynesia. *Nature Communications*, 9 (1), 285. doi:10.1038/s41467-017-02695-7.

Hamilton, S. and Shennan, I. (2005). Late Holocene relative sea-level changes and the earthquake deformation cycle around upper Cook Inlet, Alaska. *Quaternary Science Reviews*, 24 (12), 1479–1498. doi:10.1016/j.quascirev.2004.11.003.

Hamon, B. V. (1988). Spurious Long-Period Tides Due to Tide Gauge Errors. *The International Hydrographic Review*.

Hanna, E., Huybrechts, P., Cappelen, J., Steffen, K., Bales, R.C., Burgess, E., McConnell, J.R., Steffensen, P.J., Van den Broeke, M., Wake, L. et al. (2011). Greenland Ice Sheet surface mass balance 1870 to 2010 based on Twentieth Century Reanalysis, and links with global climate forcing. *Journal of Geophysical Research: Atmospheres*, *116* (D24). doi:10.1029/2011JD016387.

Hanna, E., Huybrechts, P., Steffen, K., Cappelen, J., Huff, R., Shuman, C., Irvine-Fynn, T., Wise, S. and Griffiths, M., (2008). Increased runoff from melt from the Greenland Ice Sheet: a response to global warming. *Journal of Climate*, *21* (2), 331-341. doi:10.1175/2007JCLI1964.1.

Hanna, E., Pattyn, F., Navarro, F., Favier, V., Goelzer, H., van den Broeke, M. R., Vizcaino, M., Whitehouse, P. L., Ritz, C., Bulthuis, K., et al. (2020). Mass balance of the Ice Sheets and glaciers – Progress since AR5 and challenges. *Earth-Science Reviews*, 201, 102976. doi:10.1016/j.earscirev.2019.102976.

Hannesdóttir, H., Björnsson, H., Pálsson, F., Aðalgeirsdóttir, G. and Guðmundsson, Sv. (2015). Changes in the southeast Vatnajökull ice cap, Iceland, between ~ 1890 and 2010. *The Cryosphere*, 9 (2), 565–585. doi:10.5194/tc-9-565-2015.

Haslett, S. K. (2001). The Palaeoenvironmental Implications of the Distribution of Intertidal Foraminifera in a Tropical Australian Estuary: a Reconnaissance Study. *Australian Geographical Studies*, 39 (1), 67–74. doi:10.1111/1467-8470.00130.

Haslett, S. K., Davies-Burrows, R., Panayotou, K., Jones, B. G. and Woodroff, C. D. (2010). Holocene evolution of the Minnamurra River estuary, southeast Australia: foraminiferal evidence. *Zeitschrift für Geomorphologie, Supplementary Issues*, 54 (3), 79–98. doi:10.1127/0372-8854/2010/0054S3-0020.

Haustein, K., Otto, F. E. L., Venema, V., Jacobs, P., Cowtan, K., Hausfather, Z., Way, R. G., White, B., Subramanian, A. and Schurer, A. P. (2019). A Limited Role for Unforced Internal Variability in Twentieth-Century Warming. *Journal of Climate*, 32 (16), 4893–4917. doi:10.1175/JCLI-D-18-0555.1.

Hawkes, A. D., Horton, B. P., Nelson, A. R. and Hill, D. F. (2010). The application of intertidal foraminifera to reconstruct coastal subsidence during the giant Cascadia earthquake of AD 1700 in Oregon, USA. *Quaternary International*, 221 (1–2), 116–140. doi:10.1016/J.QUAINT.2009.09.019.

Hay, C. C., Morrow, E. D., Kopp, R. E. and Mitrovica, J. X. (2017). On the Robustness of Bayesian Fingerprinting Estimates of Global Sea Level Change. *Journal of Climate*, 30 (8), 3025–3038. doi:10.1175/JCLI-D-16-0271.1.

Hay, C. C., Morrow, E., Kopp, R. E. and Mitrovica, J. X. (2013). Estimating the sources of global sea level rise with data assimilation techniques. *Proceedings of the National Academy of Sciences*, 110 3692–3699. doi:10.1073/pnas.1117683109.

Hay, C. C., Morrow, E., Kopp, R. E. and Mitrovica, J. X. (2015). Probabilistic reanalysis of twentieth-century sea-level rise. *Nature*, 517 (7535), 481–484. doi:10.1038/nature14093.

Hayward, B. W. (2014). 'Monospecific' and near-monospecific benthic foraminiferal faunas, New Zealand. *The Journal of Foraminiferal Research*, 44 (3), 300–315. doi:10.2113/gsjfr.44.3.300.

Hayward, B. W., Figueira, B. O., Sabaa, A. T. and Buzas, M. A. (2014). Multi-year life spans of high salt marsh agglutinated foraminifera from New Zealand. *Marine Micropaleontology*, 109, 54–65. doi:10.1016/j.marmicro.2014.03.002.

Hayward, B. W., Grenfell, H. R. and Scott, D. B. (1999). Tidal range of marsh foraminifera for determining former sea-level heights in New Zealand. *New Zealand Journal of Geology and Geophysics*, 42 (3), 395–413. doi:10.1080/00288306.1999.9514853.

Hayward, B. W. and Hollis, C. J. (1994). Brackish Foraminifera in New Zealand: A Taxonomic and Ecologic Review. *Micropaleontology*, 40 (3), 185–222. doi:10.2307/1485816.

Hayward, B. W., Le Coze, F. and Gross, O. *Catalogue of Life : WoRMS Foraminifera*. https://www.catalogueoflife.org/col/details/database/id/157 [Accessed 14 October 2020].

He, Z. and Morrison, R. J. (2001). Changes in the Marine Environment of Port Kembla Harbour, NSW, Australia, 1975–1995: A Review. *Marine Pollution Bulletin*, 42 (3), 193–201. doi:10.1016/S0025-326X(00)00142-9.

Hedge, P. and Kriwoken, L. K. (2000). Evidence for effects of *Spartina anglica* invasion on benthic macrofauna in Little Swanport estuary, Tasmania. *Austral Ecology*, 25 (2), 150–159. doi:10.1046/j.1442-9993.2000.01016.x.

Hegerl, G. C., Brönnimann, S., Cowan, T., Friedman, A. R., Hawkins, E., Iles, C., Müller, W., Schurer, A. and Undorf, S. (2019). Causes of climate change over the historical record. *Environmental Research Letters*, 14 (12), 123006. doi:10.1088/1748-9326/ab4557.

Hegerl, G. C., Brönnimann, S., Schurer, A. and Cowan, T. (2018). The early 20th century warming: Anomalies, causes, and consequences. *Wiley Interdisciplinary Reviews: Climate Change*, 9 (4), e522. doi:10.1002/wcc.522.

Heiri, O., Lotter, A. F. and Lemcke, G. (2001). Loss on ignition as a method for estimating organic and carbonate content in sediments: reproducibility and comparability of results. *Journal of paleolimnology*, 25 (1), 101–110.

Hendon, H. H., Lim, E.-P. and Nguyen, H. (2014). Seasonal Variations of Subtropical Precipitation Associated with the Southern Annular Mode. *Journal of Climate*, 27 (9), 3446–3460. doi:10.1175/JCLI-D-13-00550.1.

Henley, B. J., Gergis, J., Karoly, D. J., Power, S., Kennedy, J. and Folland, C. K. (2015). A Tripole Index for the Interdecadal Pacific Oscillation. *Climate Dynamics*, 45 (11–12), 3077–3090. doi:10.1007/s00382-015-2525-1.

Hill, M. O. and Gauch, H. G. (1980). Detrended correspondence analysis: an improved ordination technique. In: *Classification and ordination*. van der Maarel, E., (Ed.), Dordrecht, Netherlands: Springer. 47–58. doi: 10.1007/978-94-009-9197-2_7.

Hill, T. C., Woodland, W. A., Spencer, C. D. and Marriott, S. B. (2007). Holocene sea-level change in the Severn Estuary, southwest England: a diatom-based sea-level transfer function for macrotidal settings. *The Holocene*, 17 (5), 639–648. doi:10.1177/0959683607078988.

Hocking, E. P., Garrett, E. and Cisternas, M. (2017). Modern diatom assemblages from Chilean tidal marshes and their application for quantifying deformation during past great earthquakes. *Journal of Quaternary Science*, 32 (3), 396–415. doi:10.1002/jqs.2933.

Hogarth, P. (2014a). *Australian, New Zealand and Tasmanian tide gauge data*. https://www.psmsl.org/products/author_archive/Australian_Tidal_Data_and_References_final-b.pdf

Hogarth, P. (2014b). Preliminary analysis of acceleration of sea level rise through the twentieth century using extended tide gauge data sets. *Journal of Geophysical Research: Oceans*, 119 (11), 7645–7659. doi:10.1002/2014JC009976.

Hogarth, P., Pugh, D. T., Hughes, C. W. and Williams, S. D. P. (2021). Changes in mean sea level around Great Britain over the past 200 years. *Progress in Oceanography*, 192, 102521. doi:10.1016/j.pocean.2021.102521.

Hogg, A. G., Heaton, T. J., Hua, Q., Palmer, J. G., Turney, C. S., Southon, J., Bayliss, A., Blackwell, P. G., Boswijk, G. and Ramsey, C. B. (2020). SHCal20 Southern Hemisphere calibration, 0–55,000 years cal BP. *Radiocarbon*, 62 (4), 759–778. doi:10.1017/RDC.2020.59.

Holbrook, N. J., Goodwin, I. D., McGregor, S., Molina, E. and Power, S. B. (2011). ENSO to multi-decadal time scale changes in East Australian Current transports and Fort Denison sea level: Oceanic Rossby waves as the connecting mechanism. *Deep Sea Research Part II: Topical Studies in Oceanography*, 58 (5), 547–558. doi:10.1016/j.dsr2.2010.06.007.

Holgate, S. J., Matthews, A., Woodworth, P. L., Rickards, L. J., Tamisiea, M. E., Bradshaw, E., Foden, P. R., Gordon, K. M., Jevrejeva, S. and Pugh, J. (2013). New Data Systems and Products at the Permanent Service for Mean Sea Level. *Journal of Coastal Research*, 29 (3), 493–504. doi:10.2112/JCOASTRES-D-12-00175.1.

Hong, W., Cooke, D. R., Zhang, L., Fox, N. and Thompson, J. (2019). Cathodoluminescence features, trace elements, and oxygen isotopes of quartz in unidirectional solidification textures from the Sn-mineralized Heemskirk Granite, western Tasmania. *American Mineralogist*, 104 (1), 100–117. doi:10.2138/am-2019-6534.

Horton, B. P., Corbett, R., Culver, S. J., Edwards, R. J. and Hillier, C. (2006). Modern saltmarsh diatom distributions of the Outer Banks, North Carolina, and the development of a transfer function for high resolution reconstructions of sea level. *Estuarine, Coastal and Shelf Science*, 69 (3), 381–394. doi:10.1016/j.ecss.2006.05.007.

Horton, B. P., Culver, S. J., Hardbattle, M. I. J., Larcombe, P., Milne, G. A., Morigi, C., Whittaker, J. E. and Woodroffe, S. A. (2007). Reconstructing Holocene sea-level change for the Central Great Barrier Reef (Australia) using subtidal foraminifera. *Journal of Foraminiferal Research*, 37 (4), 327–343. doi:10.2113/gsjfr.37.4.327.

Horton, B. P. and Edwards, R. J. (2005). The application of local and regional transfer functions to the reconstruction of Holocene sea levels, north Norfolk, England. *The Holocene*, 15 (2), 216–228. doi:10.1191/0959683605hl787rp.

Horton, B. P. and Edwards, R. J. (2006). *Quantifying Holocene Sea Level Change Using Intertidal Foraminifera: Lessons from the British Isles*. http://repository.upenn.edu/ees_papershttp://repository.upenn.edu/ees_papers/50.

Horton, B. P., Edwards, R. J. and Lloyd, J. M. (1999). A foraminiferal-based transfer function: implications for sea-level studies. *Journal of Foraminiferal Research*, 29 (2), 117–129. doi:10.2113/gsjfr.29.2.117.

Horton, B. P., Larcombe, P., Woodroffe, S. A., Whittaker, J. E., Wright, M. R. and Wynn, C. (2003). Contemporary foraminiferal distributions of a mangrove environment, Great Barrier Reef coastline, Australia: implications for sea-level reconstructions. *Marine Geology*, 198 (3), 225–243. doi:10.1016/S0025-3227(03)00117-8.

Horton, B. P. and Murray, J. W. (2006). Patterns in cumulative increase in live and dead species from foraminiferal time series of Cowpen Marsh, Tees Estuary, UK: Implications for sea-level studies. *Marine Micropaleontology*, 58 (4), 287–315. doi:10.1016/j.marmicro.2005.10.006

Horton, B. P. and Murray, J. W. (2007). The roles of elevation and salinity as primary controls on living foraminiferal distributions: Cowpen Marsh, Tees Estuary, UK. *Marine Micropaleontology*, 63 (3), 169–186. doi:10.1016/j.marmicro.2006.11.006.

Howat, I. M. and Eddy, A. (2011). Multi-decadal retreat of Greenland's marine-terminating glaciers. *Journal of Glaciology*, 57 (203), 389–396. doi:10.3189/002214311796905631.

Hua, Q., Barbetti, M. and Rakowski, A. Z. (2013). Atmospheric radiocarbon for the period 1950–2010. *Radiocarbon*, 55 (4), 2059–2072. doi:10.2458/azu_js_rc.v55i2.16177.

Hunter, J. R. (2007). *Department of Primary Industries and Water Historical and Projected Sea-Level Extremes for Hobart and Burnie, Tasmania*. Hobart and Burnie, Tasmania : Antarctic Climate & Ecosystems Cooperative Research Centre. 227. http://dpipwe.tas.gov.au/Documents/CCCRMP-Hunter_Report.pdf.

Huo, X.X, Crisp, P.T, Cohen, D. D. (1999). Source Apportionment of Fine Particles in the Wollongong-Port Kembla Area during 1992 and 1993. *Clean Air and Environmental Quality*, 33 (1), 26–35.

Jackson, R. (2006). *Bruny on the Brink: Governance, Gentrification and Tourism on an Australian Island*. 201–222. https://islandstudies.ca/sites/vre2.upei.ca.islandstudies.ca/files/u2/ISJ-1-2-2006-Jackson-article.pdf.

Jevrejeva, S., Grinsted, A., Moore, J. C. and Holgate, S. (2006). Nonlinear trends and multiyear cycles in sea level records. *Journal of Geophysical Research*, 111 (C9), C09012. doi:10.1029/2005JC003229.

Jevrejeva, S., Moore, J. C., Grinsted, A., Matthews, A. P. and Spada, G. (2014). Trends and acceleration in global and regional sea levels since 1807. *Global and Planetary Change*, 113, 11–22. doi:10.1016/J.GLOPLACHA.2013.12.004.

Johannessen, O. M., Kuzmina, S. I., Bobylev, L. P. and Miles, M. W. (2016). Surface air temperature variability and trends in the Arctic: new amplification assessment and regionalisation. *Tellus A: Dynamic Meteorology and Oceanography*, 68 (1), 28234. doi:10.3402/tellusa.v68.28234.

Johnson, M. and McFarlane, I. (2015). *Van Diemen's Land: An Aboriginal History*. Sydney, Australia. UNSW Press.

Jones, R. S., Mackintosh, A. N., Norton, K. P., Golledge, N. R., Fogwill, C. J., Kubik, P. W., Christl, M. and Greenwood, S. L. (2015). Rapid Holocene thinning of an East Antarctic outlet glacier driven by marine Ice Sheet instability. *Nature Communications*, 6 (1), 1–9. doi:10.1038/ncomms9910.

Juggins, S. and Birks, H. J. B. (2012). Quantitative Environmental Reconstructions from Biological Data. In: Birks, H. J. B., Lotter, A. F., Juggins, S. and Smol, J. P. (Eds), *Tracking Environmental Change Using Lake Sediments: Data Handling and Numerical Techniques*. Developments in Paleoenvironmental Research. Dordrecht : Springer Netherlands. 431–494. doi:10.1007/978-94-007-2745-8_14.

Kassambara, A. and Mundt, F. (2017). *Package 'factoextra'. Extract and visualize the results of multivariate data analyses*. https://cran.r-project.org/web/packages/factoextra/index.html

Kaufman, L. and Rousseeuw, P. J. (1990). *Finding Groups in Data: An Introduction to Cluster Analysis*. Hoboken, New Jersey: John Wiley & Sons.

Kavan, J. (2020). Early twentieth century evolution of Ferdinand glacier, Svalbard, based on historic photographs and structure-from-motion technique. *Geografiska Annaler: Series A, Physical Geography*, 102 (1), 57–67. doi:10.1080/04353676.2020.1715124.

Keith, D. A. and Bedward, M. (1999). Native vegetation of the South East Forests region, Eden, New South Wales. *Cunninghamia*, 6, 1–218.

Kelly, J. T., McSweeney, S., Shulmeister, J. and Gontz, A. M. (2019). Bimodal climate control of shoreline change influenced by Interdecadal Pacific Oscillation variability along the Cooloola Sand Mass, Queensland, Australia. *Marine Geology*, 415, 105971. doi:10.1016/j.margeo.2019.105971.

Kemp, A.C., Bernhardt, C.E., Horton, B.P., Kopp, R.E., Vane, C.H., Peltier, W.R., Hawkes, A.D., Donnelly, J.P., Parnell, A.C. and Cahill, N., (2014). Late Holocene sea-and land-level change on the US southeastern Atlantic coast. *Marine Geology*, *357*, 90-100. doi:10.1016/j.margeo.2014.07.010.

Kemp, A. C., Hawkes, A. D., Donnelly, J. P., Vane, C. H., Horton, B. P., Hill, T. D., Anisfeld, S. C., Parnell, A. C. and Cahill, N. (2015). Relative sea-level change in Connecticut (USA) during the last 2200 yrs. *Earth and Planetary Science Letters*, 428, 217–229. doi:10.1016/j.epsl.2015.07.034.

Kemp, A. C., Hill, T. D., Vane, C. H., Cahill, N., Orton, P. M., Talke, S. A., Parnell, A. C., Sanborn, K. and Hartig, E. K. (2017a). Relative sea-level trends in New York City during the past 1500 years. *The Holocene*, 27 (8), 1169–1186. doi:10.1177/0959683616683263.

Kemp, A. C., Horton, B. P. and Culver, S. J. (2009). Distribution of modern salt-marsh foraminifera in the Albemarle–Pamlico estuarine system of North Carolina, USA: Implications for sea-level research. *Marine Micropaleontology*, 72 (3–4), 222–238. doi:10.1016/j.marmicro.2009.06.002.

Kemp, A. C., Horton, B. P., Donnelly, J. P., Mann, M. E., Vermeer, M. and Rahmstorf, S. (2011). Climate related sea-level variations over the past two millennia. *Proceedings of the National Academy of Sciences*, 108 (27), 11017–11022. doi:10.1073/pnas.1015619108.

Kemp, A. C., Horton, B. P., Nikitina, D., Vane, C. H., Potapova, M., Weber-Bruya, E., Culver, S. J., Repkina, T. and Hill, D. F. (2017b). The distribution and utility of sea-level indicators in Eurasian sub-Arctic salt marshes (White Sea, Russia). *Boreas*, 46 (3), 562–584. doi:10.1111/bor.12233.

Kemp, A. C., Horton, B. P., Vane, C. H., Bernhardt, C. E., Corbett, D. R., Engelhart, S. E., Anisfeld, S. C., Parnell, A. C. and Cahill, N. (2013a). Sea-level change during the last 2500 years in New Jersey, USA. *Quaternary Science Reviews*, 81, 90–104. doi:10.1016/j.quascirev.2013.09.024.

Kemp, A. C., Horton, B. P., Vann, D. R., Engelhart, S. E., Grand Pre, C. A., Vane, C. H., Nikitina, D. and Anisfeld, S. C. (2012a). Quantitative vertical zonation of salt-marsh foraminifera for reconstructing former sea level; an example from New Jersey, USA. *Quaternary Science Reviews*, 54, 26–39. doi:10.1016/j.quascirev.2011.09.014.

Kemp, A. C., Kegel, J. J., Culver, S. J., Barber, D. C., Mallinson, D. J., Leorri, E., Bernhardt, C. E., Cahill, N., Riggs, S. R., Woodson, A. L., et al. (2017c). Extended late Holocene relative sea-level histories for North Carolina, USA. *Quaternary Science Reviews*, 160, 13–30. doi:10.1016/j.quascirev.2017.01.012.

Kemp, A. C., Sommerfield, C. K., Vane, C. H., Horton, B. P., Chenery, S., Anisfeld, S. and Nikitina, D. (2012b). Use of lead isotopes for developing chronologies in recent salt-marsh sediments. *Quaternary Geochronology*, 12, 40–49. doi:10.1016/j.quageo.2012.05.004.

Kemp, A., C. and Telford, R., J. (2015). Chapter 31: Transfer functions. In: Shennan, I., Long, A.J., and Horton, B.P. (Eds.), *Handbook of Sea-Level Research*. Chichester, UK: John Wiley & Sons. doi:10.1002/9781118452547.ch31.

Kemp, A. C., Telford, R. J., Horton, B. P., Anisfeld, S. C. and Sommerfield, C. K. (2013b). Reconstructing Holocene sea level using salt-marsh foraminifera and transfer functions: lessons from New Jersey, USA. *Journal of Quaternary Science*, 28 (6), 617–629. doi:10.1002/jqs.2657.

Kemp, A. C., Wright, A. J. and Cahill, N. (2020). Enough is Enough, or More is More? Testing the Influence of Foraminiferal Count Size on Reconstructions of Paleo-Marsh Elevation. *Journal of Foraminiferal Research*, 50 (3), 266–278. doi:10.2113/gsjfr.50.3.266.

Kemp, A. C., Wright, A. J., Edwards, R. J., Barnett, R. L., Brain, M. J., Kopp, R. E., Cahill, N., Horton, B. P., Charman, D. J., Hawkes, A. D., et al. (2018). Relative sea-level change in Newfoundland, Canada during the past ~3000 years. *Quaternary Science Reviews*, 201, 89–110. doi:10.1016/j.quascirev.2018.10.012.

Kemp, A.C., Horton, B.P., Culver, S.J., Corbett, D.R., van de Plassche, O., Gehrels, W.R., Douglas, B.C. and Parnell, A. C. (2009). Timing and magnitude of recent accelerated sea-level rise (North Carolina, United States). *Geology*, 27 (11), 1035–1038. doi:10.1130/G30352A.1.

Kershaw, A. P., Bulman, D. and Busby, J. R. (1994). An examination of modern and pre-European settlement pollen samples from southeastern Australia—assessment of their application to quantitative reconstruction of past vegetation and climate. *Review of Palaeobotany and Palynology*, 82 (1–2), 83–96. doi:10.1016/0034-6667(94)90021-3.

Khan, N. S., Ashe, E., Shaw, T. A., Vacchi, M., Walker, J., Peltier, W. R., Kopp, R. E. and Horton, B. P. (2015). Holocene relative sea-level changes from near-, intermediate-, and far-field locations. *Current Climate Change Reports*, 1 (4), 247–262. doi:10.1007/s40641-015-0029-z.

Khan, S. A., Bjørk, A. A., Bamber, J. L., Morlighem, M., Bevis, M., Kjær, K. H., Mouginot, J., Løkkegaard, A., Holland, D. M., Aschwanden, A., et al. (2020). Centennial response of Greenland's three largest outlet glaciers. *Nature Communications*, 11 (1), 5718. doi:10.1038/s41467-020-19580-5.

Khan, S. A., Kjeldsen, K. K., Kjær, K. H., Bevan, S., Luckman, A., Aschwanden, A., Bjørk, A. A., Korsgaard, N. J., Box, J. E., van den Broeke, M., et al. (2014). Glacier dynamics at Helheim and Kangerdlugssuaq glaciers, southeast Greenland, since the Little Ice Age. *The Cryosphere*, 8 (4), 1497–1507. doi:10.5194/tc-8-1497-2014.

King, M. D., Howat, I. M., Candela, S. G., Noh, M. J., Jeong, S., Noël, B. P. Y., van den Broeke, M. R., Wouters, B. and Negrete, A. (2020). Dynamic ice loss from the Greenland Ice Sheet driven by sustained glacier retreat. *Communications Earth & Environment*, 1 (1), 1–7. doi:10.1038/s43247-020-0001-2.

King, O., Bhattacharya, A., Bhambri, R. and Bolch, T. (2019). Glacial lakes exacerbate Himalayan glacier mass loss. *Scientific Reports*, 9 (1), 18145. doi:10.1038/s41598-019-53733-x.

Kjeldsen, K. K., Korsgaard, N. J., Bjørk, A. A., Khan, S. A., Box, J. E., Funder, S., Larsen, N. K., Bamber, J. L., Colgan, W., van den Broeke, M., et al. (2015). Spatial and temporal distribution of mass loss from the Greenland Ice Sheet since AD 1900. *Nature*, 528 (7582), 396–400. doi:10.1038/nature16183.

Kopp, R. E., Horton, B. P., Kemp, A. C. and Tebaldi, C. (2015). Past and future sea-level rise along the coast of North Carolina, USA. *Climatic Change*, 132 (4), 693–707. doi:10.1007/s10584-015-1451-x.

Kopp, R. E., Horton, R. M., Little, C. M., Mitrovica, J. X., Oppenheimer, M., Rasmussen, D. J., Strauss, B. H. and Tebaldi, C. (2014). Probabilistic 21st and 22nd century sea-level projections at a global network of tide-gauge sites. *Earth's Future*, 2 (8), 383–406. doi:10.1002/2014EF000239.

Kopp, R. E., Kemp, A. C., Bittermann, K., Horton, B. P., Donnelly, J. P., Gehrels, W. R., Hay, C. C., Mitrovica, J. X., Morrow, E. D. and Rahmstorf, S. (2016). Temperature-driven global sea-level

variability in the Common Era. *Proceedings of the National Academy of Sciences of the United States of America*, 113 (11), E1434-41. doi:10.1073/pnas.1517056113.

Krabill, W.E., Hanna, E., Huybrechts, P., Abdalati, W., Cappelen, J., Csatho, B., Frederick, E., Manizade, S., Martin, C., Sonntag, J. et al. (2004). Greenland Ice Sheet: increased coastal thinning. *Geophysical Research Letters*, *31* (24). doi: 10.1029/2004GL021533.

Kristensen, L. J. (2015). Quantification of atmospheric lead emissions from 70 years of leaded petrol consumption in Australia. *Atmospheric Environment*, 111, 195–201. doi:10.1016/j.atmosenv.2015.04.012.

Kristensen, L. J. and Taylor, M. P. (2016). Unravelling a 'miner's myth' that environmental contamination in mining towns is naturally occurring. *Environmental Geochemistry and Health*, 38 (4), 1015–1027. doi:10.1007/s10653-016-9804-6.

Kristensen, L. J., Taylor, M. P. and Flegal, A. R. (2017). An odyssey of environmental pollution: The rise, fall and remobilisation of industrial lead in Australia. *Applied Geochemistry*, 83, 3–13. doi:10.1016/J.APGEOCHEM.2017.02.007.

Kylander, M. E., Ampel, L., Wohlfarth, B. and Veres, D. (2011). High-resolution X-ray fluorescence core scanning analysis of Les Echets (France) sedimentary sequence: new insights from chemical proxies. *Journal of Quaternary Science*, 26 (1), 109–117. doi:10.1002/jqs.1438.

Lal, K. K., Bonetti, C., Woodroffe, C. D. and Rogers, K. (2020). Contemporary distribution of benthic foraminiferal assemblages in coastal wetlands of south-eastern Australia. *Estuarine, Coastal and Shelf Science*, 245, 106949. doi:10.1016/j.ecss.2020.106949.

Lambeck, K. and Nakada, M. (1990). Late Pleistocene and Holocene sea-level change along the Australian coast. *Palaeogeography, Palaeoclimatology, Palaeoecology*, 89 (1), 143–176. doi:10.1016/0031-0182(90)90056-D.

Lampert, R. J. (1971). *Burrill Lake and Currarong : Coastal sites in southern New South Wales*. Canberra, ACT : Dept. of Prehistory, Research School of Pacific and Asian Studies, The Australian National University. https://openresearch-repository.anu.edu.au/handle/1885/127416

Lea, J. M., Mair, D. W., Nick, F. M., Rea, B. R., Weidick, A., Kjaer, K. H., Morlighem, M., Van As, D. and Schofield, J. E. (2014). Terminus-driven retreat of a major southwest Greenland tidewater glacier during the early 19th century: insights from glacier reconstructions and numerical modelling. *Journal of Glaciology*, 60 (220), 333–344. doi: 10.3189/2014JoG13J163.

Leclercq, P. W., Oerlemans, J., Basagic, H. J., Bushueva, I., Cook, A. J. and Bris, R. L. (2014). A data set of worldwide glacier length fluctuations. *The Cryosphere*, 8,(2),659–672. doi:10.5194/tc-8-659-2014

Leclercq, P. W., Oerlemans, J. and Cogley, J. G. (2011). Estimating the Glacier Contribution to Sea-Level Rise for the Period 1800-2005. *Surveys in Geophysics*, 32 (4–5), 519–535. doi:10.1007/s10712-011-9121-7.

Lee, E., Carrivick, J. L., Quincey, D. J., Cook, S. J., James, W. H. M. and Brown, L. E. (2021). Accelerated mass loss of Himalayan glaciers since the Little Ice Age. *Scientific Reports*, 11 (1), 24284. doi:10.1038/s41598-021-03805-8.

Leonard, M. (2008). One Hundred Years of Earthquake Recording in Australia. *Bulletin of the Seismological Society of America*, 98 (3), 1458–1470. doi:10.1785/0120050193.

Leorri, E., Fatela, F., Cearreta, A., Moreno, J., Antunes, C. and Drago, T. (2011). Assessing the performance of a foraminifera-based transfer function to estimate sea-level changes in northern Portugal. *Quaternary Research*, 75 (1), 278–287. doi: 10.1016/j.yqres.2010.10.003.

Leorri, E., Gehrels, W. R., Horton, B. P., Fatela, F. and Cearreta, A. (2010). Distribution of foraminifera in salt marshes along the Atlantic coast of SW Europe: Tools to reconstruct past sea-level variations. *Quaternary International*, 221 (1), 104–115. doi:10.1016/j.quaint.2009.10.033.

Leorri, E., Horton, B. P. and Cearreta, A. (2008). Development of a foraminifera-based transfer function in the Basque marshes, N. Spain: implications for sea-level studies in the Bay of Biscay. *Marine Geology*, 251 (1–2), 60–74. doi: 10.1016/j.margeo.2008.02.005.

Lewis, S. E., Sloss, C. R., Murray-Wallace, C. V., Woodroffe, C. D. and Smithers, S. G. (2013). Post-glacial sea-level changes around the Australian margin: a review. *Quaternary Science Reviews*, 74, 115–138. doi:10.1016/J.QUASCIREV.2012.09.006.

Lindenmayer, D. (2007). *On borrowed time: Australia's environmental crisis and what we must do about it*. Penguin Books. https://scholar.google.co.uk/scholar?hl=en&as_sdt=0%2C5&q=Lindenmayer+DB.+%2C+On+Borrowed+Time.+Australia%27s+Environmental+Crisis+and+What+We+Must+Do+About+It+%2C+2007Camberwell%2C+AustraliaPenguin+Group&btnG=#d=gs_cit&u=%2Fscholar%3Fq%3Dinfo%3A74xqZdFvE.

Lloyd, J., Moros, M., Perner, K., Telford, R. J., Kuijpers, A., Jansen, E. and McCarthy, D. (2011). A 100 yr record of ocean temperature control on the stability of Jakobshavn Isbrae, West Greenland. *Geology*, 39 (9), 867–870. doi:10.1130/G32076.1.

Long, A. J., Barlow, N. L. M., Gehrels, W. R., Saher, M. H., Woodworth, P. L., Scaife, R. G., Brain, M. J. and Cahill, N. (2014). Contrasting records of sea-level change in the eastern and western North Atlantic during the last 300 years. *Earth and Planetary Science Letters*, 388, 110–122. doi:10.1016/j.epsl.2013.11.012.

Long, A. J., Woodroffe, S. A., Milne, G. A., Bryant, C. L. and Wake, L. M. (2010). Relative sea level change in west Greenland during the last millennium. *Quaternary Science Reviews*, 29 (3), 367–383. doi:10.1016/j.quascirev.2009.09.010.

Lunney, D., Cullis, B. and Eby, P. (1987). Effects of logging and fire on small mammals in Mumbulla State Forest, near Bega, New South Wales. *Wildlife Research*, 14 (2), 163. doi:10.1071/WR9870163.

Lunney, D. and Leary, T. (1988). The impact on native mammals of land-use changes and exotic species in the Bega district, New South Wales, since settlement. *Australian Journal of Ecology*, 13, 67–92. doi:10.1111/j.1442-9993.1988.tb01417.x.

Lyle, D. M., Phillips, A. R., Balding, W. A., Burke, H., Stokes, D., Corbett, S. and Hall, J. (2006). Dealing with lead in Broken Hill—Trends in blood lead levels in young children 1991–2003. *Science of The Total Environment*, 359 (1–3), 111–119. doi:10.1016/J.SCITOTENV.2005.04.022.

Mackay, N. J., Williams, R. J., Kacprzac, J. L., Kazacos, M. N., Collins, A. J. and Auty, E. H. (1975). Heavy metals in cultivated oysters (*Crassostrea commercialis* = *Saccostrea cucullata*) from estuaries of New South Wales. *Marine and Freshwater Research*, 26 (1), 31–46. doi:10.1071/mf9750031.

Mackenzie, L., Heijnis, H., Gadd, P., Moss, P. and Shulmeister, J. (2017). Geochemical investigation of the South Wellesley Island wetlands: Insight into wetland development during the Holocene in tropical northern Australia. *The Holocene*, 27 (4), 566–578. doi:10.1177/0959683616670219

Maechler, M., Rousseeuw, P., Struyf, A., Hubert, M., Hornik, K. and Studer, M. (2013). *Package 'cluster'*. https://cran.r-project.org/web/packages/cluster/cluster.pdf

Mainville, D. M. *The Impacts of Agriculture and Plantation Forestry in a Selection of Upper Catchments of the Strzelecki Ranges, Victoria*. PhD Thesis, RMIT University. https://s3-ap-southeast-1.amazonaws.com/ap-st01.ext.exlibrisgroup.com/61RMIT_INST/storage/alma/03/AE/12/BE/4A/F1/DC/4F/F9/B1/6C/98/B4/33/F8/7D/Mainville.pdf?response-content-type=application%2Fpdf&X-Amz-Algorithm=AWS4-HMAC-SHA256&X-Amz-Date=20211223T135031Z&X-Amz-SignedHeaders=host&X-Amz-Expires=119&X-Amz-Credential=AKIAJN6NPMNGJALPPWAQ%2F20211223%2Fap-southeast-1%2Fs3%2Faws4_request&X-Amz-Signature=5fa0dc65f8d633d7db7d6a67bc5c5fe4a8b85f72313f38c3cbccedd0776a802f

Malles, J.-H. and Marzeion, B. (2021). Twentieth century global glacier mass change: an ensemble-based model reconstruction. *The Cryosphere*, 15 (7), 3135–3157. doi:10.5194/tc-15-3135-2021.

Marsden-Smedley, J. B. (1998). Changes in southwestern Tasmanian fire regimes since the early 1800s. *Papers and Proceedings of the Royal Society of Tasmania*, 132. doi:10.26749/rst132.15.

Marshall, W. A., Gehrels, W. R., Garnett, M. H., Freeman, S. P., Maden, C. and Xu, S. (2007). The use of 'bomb spike'calibration and high-precision AMS ^{14}C analyses to date salt-marsh sediments deposited during the past three centuries. *Quaternary Research*, 68 (3), 325–337. doi:10.1016/j.yqres.2007.07.005.

Martley, E., Gulson, B. L. and Pfeifer, H.-R. (2004). Metal concentrations in soils around the copper smelter and surrounding industrial complex of Port Kembla, NSW, Australia. *Science of The Total Environment*, 325 (1–3), 113–127. doi:10.1016/J.SCITOTENV.2003.11.012.

Marx, S. K., Kamber, B. S., McGowan, H. A. and Zawadzki, A. (2010). Atmospheric pollutants in alpine peat bogs record a detailed chronology of industrial and agricultural development on the Australian continent. *Environmental Pollution*, 158 (5), 1615–1628. doi:10.1016/J.ENVPOL.2009.12.009.

Marzeion, B., Champollion, N., Haeberli, W., Langley, K., Leclercq, P. and Paul, F. (2017). Observation-Based Estimates of Global Glacier Mass Change and Its Contribution to Sea-Level Change. *Surveys in Geophysics*, 38 (1), 105–130. doi:10.1007/s10712-016-9394-y.

Marzeion, B., Jarosch, A.H. and Gregory, J.M., (2014). Feedbacks and mechanisms affecting the global sensitivity of glaciers to climate change. *The Cryosphere*, *8* (1), 59-71. doi:10.5194/tc-8-59-2014.

Marzeion, B., Jarosch, A.H. and Hofer, M., (2012). Past and future sea-level change from the surface mass balance of glaciers. *The Cryosphere*, *6* (6), 1295-1322. doi: 10.5194/tc-6-1295-2012.

Marzeion, B., Leclercq, P. W., Cogley, J. G. and Jarosch, A. H. (2015). Brief Communication: Global reconstructions of glacier mass change during the 20th century are consistent. *The Cryosphere*, 9, 2399–2404. doi:10.5194/tc-9-2399-2015.

Masselink, G. and Gehrels,W.R. (2015). Introduction to coastal environments and global change. *Coastal Environments and Global Change*, 1–27.

Massey, A. C., Gehrels, W. R., Charman, D. J. and White, S. V. (2006). An intertidal foraminifera-based transfer function for reconstructing Holocene sea-level change in southwest England. *The Journal of Foraminiferal Research*, 36 (3), 215–232. doi:10.2113/gsjfr.36.3.215.

Majewski, J.M., Meltzner, A.J., Switzer, A.D., Shaw, T.A., Li, T., Bradley, S., Walker, J.S., Kopp, R.E., Samanta, D., Natawidjaja, D.H. and Suwargadi, B.W., 2022. Extending instrumental sea-level records using coral microatolls, an example from Southeast Asia. *Geophysical Research Letters*, *49*(4), p.e2021GL095710. doi:10.1029/2021GL095710.

McConnell, J. R., Maselli, O. J., Sigl, M., Vallelonga, P., Neumann, T., Anschütz, H., Bales, R. C., Curran, M. A. J., Das, S. B., Edwards, R., et al. (2015). Antarctic-wide array of high-resolution ice core records reveals pervasive lead pollution began in 1889 and persists today. *Scientific Reports*, 4 (1), 5848. doi:10.1038/srep05848.

McNiven, I. J. (2000). Treats or retreats? Aboriginal island use along the Gippsland coast. *Artefact: the Journal of the Archaeological and Anthropological Society of Victoria.* 23 (2000), 23–34.

McQueen, K. G. (2015). *Early Mining History, Broken Hill Special 1:250 000 Scale Metallogenic Map*. Maitland, NSW.

MDO. (2019). *Major Mines Projects | Mount Lyell Mine*. https://miningdataonline.com/property/849/Mount-Lyell-Mine.aspx#Production [Accessed 3 April 2019].

Mernild, S. H., Hanna, E., McConnell, J. R., Sigl, M., Beckerman, A. P., Yde, J. C., Cappelen, J., Malmros, J. K. and Steffen, K. (2015). Greenland precipitation trends in a long-term instrumental climate context (1890–2012): evaluation of coastal and ice core records. *International Journal of Climatology*, 35 (2), 303–320. doi: 10.1002/joc.3986.

Mernild, S.H., Lipscomb, W.H., Bahr, D.B., Radić, V. and Zemp, M., (2013). Global glacier changes: a revised assessment of committed mass losses and sampling uncertainties. *The Cryosphere*, *7* (5), 1565-1577. doi:10.5194/tc-7-1565-2013.

Mernild, S. H., Liston, G. E., Hiemstra, C. and Wilson, R. (2017). The Andes Cordillera. Part III: glacier surface mass balance and contribution to sea level rise (1979–2014). *International Journal of Climatology*, 37 (7), 3154–3174. doi:10.1002/joc.4907.

Milker, Y., Horton, B. P., Nelson, A. R., Engelhart, S. E. and Witter, R. C. (2015a). Variability of intertidal foraminiferal assemblages in a salt marsh, Oregon, USA. *Marine Micropaleontology*, 118, 1–16. doi:10.1016/j.marmicro.2015.04.004.

Milker, Y., Horton, B. P., Vane, C. H., Engelhart, S. E., Nelson, A. R., Witter, R. C., Khan, N. S. and Bridgeland, W. T. (2015b). Annual and seasonal distribution of intertidal foraminifera and stable carbon isotope geochemistry, Bandon Marsh, Oregon, USA. *The Journal of Foraminiferal Research*, 45 (2), 146–155. doi: 10.2113/gsjfr.45.2.146.

Miller, G. H., Magee, J. W. and Jull, A. J. T. (1997). Low-latitude glacial cooling in the Southern Hemisphere from amino-acid racemization in emu eggshells. *Nature*, 385 (6613), 241–244. doi:10.1038/385241a0.

Mills, H., Kirby, J., Holgate, S. and Plater, A. (2013). The distribution of contemporary saltmarsh foraminifera in a macrotidal estuary: an assessment of their viability for sea-level studies. *Journal of Ecosystem and Ecography*, 3, 1–16. doi:10.4172/2157-7625.1000131.

Mitrovica, J. X., Gomez, N., Morrow, E., Hay, C., Latychev, K. and Tamisiea, M. E. (2011). On the robustness of predictions of sea level fingerprints. *Geophysical Journal International*, 187 (2), 729–742. doi:10.1111/j.1365-246X.2011.05090.x.

Mitrovica, J. X., Tamisiea, M. E., Davis, J. L. and Milne, G. A. (2001). Recent mass balance of polar Ice Sheets inferred from patterns of global sea-level change. *Nature*, 409 (6823), 1026–1030. doi:10.1038/35059054.

Mitrovica, J. X., Wahr, J., Matsuyama, I. and Paulson, A. (2005). The rotational stability of an ice-age earth. *Geophysical Journal International*, 161 (2), 491–506. doi: 10.1111/j.1365-246X.2005.02609.x

Mooney, S. D. and Dodson, J. R. (2001). A Comparison of the Environmental Changes of the Post-European Period with those of the Preceding 2000 Years at Lake Keilambete, South-western Victoria. *Australian Geographer*, 32 (2), 163–179. doi:10.1080/00049180125614.

Mooney, S. D., Harrison, S. P., Bartlein, P. J., Daniau, A.-L., Stevenson, J., Brownlie, K. C., Buckman, S., Cupper, M., Luly, J., Black, M., et al. (2011). Late Quaternary fire regimes of Australasia. *Quaternary Science Reviews*, 30 (1–2), 28–46. doi:10.1016/J.QUASCIREV.2010.10.010.

Moss, P. T., Tibby, J., Petherick, L., McGowan, H. and Barr, C. (2013). Late Quaternary vegetation history of North Stradbroke Island, Queensland, eastern Australia. *Quaternary Science Reviews*, 74, 257–272. doi:10.1016/j.quascirev.2013.02.019.

Mouginot, J., Rignot, E., Bjørk, A. A., van den Broeke, M., Millan, R., Morlighem, M., Noël, B., Scheuchl, B. and Wood, M. (2019). Forty-six years of Greenland Ice Sheet mass balance from 1972 to 2018. *Proceedings of the National Academy of Sciences*, 116 (19), 9239–9244. doi:10.1073/pnas.1904242116.

Mudd, G. M. (2007). Gold mining in Australia: linking historical trends and environmental and resource sustainability. *Environmental Science & Policy*, 10 (7–8), 629–644. doi:10.1016/J.ENVSCI.2007.04.006.

Mudd, G. M. (2009). *The Sustainability of Mining in Australia : Key Production Trends and Their Environmental Implications for the Future*. http://users.monash.edu.au/ gmudd/files/SustMining-Aust-Report-2009-Master.pdf.

Müller, W. A., Matei, D., Bersch, M., Jungclaus, J. H., Haak, H., Lohmann, K., Compo, G. P., Sardeshmukh, P. D. and Marotzke, J. (2015). A twentieth-century reanalysis forced ocean model to reconstruct the North Atlantic climate variation during the 1920s. *Climate Dynamics*, 44 (7), 1935–1955. doi:10.1007/s00382-014-2267-5.

Murray, J. W. (2006). *Ecology and Applications of Benthic Foraminifera*. Cambridge University Press.

Murray, J. W. and Bowser, S. S. (2000). Mortality, protoplasm decay rate, and reliability of staining techniques to recognize 'living' foraminifera: a review. *Journal of Foraminiferal Research*, 30 (1), 66–70. doi:10.2113/0300066.

Najafi, M. R., Zwiers, F. W. and Gillett, N. P. (2015). Attribution of Arctic temperature change to greenhouse-gas and aerosol influences. *Nature Climate Change*, 5 (3), 246–249. doi:10.1038/nclimate2524.

Nakada, M. and Inoue, H. (2005). Rates and causes of recent global sea-level rise inferred from long tide gauge data records. *Quaternary Science Reviews*, 24 (10), 1217–1222. doi:10.1016/j.quascirev.2004.11.006.

Nakada, M. and Lambeck, K. (1989). Late Pleistocene and Holocene sea-level change in the Australian region and mantle rheology. *Geophysical Journal International*, 96 (3), 497–517. doi:10.1111/j.1365-246X.1989.tb06010.x.

Nethery, A. (2012). Separate and Invisible A Carceral History of Australian Islands. *The International Journal of Research into Island Cultures*, 6 (85–98), 2012–2085.

Neukom, R., Steiger, N., Gómez-Navarro, J. J., Wang, J. and Werner, J. P. (2019). No evidence for globally coherent warm and cold periods over the preindustrial Common Era. *Nature*, 571 (7766), 550–554. doi:10.1038/s41586-019-1401-2.

Newton, T. L. (2017). *Holocene sea-level changes in the Falkland Islands: new insights into accelerated sea-level rise in the 20th Century*. PhD Thesis, University of Plymouth. https://pearl.plymouth.ac.uk/handle/10026.1/9650.

Newton, T. L., Gehrels, W. R., Fyfe, R. M. and Daley, T. J. (2021). Reconstructing sea-level change in the Falkland Islands (Islas Malvinas) using salt-marsh foraminifera, diatoms and testate amoebae. *Marine Micropaleontology*, 162, 101923. doi:10.1016/j.marmicro.2020.101923.

Noël, B., van de Berg, W. J., Lhermitte, S., Wouters, B., Schaffer, N. and van den Broeke, M. R. (2018a). Six Decades of Glacial Mass Loss in the Canadian Arctic Archipelago. *Journal of Geophysical Research: Earth Surface*, 123 (6), 1430–1449. doi:10.1029/2017JF004304.

Noël, B., van de Berg, W.J., Machguth, H., Lhermitte, S., Howat, I., Fettweis, X. and Van Den Broeke, M.R., (2016). A daily, 1 km resolution data set of downscaled Greenland Ice Sheet surface mass balance (1958–2015). *The Cryosphere, 10* (5), 2361-2377 doi:10.5194/tc-10-2361-2016.

Noël, B., van de Berg, W. J., van Wessem, J. M., van Meijgaard, E., van As, D., Lenaerts, J. T. M., Lhermitte, S., Kuipers M.P., Smeets, C. J. P. P., van Ulft, L. H., et al. (2018b). Modelling the climate and surface mass balance of polar Ice Sheets using RACMO2 – Part 1: Greenland (1958–2016). *The Cryosphere*, 12 (3), 811–831. doi:10.5194/tc-12-811-2018.

NSW mining. (2020). *NSW Minerals Council - NSW Mining*. https://www.nswmining.com.au/ [Accessed 29 June 2021].

Oerlemans, J., Dyurgerov, M. and Van de Wal, R.S.W., (2007). Reconstructing the glacier contribution to sea-level rise back to 1850. *The Cryosphere, 1* (1), 59-65. doi:10.5194/tc-1-59-2007.

Oksanen, J., Kindt, R., Legendre, P., O'Hara, B., Stevens, M.H.H., Oksanen, M.J. and Suggests, M.A.S.S. (2007). *The vegan package. Community ecology package*. https://cran.r-project.org/web/packages/vegan/index.html

Ooms, M., Beyens, L. and Temmerman, S. (2012). Testate amoebae as proxy for water level changes in a brackish tidal marsh. *Acta Protozoologica*, 51 (3), 271–289. doi:10.4467/16890027AP.12.022.0768.

Ostrognay, D. B. and Haig, D. W. (2012). Foraminifera from microtidal rivers with large seasonal salinity variation, southwest Western Australia. *Journal of the Royal Society of Western Australia*, 95, 137.

Pálsson, F., Guðmundsson, S., Björnsson, H., Berthier, E. and Magnússon, E. (2012). Mass and volume changes of Langjökull ice cap, Iceland, ~1890 to 2009, deduced from old maps, satellite images and in situ mass balance measurements. *Jökull,*(62), 16.

Parker, D., Folland, C., Scaife, A., Knight, J., Colman, A., Baines, P. and Dong, B. (2007). Decadal to multidecadal variability and the climate change background. *Journal of Geophysical Research: Atmospheres*, 112 (D18). doi:10.1029/2007JD008411

Parkes, D. and Marzeion, B. (2018). Twentieth-century contribution to sea-level rise from uncharted glaciers. *Nature, 563* (7732), 551–554. doi:10.1038/s41586-018-0687-9.

Parsons, K. and Consulting, E. (2012). *State of the D'Entrecasteaux Channel and the lower Huon Estuary 2012*. Kingborough Council. https://www.bien.org.au/wp-content/ uploads/2019/09/State-of-Channel-lower-Huon_electronicversion_web.pdf.

Pearce, I., Handlinger, J. H. and Hallegraeff, G. M. (2005). Histopathology in Pacific oyster (*Crassostrea gigas*) spat caused by the dinoflagellate *Prorocentrum rhathymum*. *Harmful Algae*, 4 (1), 61–74. doi:10.1016/j.hal.2003.11.002.

Peltier, W. R., Argus, D. F. and Drummond, R. (2015). Space geodesy constrains ice age terminal deglaciation: The global ICE-6G_C (VM5a) model. *Journal of Geophysical Research: Solid Earth*, 120 (1), 450–487. doi:10.1002/2014JB011176.

Perner, K., Moros, M., Otterå, O. H., Blanz, T., Schneider, R. R. and Jansen, E. (2019). An oceanic perspective on Greenland's recent freshwater discharge since 1850. *Scientific Reports*, 9 (1), 17680. doi:10.1038/s41598-019-53723-z.

Pilia, S., Rawlinson, N., Direen, N. G., Reading, A. M., Cayley, R., Pryer, L., Arroucau, P. and Duffett, M. (2015). Linking mainland Australia and Tasmania using ambient seismic noise tomography: Implications for the tectonic evolution of the east Gondwana margin. *Gondwana Research*, 28 (3), 1212–1227. doi:/10.1016/j.gr.2014.09.014.

Plag, H.P. (2006). Recent relative sea-level trends: an attempt to quantify the forcing factors. *Philosophical Transactions of the Royal Society A: Mathematical, Physical and Engineering Sciences*, 364 (1841), 821–844. doi: 10.1098/rsta.2006.1739.

Planchon, F. A. M., van de Velde, K., Rosman, K. J. R., Wolff, E. W., Ferrari, C. P. and Boutron, C. F. (2003). One hundred fifty–year record of lead isotopes in Antarctic snow from Coats Land. *Geochimica et Cosmochimica Acta*, 67 (4), 693–708. doi:10.1016/S0016-7037(02)01136-5.

Polyakov, I. V., Alexeev, V. A., Bhatt, U. S., Polyakova, E. I. and Zhang, X. (2010). North Atlantic warming: Fingerprints of climate change and multidecadal variability. *Climate Dynamics*, 34, 439–457.

Power, S., Casey, T., Folland, C., Colman, A. and Mehta, V. (1999). Inter-decadal modulation of the impact of ENSO on Australia. *Climate Dynamics*, 15 (5), 319–324. doi:10.1007/s003820050284.

Prahalad, V. and Jones, J. (2013). *Mapping coastal saltmarshes in Southern Tasmania*. https://www.nrmsouth.org.au/wp-content/ uploads/2014/10/Mapping-Coastal-Saltmarshes-inSouthern-Tasmania.pdf.

Przybylak, R., Sviashchennikov, P., Uscka-Kowalkowska, J. and Wyszyński, P. (2020). *Solar radiation in the Arctic during the Early Twentieth Century Warming period (1921-50)*. 22, 6930. doi:10.1175/JCLI-D-20-0257.1.

PSMSL. (2021). *New Data Systems and Products at the Permanent Service for Mean Sea Level*. https://bioone.org/journals/journal-of-coastal-research/volume-29/issue-3/JCOASTRES-D-12-00175.1/New-Data-Systems-and-Products-at-the-Permanent-Service-for/10.2112/JCOASTRES-D-12-00175.1.full [Accessed 13 September 2021].

Punwong, P., Marchant, R. and Selby, K. (2013). Holocene mangrove dynamics in Makoba Bay, Zanzibar. *Palaeogeography, Palaeoclimatology, Palaeoecology*, 379–380, 54–67. doi:10.1016/j.palaeo.2013.04.004.

R Core Team. (2020). *R: A language and environment for statistical computing.* Vienna, Austria : R Foundation for Statistical Computing. https://www.R-project.org/.

Ray, R. D. and Douglas, B. C. (2011). Experiments in reconstructing twentieth-century sea levels. *Progress in Oceanography*, 91 (4), 496–515. doi:10.1016/j.pocean.2011.07.021.

Raymond, O. L. (1996). Pyrite composition and ore genesis in the Prince Lyell copper deposit, Mt Lyell mineral field, western Tasmania, Australia. *Ore Geology Reviews*, 10 (3–6), 231–250. doi:10.1016/0169-1368(95)00025-9.

RGI Consortium. (2017). *Randolph Glacier Inventory – A Dataset of Global Glacier Outlines: Version 6.0: Technical Report, Global Land Ice Measurements from Space, Colorado, USA. Digital Media.* doi:10.7265/N5-RGI-60 [Accessed 7 September 2021].

Rickard, M. J. and Love, S. (2000). Timing of megakinks and related structures: Constraints from the Devonian Bunga-Wapengo Basin, Mimosa Rocks National Park, New South Wales. *Australian Journal of Earth Sciences*, 47 (6), 1009–1013. doi:10.1046/j.1440-0952.2000.00827.x.

Rignot, E., Box, J. E., Burgess, E. and Hanna, E. (2008). Mass balance of the Greenland Ice Sheet from 1958 to 2007. *Geophysical Research Letters*, 35 (20), L20502. doi:10.1029/2008GL035417.

Rignot, E., Mouginot, J., Scheuchl, B., Van Den Broeke, M., Van Wessem, M. J. and Morlighem, M. (2019). Four decades of Antarctic Ice Sheet mass balance from 1979–2017. *Proceedings of the National Academy of Sciences*, 116 (4), 1095–1103. doi:10.1073/pnas.1812883116.

Risbey, J. S., Pook, M. J., McIntosh, P. C., Wheeler, M. C. and Hendon, H. H. (2009). On the Remote Drivers of Rainfall Variability in Australia. *Monthly Weather Review*, 137 (10), 3233–3253. doi:10.1175/2009MWR2861.1.

Riva, R. E. M., Frederikse, T., King, M. A., Marzeion, B. and van den Broeke, M. R. (2017). Brief communication: The global signature of post-1900 land ice wastage on vertical land motion. *The Cryosphere*, 11 (3), 1327–1332. doi:10.5194/tc-11-1327-2017.

Rohde, R., A. Muller, R., Jacobsen, R., Muller, E. and Wickham, C. (2013). A New Estimate of the Average Earth Surface Land Temperature Spanning 1753 to 2011. *Geoinformatics & Geostatistics: An Overview*, 01 (01). doi:10.4172/2327-4581.1000101.

Romanin, L. M., Hopf, F., Haberle, S. G. and Bowman, D. M. J. S. (2016). Fire regime and vegetation change in the transition from Aboriginal to European land management in a Tasmanian eucalypt savanna. *Australian Journal of Botany*, 64 (5), 427. doi:10.1071/BT16032.

Roper, T., Creese, B., Scanes, P., Stephens, K., Williams, R., Dela-Cruz, J., Coade, G., Coates, B. and Fraser, M. (2011). *Assessing the condition of estuaries and coastal lake ecosystems in NSW*. https://www.environment.nsw.gov.au/-/media/OEH/Corporate-Site/ Documents/Water/State-of-the-catchments-2010/Technical-report-series/assessing-condition-estuariescoastal-lake-ecosystems-110717.pdf

Rosengren, N. J. (1989). *Sites of geological and geomorphological significance in the south Gippsland marine and coastal parks : report prepared for Department of Conservation, Forests & Lands Yarram Region / Neville Rosengren.* Department of Conservation, Forests & Lands Yarram Region.

Rossi, V., Horton, B. P., Corbett, D. R., Leorri, E., Perez-Belmonte, L. and Douglas, B. C. (2011). The application of foraminifera to reconstruct the rate of 20th century sea level rise, Morbihan Golfe, Brittany, France. *Quaternary Research*, 75 (1), 24–35. doi:10.1016/j.yqres.2010.07.017.

Rovere, A., Stocchi, P. and Vacchi, M. (2016). Eustatic and Relative Sea Level Changes. *Current Climate Change Reports*, 2 (4), 221–231. doi:10.1007/s40641-016-0045-7.

Rush, G.P, McDarby, P., Edwards, R., Milker, Y., Garrett, E. and Gehrels, W. R. (2021). Development of an intertidal foraminifera training set for the North Sea and an assessment of its application for Holocene sea-level reconstructions. *Marine Micropaleontology*, 169, 102055. doi:10.1016/j.marmicro.2021.102055.

Rush, G. P. (2021). *Rapid sea-level rise and climate change: lessons from the early Holocene*. PhD Thesis, University of York. https://etheses.whiterose.ac.uk/29276/ [Accessed 22 November 2021].

Sachs, H. M., Webb, T. and Clark, D. R. (1977). Paleoecological Transfer Functions. *Annual Review of Earth and Planetary Sciences*, 5 (1), 159–178. doi:10.1146/annurev.ea.05.050177.001111.

Saher, M. H., Gehrels, W. R., Barlow, N. L. M., Long, A. J., Haigh, I. D. and Blaauw, M. (2015). Sea-level changes in Iceland and the influence of the North Atlantic Oscillation during the last half millennium. *Quaternary Science Reviews*, 108, 23–36. doi:10.1016/j.quascirev.2014.11.005.

Sakabe, R. and Lyle, J. M. (2010). The influence of tidal cycles and freshwater inflow on the distribution and movement of an estuarine resident fish *Acanthopagrus butcheri*. *Journal of Fish Biology*, 77 (3), 643–660. doi:10.1111/j.1095-8649.2010.02703.x.

Salinger, M. J., Renwick, J. A. and Mullan, A. B. (2001). Interdecadal Pacific Oscillation and South Pacific climate. *International Journal of Climatology*, 21 (14), 1705–1721. doi:10.1002/joc.691.

Sasaki, Y. N., Minobe, S., Schneider, N., Kagimoto, T., Nonaka, M. and Sasaki, H. (2008). Decadal Sea Level Variability in the South Pacific in a Global Eddy-Resolving Ocean Model Hindcast. *Journal of Physical Oceanography*, 38 (8), 1731–1747. doi:10.1175/2007JPO3915.1.

Sawai, Y., Horton, B. P. and Nagumo, T. (2004). The development of a diatom-based transfer function along the Pacific coast of eastern Hokkaido, northern Japan—an aid in paleoseismic studies of the

Kuril subduction zone. *Quaternary Science Reviews*, 23 (23), 2467–2483. doi:10.1016/j.quascirev.2004.05.006.

Scammell, M. S., Batley, G. E. and Brockbank, C. I. (1991). A field study of the impact on oysters of tributyltin introduction and removal in a pristine lake. *Archives of Environmental Contamination and Toxicology*, 20 (2), 276–281. doi:10.1007/BF01055916.

Scanes, P., Coade, G., Doherty, M. and Hill, R. (2007). Evaluation of the utility of water quality based indicators of estuarine lagoon condition in NSW, Australia. *Estuarine, Coastal and Shelf Science*, 74 (1–2), 306–319. doi:10.1016/j.ecss.2007.04.021.

Schröder-Adams, C. J., Boyd, R. L. and Tran, T. (2014). Estuarine foraminiferal biofacies pattern compared to the brackish ichnofacies model: Port Stephens, southeast Australia. *Estuarine, Coastal and Shelf Science*, 139, 78–87. doi:10.1016/j.ecss.2013.12.006.

Schurer, A. P., Hegerl, G. C., Mann, M. E., Tett, S. F. and Phipps, S. J. (2013). Separating forced from chaotic climate variability over the past millennium. *Journal of Climate*, 26 (18), 6954–6973. doi:10.1175/JCLI-D-12-00826.1

Scott, A. (1999). *History of land use in the Murrah/Dry River catchment, NSW South Coast*. Technical, Canberra : CSIRO. http://www.clw.csiro.au/publications/technical99/tr54-99.pdf.

Scott, D. B. and Hermelin, J. O. R. (1993). A device for precision splitting of micropaleontological samples in liquid suspension. *Journal of Paleontology*, 67 (1), 151–154. doi:10.1017/S0022336000021302.

Scott, D. S. and Medioli, F. S. (1978). Vertical zonations of marsh foraminifera as accurate indicators of former sea-levels. *Nature*, 272 (5653), 528–531. doi:10.1038/272528a0.

Sefton, J., Woodroffe, S. and Ascough, P. (2021). Chapter 8 - Radiocarbon dating of mangrove sediments. In: Sidik, F. and Friess, D. A. (Eds.), *Dynamic Sedimentary Environments of Mangrove Coasts*. Elsevier. 199–215. doi:10.1016/B978-0-12-816437-2.00014-8.

Serrano, O., Davis, G., Lavery, P. S., Duarte, C. M., Martinez-Cortizas, A., Mateo, M. A., Masqué, P., Arias-Ortiz, A., Rozaimi, M. and Kendrick, G. A. (2016). Reconstruction of centennial-scale fluxes of chemical elements in the Australian coastal environment using seagrass archives. *Science of The Total Environment*, 541, 883–894. doi:10.1016/J.SCITOTENV.2015.09.017.

Shaw, R. D., Yeates, A. N., Palyfreyman, W. D. and Doutch, H. F. (2000). *Surface Geology of Australia 1:5 million scale dataset. Geoscience Australia dataset.* http://pid.geoscience.gov.au/dataset/ga/34613 [Accessed 9 August 2021].

Shaw, T. A., Kirby, J. R., Holgate, S., Tutman, P. and Plater, A. J. (2016). Contemporary salt-marsh foraminiferal distribution from the Adriatic coast of Croatia and its potential for sea-level studies. *The Journal of Foraminiferal Research*, 46 (3), 314–332. doi:10.2113/gsjfr.46.3.314.

Shaw, T. A., Plater, A. J., Kirby, J. R., Roy, K., Holgate, S., Tutman, P., Cahill, N. and Horton, B. P. (2018). Tectonic influences on late Holocene relative sea levels from the central-eastern Adriatic coast of Croatia. *Quaternary Science Reviews*, 200, 262–275. doi:10.1016/j.quascirev.2018.09.015.

Shepherd, A., Ivins, E., Rignot, E., Smith, B., van den Broeke, M., Velicogna, I., Whitehouse, P., Briggs, K., Joughin, I., Krinner, G., et al. (2018). Mass balance of the Antarctic Ice Sheet from 1992 to 2017. *Nature*, 558, 219–222. doi:10.1038/s41586-018-0179-y.

Shepherd, A., Ivins, E., Rignot, E., Smith, B., van Den Broeke, M., Velicogna, I., Whitehouse, P., Briggs, K., Joughin, I. and Krinner, G. (2020). Mass balance of the Greenland Ice Sheet from 1992 to 2018. *Nature*, 579 (7798), 233–239. doi:10.1038/s41586-019-1855-2.

Sigurđjsson, O., Jónsson, T. and Jóhannesson, T. (2007). Relation between glacier-termini variations and summer temperature in Iceland since 1930. *Annals of Glaciology*, 46, 170–176. doi:10.3189/172756407782871611

Sim, T. G., Swindles, G. T., Morris, P. J., Baird, A. J., Charman, D. J., Amesbury, M. J., Beilman, D., Channon, A. and Gallego-Sala, A. V. (2021). Ecology of peatland testate amoebae in Svalbard and the development of transfer functions for reconstructing past water-table depth and pH. *Ecological Indicators*, 131, 108122. doi:10.1016/j.ecolind.2021.108122.

Sinclair, S. and Boon, P. (2012). Changes in the area of coastal marsh in Victoria since the mid 19th century. *Cunninghamia*,12 (2), 153–176.

Slangen, A. B. A., Church, J. A., Agosta, C., Fettweis, X., Marzeion, B. and Richter, K. (2016). Anthropogenic forcing dominates global mean sea-level rise since 1970. *Nature Climate Change*, 6 (7), 701–705. doi:10.1038/nclimate2991.

Slivinski, L. C., Compo, G. P., Whitaker, J. S., Sardeshmukh, P. D., Giese, B. S., McColl, C., Allan, R., Yin, X., Vose, R., Titchner, H., et al. (2019). Towards a more reliable historical reanalysis: Improvements for version 3 of the Twentieth Century Reanalysis system. *Quarterly Journal of the Royal Meteorological Society*, 145 (724), 2876–2908. doi:10.1002/qj.3598.

Sloss, C. R., Murray-Wallace, C. V. and Jones, B. G. (2007). Holocene sea-level change on the southeast coast of Australia: a review. *The Holocene*, 17 (7), 999–1014. doi:10.1177/0959683607082415.

Sloss, C. R., Nothdurft, L., Hua, Q., O'Connor, S. G., Moss, P. T., Rosendahl, D., Petherick, L. M., Nanson, R. A., Mackenzie, L. L. and Sternes, A. (2018). Holocene sea-level change and coastal landscape evolution in the southern Gulf of Carpentaria, Australia. *The Holocene*, 28 (9), 1411–1430.

Solomon, R. J. (1988). *The Richest Lode: Broken Hill 1883-1988*. 1st ed. Sydney, Australia. Hale and Iremonger Pty Limited. http://michaeldarby.net/BrokenHill.pdf.

Southall, K.E., Gehrels, W.R., Hayward, B. W. (2006). Foraminifera in a New Zealand salt marsh and their suitability as sea-level indicators. *Marine Micropaleontology*, 60 (2), 167–179. doi:10.1016/J.MARMICRO.2006.04.005.

South Gippsland Society. (1920). *The Land of the Lyre Bird*. 1st ed. The Shire of Korumburra for the South Gippsland Development League.

Spiegelhalter, D. J., Best, N. G., Carlin, B. P. and Linde, A. V. D. (2002). Bayesian measures of model complexity and fit. *Journal of the Royal Statistical Society: Series B (Statistical Methodology)*, 64 (4), 583–639. doi:10.1111/1467-9868.00353.

Spooner, P. G. (2005). On Squatters, Settlers and Early Surveyors: historical development of country road reserves in southern New South Wales. *Australian Geographer*, 36 (1), 55–73. doi:10.1080/00049180500050870.

Steig, E. J., Schneider, D. P., Rutherford, S. D., Mann, M. E., Comiso, J. C. and Shindell, D. T. (2009). Warming of the Antarctic ice-sheet surface since the 1957 International Geophysical Year. *Nature*, 457 (7228), 459–462. doi:10.1038/nature07669.

Stéphan, P., Goslin, J., Pailler, Y., Manceau, R., Suanez, S., Van Vliet-Lanoë, B., Hénaff, A. and Delacourt, C. (2014). Holocene salt-marsh sedimentary infilling and relative sea-level changes in West Brittany (France) using foraminifera-based transfer functions. *Boreas*, 44 (1), 153–177. doi:10.1111/bor.12092.

Storn, R. and Price, K. (1997). Differential Evolution - a simple and efficient heuristic for global optimisation over continuous spaces. *Journal of Global Optimisation*, 11, 341–359. doi:10.1023/A:1008202821328.

Strachan, K. L., Finch, J. M., Hill, T. and Barnett, R. L. (2014). A late Holocene sea-level curve for the east coast of South Africa. *South African Journal of Science*, 110 (1–2), Academy of Science of South Africa, 1–9.

Strachan, K. L., Hill, T. R., Finch, J. M. and Barnett, R. L. (2015). Vertical zonation of foraminifera assemblages in Galpins salt marsh, South Africa. *Journal of Foraminiferal Research*, 45 (1), 29–41. doi:10.2113/gsjfr.45.1.29.

Strotz, L. C. (2015). Spatial patterns and diversity of foraminifera from an intermittently closed and open lagoon, Smiths Lake, Australia. *Estuarine, Coastal and Shelf Science*, 164, 340–352. doi:10.1016/j.ecss.2015.07.048.

Stuhne, G. R. and Peltier, W. R. (2015). Reconciling the ICE-6G_C reconstruction of glacial chronology with Ice Sheet dynamics: The cases of Greenland and Antarctica. *Journal of Geophysical Research: Earth Surface*, 120 (9), 1841–1865. doi:10.1002/2015JF003580.

Suo, L., Otterå, O. H., Bentsen, M., Gao, Y. and Johannessen, O. M. (2013). External forcing of the early 20th century Arctic warming. *Tellus A: Dynamic Meteorology and Oceanography*, 65 (1), 20578. doi:10.3402/tellusa.v65i0.20578.

Sutterley, T. C., Velicogna, I., Rignot, E., Mouginot, J., Flament, T., Van Den Broeke, M. R., Van Wessem, J. M. and Reijmer, C. H. (2014). Mass loss of the Amundsen Sea Embayment of West Antarctica from four independent techniques. *Geophysical Research Letters*, 41 (23), 8421–8428. doi:10.1002/2014GL061940.

Svendsen, L., Keenlyside, N., Bethke, I., Gao, Y. and Omrani, N.-E. (2018). Pacific contribution to the early twentieth-century warming in the Arctic. *Nature Climate Change*, 8 (9), 793–797. doi:10.1038/s41558-018-0247-1.

Szkornik, K., Gehrels, W. R. and Kirby, J. R. (2006). Salt-marsh diatom distributions in Ho Bugt (western Denmark) and the development of a transfer function for reconstructing Holocene sea-level changes. *Marine Geology*, 235 (1–4), 137–150. doi:10.1016/j.margeo.2006.10.010.

Tamisiea, M. E., Hill, E. M., Ponte, R. M., Davis, J. L., Velicogna, I. and Vinogradova, N. T. (2010). Impact of self-attraction and loading on the annual cycle in sea level. *Journal of Geophysical Research: Oceans*, 115 (C7). doi:10.1029/2009JC005687.

Tamisiea, M. E. and Mitrovica, J. X. (2011). The Moving Boundaries of Sea Level Change: Understanding the Origins of Geographic Variability. *Oceanography*, 24, 24–39. doi:10.2307/24861266.

Telford, R. J. (2011). palaeoSig: significance tests of quantitative palaeoenvironmental reconstructions. *R package version*, 1. https://cran.r-project.org/web/packages/palaeoSig/index.html

Ter Braak, C. J. F. and Juggins, S. (1993). Weighted averaging partial least squares regression (WA-PLS): an improved method for reconstructing environmental variables from species assemblages. In: *Twelfth international diatom symposium*. 1993. Springer. 485–502.

Ter Braak, C. J. F., Juggins, S., Birks, H. J. B. and Van der Voet, H. (1993). Weighted averaging partial least squares regression (WA-PLS): definition and comparison with other methods for species-environment calibration, 525-560. In: G. P. Patil, and C. R. Rao (Eds.), *Multivariate Environmental Statistics*. Amsterdam: Elsevier Science Publishers B.V.

Ter Braak, C.J.F. and Smilauer, P. (2003). *Program CANOCO, version 4.52." Biometris-quantitative methods in the life and earth sciences*. The Netherlands, Wageningen. www.canoco.com

Ter Braak, C. J. F. and Verdonschot, P. E. M. (1995). *Canonical correspondence analysis and related multivariate methods in aquatic ecology*. Aquatic sciences, 57 (3), 255–289. doi:10.1007/BF00877430.

Ter Braak, C. J. F. (1987). Ordination. In: *Data analysis in community ecology*. 91–173.

Thirlwall, M. F. (2002). Multicollector ICP-MS analysis of Pb isotopes using a ^{207}Pb-^{204}Pb double spike demonstrates up to 400 ppm/amu systematic errors in Tl-normalization. *Chemical Geology*, 184 (3–4), 255–279. doi:10.1016/S0009-2541(01)00365-5.

Tokinaga, H., Xie, S.-P. and Mukougawa, H. (2017). Early 20th-century Arctic warming intensified by Pacific and Atlantic multidecadal variability. *Proceedings of the National Academy of Sciences of the United States of America*, 114 (24), 6227–6232. doi:10.1073/pnas.1615880114.

Townsend, A. T. and Seen, A. J. (2012). Historical lead isotope record of a sediment core from the Derwent River (Tasmania, Australia): A multiple source environment. *Science of The Total Environment*, 424, 153–161. doi:10.1016/j.scitotenv.2012.02.011.

Troels-Smith, J., 1955. Characterisation of unconsolidated sediments. *Danmarks Geologiske Undersøgelse IV. Række*, *3* (10), 1-73. doi:10.34194/raekke4.v3.6989.

Trusel, L. D., Das, S. B., Osman, M. B., Evans, M. J., Smith, B. E., Fettweis, X., McConnell, J. R., Noël, B. P. Y. and van den Broeke, M. R. (2018). Nonlinear rise in Greenland runoff in response to post-industrial Arctic warming. *Nature*, 564 (7734), 104–108. doi:10.1038/s41586-018-0752-4.

Tung, K.-K. and Zhou, J. (2013). Using data to attribute episodes of warming and cooling in instrumental records. *Proceedings of the National Academy of Sciences*, 110 (6), 2058–2063. doi:10.1073/pnas.1212471110.

Vallelonga, P., Van de Velde, K., Candelone, J.-P., Morgan, V. I., Boutron, C. F. and Rosman, K. J. R. (2002). The lead pollution history of Law Dome, Antarctica, from isotopic measurements on ice cores: 1500 AD to 1989 AD. *Earth and Planetary Science Letters*, 204 (1–2), 291–306. doi:10.1016/S0012-821X(02)00983-4.

Van Alphen, M. (1991). *The history of smelting and ore dressing in Broken Hill and the potential for mine derived lead contamination in Broken Hill*.

van den Broeke, M., Bamber, J., Ettema, J., Rignot, E., Schrama, E., van de Berg, W. J., van Meijgaard, E., Velicogna, I. and Wouters, B. (2009). Partitioning recent Greenland mass loss. *Science*, 326 (5955), 984–986. doi:10.1126/science.1178176.

van den Broeke, M., Box, J., Fettweis, X., Hanna, E., Noël, B., Tedesco, M., van As, D., van de Berg, W. J. and van Kampenhout, L. (2017). Greenland Ice Sheet Surface Mass Loss: Recent Developments in Observation and Modeling. *Current Climate Change Reports*, 3 (4), 345–356. doi:10.1007/s40641-017-0084-8.

van den Broeke, M., Enderlin, E.M., Howat, I.M., Kuipers, M.P., Noël, B.P., Berg, W.J.V.D., Meijgaard, E.V. and Wouters, B., (2016). On the recent contribution of the Greenland Ice Sheet to sea level change. *The Cryosphere*, *10* (5), 1933-1946. doi:10.5194/tc-10-1933-2016.

Van de Velde, K., Vallelonga, P., Candelone, J.-P., Rosman, K. J. R., Gaspari, V., Cozzi, G., Barbante, C., Udisti, R., Cescon, P. and Boutron, C. F. (2005). Pb isotope record over one century in snow from Victoria Land, Antarctica. *Earth and Planetary Science Letters*, 232 (1–2), 95–108. doi:10.1016/J.EPSL.2005.01.007.

Van Wessem, J.M., Van De Berg, W.J., Noël, B.P., Van Meijgaard, E., Amory, C., Birnbaum, G., Jakobs, C.L., Krüger, K., Lenaerts, J., Lhermitte, S. et al. 2018. Modelling the climate and surface mass balance of polar Ice Sheets using RACMO2–Part 2: Antarctica (1979–2016). *The Cryosphere*, *12* (4), 1479-1498 doi:10.5194/tc-12-1479-2018.

Vermassen, F., Andreasen, N., Wangner, D. J., Thibault, N., Seidenkrantz, M.-S., Jackson, R., Schmidt, S., Kjær, K. H. and Andresen, C. S. (2019). A reconstruction of warm-water inflow to Upernavik Isstrøm since 1925 CE and its relation to glacier retreat. *Climate of the Past*, 15 (3), 1171–1186. doi:10.5194/cp-15-1171-2019.

Vermassen, F., Bjørk, A. A., Sicre, M.-A., Jaeger, J. M., Wangner, D. J., Kjeldsen, K. K., Siggaard-Andersen, M.-L., Klein, V., Mouginot, J., Kjær, K. H., et al. (2020). A Major Collapse of Kangerlussuaq Glacier's Ice Tongue Between 1932 and 1933 in East Greenland. *Geophysical Research Letters*, 47 (4), e2019GL085954. doi:10.1029/2019GL085954.

Vic Basemap Services, State Government of Victoria. (2021). *Historical Photo-Maps*. https://services.land.vic.gov.au/DELWPmaps/historical-photomaps/ [Accessed 29 September 2021].

Wake, L. M., Huybrechts, P., Box, J. E., Hanna, E., Janssens, I. and Milne, G. A. (2009). Surface mass-balance changes of the Greenland Ice Sheet since 1866. *Annals of Glaciology*, 50 (50), 170–185. doi:10.3189/172756409787769636

Walker, J. S., Cahill, N., Khan, N. S., Shaw, T. A., Barber, D., Miller, K. G., Kopp, R. E. and Horton, B. P. (2020). Incorporating temporal and spatial variability of salt-marsh foraminifera into sea-level reconstructions. *Marine Geology*, 429, 106293. doi:10.1016/j.margeo.2020.106293.

Walker, J.S., Kopp, R.E., Little, C.M. and Horton, B.P., 2022. Timing of emergence of modern rates of sea-level rise by 1863. *Nature communications*, *13*(1), 1-8. doi: 0.1038/s41467-022-28564-6.

Walker, J. S., Kopp, R. E., Shaw, T. A., Cahill, N., Khan, N. S., Barber, D. C., Ashe, E. L., Brain, M. J., Clear, J. L., Corbett, D. R., et al. (2021). Common Era sea-level budgets along the U.S. Atlantic coast. *Nature Communications*, 12 (1), 1841. doi:10.1038/s41467-021-22079-2.

Walton, W.R. (1952). Techniques for recognition of living foraminifera. *Contribution from the Cushman Foundation the Foraminiferal Research*, 3 (2), 56–60.

Wang, P. and Chappell, J. (2001). Foraminifera as Holocene environmental indicators in the South Alligator River, Northern Australia. *Quaternary International*, 83–85, 47–62. doi:10.1016/S1040-6182(01)00030-1.

Wangner, D. J., Jennings, A. E., Vermassen, F., Dyke, L. M., Hogan, K. A., Schmidt, S., Kjær, K. H., Knudsen, M. F. and Andresen, C. S. (2018). A 2000-year record of ocean influence on Jakobshavn Isbræ calving activity, based on marine sediment cores. *The Holocene*, 28 (11), 1731–1744. doi:10.1177/0959683618788701.

Wangner, D. J., Sicre, M.-A., Kjeldsen, K. K., Jaeger, J. M., Bjørk, A. A., Vermassen, F., Sha, L., Kjær, K. H., Klein, V. and Andresen, C. S. (2020). Sea Surface Temperature Variability on the SE-Greenland Shelf (1796–2013 CE) and Its Influence on Thrym Glacier in Nørre Skjoldungesund. *Paleoceanography and Paleoclimatology*, 35 (3), e2019PA003692. doi: 10.1029/2019PA003692.

Watcham, E. P., Shennan, I. and Barlow, N. L. M. (2013). Scale considerations in using diatoms as indicators of sea-level change: lessons from Alaska. *Journal of Quaternary Science*, 28 (2), 165–179. doi:10.1002/jqs.2592.

Watson, P. J. (2011). Is there evidence yet of acceleration in mean sea level rise around mainland Australia? *Journal of Coastal Research*, 27 (2), 368–377. doi:10.2112/JCOASTRES-D-10-00141.1.

Wegmann, M., Brönnimann, S. and Compo, G. P. (2017). Tropospheric circulation during the early twentieth century Arctic warming. *Climate dynamics*, 48 (7–8), 2405–2418. doi: 10.1007/s00382-016-3212-6

Wegmann, M., Rohrer, M., Santolaria-Otín, M. and Lohmann, G. (2020). Eurasian autumn snow link to winter North Atlantic Oscillation is strongest for Arctic warming periods. *Earth System Dynamics*, 11 (2), 509–524. doi:10.5194/esd-11-509-2020.

Wenzel, M. and Schröter, J. (2010). Reconstruction of regional mean sea level anomalies from tide gauges using neural networks. *Journal of Geophysical Research: Oceans*, 115 (C8). doi:10.1029/2009JC005630.

Wesson, R. L., Melnick, D., Cisternas, M., Moreno, M. and Ely, L. L. (2015). Vertical deformation through a complete seismic cycle at Isla Santa María, Chile. *Nature Geoscience*, 8 (7), 547–551. doi:10.1038/ngeo2468.

Weston, T. (2010). Mining Lower Grade Ore: Changes in Mining Technology at Mount Lyell, Tasmania, 1927-1939. *Journal of Australasian Mining History*, 8, 172–183.

Weston, T. (2018). History and heritage: One hundred years of Australian copper smelting 1917-2017. *AusIMM Bulletin*, 70–74.

WGMS, (2015). Global glacier change bulletin no. 1 (2012–2013). In: Zemp M., Gärtner-Roer I., Nussbaumer S.U., Hüsler F., Machguth H., Mölg N., Paul F., Hoelzle, M., (Eds.), *World Glacier Monitoring Service*, Zurich, Switzerland: ICSU(WDS)/IUGG(IACS)/UNEP/. doi:10.5904/wgms-fog-2015-11.

White, N. J., Haigh, I. D., Church, J. A., Koen, T., Watson, C. S., Pritchard, T. R., Watson, P. J., Burgette, R. J., McInnes, K. L., You, Z.-J., et al. (2014). Australian sea levels—Trends, regional variability and influencing factors. *Earth-Science Reviews*, 136, 155–174. doi:10.1016/J.EARSCIREV.2014.05.011.

Whitehouse, P. L., Gomez, N., King, M. A. and Wiens, D. A. (2019). Solid Earth change and the evolution of the Antarctic Ice Sheet. *Nature Communications*, 10 (1), 503. doi:10.1038/s41467-018-08068-y.

Whittaker, J., Haynes, K., Tofa, M., Wilkinson, C. and Taylor, M. (2020). *Understanding bushfire risk, warnings and responses: a study of the 2018 reedy swamp fire*. Research for the NSW Rural Fire Service. https://www.bnhcrc.com.au/sites/default/files/managed/downloads/study_of_the_2018_reedy_swamp_fire_final_report_bushfire_and_natural_hazards_crc_0.pdf.

Williams, A. N., Ulm, S., Cook, A. R., Langley, M. C. and Collard, M. (2013). Human refugia in Australia during the Last Glacial Maximum and Terminal Pleistocene: a geospatial analysis of the 25–12 ka Australian archaeological record. *Journal of Archaeological Science*, 40 (12), 4612–4625. doi:10.1016/j.jas.2013.06.015.

Williams, A. N., Ulm, S., Sapienza, T., Lewis, S. and Turney, C. S. (2018). Sea-level change and demography during the last glacial termination and early Holocene across the Australian continent. *Quaternary Science Reviews*, 182, 144–154. doi:/10.1016/j.quascirev.2017.11.030.

Williams, S., Garrett, E., Moss, P., Bartlett, R. and Gehrels, W.R. (2021). Development of a Regional Training Set of Contemporary Salt-Marsh Foraminifera for Late Holocene Sea-Level Reconstructions in southeastern Australia. *Open Quaternary*, 7 (1). doi:10.5334/oq.93.

Wilson, G. P. and Lamb, A. L. (2012). An assessment of the utility of regional diatom-based tidal-level transfer functions. *Journal of Quaternary Science*, 27 (4), 360–370. doi:10.1002/jqs.1553.

Wilton, D. J., Jowett, A., Hanna, E., Bigg, G. R., Van Den Broeke, M. R., Fettweis, X. and Huybrechts, P. (2017). High resolution (1 km) positive degree-day modelling of Greenland Ice Sheet surface mass balance, 1870–2012 using reanalysis data. *Journal of Glaciology*, 63 (237), 176–193. doi:10.1017/jog.2016.133.

Winski, D., Osterberg, E., Kreutz, K., Wake, C., Ferris, D., Campbell, S., Baum, M., Bailey, A., Birkel, S., Introne, D., et al. (2018). A 400-Year Ice Core Melt Layer Record of Summertime Warming in the Alaska Range. *Journal of Geophysical Research: Atmospheres*, 123 (7), 3594–3611. doi:10.1002/2017JD027539.

Wolff, E. W. and Suttie, E. D. (1994). Antarctic snow record of southern hemisphere lead pollution. *Geophysical Research Letters*, 21 (9), 781-784. doi:10.1029/94GL00656.

Woodroffe, C. D., McGregor, H. V., Lambeck, K., Smithers, S. G. and Fink, D. (2012). Mid-Pacific microatolls record sea-level stability over the past 5000 yr. *Geology*, 40 (10), 951–954. doi:10.1130/G33344.1.

Woodroffe, S. A. (2005). Intertidal mangrove foraminifera from the Central Great Barrier Reef Shelf, Australia: implications for sea-level reconstruction. *The Journal of Foraminiferal Research*, 35 (3), 259–270. doi:10.2113/35.3.259.

Woodroffe, S. A. (2009). Testing models of mid to late Holocene sea-level change, North Queensland, Australia. *Quaternary Science Reviews*, 28 (23), 2474–2488. doi:10.1016/j.quascirev.2009.05.004.

Woodroffe, S. A. and Long, A. J. (2010). Reconstructing recent relative sea-level changes in West Greenland: Local diatom-based transfer functions are superior to regional models. *Quaternary International*, 221 (1), 91–103. doi:10.1016/j.quaint.2009.06.005.

Woodroffe, S. A., Long, A. J., Punwong, P., Selby, K., Bryant, C. L. and Marchant, R. (2015). Radiocarbon dating of mangrove sediments to constrain Holocene relative sea-level change on Zanzibar in the southwest Indian Ocean. *The Holocene*, 25 (5), 820–831. doi:10.1177/0959683615571422.

Woodward, O. H. (1965). *A Review of the Broken Hill Lead-Silver-Zinc Industry.* 2nd ed. Sydney, Australia. West Publishing Corporation Pty. Ltd.

Woodworth, P. L., White, N. J., Jevrejeva, S., Holgate, S. J., Church, J. A. and Gehrels, W. R. (2009). Evidence for the accelerations of sea level on multi-decade and century timescales. *International Journal of Climatology*, 29 (6), 777–789. doi:10.1002/joc.1771.

Wouters, B., Gardner, A. S. and Moholdt, G. (2019). Global Glacier Mass Loss During the GRACE Satellite Mission (2002-2016). *Frontiers in Earth Science*, 7, 96. doi:10.3389/feart.2019.00096.

Wright, A. J., Edwards, R. J. and van de Plassche, O. (2011). Reassessing transfer-function performance in sea-level reconstruction based on benthic salt-marsh foraminifera from the Atlantic coast of NE North America. *Marine Micropaleontology*, 81 (1–2), 43–62. doi:10.1016/J.MARMICRO.2011.07.003.

Wu, L., Taylor, M. P., Handley, H. K. and Wu, M. (2016). Australian atmospheric lead deposition reconstructed using lead concentrations and isotopic compositions of archival lichen and fungi. *Environmental Pollution*, 208, 678–687. doi:10.1016/J.ENVPOL.2015.10.046.

Xiao, H., Zhang, F., Miao, L., Liang, X. S., Wu, K. and Liu, R. (2020). Long-term trends in Arctic surface temperature and potential causality over the last 100 years. *Climate Dynamics*, 55 (5), 1443–1456. doi:10.1007/s00382-020-05330-2.

Zemp, M., Huss, M., Thibert, E., Eckert, N., McNabb, R., Huber, J., Barandun, M., Machguth, H., Nussbaumer, S. U., Gärtner-Roer, I., et al. (2019). Global glacier mass changes and their contributions to sea-level rise from 1961 to 2016. *Nature*, 568 (7752), 382–386. doi:10.1038/s41586-019-1071-0.

Zhou, J. and Tung, K.-K. (2013). Deducing Multidecadal Anthropogenic Global Warming Trends Using Multiple Regression Analysis. *Journal of the Atmospheric Sciences*, 70 (1), 3–8. doi:10.1175/JAS-D-12-0208.1.

Zhou, Y., Li, Z., Li, J., Zhao, R. and Ding, X. (2018). Glacier mass balance in the Qinghai–Tibet Plateau and its surroundings from the mid-1970s to 2000 based on Hexagon KH-9 and SRTM DEMs. *Remote Sensing of Environment*, 210, 96–112. doi:10.1016/j.rse.2018.03.020.

Zong, Y. and Horton, B. P. (1999). Diatom-based tidal-level transfer functions as an aid in reconstructing Quaternary history of sea-level movements in the UK. *Journal of Quaternary Science*, 14 (2), 153–167. doi:10.1002/(SICI)1099-1417(199903)14:2<153::AID-JQS425>3.0.CO;2-6.

Appendicies

Appendix I. Tarra local transfer function

Whilst modern surface samples were taken at Tarra, the performance of the transfer function model was very poor, and so the samples were not included in the regional model or used as a local training set in Williams et al. (2021). This appendix describes the sampling process, distribution of modern species and why the decision was made to not include the samples in the transfer function models.

Modern surface training sets of foraminifera were taken along two transects at Tarra marsh (**Figure 31**; **Figure A1**). Combined the two transects have a vertical range of 0.6 m. Forty one samples were taken in total and five samples had total counts less than 50 individuals, therefore these samples were removed from the training set. Foraminifera found in the samples include: *Trochamminita salsa*, *Haplophragmoides wilberti*, *Polysacammina ipohalina*, *Trochamminita irregularis*, *Trochammina inflata*, *Siphotrochammina lobata*, *Entzia macrescens*, *Ammobaculites exiguus* and *Ammotium fragile*. Within the remaining samples, total counts range from 51 – 636 individuals with an average of 190 individuals per sample. *Trochammina inflata* dominates the training set (24 – 98 %) representing at a minimum at least ¼ of the assemblage in every sample. *Entzia macrescens* is sub-dominant (0 – 54 %) and is found in most samples across the training set. As Transect 6 does not have a clear downward elevation gradient, the typical high-elevation species *T. salsa* (that would usually be restricted to the upper elevations in Australasian marshes (Hayward and Hollis, 1994; Williams et al. 2021)) is found both at the start and the end of the transect. *Haplophragmoides wilberti* and *M. fusca* increase down transect. *Ammobaculites exiguus* is found generally at the lower elevations which is around 50 m along

Transect 6. Along transect 7, *T. inflata*, *E. macrescens* and *M. fusca* dominate the transect, with *A. exiguus* found in the lowest elevation sample.

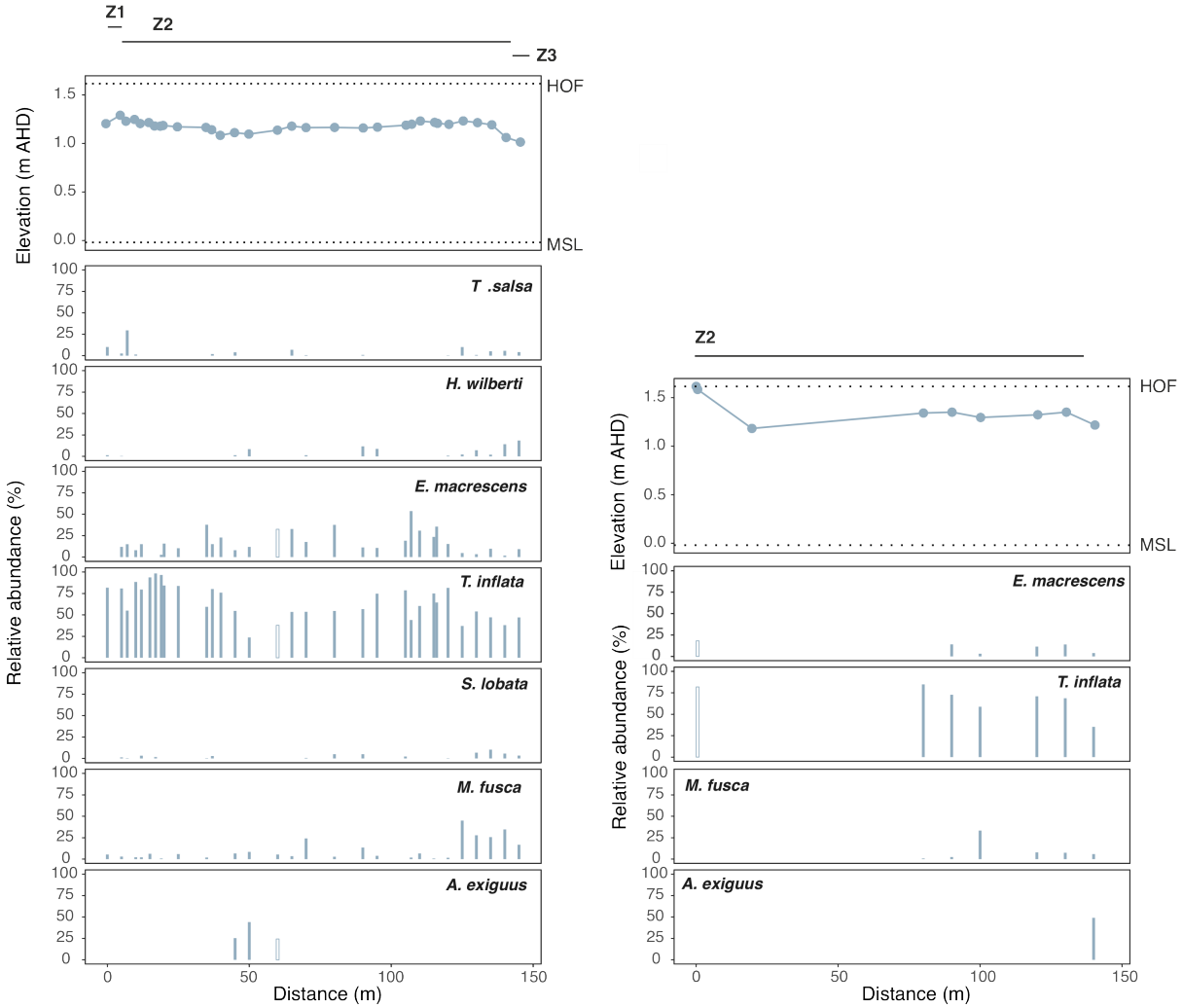

Figure A1. Relative abundance of foraminifera along surface transects 6 (left) and 7 (right) at Tarra salt marsh. Samples with total counts less than 50 are represented by unfilled bars. Species shown represent at least 10% in one sample. Vegetation zones are also plotted (See **Chapter 3**).

The Tarra local transfer function was subject to the same transfer function development steps as all other models detailed in **Chapter 4**. DCCA results yielded an axis 1 length of 0.63, therefore a PLS model was employed. Whilst the RMSEP of the model is similar to that of the

other local models (RMSEP = 0.08 m), the model performed very poorly with an r^2_{boot} of 0.02 (**Figure A2).** Many of the samples are predicted at the same elevation ~1.20 – 1.25 m. This is because *T. inflata* dominates so many of the samples which has an optima ~1.20 m (**Figure A2; Figure A3).**

As detailed in **Chapter 5**, some studies have advocated for using regional training sets to reconstruct PMSEs where no good analogues are available from a local training set or where a local transfer function model performs poorly. However, this must be done with caution as analogues derived from marshes with very different species-environment relationships may not be representative of the local marsh environment. Therefore, in order to determine whether the regional II training set would be suitable for the Tarra PMSE reconstruction, species optima and tolerances were compared between the two training sets (**Figure A4**). Data show that species-elevation relationships between the models are quite similar, especially between dominant species such as *E. macrescens* and *T. inflata* which have optima with 2 SWLI unit differences between the two training sets. There are some larger discrepancies between less common foraminifera such as *T. salsa* and *M. fusca* which have differences of 11 SWLI units and 16 SWLI units respectively. The largest difference between the two training sets is in *A. exiguus* (25 SWLI). This is due to the rarity of the species at Tarra, and, as such would not be a prominent driver in resulting transfer function reconstructions. As the differences in species optima and tolerance between the regional training set and the Tarra local training set were minimal, the Tarra reconstruction was conducted with the regional II transfer function. See **Chapter 6** for resulting PMSE reconstructions.

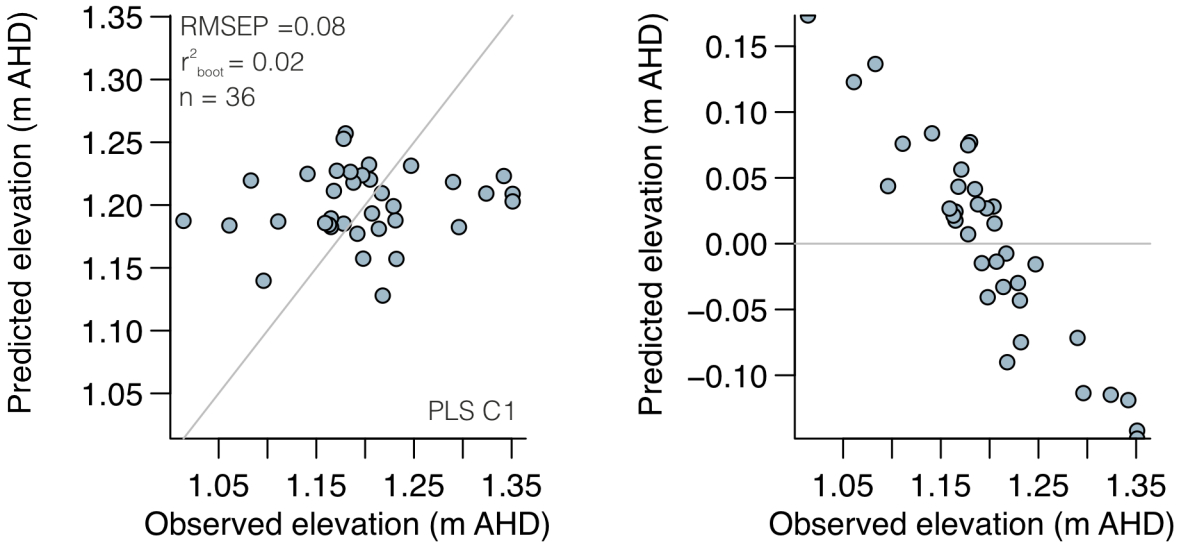

Figure A2. Tarra local transfer function model.

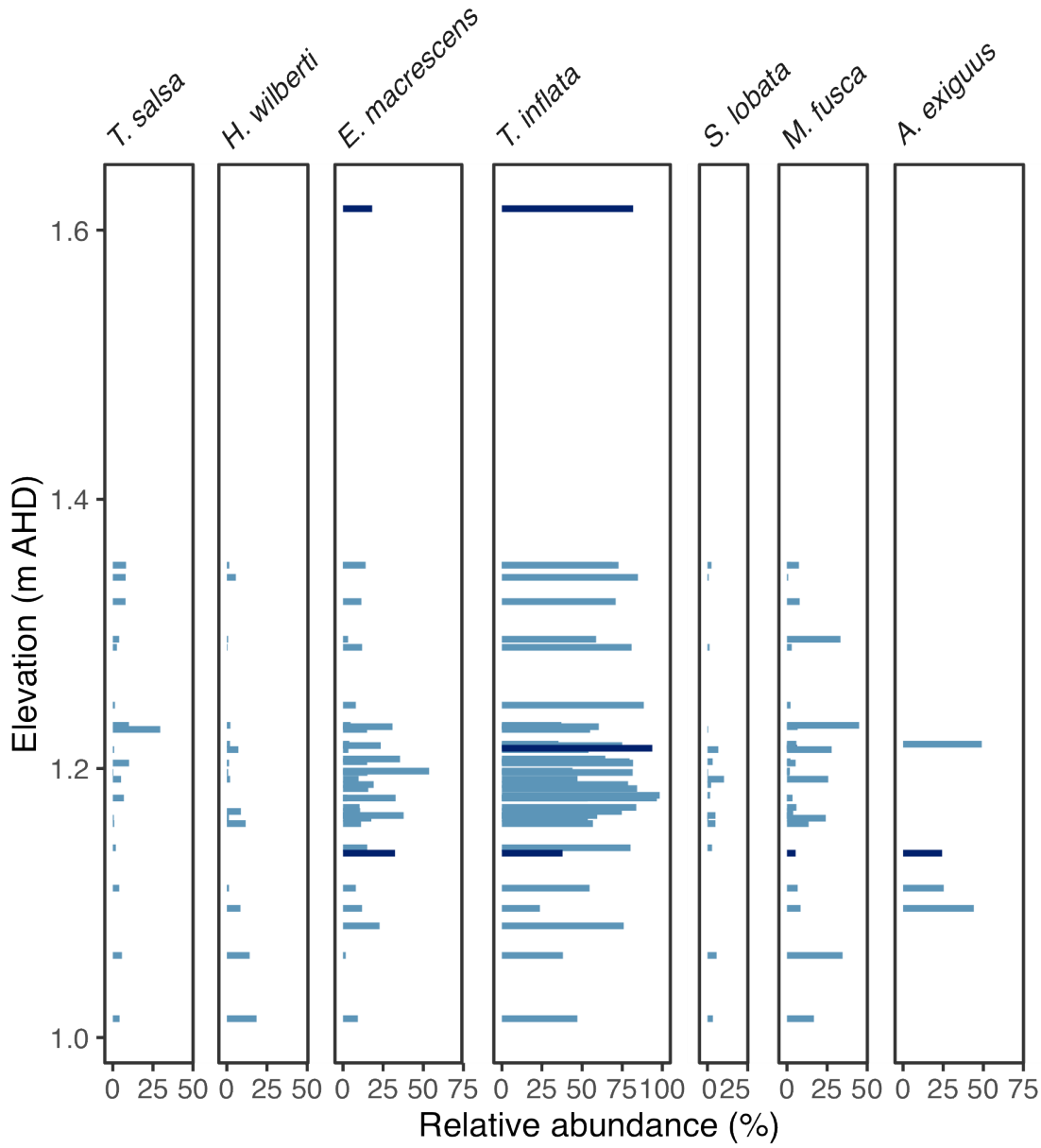

Figure A3. Modern foraminiferal abundances at Tarra showing species that contribute at least 10 % to one sample. Light blue denotes samples with counts greater than 50 individuals, dark blue denotes counts with less than 50 individuals.

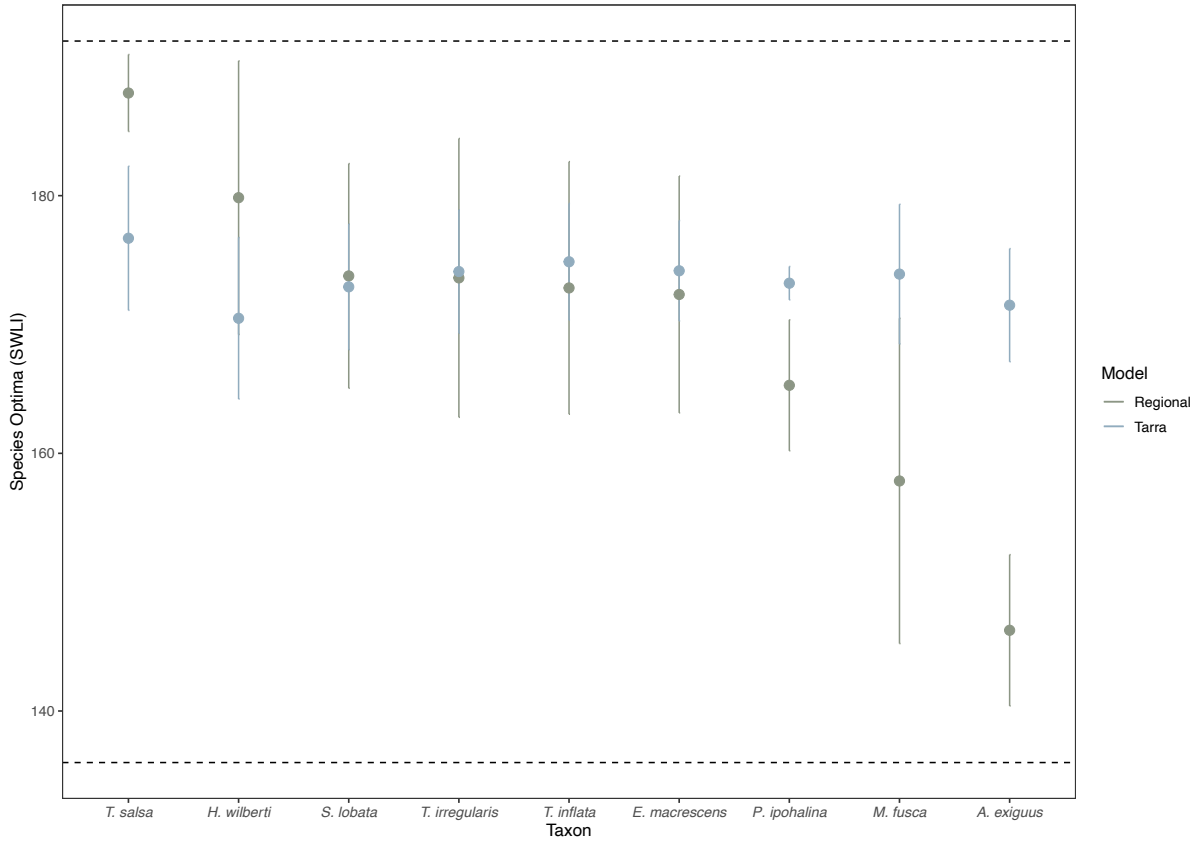

Figure A4. Comparison of species optima and tolerance in the Tarra modern training set and the regional II training set. Upper dotted line = HOF, lower dotted line = MSL.

There are several factors which may have caused the limited zonation at Tarra. Firstly, there is a fairly limited vertical range at the site which is evident in **(Figure A2)** which has led to very little contrast between the ecological zones in the marsh. This is further reflected by the largely homogenous vegetation across the marsh. *Trochammina inflata* is able to inhabit a large proportion of the sampled elevation gradient in the marsh **(Figure A2).** Another reason for the lack of zonation may pertain to the input of fresh water into the marsh. The range of *T. salsa* is large and is not just restricted to the upper elevations of the marsh, which suggests that the marsh is not particularly saline even at the lower elevations. This could relate to the position of the marsh within the estuary, as the site is located quite far up estuary and the Tarra river fronts the marsh which likely floods and inputs fresh water into the system, but also there

may be seepage from the surrounding catchment, as *Phragmites* (a common salt-intolerant reed) is found further south in the marsh beyond the section of the marsh explored in this study (Sinclair, S. 2021, pers comm 8 June). Finally, many of the wetlands along the Nooramunga and Corner Inlet have been, or currently are, used for agriculture and grazing (West Gippsland Catchment Management Authority, 2013). Around the whole area, many of the salt marshes have been subject to drainage and have been channelised which has lowered the water table in the marshes, reduced salinity and oxidised the surface soils (Capon, James and Reid, 2016) therefore it is likely that a combination of the site's position in the estuary alongside previous and current land management has resulted in significant fresh water inputs into the marsh and has reduced the lateral zonation across the marsh surface.

Appendix II. Bayesian transfer functions

Bayesian transfer functions are an alternative method by which PMSEs can be derived. Their main benefits include: **1.** the ability to incorporate 'priors' to further constrain elevation and **2.** they do not just assume linear or unimodal species responses like the classical models do (Cahill et al. 2016). Since the publication of Williams et al. (2021), code to generate Bayesian transfer functions has been made available online – package '*BTF*' (Cahill, 2021). Therefore, a comparison of the predictive performance of the classical and Bayesian models (**Table A1**) has been undertaken in order to determine the efficacy of Bayesian transfer functions on the Australian training sets (Lutregala local, Wapengo local and regional II).

Table A1 shows that for both the Lutregala local and Wapengo local models, the Bayesian predictive capability is better than the classical models (for Lutregala there is a difference in RMSEP of ~0.1 SWLI and for Wapengo there is a difference in RMSEP of ~2.3 SWLI). In regional II however, the Bayesian model has a marginally higher RMSEP than the classical model (~0.1 SWLI). Comparisons between the two models across all training sets show that whilst the Bayesian transfer function may be advantageous due to the smaller errors, using the Bayesian models for RSL reconstructions would not result in significantly different reconstructions to those generated using WA-PLS models (**Figure A5**).

Table A1. Comparison of the root-mean-squared-error-of-prediction (RMSEP) between the chosen classical models from Williams et al. (2021) and Bayesian transfer function for each model.

Model	Classical RMSEP (SWLI)	Bayesian RMSEP (SWLI)
Lutregala local	6.42	6.29
Wapengo local	9.73	7.39
Regional II	7.66	7.74

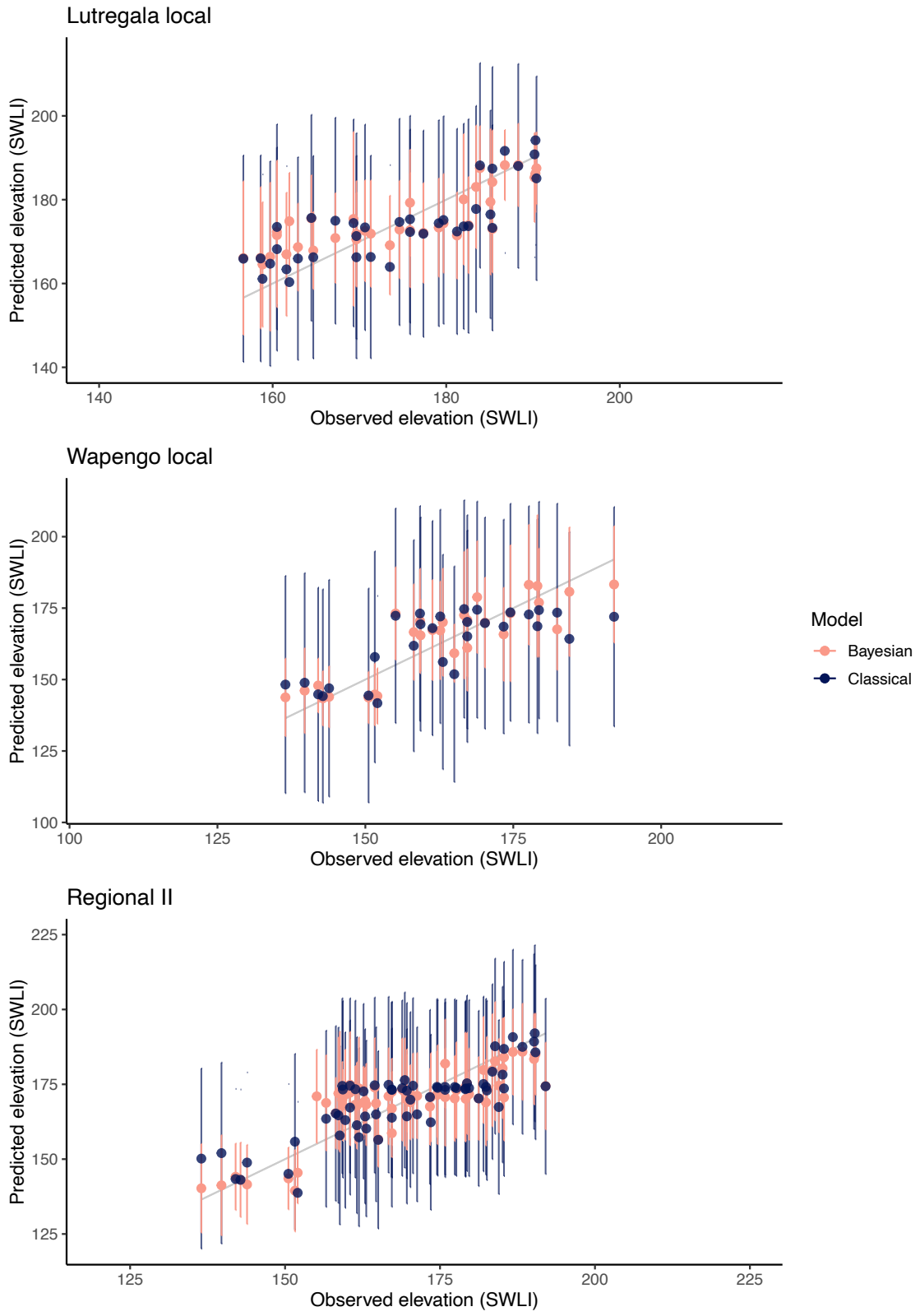

Figure A5. Comparison of Bayesian and classical (weighted-averaging partial least squares; WA-PLS) models for the Lutregala and Wapengo local training sets and regional II training set showing mean (circles) and 95 % prediction uncertainties.

Appendix III. Modern foraminifera paper (Chapter 5) supplementary material

Table A2. Detrended Correspondence Analysis axis scores for the Lutregala, Wapengo and Regional (Lutregala, Wapengo and Little Swanport combined) training sets.

Training set	DCA axis 1	DCA axis 2	DCA axis 3	DCA axis 4
Lutregala	0.56	0.24	0.12	0.13
Wapengo	0.72	0.26	0.30	0.17
Regional	0.65	0.33	0.22	0.22

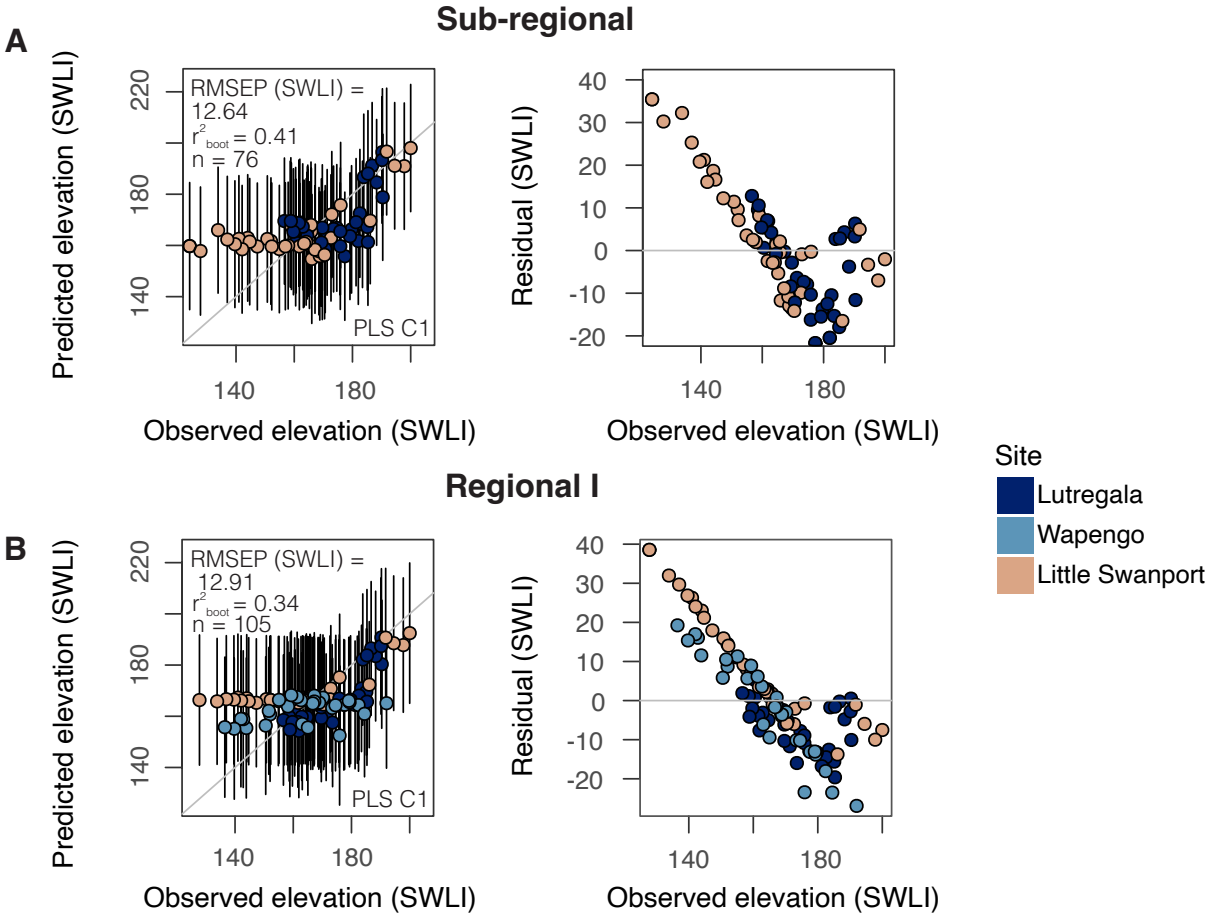

Figure A6. A. Transfer function performance for sub-regional and **B.** Regional I training sets showing plateauing of Little Swanport samples when combined with the Lutregala and Wapengo training sets. Data are presented with elevation converted to Standardised Water-Level Index (SWLI). 95 % prediction uncertainties are given for each sample.

Appendix IV. Foraminifera data tables

Table A3. Surface foraminifera counts from Lutregala (LG), Wapengo (WAP) and Tarra (TAR) converted to percentage. *T. s = T. salsa, H. w = H. wilberti, P. i = P. ipohalina, T. ir = T. irregularis, E. m = E. macrescens, T. i = T. inflata, S. i = S. lobata, M. f= M. fusca, A. a = A. agglutinans, A. e = A. exiguus, A. s = A. subcatenulatus, P. h = P. hyperhalina, H.g = H. germanica, A. f = A. fragile, A. b = A. beccarii, T* sp.= *Textularia* sp.

Sample	Elevation (m AHD)	*T. s*	*H. w*	*P. i*	*T. ir*	*E. m*	*T. i*	*S. l*	*M. f*	*A. a*	*A. e*	*A. s*	*P. h*	*H. g*	*A. f*	*A. b*	*T* sp.	Total
LG24	0.94	10.4	30.0	0.0	2.1	4.4	50.0	0.4	2.7	0.0	0.0	0.0	0.0	0.0	0.0	0.0	0.0	14
LG30	0.92	0.0	0.0	0.0	11.8	58.8	27.5	0.0	2.0	0.0	0.0	0.0	0.0	0.0	0.0	0.0	0.0	18
LG32	0.87	0.0	0.0	0.0	1.2	28.6	69.4	0.0	0.7	0.0	0.0	0.0	0.0	0.0	0.0	0.0	0.0	167
LG36	0.85	0.0	0.0	0.0	2.8	26.5	26.1	0.9	43.7	0.0	0.0	0.0	0.0	0.0	0.0	0.0	0.0	320
LG38	0.84	0.0	15.8	0.0	11.1	3.5	68.4	0.0	1.2	0.0	0.0	0.0	0.0	0.0	0.0	0.0	0.0	257
LG48	0.81	0.0	0.0	0.0	0.0	66.7	25.1	2.9	5.3	0.0	0.0	0.0	0.0	0.0	0.0	0.0	0.0	281
LG7	0.87	0.4	0.0	0.0	1.6	2.8	19.4	0.0	75.7	0.0	0.0	0.0	0.0	0.0	0.0	0.0	0.0	122
LG60	0.82	0.0	0.0	2.0	6.3	19.6	27.1	1.2	43.9	0.0	0.0	0.0	0.0	0.0	0.0	0.0	0.0	524
LG6	0.76	0.0	0.4	0.0	0.4	56.6	42.6	0.0	0.0	0.0	0.0	0.0	0.0	0.0	0.0	0.0	0.0	47
LG120	0.87	77.8	0.0	0.0	22.2	0.0	0.0	0.0	0.0	0.0	0.0	0.0	0.0	0.0	0.0	0.0	0.0	223
LG130	0.79	44.4	9.4	0.0	0.0	5.4	40.4	0.0	0.0	0.0	0.0	0.0	0.0	0.0	0.0	0.0	0.4	252
LG135	0.81	75.4	1.8	0.0	3.6	17.4	1.8	0.0	0.0	0.0	0.0	0.0	0.0	0.0	0.0	0.0	0.0	814
LG5	0.82	0.0	0.0	2.1	0.3	18.5	38.4	0.3	40.5	0.0	0.0	0.0	0.0	0.0	0.0	0.0	0.0	66
LG160	0.82	68.0	8.2	0.0	2.5	7.4	7.4	0.0	6.6	0.0	0.0	0.0	0.0	0.0	0.0	0.0	0.0	101
LG170	0.80	51.9	10.3	0.0	0.0	13.4	24.4	0.0	0.0	0.0	0.0	0.0	0.0	0.0	0.0	0.0	0.0	90
LG185	0.77	56.0	28.8	0.0	0.4	6.6	8.2	0.0	0.0	0.0	0.0	0.0	0.0	0.0	0.0	0.0	0.0	63
LG4	0.77	0.0	0.0	0.0	0.0	9.4	82.8	0.0	7.8	0.0	0.0	0.0	0.0	0.0	0.0	0.0	0.0	76

LG215	0.76	0.0	0.0	0.0	0.0	45.5	53.0	0.0	1.5	0.0	0.0	0.0	0.0	0.0	0.0	0.0	0.0	16
LG225	0.74	3.0	34.7	0.0	9.9	4.0	46.5	1.0	1.0	0.0	0.0	0.0	0.0	0.0	0.0	0.0	0.0	157
LG230	0.73	39.5	43.1	0.0	0.0	6.4	8.9	0.0	2.1	0.0	0.0	0.0	0.0	0.0	0.0	0.0	0.0	102
LG1	0.75	100.0	0.0	0.0	0.0	0.0	0.0	0.0	0.0	0.0	0.0	0.0	0.0	0.0	0.0	0.0	0.0	116
LG240	0.70	0.0	0.0	0.0	37.8	61.1	1.1	0.0	0.0	0.0	0.0	0.0	0.0	0.0	0.0	0.0	0.0	452
LG245	0.72	2.0	13.9	0.0	4.8	10.7	63.9	0.0	4.8	0.0	0.0	0.0	0.0	0.0	0.0	0.0	0.0	244
LG255	0.66	0.0	0.0	0.0	9.4	63.9	12.0	0.0	14.6	0.0	0.0	0.0	0.0	0.0	0.0	0.0	0.0	171
LG260	0.68	0.0	0.0	0.0	3.2	71.4	25.4	0.0	0.0	0.0	0.0	0.0	0.0	0.0	0.0	0.0	0.0	567
LG2	0.60	49.2	13.7	0.0	13.0	11.5	9.2	0.2	3.2	0.0	0.0	0.0	0.0	0.0	0.0	0.0	0.0	59
LG275	0.64	0.0	0.0	0.0	0.0	59.2	39.5	0.0	1.3	0.0	0.0	0.0	0.0	0.0	0.0	0.0	0.0	383
LG280	0.61	0.0	0.0	0.0	6.3	12.5	18.8	0.0	62.5	0.0	0.0	0.0	0.0	0.0	0.0	0.0	0.0	247
LG285	0.60	10.6	14.9	0.0	0.0	61.7	12.8	0.0	0.0	0.0	0.0	0.0	0.0	0.0	0.0	0.0	0.0	56
LG3	0.68	0.7	0.2	0.0	1.7	65.6	31.7	0.0	0.0	0.0	0.0	0.0	0.0	0.0	0.0	0.0	0.0	64
LG290	0.58	0.0	0.0	0.0	1.7	12.9	83.6	0.0	1.7	0.0	0.0	0.0	0.0	0.0	0.0	0.0	0.0	186
LG295	0.56	0.0	0.6	0.0	4.5	24.8	64.3	0.0	5.7	0.0	0.0	0.0	0.0	0.0	0.0	0.0	0.0	151
LG305	0.18	0.0	0.4	0.0	0.0	18.9	27.5	0.8	52.5	0.0	0.0	0.0	0.0	0.0	0.0	0.0	0.0	148
LG315	0.22	0.0	0.0	0.0	3.1	19.7	35.8	0.0	41.4	0.0	0.0	0.0	0.0	0.0	0.0	0.0	0.0	174
ST2-LG-20	0.77	0.0	0.0	0.0	0.0	0.0	0.0	0.0	0.0	0.0	0.0	0.0	0.0	0.0	0.0	0.0	0.0	0
ST-2LG0	0.79	0.0	0.7	0.4	13.3	3.2	22.9	0.0	59.5	0.0	0.0	0.0	0.0	0.0	0.0	0.0	0.0	233
ST-2LG40	0.74	0.0	0.0	0.0	0.0	0.0	0.0	0.0	90.0	0.0	0.0	0.0	0.0	0.0	0.0	10.0	0.0	410
ST-2LG60	0.69	0.0	2.3	0.0	0.0	0.6	30.5	0.0	66.1	0.6	0.0	0.0	0.0	0.0	0.0	0.0	0.0	412
ST-2LG80	0.68	0.0	0.0	0.0	0.0	0.7	1.4	0.0	97.3	0.7	0.0	0.0	0.0	0.0	0.0	0.0	0.0	171
ST-2LG100	0.63	0.0	5.4	0.0	8.9	12.5	37.5	0.0	35.7	0.0	0.0	0.0	0.0	0.0	0.0	0.0	0.0	272
ST-2LG120	0.62	0.0	10.2	0.0	6.8	11.9	64.4	0.0	6.8	0.0	0.0	0.0	0.0	0.0	0.0	0.0	0.0	255
ST-2LG140	0.61	0.0	3.7	0.0	0.6	3.0	39.6	0.0	53.0	0.0	0.0	0.0	0.0	0.0	0.0	0.0	0.0	279
ST-2LG160	0.59	0.0	3.5	0.0	0.0	0.0	19.3	1.8	75.4	0.0	0.0	0.0	0.0	0.0	0.0	0.0	0.0	328
ST-2LG190	0.58	0.0	2.2	0.0	19.9	0.5	29.0	0.0	48.4	0.0	0.0	0.0	0.0	0.0	0.0	0.0	0.0	57

ST-2LG220	0.24	0.0	15.2	0.0	0.7	2.0	23.8	0.0	58.3	0.0	0.0	0.0	0.0	0.0	0.0	0.0	0.0	10
ST-2LG235	0.32	0.0	0.0	0.0	0.0	6.7	40.0	0.0	53.3	0.0	0.0	0.0	0.0	0.0	0.0	0.0	0.0	8
ST-2LG240	0.34	0.0	0.0	0.0	0.0	12.5	25.0	0.0	62.5	0.0	0.0	0.0	0.0	0.0	0.0	0.0	0.0	15
WAP -10 ST-1	1.10	0.0	0.0	0.0	0.0	0.0	0.0	0.0	0.0	0.0	0.0	0.0	0.0	0.0	0.0	0.0	0.0	0
WAP -5 ST-1	1.07	100.0	0.0	0.0	0.0	0.0	0.0	0.0	0.0	0.0	0.0	0.0	0.0	0.0	0.0	0.0	0.0	12
WAP -7.5 ST-1	1.04	0.0	0.0	0.0	0.0	0.0	0.0	0.0	0.0	0.0	0.0	0.0	0.0	0.0	0.0	0.0	0.0	0
WAP 0 ST-2	1.02	5.2	0.0	0.0	0.0	5.8	83.2	2.3	3.5	0.0	0.0	0.0	0.0	0.0	0.0	0.0	0.0	173
WAP 1 ST-1	1.01	75.0	0.0	0.0	0.0	0.0	25.0	0.0	0.0	0.0	0.0	0.0	0.0	0.0	0.0	0.0	0.0	4
WAP 2 ST-1	1.00	0.0	0.0	0.0	0.0	0.0	0.0	0.0	0.0	0.0	0.0	0.0	0.0	0.0	0.0	0.0	0.0	0
WAP 5 ST-1	0.99	12.5	0.0	0.0	0.0	87.5	0.0	0.0	0.0	0.0	0.0	0.0	0.0	0.0	0.0	0.0	0.0	16
WAP 7 ST-1	0.98	0.0	0.0	0.0	0.0	100.0	0.0	0.0	0.0	0.0	0.0	0.0	0.0	0.0	0.0	0.0	0.0	3
WAP 22 ST-1	0.96	0.0	0.0	0.0	0.0	100.0	0.0	0.0	0.0	0.0	0.0	0.0	0.0	0.0	0.0	0.0	0.0	17
WAP 28 ST-1	0.94	0.0	0.0	0.0	0.0	0.0	0.0	0.0	0.0	0.0	0.0	0.0	0.0	0.0	0.0	0.0	0.0	0
WAP 110 ST1	0.91	0.0	1.2	1.2	0.0	6.0	91.6	0.0	0.0	0.0	0.0	0.0	0.0	0.0	0.0	0.0	0.0	83
WAP 35 ST-1	0.90	0.0	0.0	0.0	0.0	0.0	0.0	0.0	0.0	0.0	0.0	0.0	0.0	0.0	0.0	0.0	0.0	0
WAP 120 ST-1	0.87	0.0	9.1	0.0	0.0	10.9	76.4	3.6	0.0	0.0	0.0	0.0	0.0	0.0	0.0	0.0	0.0	55
WAP 60 ST-1	0.87	1.4	0.0	0.0	0.0	54.9	39.4	0.0	4.2	0.0	0.0	0.0	0.0	0.0	0.0	0.0	0.0	142
WAP 10 ST-2	0.85	0.4	0.0	0.0	0.0	12.7	78.0	5.5	3.4	0.0	0.0	0.0	0.0	0.0	0.0	0.0	0.0	236
WAP 15 ST-2	0.84	0.0	0.0	0.0	0.0	0.0	71.4	14.3	14.3	0.0	0.0	0.0	0.0	0.0	0.0	0.0	0.0	7
WAP 20 ST-2	0.83	0.0	0.0	0.0	0.0	0.0	0.0	0.0	0.0	0.0	0.0	0.0	0.0	0.0	0.0	0.0	0.0	0
WAP 122 ST-1	0.83	0.0	0.0	0.0	0.0	0.0	0.0	0.0	72.8	1.2	26.0	0.0	0.0	0.0	0.0	0.0	0.0	254
WAP 5 m ST-2	0.83	0.4	0.0	0.0	1.2	19.2	48.5	0.4	30.4	0.0	0.0	0.0	0.0	0.0	0.0	0.0	0.0	260
WAP 30 ST-2	0.82	0.0	0.0	0.0	0.0	100.0	0.0	0.0	0.0	0.0	0.0	0.0	0.0	0.0	0.0	0.0	0.0	2
WAP 25 ST-2	0.82	0.0	0.0	0.0	0.0	11.8	86.8	0.0	1.5	0.0	0.0	0.0	0.0	0.0	0.0	0.0	0.0	68
WAP 125 ST1	0.80	0.0	0.0	1.4	0.0	21.4	61.4	0.0	15.7	0.0	0.0	0.0	0.0	0.0	0.0	0.0	0.0	70
WAP 35 ST -2	0.78	0.0	0.0	4.3	0.0	21.7	65.2	0.0	8.7	0.0	0.0	0.0	0.0	0.0	0.0	0.0	0.0	23
WAP 130 ST1	0.77	0.0	0.0	35.2	0.0	23.1	36.3	5.5	0.0	0.0	0.0	0.0	0.0	0.0	0.0	0.0	0.0	91

WAP 135 ST-1	0.75	0.4	1.5	9.3	0.0	1.5	81.7	4.1	1.5	0.0	0.0	0.0	0.0	0.0	0.0	0.0	0.0	268
WAP 140 ST-1	0.73	0.0	0.0	71.0	1.7	9.1	13.9	0.0	2.6	0.0	1.7	0.0	0.0	0.0	0.0	0.0	0.0	231
WAP 144 ST-1	0.73	0.0	0.0	3.9	0.0	46.1	46.1	0.0	3.9	0.0	0.0	0.0	0.0	0.0	0.0	0.0	0.0	76
WAP 40 ST-2	0.73	0.0	0.0	0.0	0.0	10.8	89.2	0.0	0.0	0.0	0.0	0.0	0.0	0.0	0.0	0.0	0.0	74
WAP 45 ST-2	0.71	0.0	0.0	7.8	0.0	19.6	0.0	0.0	71.6	1.0	0.0	0.0	0.0	0.0	0.0	0.0	0.0	102
WAP 150 ST-1	0.69	0.0	0.0	3.1	4.7	20.3	10.9	0.0	60.9	0.0	0.0	0.0	0.0	0.0	0.0	0.0	0.0	64
WAP 50 ST-2	0.68	0.0	0.0	17.0	0.0	19.9	62.4	0.0	0.3	0.0	0.0	0.0	0.0	0.3	0.0	0.0	0.0	311
WAP 55 ST-2	0.67	0.0	0.0	3.5	0.0	85.0	7.1	0.0	4.4	0.0	0.0	0.0	0.0	0.0	0.0	0.0	0.0	113
WAP 60 ST-2	0.64	0.0	0.0	13.0	0.0	71.3	15.7	0.0	0.0	0.0	0.0	0.0	0.0	0.0	0.0	0.0	0.0	115
WAP 155 ST-1	0.64	0.0	0.0	3.6	0.0	29.1	67.3	0.0	0.0	0.0	0.0	0.0	0.0	0.0	0.0	0.0	0.0	55
WAP 159 ST1	0.63	0.0	0.0	27.4	0.0	43.8	0.0	0.0	28.8	0.0	0.0	0.0	0.0	0.0	0.0	0.0	0.0	73
WAP 160 ST-1	0.60	1.7	0.0	5.1	0.0	30.5	59.3	0.0	3.4	0.0	0.0	0.0	0.0	0.0	0.0	0.0	0.0	59
WAP 165 ST-1	0.58	0.0	0.0	0.0	0.0	9.5	71.4	0.0	14.3	4.8	0.0	0.0	0.0	0.0	0.0	0.0	0.0	21
WAP 170 ST-1	0.56	0.0	0.0	0.0	0.0	0.0	0.9	0.0	33.3	7.1	49.3	0.4	8.9	0.0	0.0	0.0	0.0	225
WAP 175 ST 1	0.56	0.0	0.0	0.0	0.0	0.0	46.1	0.0	16.6	1.8	34.0	0.0	1.5	0.0	0.0	0.0	0.0	453
WAP 180 ST-1	0.54	0.0	0.0	0.0	0.0	0.0	0.0	0.0	63.6	2.9	30.1	0.0	3.5	0.0	0.0	0.0	0.0	173
WAP 190 ST-1	0.47	0.0	0.0	0.0	0.0	0.0	0.0	0.0	80.0	0.0	19.3	0.0	0.7	0.0	0.0	0.0	0.0	140
WAP 200 ST-1	0.46	0.0	0.0	0.0	0.0	0.0	0.0	0.0	50.0	1.0	47.9	0.0	1.0	0.0	0.0	0.0	0.0	96
WAP 210 ST-1	0.45	0.0	0.0	0.7	0.0	0.0	0.3	0.0	48.2	5.6	44.6	0.0	0.7	0.0	0.0	0.0	0.0	303
WAP 230 ST-1	0.42	0.0	0.0	0.0	0.0	0.0	1.5	0.0	89.6	0.0	9.0	0.0	0.0	0.0	0.0	0.0	0.0	67
WAP 240 ST-1	0.38	0.0	0.0	0.0	0.0	0.0	0.6	0.0	82.0	0.0	17.4	0.0	0.0	0.0	0.0	0.0	0.0	328
TAR ST -2 0.5	1.62	0.0	0.0	0.0	0.0	18.2	81.8	0.0	0.0	0.0	0.0	0.0	0.0	0.0	0.0	0.0	0.0	11
TAR ST-2 1	1.59	0.0	0.0	0.0	0.0	0.0	0.0	0.0	0.0	0.0	0.0	0.0	0.0	0.0	0.0	0.0	0.0	0
TAR ST-2 90	1.35	8.3	0.0	0.0	0.0	14.0	72.7	2.5	2.5	0.0	0.0	0.0	0.0	0.0	0.0	0.0	0.0	121
TAR ST-2 130	1.35	8.0	1.5	0.0	0.5	13.9	68.7	0.0	7.5	0.0	0.0	0.0	0.0	0.0	0.0	0.0	0.0	201
TAR ST-2 80	1.34	8.0	5.6	0.0	0.0	0.0	84.8	0.8	0.8	0.0	0.0	0.0	0.0	0.0	0.0	0.0	0.0	125
TAR ST-2 120	1.32	7.9	0.0	0.0	1.8	11.5	70.9	0.0	7.9	0.0	0.0	0.0	0.0	0.0	0.0	0.0	0.0	227

TAR ST-2 100	1.30	4.0	0.8	0.0	0.0	3.2	58.7	0.0	33.3	0.0	0.0	0.0	0.0	0.0	0.0	0.0	0.0	126
TAR ST-1 5	1.29	2.6	0.4	0.0	0.0	11.9	80.9	1.3	3.0	0.0	0.0	0.0	0.0	0.0	0.0	0.0	0.0	235
TAR ST-1 10	1.25	1.3	0.0	0.0	0.0	8.0	88.4	0.0	2.2	0.0	0.0	0.0	0.0	0.0	0.0	0.0	0.0	225
TAR ST-1 125	1.23	10.1	2.2	0.0	0.9	4.7	37.1	0.0	45.0	0.0	0.0	0.0	0.0	0.0	0.0	0.0	0.0	636
TAR ST-1 110	1.23	0.0	0.0	0.0	2.1	30.8	60.4	0.0	6.7	0.0	0.0	0.0	0.0	0.0	0.0	0.0	0.0	240
TAR ST-1 7	1.23	29.5	0.0	0.0	0.0	15.0	55.0	0.5	0.0	0.0	0.0	0.0	0.0	0.0	0.0	0.0	0.0	220
TAR ST-2 140	1.22	0.0	2.0	0.0	0.0	3.9	35.3	0.0	5.9	0.0	49.0	0.0	0.0	0.0	3.9	0.0	0.0	51
TAR ST-1 115	1.22	0.0	0.0	0.0	0.7	23.5	75.0	0.0	0.7	0.0	0.0	0.0	0.0	0.0	0.0	0.0	0.0	272
TAR ST-1 15	1.22	0.0	0.0	0.0	0.0	0.0	93.8	0.0	6.3	0.0	0.0	0.0	0.0	0.0	0.0	0.0	0.0	16
TAR ST-1 130	1.21	0.8	7.2	0.0	0.0	3.4	54.0	6.8	27.8	0.0	0.0	0.0	0.0	0.0	0.0	0.0	0.0	237
TAR ST-1 116	1.21	0.0	0.0	0.0	0.0	35.5	64.5	0.0	0.0	0.0	0.0	0.0	0.0	0.0	0.0	0.0	0.0	287
TAR ST-1 12	1.21	0.0	0.0	0.0	0.0	15.1	79.6	3.2	2.2	0.0	0.0	0.0	0.0	0.0	0.0	0.0	0.0	93
TAR ST-1 0	1.20	10.1	1.4	0.0	1.4	0.0	81.8	0.0	5.4	0.0	0.0	0.0	0.0	0.0	0.0	0.0	0.0	148
TAR ST-1 107	1.20	0.0	0.0	0.5	0.0	53.7	44.0	0.0	1.8	0.0	0.0	0.0	0.0	0.0	0.0	0.0	0.0	218
TAR ST-1 120	1.20	0.4	0.8	0.0	0.0	15.3	81.5	0.4	1.6	0.0	0.0	0.0	0.0	0.0	0.0	0.0	0.0	249
TAR ST-1 135	1.19	5.1	2.0	0.0	0.0	9.7	47.1	10.3	25.7	0.0	0.0	0.0	0.0	0.0	0.0	0.0	0.0	350
TAR ST-1 105	1.19	0.0	0.0	0.0	0.0	19.1	78.7	2.2	0.0	0.0	0.0	0.0	0.0	0.0	0.0	0.0	0.0	178
TAR ST-1 20	1.19	0.0	0.0	0.0	0.0	15.7	84.3	0.0	0.0	0.0	0.0	0.0	0.0	0.0	0.0	0.0	0.0	229
TAR ST -2 20	1.18	0.0	0.0	0.0	0.0	0.0	0.0	0.0	0.0	0.0	0.0	0.0	0.0	0.0	0.0	0.0	0.0	0
TAR ST-1 17	1.18	0.0	0.0	0.0	0.0	0.0	98.4	1.6	0.0	0.0	0.0	0.0	0.0	0.0	0.0	0.0	0.0	123
TAR ST-1 19	1.18	0.0	0.0	0.0	0.0	2.7	96.6	0.0	0.8	0.0	0.0	0.0	0.0	0.0	0.0	0.0	0.0	263
TAR ST -1 65	1.18	6.9	0.0	0.0	3.4	32.8	53.4	0.0	3.4	0.0	0.0	0.0	0.0	0.0	0.0	0.0	0.0	58
TAR ST-1 25	1.17	0.0	0.0	0.0	0.0	10.3	83.8	0.0	5.9	0.0	0.0	0.0	0.0	0.0	0.0	0.0	0.0	271
TAR ST-1 95	1.17	0.0	8.7	1.0	1.0	10.7	74.8	0.0	3.9	0.0	0.0	0.0	0.0	0.0	0.0	0.0	0.0	103
TAR ST-1 35	1.17	0.0	0.0	0.0	0.5	37.7	59.4	0.5	1.9	0.0	0.0	0.0	0.0	0.0	0.0	0.0	0.0	212
TAR ST-1 80	1.17	0.0	0.0	0.0	0.0	37.6	54.6	5.0	2.8	0.0	0.0	0.0	0.0	0.0	0.0	0.0	0.0	141
TAR ST-1 70	1.16	0.7	1.3	0.0	2.0	17.6	53.6	0.7	24.2	0.0	0.0	0.0	0.0	0.0	0.0	0.0	0.0	153

TAR ST -1 90	1.16	0.9	11.7	0.0	0.9	11.3	56.8	5.0	13.5	0.0	0.0	0.0	0.0	0.0	0.0	0.0	0.0	222
TAR ST-1 37	1.14	1.9	0.0	0.0	0.0	15.1	80.2	2.8	0.0	0.0	0.0	0.0	0.0	0.0	0.0	0.0	0.0	106
TARST-1 60	1.14	0.0	0.0	0.0	0.0	32.4	37.8	0.0	5.4	0.0	24.3	0.0	0.0	0.0	0.0	0.0	0.0	37
TAR ST-1 45	1.11	4.0	1.3	0.0	0.0	8.0	54.7	0.0	6.7	0.0	25.3	0.0	0.0	0.0	0.0	0.0	0.0	75
TAR ST-1 50	1.10	0.0	8.5	0.0	0.0	11.9	23.7	0.0	8.5	0.0	44.1	0.0	0.0	0.0	3.4	0.0	0.0	59
TAR ST-1 40	1.08	0.0	0.0	0.0	1.3	22.8	75.9	0.0	0.0	0.0	0.0	0.0	0.0	0.0	0.0	0.0	0.0	79
TAR ST -1 140	1.06	5.7	14.2	0.0	0.0	1.7	38.1	5.7	34.7	0.0	0.0	0.0	0.0	0.0	0.0	0.0	0.0	176
TAR ST-1 145	1.01	4.2	18.5	0.0	0.8	9.2	47.1	3.4	16.8	0.0	0.0	0.0	0.0	0.0	0.0	0.0	0.0	119

Table A4. Fossil foraminifera counts from LG-1 (Lutregala), WAP-100 (Wapengo) and TAR-40 (Tarra). *T. s = T. salsa, H. w = H. wilberti, E. m = E. macrescens, P. i = P. ipohalina, T. ir = T. irregularis, S. l = S. lobata, T. i = T. inflata, M. f= M. fusca.*

Site	Depth (cm)	*T. s*	*H. w*	*E. m*	*P. i*	*T. ir*	*S. l*	*T. i*	*M. f*	Total
Lutregala	0.5	0.0	0.0	11.8	0.0	0.0	0.0	85.6	2.6	153
Lutregala	1.5	0.0	0.0	30.0	0.0	1.4	0.5	68.2	0.0	220
Lutregala	2.5	0.0	0.0	19.9	0.0	1.7	0.0	77.2	1.2	241
Lutregala	3.5	0.0	0.0	26.6	0.0	0.0	0.0	72.9	0.5	188
Lutregala	4.5	0.0	0.0	30.3	0.0	1.8	0.0	67.9	0.0	109
Lutregala	5.5	0.7	0.0	16.5	0.0	3.9	0.0	58.8	20.1	284
Lutregala	6.5	0.4	0.0	16.5	0.0	6.8	0.4	57.2	18.7	278
Lutregala	7.5	0.8	0.0	27.7	0.0	1.9	0.0	66.3	3.3	365
Lutregala	8.5	0.0	0.0	10.5	0.0	1.7	2.2	75.1	10.5	229
Lutregala	9.5	0.4	0.4	9.6	0.4	1.8	1.4	84.0	2.1	282
Lutregala	10.5	1.0	2.0	7.5	0.0	1.5	0.0	86.0	2.0	200
Lutregala	11.5	0.0	1.2	4.2	0.0	0.0	0.3	93.3	0.9	330
Lutregala	12.5	0.0	18.1	1.4	0.0	0.0	0.0	80.5	0.0	215
Lutregala	13.5	0.9	36.7	0.9	0.0	0.9	0.5	57.5	2.7	221
Lutregala	14.5	3.6	15.0	5.2	2.1	6.2	0.0	67.4	0.5	193
Lutregala	15.5	40.3	7.5	35.8	0.0	0.6	0.0	15.1	0.6	159
Lutregala	16.5	59.5	7.1	19.5	0.0	1.4	0.0	12.4	0.0	210
Lutregala	17.5	69.6	10.1	17.4	0.0	0.0	0.0	2.8	0.0	247
Lutregala	18.5	73.5	7.4	17.5	0.0	0.8	0.0	0.8	0.0	257
Lutregala	19.5	77.5	4.3	14.7	0.4	0.9	0.0	2.2	0.0	231
Lutregala	20.5	73.7	4.9	15.6	0.4	0.9	0.4	4.0	0.0	224
Lutregala	21.5	81.9	0.0	13.9	0.0	2.5	0.0	1.7	0.0	237

Lutregala	22.5	66.1	0.8	12.4	0.0	4.1	0.0	16.5	0.0	121
Lutregala	23.5	17.0	0.0	11.5	0.0	2.0	0.4	68.8	0.4	253
Lutregala	24.5	10.6	0.0	9.9	0.0	0.0	0.4	79.2	0.0	283
Lutregala	25.5	0.0	0.0	4.1	0.0	0.0	0.8	95.1	0.0	244
Lutregala	26.5	0.0	0.0	0.0	0.0	0.0	0.0	100.0	0.0	180
Lutregala	27.5	0.0	0.0	0.0	0.0	0.0	2.5	97.5	0.0	122
Lutregala	28.5	0.0	0.0	0.0	0.0	0.0	1.4	98.6	0.0	69
Lutregala	29.5	2.4	0.0	0.0	0.0	3.5	1.2	92.9	0.0	85
Lutregala	30.5	0.0	0.0	0.0	0.0	0.0	0.0	100.0	0.0	13
Lutregala	31.5	1.9	0.0	5.7	0.0	0.0	0.0	92.5	0.0	53
Lutregala	32.5	0.0	0.0	0.0	0.0	0.0	0.0	100.0	0.0	3
Lutregala	33.5	0.0	0.0	0.0	0.0	0.0	0.0	0.0	0.0	0
Wapengo	0.5	3.2	27.0	0.0	0.0	0.0	3.2	57.1	9.5	63
Wapengo	1.5	0.0	36.1	0.0	1.4	0.0	6.8	38.8	17.0	147
Wapengo	2.5	0.0	25.6	1.1	0.0	1.1	0.0	57.1	15.0	266
Wapengo	3.5	0.0	0.0	2.3	0.0	0.9	0.0	48.4	48.4	213
Wapengo	4.5	2.8	20.4	8.4	0.4	1.2	0.4	40.4	26.0	250
Wapengo	5.5	0.0	15.0	6.9	4.0	4.0	0.9	32.4	36.7	346
Wapengo	6.5	12.2	6.9	2.8	7.2	6.9	0.0	26.2	37.8	362
Wapengo	7.5	0.8	2.5	7.1	24.1	6.2	0.8	23.2	35.3	241
Wapengo	8.5	1.2	0.6	23.6	25.1	1.5	2.3	29.7	16.0	343
Wapengo	9.5	0.0	0.0	5.6	33.9	0.6	0.9	38.2	20.7	319
Wapengo	10.5	0.2	0.0	13.6	13.4	0.7	1.2	34.0	36.9	426
Wapengo	11.5	0.8	0.0	11.2	8.5	0.4	1.7	19.6	57.8	902
Wapengo	12.5	0.2	0.4	24.3	6.3	0.2	0.2	16.2	52.2	1307
Wapengo	13.5	0.7	4.9	6.5	3.7	0.7	0.7	23.8	58.9	1420
Wapengo	14.5	11.4	4.1	5.0	2.3	0.6	0.0	35.2	41.3	341

Wapengo	15.5	14.9	0.0	4.3	0.3	1.7	1.0	59.1	18.8	303
Wapengo	16.5	6.3	0.0	9.9	1.7	0.7	1.3	71.2	8.9	302
Wapengo	17.5	10.2	0.0	6.0	0.0	0.0	2.3	80.1	1.5	266
Wapengo	18.5	5.6	0.9	3.7	0.0	0.0	0.0	89.7	0.0	214
Wapengo	19.5	8.6	0.0	1.0	0.0	0.0	1.0	86.2	3.3	210
Wapengo	20.5	22.4	0.0	2.4	0.0	3.2	0.0	69.6	2.4	125
Wapengo	21.5	19.6	0.0	8.9	0.0	0.0	1.8	64.3	5.4	56
Wapengo	22.5	60.3	1.4	0.0	1.4	1.4	1.4	32.9	1.4	73
Wapengo	23.5	23.5	2.0	2.0	9.8	0.0	0.0	62.7	0.0	51
Wapengo	24.5	51.7	0.0	0.0	0.0	1.1	0.0	44.8	2.3	87
Wapengo	25.5	73.6	0.0	0.0	0.0	0.0	0.0	26.4	0.0	53
Wapengo	26.5	40.4	0.0	0.0	1.9	3.8	0.0	53.8	0.0	52
Wapengo	27.5	42.1	0.0	3.5	14.0	0.0	0.0	38.6	1.8	57
Wapengo	28.5	19.3	0.0	0.0	0.0	5.3	0.0	66.7	8.8	57
Wapengo	29.5	0.0	0.0	18.2	0.0	0.0	0.0	81.8	0.0	11
Wapengo	30.5	0.0	0.0	0.0	0.0	0.0	0.0	50.0	50.0	4
Wapengo	31.5	0.0	0.0	33.3	33.3	0.0	0.0	33.3	0.0	3
Wapengo	32.5	0.0	0.0	0.0	0.0	0.0	0.0	100.0	0.0	1
Wapengo	33.5	0.0	0.0	0.0	0.0	0.0	0.0	0.0	100.0	1
Wapengo	34.5	0.0	0.0	0.0	0.0	0.0	0.0	100.0	0.0	2
Wapengo	35.5	0.0	0.0	0.0	0.0	0.0	0.0	100.0	0.0	1
Wapengo	36.5	0.0	0.0	0.0	0.0	0.0	0.0	0.0	100.0	1
Wapengo	37.5	0.0	0.0	0.0	0.0	0.0	0.0	0.0	0.0	0
Wapengo	38.5	0.0	0.0	0.0	0.0	0.0	0.0	0.0	0.0	0
Wapengo	39.5	0.0	0.0	0.0	0.0	0.0	0.0	0.0	0.0	0
Wapengo	40.5	0.0	0.0	0.0	0.0	0.0	0.0	0.0	100.0	1
Wapengo	41.5	0.0	11.1	11.1	0.0	11.1	0.0	66.7	0.0	9

Wapengo	42.5	4.0	14.0	12.0	0.0	4.0	0.0	56.0	10.0	50
Wapengo	43.5	0.0	7.7	7.7	0.0	0.0	0.0	76.9	7.7	13
Wapengo	44.5	0.0	5.9	17.6	0.0	11.8	0.0	58.8	5.9	17
Wapengo	45.5	0.0	0.0	16.7	0.0	0.0	0.0	83.3	0.0	6
Wapengo	46.5	6.9	15.5	1.7	0.0	3.4	0.0	70.7	1.7	58
Tarra	0.5	0.0	1.4	32.1	0.0	0.0	0.0	57.9	6.2	209
Tarra	1.5	0.0	0.0	53.2	0.5	1.5	0.0	43.8	1.0	203
Tarra	2.5	9.0	4.7	15.4	0.9	10.7	2.1	48.3	9.0	234
Tarra	3.5	19.8	4.4	15.0	2.9	12.1	0.4	38.8	6.6	273
Tarra	4.5	16.9	2.5	23.3	0.9	11.7	0.2	36.4	8.0	437
Tarra	5.5	0.9	0.3	14.1	0.6	0.9	1.8	78.2	3.1	326
Tarra	6.5	1.5	1.0	46.6	1.8	0.8	0.0	46.9	1.3	388
Tarra	7.5	0.0	0.0	16.4	2.1	0.0	0.0	77.5	3.9	280
Tarra	8.5	0.7	0.0	20.8	5.5	1.0	0.0	66.6	5.5	293
Tarra	9.5	1.9	0.0	17.9	1.9	0.3	0.0	77.6	0.3	313
Tarra	10.5	5.1	0.0	21.5	0.0	0.2	0.2	71.5	1.5	410
Tarra	11.5	5.3	0.0	23.8	0.0	0.0	0.5	69.9	0.5	206
Tarra	12.5	2.5	2.3	19.8	0.0	0.0	0.0	71.2	4.3	611
Tarra	13.5	7.4	0.5	7.4	0.0	0.0	1.4	81.9	1.4	216
Tarra	14.5	8.3	3.9	9.4	0.0	0.9	1.3	72.3	3.9	542
Tarra	15.5	3.5	11.1	6.6	0.7	0.3	1.4	68.2	8.3	289
Tarra	16.5	4.3	11.0	9.7	0.0	0.7	5.0	43.1	26.1	299
Tarra	17.5	4.0	11.0	4.0	0.0	0.4	2.9	45.6	32.0	272
Tarra	18.5	12.8	8.9	10.1	0.0	0.6	2.8	44.1	20.7	179
Tarra	19.5	15.4	6.7	11.4	0.0	0.7	4.7	50.3	10.7	149
Tarra	20.5	20.0	4.3	10.4	0.0	1.3	1.3	41.7	20.9	230
Tarra	21.5	13.9	5.0	5.0	0.0	0.8	2.9	41.6	30.7	238

Tarra	22.5	9.8	5.1	4.3	0.0	1.2	0.0	55.1	24.4	254
Tarra	23.5	11.3	5.1	3.5	0.4	0.0	6.2	56.4	17.1	257
Tarra	24.5	18.1	9.5	4.8	0.5	0.0	1.4	56.7	9.0	210
Tarra	25.5	24.2	12.9	6.5	1.6	0.0	3.2	46.8	4.8	62
Tarra	26.5	36.7	2.5	3.8	0.0	1.3	1.3	51.9	2.5	79
Tarra	27.5	33.3	11.1	0.0	0.0	0.0	0.0	55.6	0.0	9
Tarra	28.5	29.4	0.0	0.0	0.0	0.0	0.0	64.7	5.9	17
Tarra	29.5	0.0	0.0	0.0	0.0	0.0	0.0	0.0	0.0	0
Tarra	30.5	0.0	0.0	0.0	0.0	0.0	0.0	0.0	0.0	0
Tarra	31.5	0.0	0.0	0.0	0.0	0.0	0.0	0.0	0.0	0
Tarra	32.5	0.0	0.0	0.0	0.0	0.0	0.0	0.0	0.0	0
Tarra	33.5	0.0	0.0	100.0	0.0	0.0	0.0	0.0	0.0	1
Tarra	34.5	0.0	0.0	0.0	0.0	0.0	0.0	0.0	0.0	0
Tarra	35.5	0.0	0.0	0.0	0.0	0.0	0.0	0.0	0.0	0
Tarra	36.5	0.0	0.0	0.0	0.0	0.0	0.0	100.0	0.0	1
Tarra	37.5	0.0	20.0	0.0	0.0	0.0	0.0	80.0	0.0	5
Tarra	38.5	0.0	83.3	0.0	0.0	0.0	0.0	16.7	0.0	6
Tarra	39.5	0.0	0.0	0.0	0.0	0.0	0.0	0.0	0.0	0
Tarra	40.5	0.0	0.0	0.0	0.0	0.0	0.0	0.0	0.0	0
Tarra	41.5	0.0	12.5	12.5	0.0	0.0	0.0	75.0	0.0	8
Tarra	42.5	50.0	0.0	0.0	0.0	0.0	0.0	0.0	50.0	2
Tarra	43.5	100.0	0.0	0.0	0.0	0.0	0.0	0.0	0.0	1
Tarra	44.5	0.0	0.0	0.0	0.0	0.0	0.0	0.0	0.0	0
Tarra	45.5	0.0	100.0	0.0	0.0	0.0	0.0	0.0	0.0	3
Tarra	46.5	0.0	12.5	0.0	0.0	0.0	0.0	62.5	25.0	8
Tarra	47.5	0.0	0.0	0.0	0.0	0.0	0.0	0.0	0.0	0
Tarra	48.5	0.0	0.0	0.0	0.0	0.0	0.0	0.0	0.0	0

Tarra	49.5	0.0	0.0	0.0	0.0	0.0	0.0	100.0	0.0	1

Table A5. Live core foraminifera for core LG-1 (Lutregala), WAP-100 (Wapengo) and TAR-40 (Tarra). *T. s = T. salsa, H. w = H. wilberti, E. m = Entzia macrescens, P. i = P. ipohalina, T. ir = T. irregularis, S. l = S. lobata, T. i = T. inflata, M. f= M. fusca, A sp = Ammobaculites species.*

Site	Depth	*T. s*	*H. w*	*E. m*	*P. i*	*T. ir*	*T. i*	*S. l*	*M. f*	*A* sp.	Total	Density (cc)
Lutregala	0.5	0.0	0.0	11.2	0.0	1.5	9.0	78.4	0.0	0.0	134	1.25
Lutregala	1.5	0.0	0.0	6.9	0.0	0.0	0.0	93.1	0.0	0.0	58	3.75
Lutregala	2.5	0.0	0.0	14.8	0.0	0.0	3.7	81.5	0.0	0.0	54	3.75
Lutregala	3.5	0.0	0.0	16.0	0.0	0.0	0.0	84.0	0.0	0.0	25	5
Lutregala	4.5	0.0	0.0	17.2	0.0	3.4	3.4	75.9	0.0	0.0	29	5
Lutregala	5.5	0.0	0.0	28.6	0.0	0.0	0.0	57.1	14.3	0.0	14	5
Lutregala	6.5	0.0	0.0	6.3	0.0	6.3	0.0	87.5	0.0	0.0	16	5
Lutregala	7.5	0.0	0.0	27.3	0.0	0.0	0.0	72.7	0.0	0.0	22	5
Lutregala	8.5	0.0	0.0	26.3	0.0	0.0	0.0	73.7	0.0	0.0	19	5
Lutregala	9.5	0.0	0.0	28.6	0.0	0.0	0.0	71.4	0.0	0.0	21	5
Wapengo	0.5	0.0	1.2	0.2	0.0	0.0	7.6	0.0	0.0	0.0	45	5
Wapengo	1.5	0.4	1.6	0.0	0.0	0.0	3.4	0.2	0.2	0.0	29	5
Wapengo	2.5	0.0	5.9	0.3	0.0	0.5	5.9	1.1	0.8	0.0	54	3.75
Wapengo	3.5	0.0	1.6	0.0	0.0	0.0	2.0	0.6	1.2	0.0	27	5
Wapengo	4.5	0.0	3.0	1.0	0.0	0.0	8.0	0.0	0.0	0.0	12	5.0
Wapengo	5.5	0.2	0.0	0.0	0.0	0.0	1.2	0.0	0.4	0.0	9	5
Wapengo	6.5	0.4	0.2	0.2	0.0	0.0	2.4	0.2	0.2	0.0	18	5
Wapengo	7.5	0.0	0.0	0.0	0.4	0.0	0.2	0.0	0.0	0.0	3	5
Wapengo	8.5	0.0	0.2	0.2	0.2	0.0	0.4	0.0	0.0	0.0	5	5
Wapengo	9.5	0.0	0.0	0.4	0.4	0.0	1.0	0.0	0.0	0.0	9	5
Tarra	0.5	0.0	2.9	11.6	0.0	0.0	84.1	0.0	1.4	0.0	69	2.5
Tarra	1.5	0.0	4.3	44.9	0.0	0.0	47.8	0.0	0.0	2.9	69	3.75
Tarra	2.5	0.0	1.8	17.5	0.0	1.8	78.9	0.0	0.0	0.0	57	5
Tarra	3.5	0.0	3.4	6.9	0.0	0.0	89.7	0.0	0.0	0.0	29	5

Tarra	4.5	0.0	1.7	13.3	0.0	0.0	81.7	0.0	3.3	0.0	60	3.75
Tarra	5.5	0.0	0.0	32.1	5.7	7.5	54.7	0.0	0.0	0.0	53	3.75
Tarra	6.5	0.0	0.0	23.6	9.1	0.0	67.3	0.0	0.0	0.0	55	3.75
Tarra	7.5	0.0	0.0	12.5	37.5	0.0	50.0	0.0	0.0	0.0	32	5
Tarra	8.5	0.0	0.0	0.0	20.0	0.0	80.0	0.0	0.0	0.0	20	5
Tarra	9.5	0.0	0.0	4.5	4.5	4.5	86.4	0.0	0.0	0.0	22	5

Appendix V. Pollen diagrams

Colleagues at the University of Queensland (Dr Patrick Moss, Claire Ellison, Kallen Marecic and Jody Daniels) prepared and analysed pollen downcore in LG-1, WAP-100 and TAR-40. Their results were used to identify chronostratigraphic markers in **Chapter 6**. A private link to the data on figshare has been added to the caption of each pollen diagram as the data are not yet published.

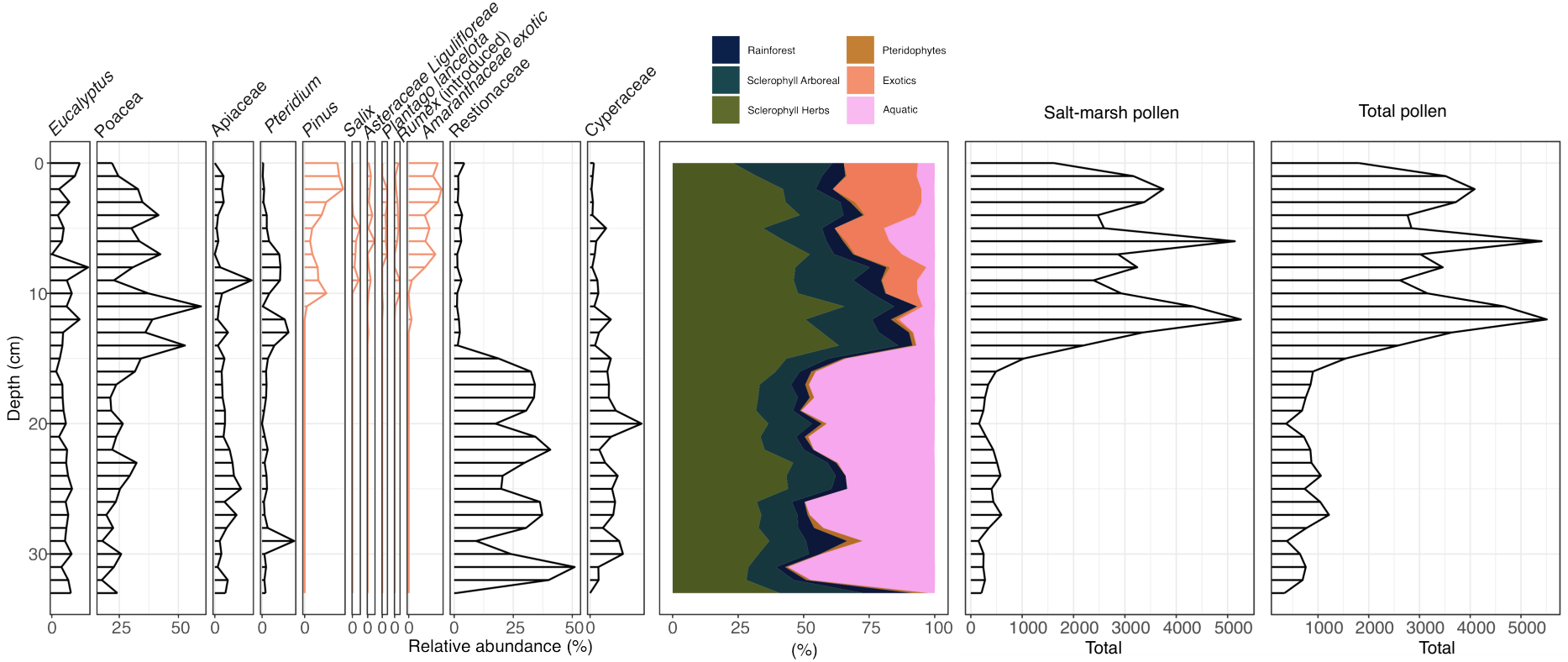

Figure A7. Pollen diagram for core LG-1 (Lutregala) showing either species that exceed 10 % relative abundance or exotics which can be used to identify European settlement (orange). Full data set available on figshare: https://figshare.com/s/35126122b7576411e302

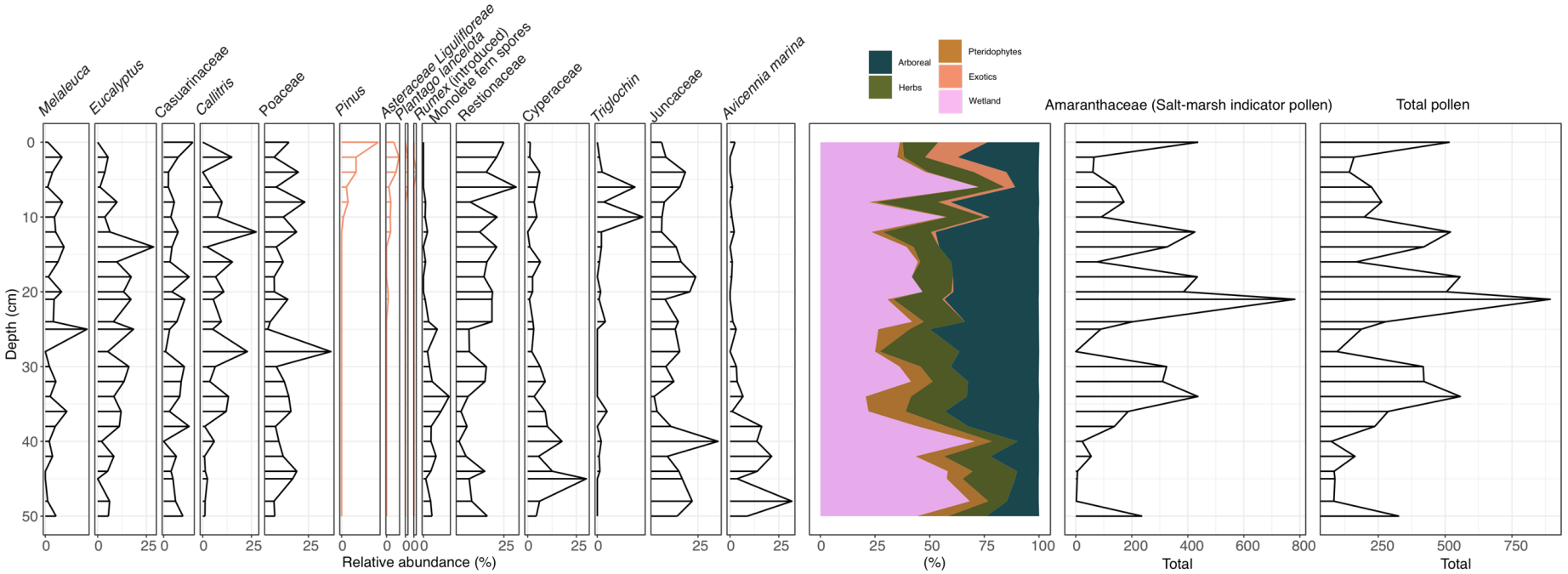

Figure A8. Pollen diagram for core WAP-100 (Wapengo) showing either species that exceed 10 % relative abundance or exotics which can be used to identify European settlement (orange). Full data set available on figshare: https://figshare.com/s/17a84cede94b339b43b6

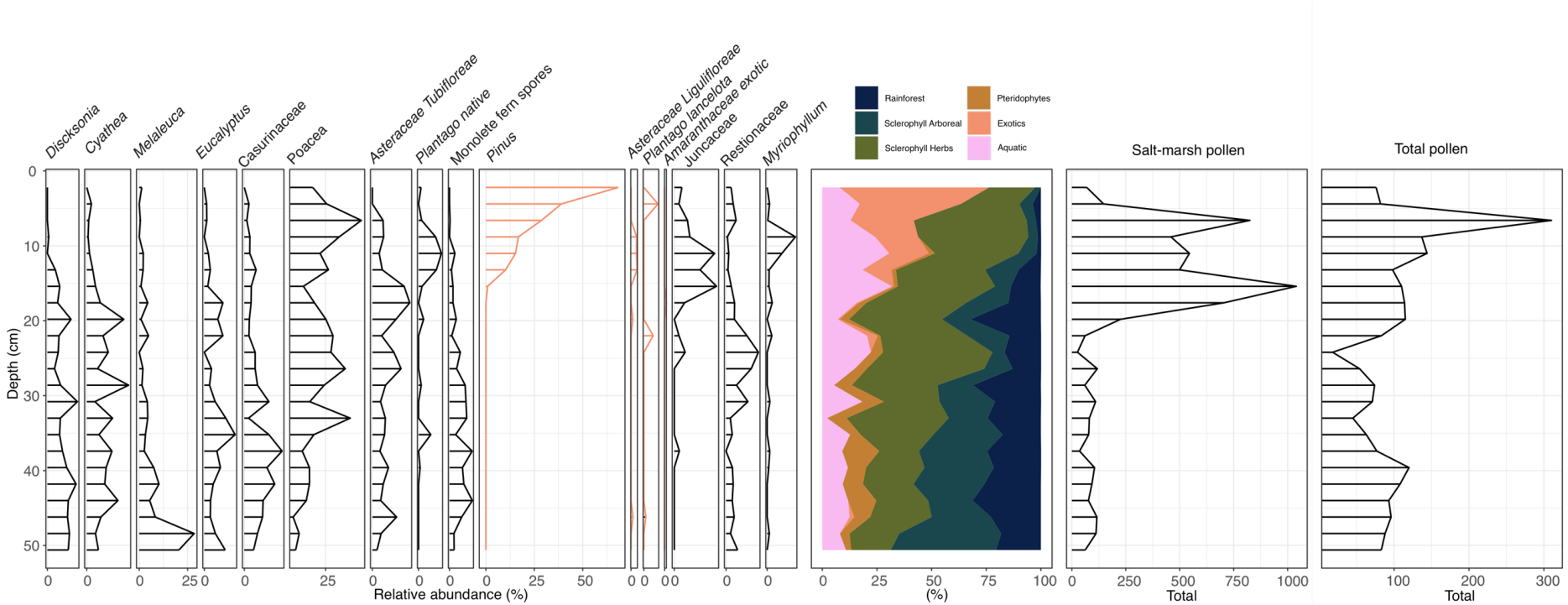

Figure A9. Pollen diagram for core TAR-40 (Tarra) showing either species that exceed 10 % relative abundance or exotics which can be used to identify European settlement (orange). Full data set available on figshare: https://figshare.com/s/2d3caedf6944dda8fe79

Appendix VI. Lutregala stable lead isotope data

Table A6. Stable lead isotope data for core LG-1.

Sample	$^{206}Pb/^{204}Pb$	± 2SE	$^{207}Pb/^{204}Pb$	± 2SE	$^{208}Pb/^{204}Pb$	± 2SE	$^{208}Pb/^{207}Pb$	± 2SE	$^{206}Pb/^{207}Pb$	± 2SE	$^{208}Pb/^{206}Pb$	± 2SE	Total Pb
0–1 cm	18.0799	0.0036	15.5928	0.0028	38.1746	0.0082	2.44831	0.00025	1.15953	0.00143	2.11147	0.00032	4.4
0–1 cm	18.2035	0.0009	15.6160	0.0007	39.1819	0.0018	2.50916	0.01418	1.16568	0.00002	2.15253	0.00004	16.40
1–2 cm	18.6822	0.0038	15.6350	0.0029	39.5070	0.0087	2.52686	0.00025	1.19490	0.00134	2.11471	0.00026	10.3
1–2 cm	18.6780	0.0041	15.6316	0.0032	39.5018	0.0095	2.52988	0.00026	1.19485	0.00135	2.11490	0.00027	6.2
2–3 cm	17.8454	0.0038	15.5772	0.0030	37.7441	0.0086	2.42309	0.00024	1.14567	0.00128	2.11500	0.00026	5.6
3–4 cm	17.8323	0.0038	15.5761	0.0032	37.7213	0.0091	2.42173	0.00025	1.14482	0.00132	2.11538	0.00028	6.0
4–5 cm	17.8342	0.0038	15.5741	0.0030	37.7485	0.0085	2.42382	0.00024	1.14512	0.00129	2.11664	0.00027	6.1
5–6 cm	17.8714	0.0037	15.5765	0.0029	37.8095	0.0084	2.42739	0.00024	1.14731	0.00129	2.11572	0.00027	7.7
6–7 cm	17.8595	0.0038	15.5780	0.0031	37.8273	0.0087	2.42825	0.00024	1.14645	0.00130	2.11805	0.00027	5.9
7–8 cm	17.7838	0.0037	15.5678	0.0030	37.6799	0.0085	2.42044	0.00024	1.14234	0.00129	2.11884	0.00027	7.8
8–9 cm	17.7432	0.0038	15.5656	0.0030	37.6285	0.0087	2.41743	0.00024	1.13989	0.00129	2.12076	0.00027	8.1
9–10 cm	17.6743	0.0037	15.5589	0.0029	37.5617	0.0084	2.41415	0.00024	1.13596	0.00128	2.12520	0.00027	8.0
10–11 cm	17.5911	0.0037	15.5443	0.0030	37.4300	0.0086	2.40794	0.00025	1.13165	0.00129	2.12782	0.00028	6.6
10–11 cm	17.5945	0.0037	15.5481	0.0030	37.4386	0.0084	2.40798	0.00024	1.13161	0.00128	2.12792	0.00027	8.2
11–12 cm	17.6012	0.0038	15.5417	0.0031	37.4508	0.0088	2.40976	0.00025	1.13252	0.00129	2.12779	0.00028	5.4
11–12 cm	17.6740	0.0005	15.5708	0.0005	37.5684	0.0014	2.41276	0.01164	1.13506	0.00001	2.12566	0.00004	27.38
12–13 cm	17.6136	0.0037	15.5530	0.0030	37.4695	0.0086	2.40912	0.00024	1.13249	0.00128	2.12729	0.00027	6.6
13–14 cm	17.7126	0.0038	15.5605	0.0031	37.5890	0.0088	2.41561	0.00025	1.13829	0.00130	2.12213	0.00027	4.5
14–15 cm	17.7665	0.0040	15.5644	0.0033	37.6491	0.0094	2.41902	0.00024	1.14150	0.00130	2.11916	0.00027	4.2
15–16 cm	17.7454	0.0013	15.5813	0.0012	37.6562	0.0032	2.41674	0.02539	1.13889	0.00002	2.12202	0.00008	6.78
16–17 cm	17.9339	0.0012	15.5942	0.0009	37.8625	0.0023	2.42806	0.02199	1.15002	0.00003	2.11131	0.00006	8.75
17–18 cm	17.7781	0.0012	15.5845	0.0011	37.6967	0.0029	2.41892	0.01861	1.14075	0.00003	2.12046	0.00005	8.86
18–19 cm	17.8436	0.0009	15.5918	0.0011	37.7694	0.0023	2.42254	0.02374	1.14445	0.00003	2.11677	0.00006	8.43

19–20 cm	17.8586	0.0018	15.5932	0.0015	37.7930	0.0035	2.42371	0.02574	1.14534	0.00003	2.11615	0.00007	7.04
20–21 cm	17.8342	0.0013	15.5882	0.0011	37.7444	0.0027	2.42137	0.01428	1.14408	0.00002	2.11643	0.00003	11.10
21–22 cm	18.0825	0.0012	15.6104	0.0007	38.0282	0.0018	2.43617	0.02443	1.15837	0.00003	2.10311	0.00007	15.46
22–23 cm	18.4416	0.0010	15.6394	0.0009	38.4319	0.0023	2.45743	0.02302	1.17920	0.00003	2.08399	0.00007	11.62
23–24 cm	18.5535	0.0010	15.6481	0.0007	38.5593	0.0019	2.46417	0.02983	1.18567	0.00003	2.07830	0.00009	10.45
24–25 cm	18.5552	0.0021	15.6341	0.0016	38.5211	0.0042	2.46392	0.00016	1.18681	0.00004	2.07609	0.00011	6.70
25–26 cm	18.6446	0.0019	15.6404	0.0014	38.6317	0.0039	2.47000	0.00017	1.19207	0.00005	2.07203	0.00012	8.31
26–27 cm	18.6810	0.0018	15.6430	0.0013	38.6762	0.0035	2.47244	0.00016	1.19420	0.00004	2.07037	0.00011	14.22
27–28 cm	18.6911	0.0018	15.6422	0.0013	38.6955	0.0036	2.47380	0.00017	1.19491	0.00005	2.07028	0.00011	10.78
28–29 cm	18.7332	0.0018	15.6447	0.0013	38.7700	0.0037	2.47813	0.00016	1.19741	0.00004	2.06957	0.00011	12.15
29–30 cm	18.7328	0.0019	15.6458	0.0014	38.7755	0.0039	2.47834	0.00016	1.19731	0.00004	2.06992	0.00011	9.13
30–31 cm	18.7720	0.0019	15.6473	0.0014	38.7927	0.0038	2.47925	0.00016	1.19968	0.00005	2.06659	0.00011	10.29
31–32 cm	18.7537	0.0019	15.6417	0.0013	38.8187	0.0037	2.48178	0.00016	1.19894	0.00004	2.06997	0.00011	9.78
31–32 cm	18.7539	0.0018	15.6424	0.0012	38.8209	0.0035	2.48178	0.00016	1.19893	0.00004	2.07000	0.00011	10.19

Appendix VII. Wapengo stable lead isotope data

Table A7. Stable lead isotope data for core WAP-100.

Sample	$^{206}Pb/^{204}Pb$	± 2SE	$^{207}Pb/^{204}Pb$	± 2SE	$^{208}Pb/^{204}Pb$	± 2SE	$^{208}Pb/^{207}Pb$	± 2SE	$^{206}Pb/^{207}Pb$	± 2SE	$^{208}Pb/^{206}Pb$	± 2SE	Total Pb
0-1cm	18.4623	0.0040	15.6466	0.0030	38.6900	0.0090	2.47277	0.00025	1.17995	0.00012	2.09566	0.00027	6.0
1-2cm	18.5571	0.0039	15.6563	0.0030	38.8549	0.0089	2.48178	0.00025	1.18527	0.00012	2.09386	0.00026	5.6
2-3cm	18.4933	0.0041	15.6462	0.0034	38.7461	0.0097	2.47651	0.00026	1.18199	0.00013	2.09520	0.00028	4.1
3-4cm	18.5256	0.0039	15.6511	0.0030	38.7522	0.0087	2.47594	0.00025	1.18364	0.00012	2.09180	0.00027	7.7
4-5cm	18.5251	0.0038	15.6510	0.0029	38.7492	0.0088	2.47588	0.00024	1.18363	0.00012	2.09178	0.00027	12.3
4-5cm	18.6680	0.0019	15.6618	0.0014	38.9316	0.0038	2.48582	0.00016	1.19197	0.00004	2.08547	0.00011	7.54
5-6cm	18.6042	0.0018	15.6591	0.0014	38.8842	0.0038	2.48320	0.00017	1.18807	0.00005	2.09011	0.00012	11.87
6-7cm	18.3729	0.0018	15.6357	0.0013	38.5614	0.0035	2.46629	0.00016	1.17507	0.00004	2.09884	0.00011	11.81
7-8cm	18.3309	0.0018	15.6326	0.0013	38.5179	0.0037	2.46399	0.00015	1.17262	0.00004	2.10127	0.00011	10.77
7-8cm	18.3317	0.0017	15.6331	0.0013	38.5177	0.0035	2.46385	0.00016	1.17261	0.00004	2.10116	0.00011	11.28
8-9cm	18.3485	0.0027	15.6356	0.0021	38.5392	0.0067	2.46491	0.00014	1.17351	0.00006	2.10045	0.00006	10.09
9-10cm	18.4627	0.0028	15.6449	0.0021	38.7071	0.0067	2.47412	0.00014	1.18011	0.00006	2.09651	0.00005	9.71
10-11cm	18.4580	0.0027	15.6432	0.0021	38.6949	0.0067	2.47361	0.00014	1.17994	0.00006	2.09639	0.00006	12.25
11-12cm	18.4439	0.0027	15.6435	0.0021	38.6778	0.0066	2.47248	0.00014	1.17902	0.00006	2.09707	0.00006	9.42
12-13cm	18.4429	0.0027	15.6435	0.0020	38.6846	0.0066	2.47293	0.00013	1.17896	0.00006	2.09755	0.00005	17.39
13-14cm	18.4240	0.0027	15.6415	0.0020	38.6538	0.0066	2.47130	0.00013	1.17790	0.00006	2.09806	0.00005	13.15
13-14cm	18.4230	0.0017	15.6408	0.0013	38.6535	0.0035	2.47134	0.00016	1.17787	0.00004	2.09814	0.00011	12.67
13-14cm	18.4245	0.0017	15.6415	0.0010	38.6535	0.0030	2.47129	0.00009	1.17790	0.00002	2.09804	0.00006	12.97
14-15cm	18.4750	0.0027	15.6477	0.0020	38.7327	0.0065	2.47533	0.00013	1.18069	0.00006	2.09651	0.00005	12.04
15-16cm	18.4535	0.0027	15.6471	0.0021	38.6804	0.0066	2.47212	0.00014	1.17935	0.00006	2.09616	0.00006	16.04
16-17cm	18.5386	0.0027	15.6554	0.0021	38.7893	0.0067	2.47778	0.00013	1.18419	0.00006	2.09238	0.00005	12.21
17-18cm	18.7223	0.0027	15.6719	0.0020	39.0495	0.0066	2.49174	0.00014	1.19465	0.00006	2.08575	0.00006	15.60
18-19cm	18.7193	0.0027	15.6710	0.0020	39.0319	0.0067	2.49075	0.00013	1.19453	0.00006	2.08513	0.00005	11.39
18-19cm	18.7183	0.0016	15.6705	0.0009	39.0288	0.0025	2.49067	0.00008	1.19449	0.00002	2.08513	0.00006	10.33
19-20cm	18.7311	0.0027	15.6707	0.0020	39.0487	0.0064	2.49180	0.00013	1.19527	0.00006	2.08473	0.00004	14.81

20-21cm	18.7528	0.0028	15.6715	0.0021	39.0854	0.0067	2.49405	0.00013	1.19661	0.00006	2.08427	0.00005	14.45
21-22cm	18.7383	0.0027	15.6714	0.0020	39.0546	0.0065	2.49212	0.00013	1.19570	0.00006	2.08424	0.00004	10.21
22-23cm	18.7688	0.0027	15.6720	0.0020	39.1022	0.0066	2.49513	0.00014	1.19762	0.00006	2.08341	0.00006	19.29
22-23cm	18.7698	0.0018	15.6723	0.0013	39.1045	0.0036	2.49513	0.00016	1.19764	0.00004	2.08336	0.00011	16.05
23-24cm	18.7742	0.0027	15.6751	0.0021	39.1373	0.0068	2.49683	0.00015	1.19769	0.00006	2.08470	0.00006	13.97
24-25cm	18.7333	0.0027	15.6707	0.0020	39.0530	0.0066	2.49214	0.00013	1.19542	0.00006	2.08473	0.00005	15.67
25-26cm	18.7801	0.0006	15.6941	0.0006	39.1934	0.0017	2.49739	0.00005	1.19664	0.00001	2.08700	0.00003	27.08
26-27cm	18.7538	0.0009	15.6934	0.0009	39.1283	0.0025	2.49334	0.00008	1.19501	0.00002	2.08646	0.00006	17.76
27-28cm	18.7627	0.0006	15.6948	0.0005	39.1422	0.0015	2.49404	0.00004	1.19547	0.00001	2.08625	0.00003	31.37
28-29cm	18.7520	0.0005	15.6954	0.0004	39.1203	0.0023	2.49250	0.00012	1.19474	0.00001	2.08622	0.00010	32.91
29-30cm	18.6987	0.0007	15.6859	0.0008	39.0261	0.0023	2.48801	0.00008	1.19206	0.00002	2.08716	0.00006	26.91
30-31cm	18.7827	0.0006	15.6946	0.0006	39.1542	0.0020	2.49479	0.00007	1.19676	0.00002	2.08462	0.00005	22.05
31-32cm	18.7675	0.0004	15.6862	0.0004	39.1161	0.0012	2.49368	0.00006	1.19643	0.00002	2.08427	0.00003	25.00
32-33cm	18.8025	0.0009	15.6949	0.0007	39.2174	0.0022	2.49875	0.00007	1.19798	0.00002	2.08581	0.00005	21.71
33-34cm	18.7672	0.0006	15.6898	0.0006	39.1283	0.0017	2.49393	0.00005	1.19614	0.00002	2.08499	0.00003	31.25
34-35cm	18.7885	0.0009	15.6965	0.0008	39.2057	0.0023	2.49778	0.00007	1.19699	0.00002	2.08672	0.00005	22.75
35-36cm	18.7911	0.0005	15.6952	0.0004	39.1970	0.0017	2.49743	0.00006	1.19724	0.00001	2.08598	0.00005	29.33
36-37cm	18.7918	0.0009	15.6941	0.0012	39.2032	0.0033	2.49801	0.00010	1.19735	0.00002	2.08628	0.00007	20.24
37-38cm	18.7476	0.0007	15.6887	0.0008	39.1326	0.0021	2.49434	0.00006	1.19497	0.00002	2.08737	0.00004	31.73
38-39cm	18.8171	0.0006	15.6940	0.0006	39.1833	0.0016	2.49674	0.00006	1.19900	0.00002	2.08234	0.00004	22.75
39-40cm	18.7986	0.0008	15.6936	0.0009	39.1903	0.0030	2.49726	0.00011	1.19787	0.00002	2.08475	0.00009	25.19
40-41cm	18.7992	0.0006	15.6929	0.0005	39.1854	0.0017	2.49706	0.00007	1.19793	0.00002	2.08447	0.00006	25.38
41-42cm	18.7953	0.0006	15.6963	0.0006	39.1942	0.0017	2.49706	0.00006	1.19742	0.00001	2.08536	0.00004	28.94
42-43cm	18.7555	0.0009	15.6910	0.0008	39.1082	0.0026	2.49244	0.00006	1.19531	0.00001	2.08519	0.00005	19.38
43-44cm	18.7693	0.0010	15.6909	0.0009	39.1473	0.0031	2.49499	0.00009	1.19620	0.00002	2.08577	0.00007	19.76
44-45cm	18.7671	0.0006	15.6917	0.0008	39.1387	0.0020	2.49419	0.00007	1.19596	0.00002	2.08550	0.00005	23.79
45-46cm	18.7733	0.0009	15.6908	0.0009	39.1598	0.0026	2.49576	0.00008	1.19645	0.00002	2.08596	0.00006	26.37

46-47cm	18.6926	0.0009	15.6850	0.0007	38.9899	0.0028	2.48584	0.00008	1.19175	0.00001	2.08587	0.00006	20.71
47-48cm	18.7412	0.0006	15.6903	0.0005	39.1363	0.0018	2.49430	0.00008	1.19442	0.00003	2.08830	0.00006	33.05

Appendix VIII. Tarra stable lead isotope data

Table A8. Stable lead isotope data for core TAR-40.

Sample	$^{206}Pb/^{204}Pb$	± 2SE	$^{207}Pb/^{204}Pb$	± 2SE	$^{208}Pb/^{204}Pb$	± 2SE	$^{208}Pb/^{207}Pb$	± 2SE	$^{206}Pb/^{207}Pb$	± 2SE	$^{208}Pb/^{206}Pb$	± 2SE	Total Pb
0-1cm	18.3447	0.0010	15.6324	0.0010	38.4046	0.0025	2.45678	0.00007	1.17354	0.00002	2.09347	0.00004	13.49
1-2cm	18.1919	0.0009	15.6194	0.0010	38.2002	0.0026	2.44575	0.00008	1.16468	0.00002	2.09994	0.00005	16.86
2-3cm	18.0378	0.0011	15.6031	0.0010	38.0061	0.0026	2.43586	0.00007	1.15605	0.00001	2.10706	0.00005	14.35
3-4cm	18.1386	0.0006	15.6138	0.0005	38.1321	0.0018	2.44224	0.00007	1.16168	0.00002	2.10234	0.00005	16.03
4-5cm	18.0589	0.0008	15.6070	0.0006	38.0351	0.0016	2.43711	0.00007	1.15711	0.00002	2.10621	0.00006	17.74
5-6cm	18.1805	0.0007	15.6166	0.0006	38.1933	0.0017	2.44570	0.00005	1.16420	0.00001	2.10076	0.00004	21.18
6-7cm	18.2348	0.0007	15.6247	0.0007	38.2845	0.0021	2.45025	0.00008	1.16704	0.00002	2.09953	0.00006	17.39
7-8cm	18.2659	0.0007	15.6284	0.0009	38.3489	0.0031	2.45373	0.00011	1.16875	0.00003	2.09945	0.00008	19.75
8-9cm	18.2634	0.0009	15.6269	0.0009	38.3443	0.0024	2.45378	0.00006	1.16871	0.00002	2.09956	0.00004	25.64
9-10cm	18.3045	0.0008	15.6338	0.0008	38.3973	0.0020	2.45607	0.00006	1.17084	0.00002	2.09770	0.00004	23.95
10-11cm	18.3777	0.0007	15.6418	0.0008	38.4870	0.0023	2.46055	0.00008	1.17489	0.00002	2.09427	0.00006	26.42
11-12cm	18.4528	0.0006	15.6488	0.0006	38.5779	0.0018	2.46520	0.00009	1.17918	0.00002	2.09062	0.00007	19.40
12-13cm	18.6083	0.0008	15.6616	0.0006	38.7718	0.0020	2.47563	0.00009	1.18815	0.00002	2.08360	0.00007	17.70
13-14 cm	18.7505	0.0011	15.6484	0.0010	38.8222	0.0028	2.48102	0.00009	1.19833	0.00002	2.07041	0.00007	10.15
14-15 cm	18.8121	0.0011	15.6530	0.0011	38.9098	0.0026	2.48584	0.00008	1.20180	0.00002	2.06843	0.00006	8.81
15-16 cm	18.8268	0.0010	15.6544	0.0011	38.9322	0.0028	2.48697	0.00009	1.20261	0.00003	2.06798	0.00006	7.53
16-17cm	18.8054	0.0010	15.6482	0.0009	38.8794	0.0027	2.48468	0.00010	1.20179	0.00002	2.06748	0.00008	8.84
17-18 cm	18.8156	0.0011	15.6539	0.0011	38.9000	0.0031	2.48515	0.00010	1.20204	0.00003	2.06744	0.00008	8.91
18-19 cm	18.8134	0.0013	15.6560	0.0011	38.9466	0.0034	2.48778	0.00009	1.20173	0.00002	2.07018	0.00006	7.05
19-20 cm	18.8200	0.0014	15.6555	0.0012	38.9150	0.0031	2.48576	0.00010	1.20220	0.00002	2.06768	0.00007	9.34
20-21 cm	18.8243	0.0010	15.6539	0.0009	38.9304	0.0025	2.48699	0.00008	1.20258	0.00002	2.06805	0.00005	11.72

21-22 cm	18.8252	0.0009	15.6549	0.0008	38.9456	0.0022	2.48788	0.00007	1.20250	0.00002	2.06893	0.00005	14.17
22-23 cm	18.8193	0.0012	15.6528	0.0011	38.9138	0.0032	2.48608	0.00010	1.20229	0.00002	2.06778	0.00007	9.70
23-24 cm	18.8249	0.0014	15.6564	0.0011	38.9446	0.0030	2.48754	0.00009	1.20243	0.00003	2.06876	0.00007	7.85
24-25 cm	18.8230	0.0011	15.6553	0.0010	38.9012	0.0028	2.48487	0.00009	1.20237	0.00002	2.06665	0.00006	9.86
25-26 cm	18.8182	0.0008	15.6532	0.0008	38.8943	0.0023	2.48480	0.00008	1.20225	0.00002	2.06679	0.00006	12.88
26-27 cm	18.6020	0.0007	15.6265	0.0007	38.5888	0.0020	2.46957	0.00007	1.19045	0.00002	2.07449	0.00005	18.81
27-28 cm	18.7830	0.0008	15.6495	0.0009	38.8442	0.0028	2.48221	0.00010	1.20027	0.00002	2.06804	0.00007	16.65
28-29 cm	18.6053	0.0009	15.6308	0.0008	38.6431	0.0022	2.47234	0.00008	1.19034	0.00002	2.07700	0.00006	10.94
29-30 cm	18.8168	0.0012	15.6542	0.0010	38.9505	0.0029	2.48829	0.00007	1.20204	0.00002	2.07006	0.00005	7.17
30-31 cm	18.8334	0.0014	15.6556	0.0014	39.0280	0.0034	2.49280	0.00008	1.20296	0.00002	2.07222	0.00005	5.82
31-32 cm	18.8128	0.0012	15.6560	0.0011	38.9292	0.0028	2.48668	0.00007	1.20168	0.00002	2.06933	0.00005	6.13
32-33 cm	18.6976	0.0011	15.6406	0.0009	38.7517	0.0024	2.47773	0.00008	1.19549	0.00002	2.07256	0.00005	7.10
33-34 cm	18.6220	0.0010	15.6356	0.0009	38.6808	0.0025	2.47395	0.00009	1.19104	0.00002	2.07714	0.00007	8.52
34-35 cm	18.5930	0.0011	15.6324	0.0010	38.6433	0.0027	2.47203	0.00007	1.18942	0.00002	2.07835	0.00005	10.28
35-36 cm	18.6578	0.0011	15.6435	0.0010	38.7949	0.0027	2.48007	0.00008	1.19266	0.00002	2.07944	0.00006	9.47
36-37 cm	18.6634	0.0007	15.6422	0.0008	38.7384	0.0022	2.47661	0.00009	1.19316	0.00002	2.07568	0.00006	16.46
37-38 cm	18.6544	0.0140	15.6479	0.0128	38.7285	0.0289	2.47523	0.00024	1.19239	0.00009	2.07587	0.00012	0.41
38-39 cm	18.7899	0.0007	15.6533	0.0007	38.8689	0.0018	2.48316	0.00006	1.20041	0.00002	2.06860	0.00004	18.37
39-40 cm	18.8126	0.0010	15.6548	0.0009	38.9240	0.0027	2.48643	0.00007	1.20175	0.00001	2.06901	0.00005	11.93
40-41 cm	18.8150	0.0009	15.6543	0.0008	38.9365	0.0025	2.48733	0.00009	1.20188	0.00002	2.06953	0.00007	10.10
41-42 cm	18.7943	0.0009	15.6521	0.0009	38.8940	0.0025	2.48497	0.00007	1.20078	0.00002	2.06946	0.00005	10.07
42-43 cm	18.8061	0.0009	15.6532	0.0009	38.9225	0.0023	2.48656	0.00008	1.20145	0.00002	2.06964	0.00005	10.87
43-44 cm	18.8086	0.0010	15.6553	0.0010	38.9464	0.0026	2.48773	0.00008	1.20147	0.00002	2.07057	0.00005	7.48
44-45 cm	18.8159	0.0014	15.6552	0.0012	38.9317	0.0033	2.48692	0.00006	1.20194	0.00002	2.06910	0.00004	9.07
45-46 cm	18.8199	0.0008	15.6535	0.0008	38.9538	0.0023	2.48858	0.00007	1.20231	0.00002	2.06983	0.00005	11.99
46-47 cm	18.8176	0.0010	15.6533	0.0009	38.9062	0.0027	2.48557	0.00008	1.20219	0.00002	2.06753	0.00005	13.13

Appendix IX. Source stable isotope data table

Table A9. Lead isotope compositions of relevant environmental and mining sources for each site – LG= Lutregala; WAP = Wapengo; TAR = Tarra.

Source	Local site	$^{206}Pb/^{207}Pb$	$^{208}Pb/^{207}Pb$	$^{208}Pb/^{206}Pb$	$^{206}Pb/^{204}Pb$	Reference
Coal	All	1.205	2.487	2.063	–	Díaz-Somoano et al. (2009)
Broken Hill ore	All	1.041	2.315	2.225	16.003	Chiaradia et al. (1997)
Mount Isa	All	1.043	2.318	2.222	16.112	Chiaradia et al. (1997)
Tambora lava	All	1.211	2.494	2.060	–	Turner and Foden (2001)
Krakatoa1 (1883)	All	1.191	2.479	2.082	–	Turner and Foden (2001)
Pinatubo (1991)	All	1.182	2.476	2.096	–	Bernard et al. (1996)
Roseberry ore (Risdon smelter)	LG	1.171	2.440	2.084	18.270	Townsend and Seen (2012)
Hellyer ore (Risdon smelter)	LG	1.176	2.447	2.081	18.350	Townsend and Seen (2012)
Elura ore (Risdon smelter)	LG	1.159	2.448	2.112	18.130	Townsend and Seen (2012)
Century ore (Risdon smelter)	LG	1.053	2.328	2.211	16.330	Townsend and Seen (2012)
Hobart, TAS (aerosol)	LG	1.068	2.340	2.191	–	Bollhöfer and Rosman (2000)
Smithton, TAS (aerosol)	LG	1.089	2.356	2.163	–	Bollhöfer and Rosman (2000)

Smithton, TAS (aerosol)	LG	1.106	2.373	2.146	–	Bollhöfer and Rosman (2000)
Eastern Tasmanian granites	LG	1.179	2.445	2.073	–	Black et al. (2010)
Western Tasmanian granites	LG	1.203	2.453	2.039	–	Black et al. (2010)
Deep Glen Bay granite	LG	1.185	2.437	2.056	–	Black et al. (2010)
Stony Head sandstone	LG	1.171	2.420	2.067	–	Black et al. (2010)
Derwent river background	LG	1.200	2.464	2.053	18.750	Townsend and Seen (2012)
Hobart aerosols (1995)	LG	1.068	2.340	2.191	–	Bollhöfer and Rosman (2000)
Melbourne, VIC (aerosol)	TAR	1.067	2.339	2.192	–	Bollhöfer and Rosman (2000)
Melbourne, VIC (aerosol)	TAR	1.069	2.341	2.190	–	Bollhöfer and Rosman (2000)
Melbourne, VIC (aerosol)	TAR	1.067	2.342	2.195	–	Bollhöfer and Rosman (2000)
Melbourne, VIC (aerosol)	TAR	1.069	2.339	2.188	–	Bollhöfer and Rosman (2000)
Melbourne, VIC (aerosol)	TAR	1.102	2.369	2.150	–	Bollhöfer and Rosman (2000)
Eltham, VIC (aerosol)	TAR	1.092	2.368	2.168	–	Bollhöfer and Rosman (2000)
Bundoora, VIC (aerosol)	TAR	1.066	2.341	2.196	–	Bollhöfer and Rosman (2000)
Melbourne soil/bedrock	TAR	1.185	2.472	2.086	18.800	Wu et al. (2016a)
Melbourne soil/bedrock	TAR	1.192	2.477	2.078	18.800	Wu et al. (2016a)

Melbourne soil/bedrock	TAR	1.167	2.457	2.105	18.300	Wu et al. (2016a)
Melbourne soil/bedrock	TAR	1.167	2.455	2.104	18.200	Wu et al. (2016a)
Melbourne soil/bedrock	TAR	1.139	2.420	2.125	17.800	Wu et al. (2016a)
Melbourne soil/bedrock	TAR	1.147	2.420	2.110	17.900	Wu et al. (2016a)
Melbourne soil/bedrock	TAR	1.172	2.461	2.100	18.300	Wu et al. (2016a)
Melbourne soil/bedrock	TAR	1.131	2.414	2.134	17.500	Wu et al. (2016a)
Melbourne soil/bedrock	TAR	1.139	2.420	2.125	17.700	Wu et al. (2016a)
Melbourne soil/bedrock	TAR	1.136	2.422	2.132	17.800	Wu et al. (2016a)
Melbourne soil/bedrock	TAR	1.216	2.497	2.053	19.100	Wu et al. (2016a)
Mount Macedon Gold Mine (lichen sample)	TAR	1.143	2.418	2.115	17.700	Wu et al. (2016a)
Trentham gold mine (Lichen sample)	TAR	1.077	2.354	2.186	16.700	Wu et al. (2016a)
Bendigo and Ballarat Ore	TAR	1.153	2.434	2.111	–	Wu et al. (2016a)
Sydney bedrock	WAP	1.140	2.440	2.140	–	Wu et al. (2016b)
Sydney Harbour National Park bedrock	WAP	1.159	2.478	2.138	–	Wu et al. (2016b)
Sydney Harbour National Park bedrock	WAP	1.160	2.434	2.098	–	Wu et al. (2016b)
Sydney Harbour National Park bedrock	WAP	1.142	2.447	2.143	–	Wu et al. (2016b)
Sydney Harbour National Park bedrock	WAP	1.124	2.413	2.147	–	Wu et al. (2016b)

Sydney Harbour National Park bedrock	WAP	1.158	2.464	2.128	–	Wu et al. (2016b)
Lane Cove National Park bedrock	WAP	1.127	2.434	2.160	–	Wu et al. (2016b)
Lane Cove National Park bedrock	WAP	1.165	2.476	2.125	–	Wu et al. (2016b)
Lane Cove National Park bedrock	WAP	1.176	2.500	2.126	–	Wu et al. (2016b)
Lane Cove National Park bedrock	WAP	1.156	2.467	2.134	–	Wu et al. (2016b)
Duffys Forest bedrock	WAP	1.134	2.426	2.139	–	Wu et al. (2016b)
Sydney Harbour National Park bedrock	WAP	1.114	2.402	2.156	–	Wu et al. (2016b)
Sydney Harbour National Park bedrock	WAP	1.108	2.388	2.155	–	Wu et al. (2016b)
Lane Cove National Park bedrock	WAP	1.098	2.394	2.180	–	Wu et al. (2016b)
Duffys Forest bedrock	WAP	1.121	2.432	2.169	–	Wu et al. (2016b)
Sydney Harbour National Park bedrock	WAP	1.144	2.459	2.149	–	Wu et al. (2016b)
Sydney Harbour National Park bedrock	WAP	1.146	2.445	2.134	–	Wu et al. (2016b)
Lane Cove National Park bedrock	WAP	1.123	2.441	2.174	–	Wu et al. (2016b)
Duffys Forest bedrock	WAP	1.135	2.430	2.141	–	Wu et al. (2016b)
Bega granite (feldspar)	WAP	1.166	2.441	2.093	–	McCulloch and Woodhead (1993)
Bega granite (whole rock)	WAP	1.161	2.438	2.099	–	McCulloch and Woodhead (1993
Berridale granite (feldspar)	WAP	1.159	2.445	2.109	–	McCulloch and Woodhead (1993
Petrol Sydney 1978-1981	WAP	1.137	2.397	2.108	–	Wu et al. (2016b)
Petrol Sydney 1900-1999	WAP	1.093	2.358	2.157	–	Wu et al. (2016b)
Slag North Lake Maquarie Zn-Pb smelter	WAP	1.140	2.424	2.127	17.780	Gulson et al. (2004)
Cobar copper	WAP	1.159	2.442	2.108	18.105	Gulson et al. (2004)
Southern Copper fume (PK)	WAP	1.148	2.436	2.122	17.943	Gulson et al. (2004)
BHP (PK) blast furnace	WAP	1.213	2.415	1.991	19.053	Gulson et al. (2004)
Kanahooka smelter soil (PK)	WAP	1.055	2.333	2.211	16.249	Gulson et al. (2004)
Kanahooka smelter fume (PK)	WAP	1.058	2.336	2.209	16.322	Gulson et al. (2004)

Tallawarra Power station (fly ash) (PK)	WAP	1.211	2.488	2.055	18.912	Gulson et al. (2004)
Sydney, NSW (aerosol)	WAP	1.067	2.342	2.195	–	Bollhöfer and Rosman (2000)
Cammeray, NSW (aerosol)	WAP	1.065	2.338	2.195	–	Bollhöfer and Rosman (2000))
Orange, NSW (aerosol)	WAP	1.071	2.345	2.190	–	Bollhöfer and Rosman (2000)
Canberra, NSW (aerosol)	WAP	1.064	2.337	2.196	–	Bollhöfer and Rosman (2000))
Sydney aerosols (1994)	WAP	1.067	2.342	2.195	–	Bollhöfer and Rosman (2000)

Appendices references

Bernard, A., Knittel, U., Weber, B., Weis, D., Albrecht, A., Hattori, K., Klein, J. and Oles, D. (1996). Petrology and geochemistry of the 1991 eruption products of Mount Pinatubo. *Fire and mud: eruptions and lahars of Mount Pinatubo, Philippines*. 767–797.

Black, L. P., Everard, J. L., McClenaghan, M. P., Korsch, R. J., Calver, C. R., Fioretti, A. M., Brown, A. V. and Foudoulis, C. (2010). Controls on Devonian–Carboniferous magmatism in Tasmania, based on inherited zircon age patterns, Sr, Nd and Pb isotopes, and major and trace element geochemistry. *Australian Journal of Earth Sciences*, 57 (7), 933–968. doi:10.1080/08120099.2010.509407.

Bollhöfer, A. and Rosman, K. J. R. (2000). Isotopic source signatures for atmospheric lead: the Southern Hemisphere. *Geochimica et Cosmochimica Acta*, 64 (19), 3251–3262. doi:10.1016/S0016-7037(00)00436-1.

Cahill, N. (2021). *ncahill89/BTF*. https://github.com/ncahill89/BTF [Accessed 31 August 2021].

Cahill, N., Kemp, A. C., Horton, B. P. and Parnell, A. C. (2016). A Bayesian hierarchical model for reconstructing relative sea level: from raw data to rates of change. *Climate of the Past*, 12 (2), 525–542. doi:10.5194/cp-12-525-2016.

Capon, S., James, C. and Reid, M. (2016). *Vegetation of Australian Riverine Landscapes: Biology, Ecology and Management*.
https://researchonline.jcu.edu.au/43710/6/43710%20Capon%20et%20al%202017.pdf

Chiaradia, M., Chenhall, B. E., Depers, A. M., Gulson, B. L. and Jones, B. G. (1997). Identification of historical lead sources in roof dusts and recent lake sediments from an industrialized area: indications from lead isotopes. *Science of The Total Environment*, 205 (2–3), 107–128. doi:10.1016/S0048-9697(97)00199-X.

Díaz-Somoano, M., Kylander, M. E., López-Antón, M. A., Suárez-Ruiz, I., Martínez-Tarazona, M. R., Ferrat, M., Kober, B. and Weiss, D. J. (2009). Stable lead isotope compositions in selected coals from around the world and implications for present day aerosol source tracing. *Environmental science & technology*, 43 (4), 1078–1085. doi:10.1021/es801818r.

Gulson B.L, Mizon K.J, Davis J.D, Palmer J.M and Vimpani, G. (2004). Identification of sources of lead in children in a primary zinc-lead smelter environment. *Environmental Health Perspectives*, 112 (1), 52–60. doi:10.1289/ehp.6465.

McCulloch, M. T. and Woodhead, J. D. (1993). Lead isotopic evidence for deep crustal-scale fluid transport during granite petrogenesis. *Geochimica et Cosmochimica Acta*, 57 (3), 659–674. doi:10.1016/0016-7037(93)90376-8.

Townsend, A. T. and Seen, A. J. (2012). Historical lead isotope record of a sediment core from the Derwent River (Tasmania, Australia): A multiple source environment. *Science of The Total Environment*, 424, 153–161. doi:10.1016/j.scitotenv.2012.02.011.

Turner, S. and Foden, J. (2001). U, Th and Ra disequilibria, Sr, Nd and Pb isotope and trace element variations in Sunda arc lavas: predominance of a subducted sediment component. *Contributions to Mineralogy and Petrology*, 142 (1), 43–57. doi:10.1007/s004100100271.

West Gippsland Catchment Management Authority. (2013). *Corner Inlet Water Quality Improvement Plan 2013*. https://www.wgcma.vic.gov.au/wp-content/uploads/2015/01/corner-inlet-wqipweb.pdf.

Williams, S., Garrett, E., Moss, P., Bartlett, R. and Gehrels, R. (2021). Development of a Regional Training Set of Contemporary Salt-Marsh Foraminifera for Late Holocene Sea-Level Reconstructions in southeastern Australia. *Open Quaternary*, 7 (1). doi:10.5334/oq.93.

Wu, L., Taylor, M. P., Handley, H. K. and Gulson, B. L. (2016a). Insights into past atmospheric lead emissions using lead concentrations and isotopic compositions in historic lichens and fungi (1852–2008) from central and southern Victoria, Australia. *Atmospheric Environment*, 139, 46–55. doi:10.1016/j.atmosenv.2016.05.022.

Wu, L., Taylor, M. P., Handley, H. K. and Wu, M. (2016b). Australian atmospheric lead deposition reconstructed using lead concentrations and isotopic compositions of archival lichen and fungi. *Environmental Pollution*, 208, 678–687. doi:10.1016/J.ENVPOL.2015.10.046.